Self-assembling peptide/glycosaminoglycan hydrogels for spinal therapies

Danielle Elizabeth Miles

Submitted in accordance with the requirements for the degree of
Doctor of Philosophy

The University of Leeds

School of Chemistry

September 2012

Intellectual Property and Publication Statements

The candidate confirms that the work submitted is her own, except where work which has formed part of jointly-authored publications has been included. The contribution of the candidate and the other authors to this work has been explicitly indicated below. The candidate confirms that appropriate credit has been given within the thesis where reference has been made to the work of others.

Chapter 1 - Introduction (D.E. Miles, R.K. Wilcox and A. Aggeli “Self-assembling peptides as a new class of medical device for regenerative medicine” in “Self-assembled peptide nanostructures: Advantages and challenges for their use in nanobiotechnology”. Stanford Publishing Pte Ltd, Singapore, 2012.)

Chapter 2 - Materials and methods - TEM, NMR, FTIR, CDUV (published in S. Maude, D. E. Miles, S. H. Felton, J. Ingram, L. M. Carrick, R. K. Wilcox, E. Ingham and A. Aggeli, Soft Matter, 2011, 7, 8085-8099)

Chapter 3 - Self-assembly and, morphology of peptide nanostructures and mechanical properties of their hydrogels - P_{11}-12 NMR, FTIR and CDUV data as well as TEM images (published in S. Maude, D. E. Miles, S. H. Felton, J. Ingram, L. M. Carrick, R. K. Wilcox, E. Ingham and A. Aggeli, Soft Matter, 2011, 7, 8085-8099). The remainder of the work in the publication was carried out by the other authors

Acknowledgements

It would not have been possible to write this thesis without the help and support of the kind people around me, to only some of whom it is possible to give particular mention here.

First of all I would like to thank my supervisors Dr. Amalia Aggeli and Prof. Ruth Wilcox. Both of whom have provided me with endless knowledge, support, advice and encouragement throughout my PhD as well as always remaining positive.

A big thank you also goes to Dr Elizabeth Mitchell who has known the answer to every question I've ever asked her regarding the disc and to life in general. She helped me keep my sanity when there was an oxtail shortage and during the final stages of my PhD. I certainly could not have done this without her. I'd also like to thank Dr Nik Kapur for his expertise in Rheology.

I would like to thank all in CMNS that have made my time in and out of the lab enjoyable. I'm particularly grateful to the peptide group who made me feel welcome from day one and took the time to show me what I needed to know in the early stages of this work, in particular Shane with TEM, Phil with CDUV and Steve with NMR and FTIR (whom I am also especially indebted to for taking up the arduous task of proof reading my thesis). They have also provided great travelling companions for the few conferences I have been lucky enough to attend.

Thank you to all the members of iMBE for their help and support, especially the technical staff Phil, Irivin and Lee, and for putting up with my slightly competitive side during sports days. Special thanks go to the spine group that have educated me in the world of the spine and mechanical engineering, as well as, providing a friendly forum for more of my questions and for practicing of presentations.

Special thanks go to my family for always being there, in particular my mum Angela and stepdad Ken, who are always at the end of the phone when I need them. Finally I may not have made it through without the support of such wonderful friends around me of whom there are too many to mention individually, but you should know who you are, and I am eternally grateful to have you all in my life.

Abstract

Back pain affects 80% of adults at some stage during their lifetimes, with one of the most common causes being disc degeneration. Currently, early stage interventions are limited and many patients continue to suffer further. This work focuses for the first time on using self-assembling peptide gels in the treatment of disc degeneration by providing an injectable nucleus replacement that can mimic the mechanical function of the natural tissue and restore the swelling pressure of the disc.

Here the behaviour of a range of designed P_{11} peptide blocks with systematic variations in their structure was studied and the design criteria for a suitable peptide hydrogel were established. The peptides were analysed using a series of complementary analytical techniques (proton nuclear magnetic resonance spectroscopy, Fourier transform infra-red spectroscopy, circular dichroism ultra-violet spectroscopy and transmission electron microscopy) to determine their behaviour at the molecular and nanoscale levels. Tests were also carried out on the gels to establish their behaviour both inside and outside the disc. The results have shown that the mechanical properties of the gels can be controlled by allowing up to a 10,000 fold variation in the stiffness.

The peptides were further optimised by mixing with glycosaminoglycans (GAGs) that occur naturally within the disc. It was found that the presence of GAGs in the peptide gels can enhance their material properties, making them more similar to that of the natural nucleus. The GAGs also acted as a trigger to the onset of gelation and speed up the time for gelation to occur.

P_{11}-12:GAG solutions, injected in bovine caudal discs *ex vivo,* were evaluated under compressive loading, and they were found to partly restore the biomechanical function of degenerated discs. The results also demonstrate that the new peptide:GAG materials could have applications in other fields of regenerative medicine, e.g. as substrates for cell growth or cartilage tissue engineering.

Table of contents

List of figures

List of tables

List of abbreviations

Ac	CH_3CO
AF	annulus fibrosus
Am	$CONH_2$
BMP-2	bone morphogenetic protein 2
c*	critical aggregation concentration
c^*_{gel}	critical gelation concentration
CDUV	circular dichroism ultra violet spectroscopy
Cl	chlorine
CMC	critical micelle concentration
CS	chondroitin sulphate
DMEM	Dulbecco's Modified Eagle Medium
DMMB	1,9 dimethylmethylene blue
ECM	extra cellular matrix
EM	electron microscope
FDA	Food and Drug administration
FID	free induction decay
FTIR	Fourier transform infra-red spectroscopy
FWHM	full width half maximum
G'	elastic /storage modulus
G''	viscous / loss modulus
GAG	glycosaminoglycan
HFIP	hexafluoroisopropanol
HPLC	high performance liquid chromatography
IVD	intervertebral disc
LVER	linear viscoelastic region
MMPs	matrix metalloproteinase
Na	sodium
NMR	nuclear magnetic resonance spectroscopy
NP	nucleus pulposus
PBS	phosphate buffered saline
PDN	Prosthetic Disc Nucleus
ppm	parts per million
TFA	trifluoroacetic acid
TGF-β	transforming growth factor beta
TMSP	3-(trimethylsilyl)propionate-2,2,3,3-d_4
UV	ultra violet
w/v	weight to volume ratio
w/w	weight to weight ratio

This PhD thesis is dedicated

to the wonderful horse that was Sunset.

Chapter 1

1 Introduction

1.1 Intervertebral disc degeneration in the spine and potential treatments

Back pain affects a large proportion of the population. In the United Kingdom it was found to impose the greatest economic burden of any illness studied, costing up to £12 billion per annum.[1] 80% of adults will experience an episode of back pain during their lifetimes, resulting in a wide range of effects from mild discomfort to complete immobilisation. Intervertebral disc degeneration in the lower back is one of the most common causes of back pain and in an autopsy study, 97% of individuals 50 years or older showed disc degeneration.[2,3,4]

The intervertebral disc is a complex hierarchical structure made up of the annulus fibrosus (AF) and the nucleus pulposus (NP), which are attached to the vertebral bodies by cartilaginous endplates (Figure 1).[5] Normal discs are approximately 7-10 mm thick and 40 mm in diameter.[4]

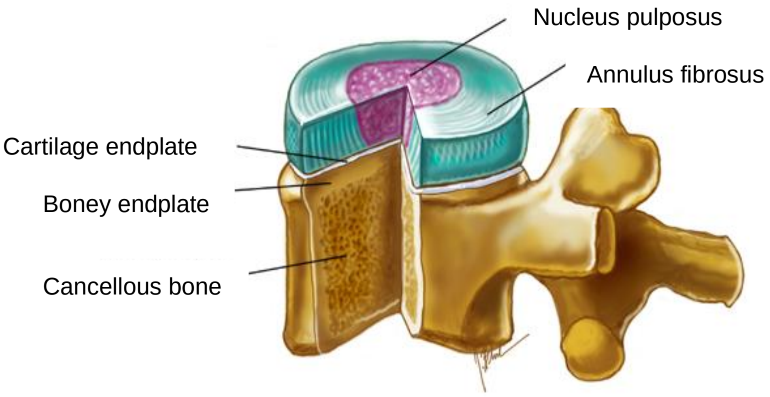

Figure 1 - The intervertebral disc structure taken from http://www.backpain-guide.com/Chapter_Fig_folders/Ch05_Anatomy_Folder/6LumbarDisk.html[6]

Together the annulus fibrosus (annulus) and nucleus pulposus (nucleus) permit motion in the spinal column as well as helping to transmit loads down the spine. The annulus is formed from 15-25 concentric lamellae consisting of dense collagen bundles, with elastin fibres lying between the lamellae.[1,4] In contrast, the central nucleus has a loose collagen network organised randomly with elastin fibres up to 150 μm in length arranged radially.[1,7] These nucleus fibres are embedded in a highly hydrated proteoglycan-containing gel.[7] The healthy adult disc has very few blood vessels and some nerves.[7] In the normal disc, oxygen and glucose concentrations are low and lactic acid concentrations are high, causing steep gradients in metabolites to develop resulting in the pH in the disc centre being acidic.[1]

Proteoglycans make up 5-15% of the wet tissue weight of the disc with the largest concentration being found within the nucleus pulposus.[1] The main proteoglycan of the disc is aggrecan.[8-10] Aggrecan consists of a protein core with up to 100 highly sulphated glycosaminoglycan (GAG) chains covalently attached.[9] The GAG chains are principally chondroitin and keratan sulphate.[9] The disc aggrecan molecules are less aggregated (30%) than in articluar cartilage (80%) and with increasing age become more difficult to extract from the matrix due to extensive cross-linking.[8] The ability of the disc to resist compression has been found to be dependent on a high proteoglycan concentration.[11]

During growth, the boundary between the annulus and nucleus becomes less obvious[4] and the nucleus pulposus undergoes major morphological and compositional changes with age and degeneration. The most significant biochemical change to occur in disc degeneration is a decrease in size and quantity of proteoglycan aggregates, resulting in the nucleus becoming more fibrotic and less gel-like.[4,11] The aggrecan molecules degrade and the smaller fragments are then able to leach from the tissue more readily than the large portions, which in turn results in a loss of GAGs.[4] This is significant because the osmotic pressure provided by the sulphated side chains of aggrecan is thought to be responsible for maintaining tissue hydration, which helps to maintain disc height and turgor against high compressive loads.[9] The elevated osmotic pressure is due to the greatly sulphated GAG groups providing a highly fixed negative charge on the matrix. This in turn attracts positively charged molecules such as small cations into the tissue to balance the negative charges. In the centre of a normal disc the concentration of Na^+ is around 400 mM and the concentration of Cl^- is around

80-100 mM compared to a concentration of around 130 mM for both ions in serum.[9] The osmotic pressure arising from this increased number of ions is responsible for the swelling pressure of the disc. Disc degeneration alters disc height and the mechanics of the rest of the spinal column, which in some cases results in patient pain.

Since the disc is avascular, its regenerative ability is limited.[12] Damage to the annulus fibrosus as it occurs in either disc degeneration or surgical disectomy causes gradual loss of disc height, which leads to changes in the biomechanics of the remaining disc. A loss in disc height causes additional loading of the facet joints and can lead to circumferential spinal segment degenerative changes.[13,14]

There are no cures for back pain and current interventions that aim at limiting pain often involve highly invasive surgeries such as total disc replacement or spinal fusion. Spinal fusion is currently the standard surgical treatment, and although it addresses both the disc and facet joint as potential sources of pain, it completely eliminates movement from the motion segment. This treatment option has unpredictable results with satisfactory clinical outcomes reported as low as 46%[15] and reoperation rates for adjacent level disc disease (i.e. a symptomatic condition) of 20%.[16] Total disc replacements aim to preserve the motion of the joint as well as restoring disc height, but there are concerns around wear particle generation and the success rates are still in the range of the spinal fusion procedure with reoperation rates being around 10%.[17,18] Therefore, in recent years there has been an interest in developing new therapies to address disc degeneration, such as transplantation, regeneration, repair and replacement.[10,19-24]

1.1.1 Transplantation

Disc allografts have seen some success in canine and non-human primate models.[25,26] Disc allografts have also been successfully transplanted into the cervical spine of five patients with a minimum five year follow up, with no immunoreactions and improved neurological symptoms of all patients.[27] However, this technique is obviously limited by the availability of non-degenerate human allografts.[27]

1.1.2 Regeneration

Some studies have explored potential therapies that focus on reviving or healing disc tissue by altering the native cells or implanting new cell populations.[28-31] In order to stimulate extracellular matrix (ECM) production and cell proliferation, injections of proteins including growth factors, such as TGF-β and BMP-2 have been investigated.[32-34] Furthermore, injections of mesenchymal stem cells have reduced degenerative changes in animal models. Such therapies are injectable and therefore minimally invasive; however, these require a structurally sound disc in the very early stages of degeneration.

1.1.3 Repair

Repair strategies concentrate on either augmenting or replacing degenerative tissue in order to re-establish healthy disc function. NP region containing chondrocyte-like cells and/or AF region containing fibroblast-like cells have been seeded in a variety of scaffolds or hydrogels.[35,36] The critical role of swelling pressure in the NP has not yet been sufficiently addressed in engineered NP constructs, whereas a particular challenge for the engineered AF tissue is in providing the mechanical function of this tissue, specifically the multilamellar organization.[37] A few groups have attempted to engineer the entire disc. However, even if the cells inside the constructs achieved appropriate phenotypes the mechanics remained inferior to the native disc.[38,39]

1.1.4 Nucleus pulposus replacement

The main challenge with the tissue engineered approaches is successfully growing/keeping the cells alive in the hostile environment inside the disc due to the disc being the largest avascular tissue in the body. An alternative to the cell based therapies is to replace the tissue with a synthetic equivalent.

In order to maintain motion in the spinal segment, the replacement of the NP without annular obliteration represents a tempting alternative to spinal fusion and total disc replacement procedures.

The aims in nucleus pulposus replacement are to slow adjacent level degeneration, restore normal load distribution to the diseased level and restore segmental spinal mechanics. The primary aim is to reconstruct the nucleus pulposus, whilst preserving the biomechanics of the annulus fibrosus and cartilage endplates. At present, the indications for nucleus pulposus replacement are for symptomatic lumbar discogenic back pain not responding to active conservative treatment for a minimum of six months.[13]

The use of synthetic hydrogels has been explored, particularly because their hydrophilic nature can mimic the transport and biomechanical properties of the natural tissue.[10] There are three classes of hydrogels currently being investigated as nucleus replacements: constrained devices, unconstrained devices and injectable devices.

1.1.4.1 Constrained devices

The most extensively studied nucleus replacement is the Prosthetic Disc Nucleus (PDN), produced by Raymedica Inc. (Minneapolis, United States), which is a hydrogel pellet surrounded by a polyethylene layer (Figure 2a). The pellet can absorb up to 80% of its weight in water because of its hydrophilic and non-hydrophilic copolymers (polyacrylamide and polyacrylonitrile), which maintain disc height, while the polyethylene layer prevents over swelling and therefore avoids consequent fractures of the vertebral endplates.[10,13]

The PDN has performed favourably in both biocompatibility and biomechanical testing. The device was found to maintain disc height, implant form and viscoelasticity up to 50 million cycles, with loads ranging from 200-800 N.[13] A schematic of the device being inserted into a cavity of the disc after the nucleus material is removed is shown in Figure 2b.

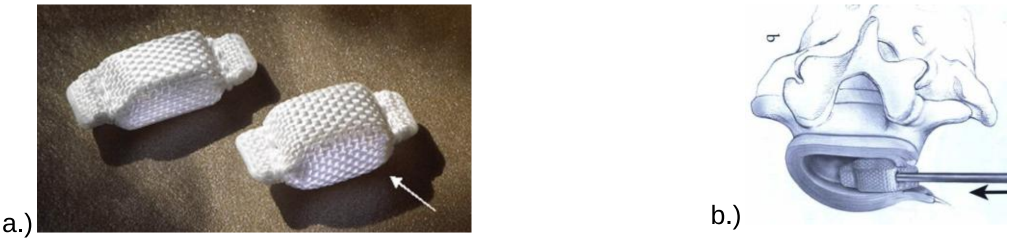

Figure 2 – a.)PDN-SOLO device in dehydrated and hydrated states. Partially taken from Di Martino *et al*.[13] b.) A schematic of the PDBN device being implanted. Adapted from Viscogliosi *et al*.[40]

Implantation of the PDN device into cadaveric lumbar spinal motion segments restored disc height and mobility of the segment close to that of the disc before nucleus removal.[41] In 2002, Klara and Ray reported favourably on clinical trials carried out on this device, with over 400 completed procedures resulting in an increase in disc height and overall reduction of pain. From 1996 – 2002, 423 patients had a surgical success rate of 90% and four year follow up data on these patients showed a significant reduction in the symptoms of disc degeneration.[42]

The NeuDisc (Figure 3) produced by Replication Medical Inc., (New Brunswick, NJ) is a hydrogel implant composed of two grades of a modified hydrolyzed polyacrylonitrile polymer. This device uses structured layers of a Dacron mesh inside the disc to prevent unlimited swelling.[10]

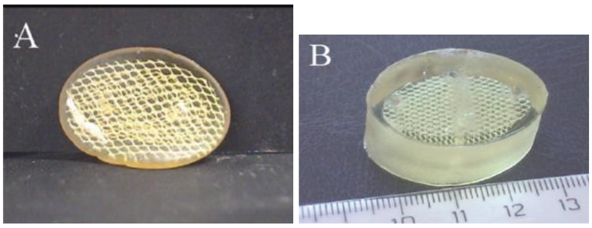

Figure 3 - Neudisc hydrogel, prehydration (A) and posthydration (B) Hydration occurs in an anisotropic fashion, mainly in the vertical plane. Taken from Di Martino *et al*.[13]

The disc can be inserted by minimally invasive methods because it is implanted in a dehydrated state. Implants of the device into the paravertebral muscle of New Zealand rabbits have not elicited toxic reactions; however results of mechanical testing are not yet available.[13]

The DASCOR produced by Disc Dynamics Inc. is a polyurethane balloon device that is filled with an injectable cool polyurethane polymer that polymerises in minutes.[10] The DASCOR® System received CE Mark approval in Europe and was sold on a limited basis for three years prior to 2010. Disc Dynamics, Inc. was unable to obtain United States Food and Drug Administration (FDA) approval to start a pivotal clinical trial in the United States and, in December 2009, Disc Dynamics shut down operations.[43]

1.1.4.2 Unconstrained devices:

Zimmer Spine (Warsaw, Indiana) have developed an elastic memory coiling spiral called the Newcleus (Figure 4). It is made of a polycarbonate urethane elastomeric material that is a biocompatible and biostable polymer with a history of use in cardiovascular applications.[10,44,45] It works by acting as a spacer with some ability to act as a shock absorber.[40,46,47]

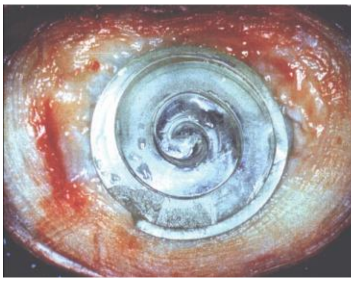

Figure 4 - The Newcleus Spiral Implant; once implanted, the device reconstitutes its original spiral shape. Taken from Di Martino *et al*.[13]

After implantation the device absorbs water up to 3-5% of its weight. The device has been tested in fatigue loading for up to 50 million cycles with 1200 N multidirectional loads. No significant wear was observed and static testing did not reveal failure as a result of the compressive load.[44] Histological studies after implantation in an animal model demonstrated good compatibility.[44] A preliminary clinical trial on five patients with a mean follow up time of 24 months resulted in decreased radicular and low back pain as well as all patients being satisfied with the outcome.[44]

The Aquarelle by Stryker Spine Corp. (Allendale, NJ) is a polyvinyl alcohol hydrogel that is implanted in a semi-hydrated state and provides uniform pressure across the endplates (Figure 5).[10] The implanted component contains 80% water, which is responsible for its viscoelastic properties.

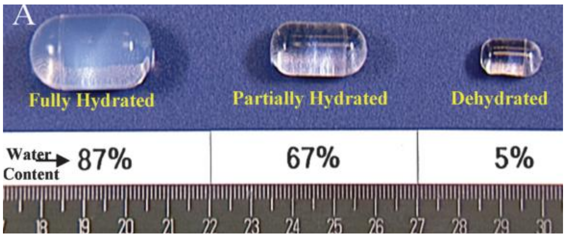

Figure 5 - The Aquerelle hydrogel final volume depends on the water content at equilibrium. Taken from Di Martino *et al*.[13]

The Aquarelle gel has shown no evidence of device-related pathology in the adjacent disc tissue, spinal cord, or remote tissues when tested in animal models[46] and has also shown biomechanical durability up to 40 million cycles.[13] The device is inserted semi-hydrated through a small anulotomy via a 4-5 mm tapered cannula and it is delivered into the cavity by a pressurised trochar.[13] However, when tested in an experimental baboon model, high rates of extrusion have been reported depending on the insertion approach.[46] High extrusion rates of 20-33% have also been reported in cadaveric studies, although when fully hydrated extrusion only occurred when the disc was placed under higher loads than expected *in vivo*. Clinical trials in Europe are currently ongoing.[46]

1.1.4.3 Injectable Devices

The injectable devices are often liquid-based *in situ* curing polymers and act as a void filler, they are advantageous to the devices discussed above because their implantation is minimally invasive and they minimize the risk of implant migration following implantation.[13] Some of the most common injectable elastomers used within the disc space are silicon and polyurethane because both can be implanted through a small anulotomy.[13,47] The polymers are designed to perform best with an intact or minimally violated annulus, therefore minimizing the possibility of polymer spread. The polymers have fast polymerising times because most monomers are toxic if absorbed in high doses.[13]

Vernengo *et al.* have developed an *in situ* forming replacement for the nucleus, which is based on branched copolymers of poly(*N*-isopropylacrylamide) (PNIPAAm) and poly(ethylene glycol) (PEG).[48] The PNIPAAm component is a thermoresponsive polymer and is free flowing at ambient temperatures and a gel at body temperature. The PEG component was used to enhance the swelling and mechanical properties of the PNIPAAm polymer: the resulting gels had a stiffness value of over 50 kPa.[48]

J&J DePuy (Raynham, Massachusetts) have developed a liquid polymethylsiloxane polymer called the SINUX ANR, which is injected in after the nuclear material is completely removed and forms an elastic mass.[10] The SINUX ANR received its CE mark in January 2004.[40]

Gelifex, Inc., (Philadelphia, Pennsylvania) have developed a polymer hydrogel (Gelifex) that is liquid at room temperature and solidifies at body temperature.[10]

Replication Medical Inc., (Cranbury, New Jersey) developed a thermoplastic hydrogel based on acrylic multiblock copolymers called GelStix$^{\text{TM}}$.[49] The hydrogel is injected in a hydrated state through an 18 G needle and reaches full hydration within an hour (Figure 6).[50]

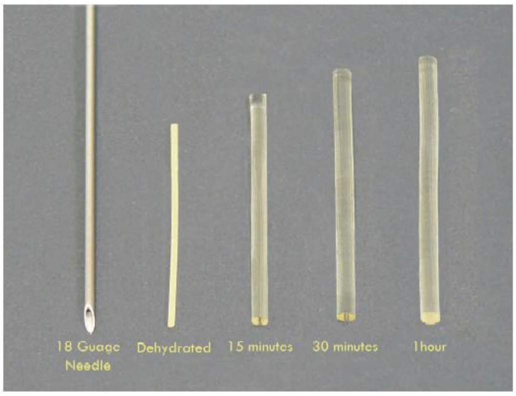

Figure 6 - GelStix$^{\text{TM}}$ Hydration. Taken from http://d2grup.com/files/GelStix%20Datasheet%2009Mar2011-2.pdf.[50]

Once implanted the hydrogel increases the pH of the disc, which is believed to enable the proteoglycans within the disc to bind water more effectively. Over 20 patients between the ages of 41 and 65 have been treated with GelStix to date with no reported complications.[50] All patients followed up have shown significant and prolonged reduction in pain with average reduction in visual analogue pain scores of 40% at one week post-operative and 80% at three months follow up. [50]

The Biodisc developed by Cryolife Inc. is an injectable protein-based hydrogel consisting of a mixture of protein solution (serum albumin) and a cross-linking component (gluteraldehyde). The distinct solutions are kept in separate chambers prior to exposure inside the wall of the annulus. The solutions mix as liquids *in vivo*, forming a polymerized matrix within minutes after direct injection into the disc space.[13] The cross-linking component also allows the hydrogel to be covalently bound to the surrounding annular tissue.[51] The Biodisc material is similar to epoxy glue.

Figure 7 - Schematic of the Biodisc being injected into the disc. Taken from www.cryolife.com/about/research/emerging/biodisc[51]

The NuCore injectable nucleus by Spine Wave Inc., (Shelton, Connecticut) is another protein polymer produced through DNA bacterial synthesis fermentation.[10] The advantage of using these bacterially synthesised proteins is that they are biocompatible when used or implanted in humans, but contain no human or animal components that could potentially transmit or cause disease. As a result of the synthetic design, protein polymers are capable of combining the biological functionality of natural proteins with the chemical functionality and exceptional physical properties of synthetic polymers.[40]

The NuCore material comprises a binary formula of a diisocyanate-based chemical cross-linker and a protein co-polymer solution of silk and elastin that, when injected into the disc nucleus space, cures rapidly *in situ* forming a durable, adhesive hydrogel. In extensive preclinical bench and animal testing, the injected material, when cured, has shown to be very resistant to the extrusion seen in other nuclear devices. This is due to, firstly, the bolus of cured material being much larger than the surgical entry site, therefore forming a mechanical barrier, and, secondly, to the hydrogel's adhesive properties contributing to its ability to resist extrusion.[40]

Studies have shown extensive integration of the Nucore material into the surrounding disc tissue, which prevented the implant from being extruded in any of the test specimens. The biomechanical properties of the biomaterial closely mimic the intact disc and, most importantly, extensive animal studies have shown it to be biocompatible and non-toxic.[40]

The NuCore is currently classed as an Investigational Device and its use is limited to clinical investigation only. Currently patient enrolment in clinical trials for the NuCore® injectable nucleus include patients in Switzerland, Germany, Australia and the United States.[52]

1.1.5 Discussion

Advances in nucleus augmentation therapies are underway; however, most of the devices are still in the early stages of development and further optimisation is still required.

Often the constrained devices restore disc height and provide similar biomechanical properties, but they do not perform the biological function that a hydrogel implant theoretically performs of maintaining the osmotic nutrient pumping action of an intact disc nucleus. One of the issues with the hard devices such as the Newcleus is the potential to produce wear particles. The constrained and unconstrained devices offer mechanical support but invasive surgeries are still frequently required to put them in place leaving tears in the annulus, which can lead to high levels of implant extrusion.

The injectable devices are minimally invasive and so tend to observe lower levels of implant extrusion. However, they are often injected as gels either in a hydrated or dehydrated state, therefore requiring a wide bore needle. There are concerns that the use of wide bore needles can damage the annulus beyond repair, which causes problems not only with hydrogel expulsion but has also been linked to further degenerative changes. The use of totally synthetic polymers can also lead to biocompatibility problems if the monomers are toxic. Polymers that polymerise *in situ* can lead to cell death if an excessive amount of heat is given off upon curing.

From previous studies, it is clear that in order to be successful an ideal nucleus replacement device should be:

1. biocompatible without significant systemic reactions of toxicity or carcinogenicity
2. able to endure a considerable amount of loading and exhibit low wear characteristics
3. capable of restoring disc height and osmotic pressures
4. similar in stiffness to the native tissue
5. implanted using minimally invasive procedures, which limit the destruction of the surrounding tissue, for example, a hydrogel that forms *in situ* and is injected through a narrow gauge needle as a liquid.

A class of materials not yet considered for a potential spinal therapy in the form of a nucleus pulposus replacement is that of self-assembling peptides.

1.2 Introduction to peptides

Peptides are linear biopolymers, which are made up of amino acids through their condensation to form peptide bonds as shown in Figure 8.[53]

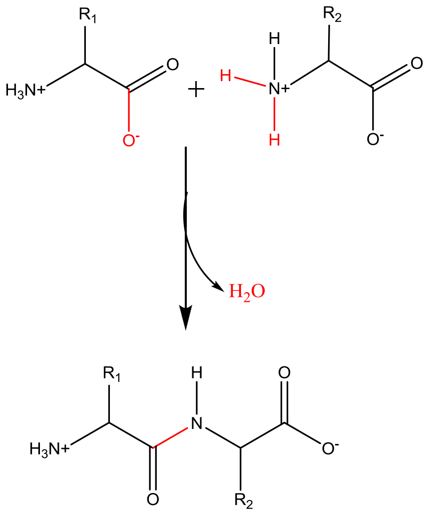

Figure 8 - The condensation of two amino acids to form a dipeptide bond. The peptide bond is shown in red.

There are 20 common natural amino acids that are used to synthesise peptides and proteins in biology, and they are often classified according to the polarities of their side chains. All 20 amino acids except for glycine are chiral and have the same basic structure as can be seen in Figure 9, varying only in R group.[54]

In the physiological pH range all amino acids, apart from histidine, that has a pKa in the range, are completely ionized and therefore can act as either an acid or a base. The salt concentration can have an effect on the behaviour of peptides, as salt ions act electrostatically to shield the side chain charges from one another, therefore reducing the charge-charge interactions.

Proteins can be considered to have four levels of structural organisation, making them more complex than peptides which generally only have two levels.[55] These two orders are the primary structure, which is the sequence of the amino acid residues in the chain that determines the specific conformation that is adopted by the peptide, and the secondary structure, which refers to the regular orientation of the peptide backbone due to hydrogen bonding.[56] The main secondary structures are the α-helix and the β-sheet.

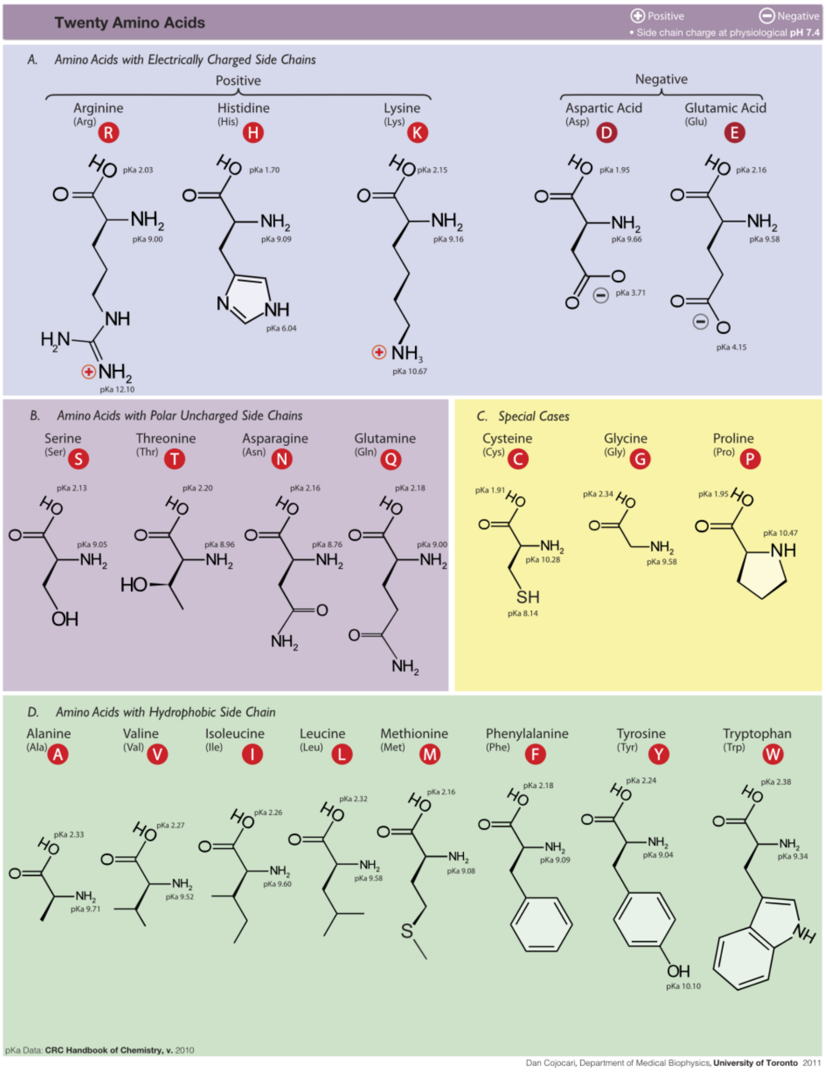

Figure 9 - Chemical structure of the 20 natural amino acids,[57] taken from http://en.wikipedia.org/wiki/Amino_acid.

1.2.1 α-helix

As is seen in Figure 10, hydrogen bonds are formed between the C=O and the N-H groups on the peptide backbone causing the peptide to coil into a helical structure.[58] Many α-helices are polar on one side and non-polar on the other and so are said to be amphipathic. This often causes them to aggregate along the non-polar side.

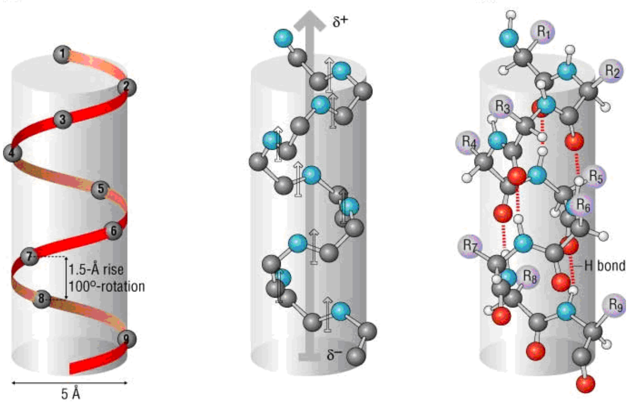

Figure 10 – Diagram of α-helix showing its rotation, hydrogen bonding and macroscopic dipole, taken from http://wiz2.pharm.wayne.edu/biochem/prot.html[59]

The α-helix structure is stabilised by intramolecular hydrogen bonds of the peptide backbone between residues i and i+4, as well as side chain interactions along the same side of the helix. The helix has a macroscopic dipole so helices tend to pack in an antiparallel manner to form bundles of helices.

1.2.2 β-sheet

Peptides can exist as extended macromolecules with a zigzag backbone. This conformation has rows of complementary hydrogen bonding sites protruding out on both sides of the peptide backbone, with rows of side chains decorating the upper and lower surfaces and is known as the β-strand. The β-sheet consists of several β-strands arranged in either a parallel or anti-parallel manner as is demonstrated in Figure 11.[58]

Hydrogen bonds form when two electronegative atoms compete for the same hydrogen atom: the hydrogen atom is covalently bound to the donor atom but interacts with the acceptor atom. The scission energy/bond strength of a hydrogen bond is typically around 20 kJ mol^{-1}, which is weak in comparison to a covalent bond that has a typical bond strength of 200-500 kJ mol^{-1} or an ionic bond, which has a typical bond strength of 250 kJ mol^{-1}.[60] In the anti-parallel structure the dipoles associated with the parallel hydrogen bond interactions enhance the overall stability, however, in the parallel structure the dipoles associated with each diagonal hydrogen bond partially cancel each other out and so do not have a stabilising effect. The stabilising effect of the hydrogen bond dipoles on the anti-parallel sheet means that it is more favourable than the parallel β-sheet.

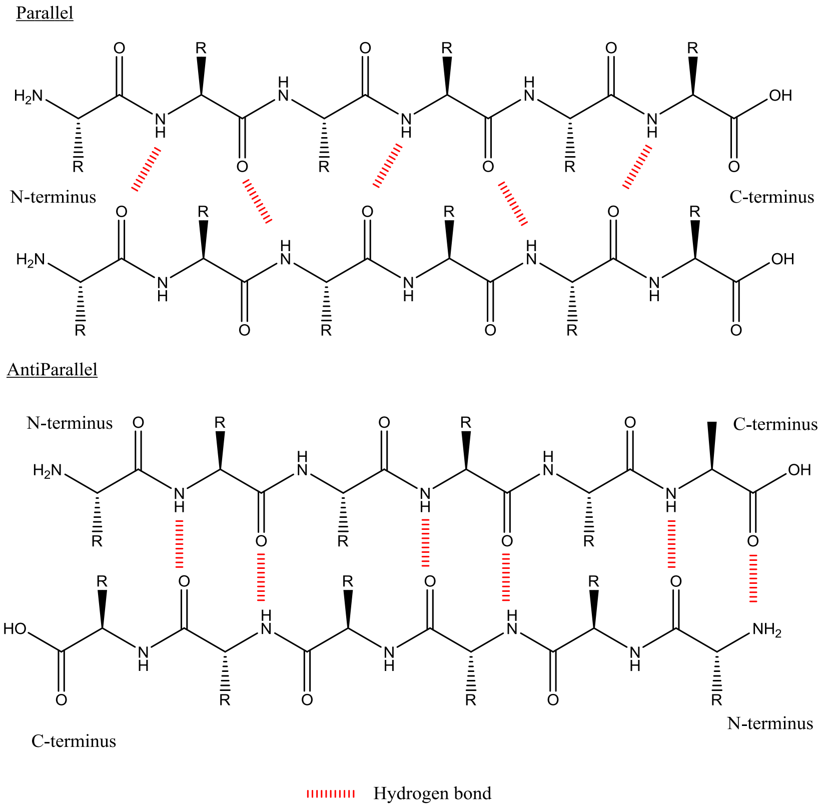

Figure 11 – β-sheet structures

A β-strand composed of all L amino acids will have a right-handed twist along its long axis to minimise the steric clashes between side chains, this will in turn cause the resulting β-sheet to have an intrinsic left handed twist along its long axis.

Since the development of solid phase peptide synthesis by Merrifield in 1959,[61-66] peptide synthesis at the laboratory scale can be readily carried out as can be seen in Figure 12.

This allows peptides to be exploited as self-assembly building blocks.

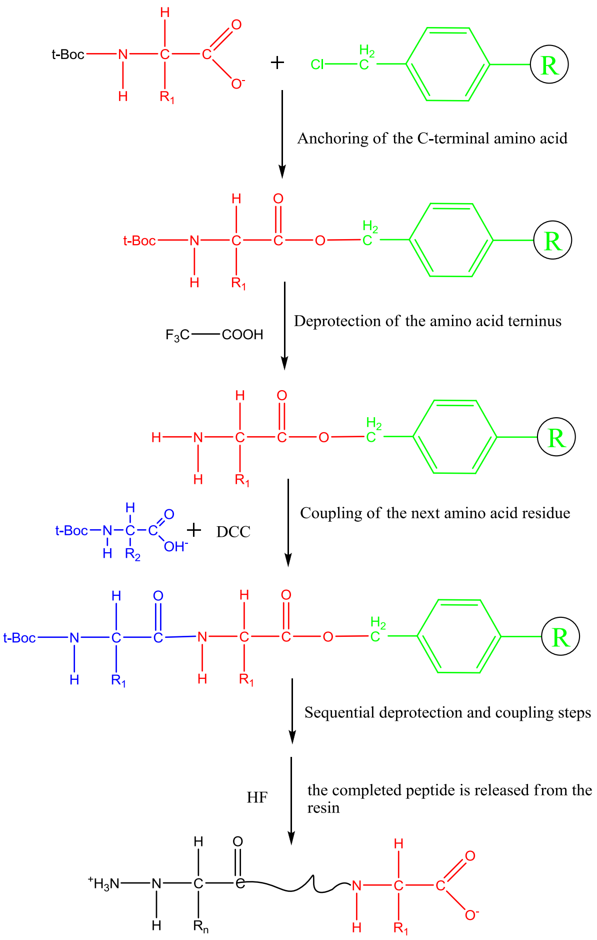

Figure 12 - Sequence of steps in solid-phase peptide synthesis.[55]

1.3 Introduction to self-assembly

Molecular self-assembly is the reversible association of molecules into thermodynamically stable, structurally well-defined aggregates (1-100 nm) held together by weak non-covalent forces, such as hydrogen bonds, ionic bonds, electrostatic interactions and van der Waals interactions.[54,67-69]

In recent years, the concept of molecular self-assembly has become a driving force for the development of new biomaterials. Molecular self-assembly is one of the two main approaches to the production of well defined, functional nanostructures essential for the fast growing field of nanotechnology; in particular molecular self-assembly is seen as the main bottom-up approach in nanoscience and nanotechnology.

All information for self-assembly is programmed into the structure of the individual building blocks and therefore the design of the building blocks is vital to achieve materials with the desirable self-assembly and functional properties. The non-covalent forces govern the energetics and dynamics of the self-assembling systems.

The process of self-assembly can occur via two different routes, nucleated or non-nucleated (classical). Which mechanism is followed can be determined by constructing a self-assembly curve that gives the fraction of molecules in aggregates or the fraction present as monomers as a function of increasing concentration.[70] In the non-nucleated process, self-assembly takes place continuously at all concentrations and only one energetic parameter is involved; the free energy change accompanying the formation of one dimer ($\alpha K_B T$, where α=association energy, K_B = Boltzmann constant, T = temperature). In nucleated self-assembly there is a critical concentration for the formation of the first aggregates (nuclei) and two energetic parameters are involved; nucleation energy and growth energy.

Many biomolecules undergo self-assembly from protein aggregation, DNA double helix annealing to lipid tubes development,[67] however, some of the most diverse building blocks in terms of chemistry, nanostructure formation and functionality are peptides and proteins.

1.4 Self-assembling model peptides

In most cases the self-assembly of linear peptides follows a nucleated mechanism and so only occurs at peptide concentrations greater than a certain value known as the critical concentration (c*). Self-assembly starts when the loss of entropy is balanced by a gain of enthalpy in the process. The main entropy loss is associated with straightening out a peptide chain from its random coil to its β-strand conformation. This is described by the energetic parameter, $\varepsilon_{trans} K_B T$, (where ε_{trans} = peptide conformational energy), and is the free energy change per molecule. Self-assembly will only progress when there are positive bonding interactions between the monomers, this is described by the energetic parameter, $\varepsilon_x K_B T$ (where ε_x = free energy change per molecule in the aggregate of type x), due to the association of two peptides.[70] The enthalpy can be gained from interactions between the hydrophilic charged and uncharged residues, which can be involved in hydrogen bonding and electrostatic interactions. The presence of aromatic hydrophobic residues can not only provide a hydrophobic environment, but the residues can also be involved in π-π stacking through the overlap of p-orbitals in the conjugated π system.[54]

As the self-assembly of peptides follows a nucleated mechanism, it has three distinct phases. The first phase is nucleation, during which there are stable monomeric peptides and some small unstable tapes rapidly forming and unforming due to the enthalpic energy gain not being great enough to counteract the entropic energy loss. The second phase is the nucleus. At this phase the enthalpic gain balances the entropic loss and so the first stable aggregates begin to form. The concentration at which this happens is the c*. The final stage is the growth stage, where the aggregates grow in size until they precipitate out of solution, phase separation occurs and a new equilibrium is set up. These three phases are observed in what is known as the self-assembly curve, which is the fraction of aggregate vs. the total peptide concentration, a schematic of an ideal self-assembly curve is given in Figure 13.

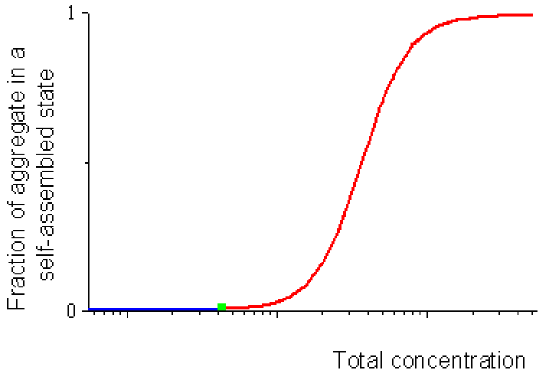

Figure 13 – Schematic of the self-assembly curve for the nucleated self-assembly of peptides. Blue line = nucleation phase, green point = nucleus or c*, red line= growth phase.

It is possible to experimentally determine the c* value by plotting a graph of monomer concentration as a function of peptide concentration. An ideal curve is shown in Figure 14.

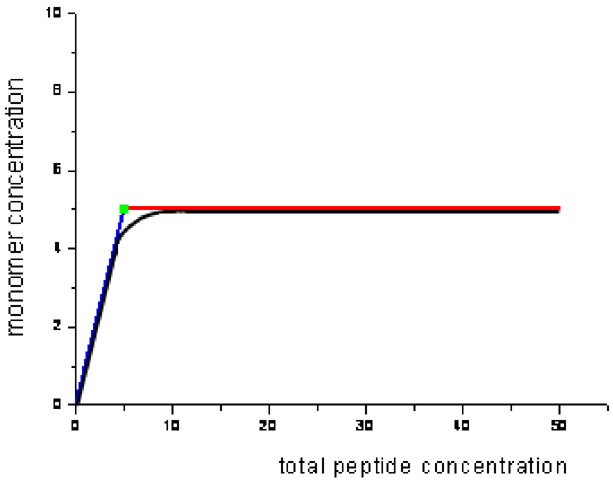

Figure 14 – Schematic of the ideal plot of monomer concentration as a function of peptide concentration for the nucleated self-assembly of peptides. Blue line = linear regime, green point = c*, red line= plateau regime.

A plot of monomer concentration as a function of peptide concentration for the nucleated self-assembly of peptides should have a linear regime below c*, where the concentration of monomers is equal to the total peptide concentration. The c* is the point at which this linear regime ceases to exist, aggregation begins to occur and the monomer concentration is less than the total peptide concentration. At a total peptide concentration greater than the c*, there is a plateau where the concentration of monomer is equal to that of the c*.

This method for calculating the critical aggregation concentration follows the standard method for establishing the critical micelle concentration (CMC) used within the surfactant field, where the monomer and or aggregate concentrations are plotted as a function of total concentration (Figure 15). The CMC is the point at which the linear and non-linear regimes intercept.

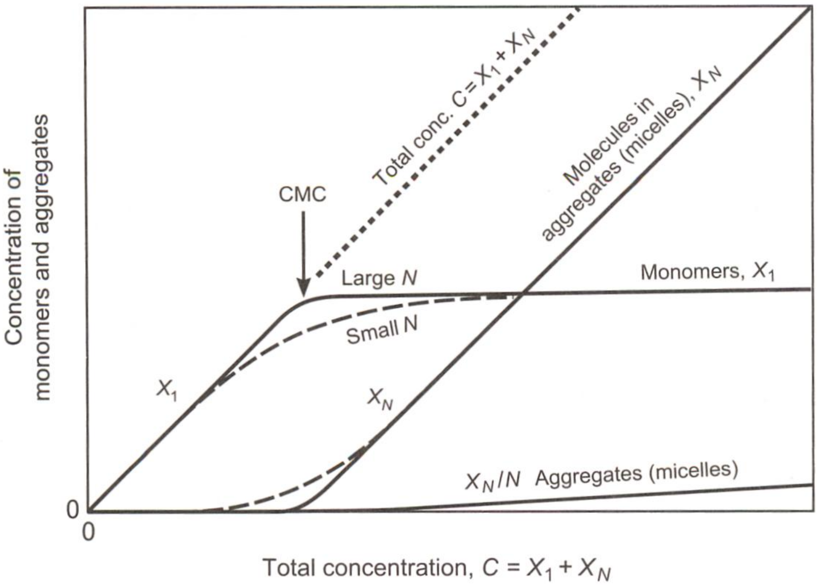

Figure 15 – Monomer (X_1) and aggregate (X_N) concentrations as a function of total concentration. The larger the aggregation number (N) the sharper the transition at the CMC. Taken from Israelachvili *et al*. [71]

The methods used most commonly to determine the CMC of surfactants experimentally are light scattering, conductivity, density, surface tension and viscosity. These methods are used to determine the point at which the linear regime changes i.e. where aggregation begins. The CMC corresponds to the intercept of the lines through the data points below and above the CMC as can be seen in the following examples:

In Figure 16 the CMC of 6-0 stearoyl ascorbate is determined by the crossing point of the two straight lines obtained from the least square fitting of the surface tension vs. log c data.[72]

In Figure 17, determination of the N-Acetyl-S-geranylgeranyl-L-cysteine (AGGC) CMC in the buffer used to extract Rho proteins by absorption spectroscopy is shown.

The CMC of cationic micelles can be determined by electrical conductivity measurements; Figure 18 shows the variation of the electrical conductivity with the cationic surfactant concentration. Again, the CMC is obtained from the interception of conductivity lines above and below the CMC.

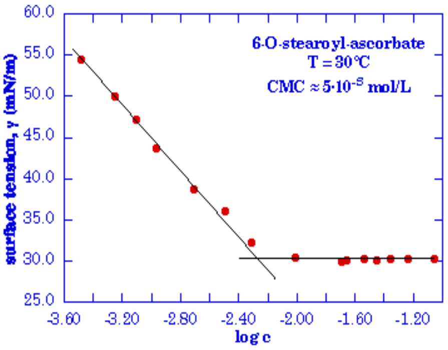

Figure 16 – Calculation of the CMC value from the surface tension vs. concentration plot. The red spots are the experimental data, the black lines are the fitting linear curves. CMC is determined as the intersection point of the two lines. Taken from http://www.netsci-journal.com/97v4/97014/vitc4.html[72]

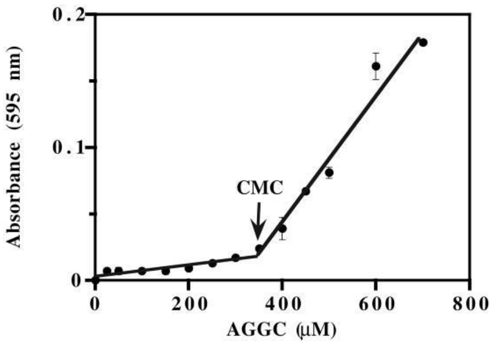

Figure 17 - Determination of AGGC critical micellar concentration using absorption spectroscopy. Taken from Desrosiers *et al.*[73]

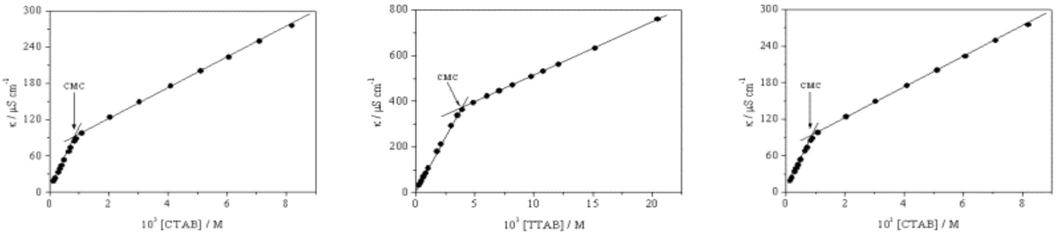

Figure 18 - Variation of the electrical conductivity with concentration for cationic surfactants. Taken from López-Díaz and Velázquez [73]

Although the above methods commonly used for surfactant self-assembly could be used to measure the critical concentration for peptide self-assembly, similar but more appropriate methods will be used within this thesis, i.e. ones that are more informative and more quantitative. The above methods provide the CMC value, however, they do not provide important structural information such that Fourier transform infra-red (FTIR) or circular dichroism ultraviolet (CDUV) spectroscopy can provide, or the background monomer concentration as provided by proton nuclear magnetic resonance spectroscopy (^{1}HNMR).

1.5 Self-assembling peptides as a new class of medical devices

It is essential to study simple model peptides so that the basic scientific principles can then be applied to much more complicated systems such as the proteins found in nature. Not only will studying model peptides help to gain an understanding of the properties and structures of peptides found in biology, but this knowledge can then be used to develop new and useful materials.

Regenerative medicine is defined by the National Institute of Health as *"the process of creating living, functional tissues to repair or replace tissue or organ function lost due to age, disease, damage, or congenital defects."*[74] This field holds the promise of regenerating damaged tissues and organs in the body by stimulating previously irreparable organs to heal themselves as well as allowing scientists to grow tissues and organs in the laboratory and safely implant them when the body cannot heal itself.[74] Although self-assembling peptides have not yet been investigated for their use as a nucleus pulposus replacement, they have been investigated in general for their potential use as medical devices, in particular in regenerative medicine and tissue engineering. In this section, the use of self-assembling peptides in regenerative medicine will be presented, with a focus on tissue engineering because this not only demonstrates their ability to self-assemble in physiological conditions but also shows their non-cytotoxicity and biocompatibility with numerous cell lines and types.

One of the most important branches of regenerative medicine is that of tissue engineering. The aim of which is to replace damaged or lost tissue by new healthy or equivalent tissue usually by the application of a combination of cells, bioactive reagents and a scaffold. In this context, the scaffold is classified as a medical device and holds a prominent place in regenerative medicine. The US Food and Drug Administration (FDA) definition of a medical device is amongst others, "*an implant or in vitro reagent intended for use in the cure or treatment of disease, which does not achieve any of its intended purposes through chemical action in the body and is not dependent upon being metabolised for the achievement of its intended purposes"*.[75] In recent years, significant research effort internationally has been undertaken to establish self-assembling peptide nanostructures as a new type of biomaterial that can act as a scaffold for tissue engineering and thus be considered as an innovative kind of medical device for regenerative medicine.

Not only do new biomaterials for biomedical applications such as regenerative medicine need to have the correct chemical, physical and mechanical properties, but they also need to be biocompatible. This means that the material must not have any toxic, allergenic, carcinogenic or mutagenic effects, as well as not affect the fertility of the patient.[76] Testing for biocompatibility can be split roughly into four levels starting with *in vitro* cell free tests, followed by *in vitro* cell based and i*n vivo* animal studies and finally with human clinical trials. Biocompatibility ideally should be confirmed at the previous level prior to investigation at the next level, due to the added costs and complexity involved as well as ethical issues.

Peptide based biomaterials have various advantages over most synthetic materials, such as they may be biocompatible and easily degraded within the body and therefore are desirable for use in the field of regenerative medicine and in particular tissue engineering.

In tissue engineering, cells (usually within a medical device known as a scaffold and in the presence of biological factors) are used to repair damaged tissue. As the scaffold is ideally meant to mimic the extracellular matrix (ECM), it is vital that it allows the cells to migrate and proliferate, whilst providing a porous network to allow the movement of nutrients and metabolites to and from the cells. The scaffold needs to be non-cytotoxic, able to withstand mechanical stimuli, and an added benefit would be the ability to deliver important bioactive substances such as growth factors

Peptides are logical building blocks for tissue engineering scaffolds for many reasons including:

- the peptide building blocks are easily synthesised, and recombinant approaches are currently being investigated to make their synthesis even more efficient.[77]

- the building blocks are chemically versatile and so structure activity relationships can be determined.
- self-assembly and gelation can be designed to be externally responsive, and so can occur *in situ*, leading to injectable and minimally invasive treatments for patients.[78]
- the gels that are formed are fairly strong despite being intrinsically soft matter, therefore giving mechanical rigidity to provide a self-supporting scaffold in the presence of the desired cells.
- the gel networks are not covalently linked and so the matrix has the ability to remodel during cell proliferation.
- peptide gels consist of a very low dry peptide weight (typically 0.5-3%) and their porous structure allows both cellular nutrients and waste to diffuse through the gel.
- peptide materials are biodegradable.
- if natural amino acids are used, then minimum immunogenicity and maximum biocompatibility is expected.
- bioactivity can be incorporated into the building block design such as the RGD (Arg-Gly-Asp) cell adhesion domain.[79]
- peptide nanofibres are similar in size to the extracellular matrix *in vivo.*

Not only are peptide nanofibres currently being investigated for their potential applications as scaffolds for musculoskeletal, skin, neural, and vascular tissue engineering, but there is also interest in their use as controlled delivery vehicles for drugs, proteins and DNA.[80]

In the following section, an overview of the self-assembly of peptides will be discussed, in particular how self-assembling peptides can be used as biomedical devices in regenerative medicine, especially within the context of tissue engineering, where most of the advancements have taken place in the past years. The individual main families of peptide building blocks will be considered alongside their self-assembly pathways, their biocompatibility and usefulness as new scaffolds.

1.5.1 Self-assembling *de novo* designed peptides in physiological conditions and their applications as scaffolds in tissue engineering

In the early 1950's Pauling and Corey[81] and others identified possible structures that proteins and peptides could adopt such as the parallel and anti-parallel β-sheets. Early research found that alternating hydrophobic and hydrophilic residues led to the formation of water soluble β-sheet structures through self-assembly in the presence of salts.[67]

1.5.1.1 β-structured systems

The self-assembly of β-structured peptides typically follows a nucleated mechanism as described above in Section 1.4. A range of peptide building blocks have been designed to undergo self-assembly in physiological-like conditions for applications in tissue engineering. These β-structured peptides can be broadly divided into five categories: ionic β-sheet peptides, tape-forming peptides, β-hairpins, aromatic short peptides and peptide amphiphiles.

Ionic β-sheet peptides

The first peptide structures on the nanoscale were designed by Ghadiri *et al.* in the 1990s. His group developed cyclic peptide nanotubes.[69,82] At around the same time Shuguang Zhang and his co-workers were investigating the use of charged peptide building blocks, which would readily self-assemble into peptide nanostructures due to charge complementary interactions between negatively charged glutamic and aspartic acids and positively charged lysines and arginines.[83,84]

EAK16 and RAD16 (Figure 19) both have 16 residues and were designed to study the properties of ionic complementary peptides and to develop biological scaffolds for tissue engineering.[78,85]

$$\text{EAK}_{16}\text{:}\quad \text{AcN-A}\overset{-}{\text{E}}\text{A}\overset{-}{\text{E}}\text{A}\overset{+}{\text{K}}\text{A}\overset{+}{\text{K}}\text{A}\overset{-}{\text{E}}\text{A}\overset{-}{\text{E}}\text{A}\overset{+}{\text{K}}\text{A}\overset{+}{\text{K}}\text{-CNH}_2$$

$$\text{RAD}_{16}\text{:}\quad \text{AcN-}\overset{+}{\text{R}}\text{A}\overset{+}{\text{R}}\text{A}\overset{-}{\text{D}}\text{A}\overset{-}{\text{D}}\text{A}\overset{+}{\text{R}}\text{A}\overset{+}{\text{R}}\text{A}\overset{-}{\text{D}}\text{A}\overset{-}{\text{D}}\text{A-CNH}_2$$

Figure 19 - Zhang *et al.* complementary ionic peptides[78]

The RAD16-I self-assembles into a nanofibre structure as demonstrated in Figure 20.

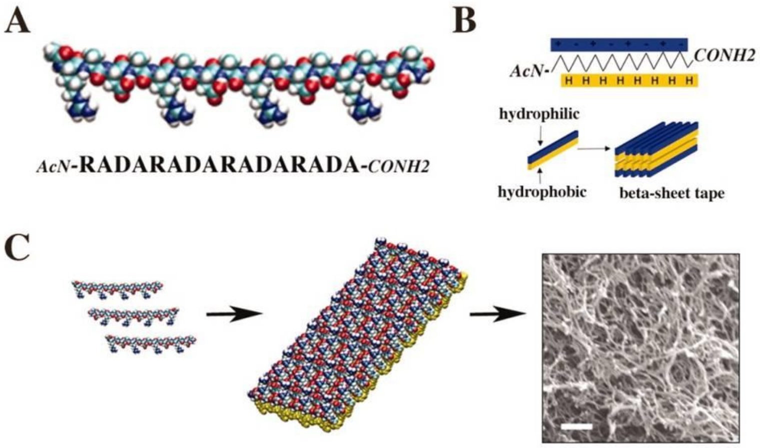

Figure 20 - (A) Molecular model of peptide RAD16-I. (B) Molecular model of the nanofiber developed by self-assembling RAD16-I molecules. (C) RAD16-I nanofiber network viewed by SEM. White bar represents 200 nm. Taken from Semino *et al*.[67]

From these building blocks it was proposed that several features of the monomer contributed to the formation and stability of the self-assembled structures such as:[78]

i. the formation of intermolecular ionic bonds between the side chains of the charged residues;

ii. formation of hydrophobic β-sheet interactions between methyl groups of the alanine residues;

iii. staggered individual peptides, suggesting initially a two-dimensional rather than a one-dimensional self-assembly process.

Some of the ionic self-complementary peptides of the Zhang group have been found to form both stable β-sheets and α-helices, with the resulting structure being dependent on the environment.[84] However, the β-sheet forming peptides were selected for evaluation as medical devices in tissue engineering.

Control of the process in molecular self-assembly is of great importance. Many systems suffer from the disadvantage of spontaneous self-assembly as soon as the sample is placed in to solution, due to the nucleation and growth being poorly controlled.[54] For this reason there has been a large amount of interest in developing methods to trigger self-assembly or dis-assembly on cue. The size of the energetic parameters of the self-assembling peptides are dependent on a number of variables including solution conditions, therefore peptides can be designed to undergo self-assembly after an external trigger, such as a change in pH, ionic strength or temperature.[70,86,87] It has been established that the presence of glutamic acid or ornithine amino acid residues in the primary structure of the peptide can provide a reversible control through changing the pH or ionic strength of the solution.[70,88,89] Further stimuli of use can be metal ions, enzymes and light.[90]

Zhang and co-workers have used the pH stimuli to trigger reversible α-helix to β-sheet transitions. They have used the EAK amino acid sequence originally found in zuotin, a yeast protein, to demonstrate how the nanostructures formed are dependent on the pH of the solution. The EAK16-IV peptide (Ac-AEAEAEAEAKEKEKEKEK-Am) forms globular assemblies in the physiological pH range but below 6.5 or above 7.5 it forms fibrillar structures.[91] The EAK12 peptide (Ac-AEAEAEAEAKAK-Am) forms a stable β-sheet at pH 1-3 but with an increase of pH up to 5, 30% helical structure was observed.[84] Their DAR16-IV (Ac-ADADADADARARARAR-Am) peptide showed the opposite behaviour.

The Tan group use a design principle similar to that above exploiting the protonation of glutamic acid and arginine residues. Their peptide RATEA16 (Ac-RATARAEARATARAEA-Am) forms a high water content hydrogel around neutral pH, because the peptide has an overall charge of +2 and so electrostatic interaction between arginine and glutamate residues occur as well as interstrand repulsion. By contrast, below pH 3.5, due to an overall peptide charge of +4, the peptide exists as a monomer, while above pH 12.5 the peptide has no net charge and so aggregation occurs with no interstrand repulsion.[92]

The solution property of ionic strength has also been exploited by designing a series of self-complementary ionic *de novo* peptides that have been found to form hydrogels when exposed to physiological concentrations of monovalent alkaline salts.[84]

Peptide folding is sensitive to temperature changes and therefore temperature can be used as another self-assembly stimuli. Temperature as well as pH can be used to trigger the reversible β-sheet to α-helix transition of the two peptides EAK12 and DAR16-IV. For EAK12 a β-sheet conformation is seen at 25°C and an α-helical conformation at 85°C, whereas for the DAR16-IV peptide the transition to an α-helix conformation occurred at 75°C.

One of the most comprehensively studied self-assembling peptide systems applied to tissue engineering is the RAD-based self-assembling ionic peptides, RAD16-I (Ac-RADARADARADARADA-Am) and RAD16-II (Ac-RARADADARARADADA-Am), which, form hydrogels in physiological conditions. It is the RAD16-I peptide, which was one of the first commercially available self-assembling peptides and is marketed under the name of PuraMatrix (3DM, Inc. Cambridge, MA, USA) (BD, Erembodegem,Belgium). It has been shown that these peptide hydrogels can support cell attachment of numerous types of mammalian cells including human carcinoma, embryonic kidney, hepatocytes, neuroblastoma, fibroblasts, neural cells, and osteoblasts.[3,93-98] Six week old BALB/cAnNCrl mice have been used to test the biocompatibility of RAD16-I peptide cell culture scaffolds and it was found to elicit no inflammation or immunologic responses.[99,100]

A study was carried out comparing several hydrogels including PuraMatrix to test their compatibility with human neural stem cells, hNSC.[101] PuraMatrix was found to be a superior hydrogel to both Matrigel and pluronic F127, showing less toxicity, lower gelation concentrations, allowing hNSC migration and neuronal differentiation.[101] McGrath *et al.* confirmed these findings in another investigation using PuraMatrix as a cell carrier for neurotransplantation in peripheral nerve regeneration: the peptide gel supported cell attachment and differentiation by providing a suitable extracellular matrix for cultured Schwann cells and also provided a substrate for neurite outgrowth from dorsal root ganglia.[102] The RAD16-I peptide 3D scaffold has also been found to promote the survival and growth of implanted mouse embryonic fibroblast cells.[99]

RAD16-I has been used to promote axon regeneration in hamsters with a severed optic tract, the result of which was functional return of vision. The self-assembled peptide scaffold provided an environment similar in scale to the extracellular matrix for axons to regenerate and to reconnect to brain tissue.[100] Functionalisation of RAD16-I, with the addition of either an RGD binding sequence or a growth factor specific to endothelial cells, has led to successful 2D and 3D cell culture of human umbilical vein endothelial cells, promoting cell survival, proliferation and morphological differentiation *in vitro*.[103]

Zou *et al.* have enriched the RAD16-I peptide further by linking it to the FGL neural cell adhesion motif. This peptide nanofibre scaffold again showed no cytotoxicity, and promoted adhesion and neurite sprouting of dorsal root ganglion neurons.[104]

Kisiday *et al.* used another ionic β-sheet forming peptide KLD-12 (Ac-KLDLKLDLKLDL-Am), to produce a self-assembled peptide hydrogel 3D cell culture scaffold. This supported the growth of chondrocytes and therefore has the potential for the repair of cartilage. During 4 weeks in the scaffold, the cells maintained their morphologies and developed a cartilage extracellular matrix. [96,105,106]

The KLD-12 peptide has also been shown to have good biocompatibility with nucleus pulposus cells and shown to provide a microenvironment for the cells to survive and divide *in vitro*. The nucleus cells grown in 3D within the hydrogel scaffold were found to be functionally normal and phenotypically stable.[107]

Another short ionic peptide RWDW was found to undergo spontaneous self-assembly into a gel in cell culture medium. Desil *et al.* investigated it as a support for cell adhesion and growth. They found that the peptide is not cytotoxic up to a concentration of at least 70 mg/L and that it supports human hepatoblastoma cell growth in 3D.[108]

Tape-forming peptides

The Aggeli group have designed *de novo* β-sheet tape forming peptides taking inspiration from the biological β-sheet motif. These peptides self-assemble in one dimension into a hierarchy of well defined structures.[70,109] If used at high enough concentrations, these peptides can form hydrogels, organogels, or nematic fluids and gels.[109] This behaviour has been explained by a model suggesting hierarchical self-assembly of β-sheet tapes (Figure 21). The model in principle applies to self-assembly in all solvents, but to date it has only been experimentally verified in polar organic solvents (methanol) and pure water.[70,110]

Due to the chirality of the amino acid residues, the hierarchical structures of the peptides will have an intrinsic twist. For aggregation to occur, these twisted peptides must bend and change their twist to fit the packing constraints imposed by their neighbours. This results in an elastic energy cost that must be compensated for by the gain in attraction energy from the aggregation itself.[70,110]

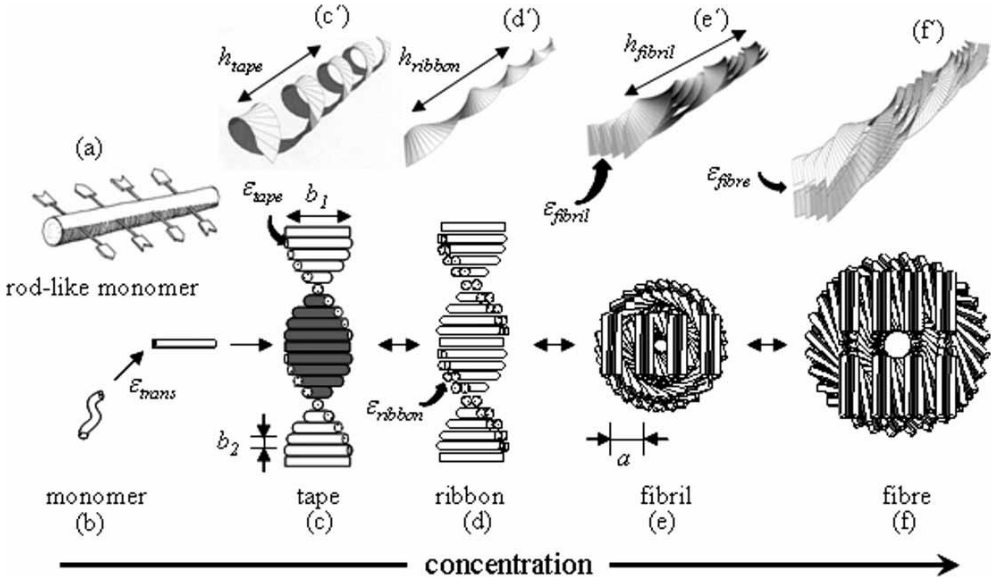

Figure 21 – Model of hierarchical self-assembly of chiral rod-like units. Local arrangements (c–f) and the corresponding global equilibrium conformations (c'–f') for the hierarchical self-assembling structures formed in solutions of chiral molecules (a), which have complementary donor and acceptor groups, shown by arrows, via which they interact and align to form tapes (c). Taken from Davies *et al*.[70]

The tape is the simplest form of β-sheet aggregate and they are usually helical in shape at equilibrium, due to simultaneous twisting and bending. The twisting comes from the chirality, and the bending from the asymmetry of the two faces.[111] For tape formation to occur the free energy gained, $\varepsilon_{tape,}$ (mainly enthalpic in nature) from hydrogen bond backbone interactions and side chain interactions needs to be greater than the free energy lost, ε_{trans} (mainly entropic in nature).[70]

Two tapes can stack together to form a pair. This type of aggregate is called a ribbon and they are stabilised by $\varepsilon_{ribbon}K_BT$, which is mainly the enthalpy gain per stacked peptide pair. The size of $\varepsilon_{ribbon}K_BT$ is dependent on intermolecular side chain – side chain interactions.[70] Ribbons have a twist but no bend, and are more rigid and longer than tapes.[110,112]

Several ribbons can further stack one on top of the other to form a fibril stabilised by $\varepsilon_{fibril}K_BT$, which is mainly the enthalpy gain per pair of stacked peptides in a fibril. The magnitude of ε_{fibril} is determined by favourable interactions between side chains on the exposed side of the ribbons. One side of the aggregate consists of N and C termini.[70,110] Again fibrils have a twist but no bend and a well defined diameter; they are more rigid and longer than ribbons.[109,110]

A pair of fibrils can undergo further self-assembly by entwining edge to edge to form a fibre. Fibres are stabilised by $\varepsilon_{fibre}K_BT$, which is mainly the enthalpy gain because of interactions between groups at N and C termini per peptide pair in the fibre.[70]

$\varepsilon_{tape,}$ ε_{ribbon}, ε_{fibril} and ε_{fibre} are all free energy changes per molecule in the aggregate. If $\varepsilon_{trans}>\varepsilon_{tape}>\varepsilon_{ribbon}>\varepsilon_{fibril}>\varepsilon_{fibre}$, then the critical concentrations necessary for the corresponding aggregates to form are in the order of $c^*_{tape} < c^*_{ribbon} < c^*_{fibril} < c^*_{fibre}$.[70]

Peptides of 7-40 amino acid residues have a tendency to form β-sheets[88] and previous work in the Aggeli group has established a set of design criteria that will produce β-sheet tapes in solution:[113]

i.) cross-strand attractive forces;
ii.) lateral recognition between adjacent β-strands;
iii.) strong adhesion of solvent to the surface of the tapes.

If followed, these will constrain the self-assembly in one dimension and avoid heterogeneous aggregates, as well as providing control of solubility.[36]

Various *de novo* β-sheet tape-forming peptides have been found to respond to pH changes (Table 1). [70,89,114] P_{11}-2 forms a stable gel below pH 5, and a study of this peptide showed that stabilisation of fibrillar dispersions requires the order of one unit of net charge per peptide in low ionic strength aqueous solution.[70,89]

Peptide	**Primary Structure**
P_{11}-2	CH_3CO-Q-Q-R-F-Q-W-Q-F-E-Q-Q- NH_2
P_{11}-4	CH_3CO-Q-Q-R-F-E-W-E-F-E-Q-Q-NH_2
P_{11}-5	CH_3CO-Q-Q-O-F-O-W-O-F-Q-Q-Q-NH_2

Table 1 - Peptide primary structures for P_{11}-2, P_{11}-4 and P_{11}-5

Insertion of further charged groups to the primary structure of P_{11}-2, as is the case with P_{11}-4 and P_{11}-5, enables self-assembly to be rapidly and reversibly controlled by small additions of acid or base.[89]

P_{11}-4 was designed to form fibrils at low pH and to be in the monomeric state at high pH whereas P_{11}-5 was designed to have the opposite switching behaviour.[89] Changes in pH were not only found to trigger self-assembly but could also be used to instantaneously switch between nematic gels and isotropic fluids.[89]

An increase in the ionic strength of the solution would be expected to screen the charged groups from each other and therefore shift the critical self-assembly concentration.[114]

Model peptides of 11 residues (see Table 2) were used to show that a change in the ionic strength of solution altered the pH responsiveness of the peptides gel-fluid transitions.[114]

Peptide	Primary Structure
P_{11}-4	CH_3CO-Q-Q-R-F-E-W-E-F-E-Q-Q-NH_2
P_{11}-8	CH_3CO-Q-Q-R-F-O-W-O-F-E-Q-Q-NH_2
P_{11}-9	CH_3CO-S-S-R-F-E-W-E-F-E-S-S-NH_2

Table 2 - Peptide primary structures for P_{11}-4, P_{11}-8 and P_{11}-9

In the study, the addition of 130 mM NaCl to P_{11}-4, a peptide designed to form β-sheet fibrils and gels at low pH, shifted the transition to monomer to higher pH values by more than 4 units, and the pH regions over which a nematic gel occurs was also increased. The most frequently observed fibrillar morphologies were found to be independent of ionic strength.[114] Addition of 130 mM NaCl to a solution of P_{11}-8, a peptide which was designed to have the opposite pH switching behaviour to P_{11}-4, was found to switch the random coil to β-sheet transition by three units to a lower pH.[114] Addition of 130 mM NaCl to P_{11}-9, a peptide that was designed to have the same pH responsiveness to P_{11}-4 but a higher relative hydrophilicity, resulted in a shift in the conformation transition by more than three units to a higher pH and also broadened the transition.[114]

The potential use of peptide based materials in biomedical applications leads to a need to assess their biological membrane activity. It is thought that peptides with an increased tendency to interact with phospholipid bilayers might exhibit membrane toxicity. Nelson *et al.* investigated the interaction of six self-assembling β-sheet peptides from the Aggeli group with phospholipid monolayers. They examined the effect of four factors using the model system of a phospholipid monolayer on a mercury electrode: peptide aggregation, polarity, net charge and applied electric field. They concluded that: i.) the solution monomer peptide species is the monolayer active moiety, ii.) β-sheet tape forming peptides are significantly less monolayer disruptive than antimicrobial peptides, iii.) amphiphilic peptides are more monolayer active than polar ones and iv.) neutral amphiphilic peptides permeabilise the phospholipid layers to ions to the greatest extent.[115]

Nelson and co-workers, also carried out a study into the effect serine, threonine, glutamine and asparagine amino acids in β-sheet tape forming peptides again on phospholipid monolayers.[116] They found that peptides with serine/threonine side chains and therefore an –OH group interact more strongly with the phospholipid monolayer than glutamine/asparagine side chains with a $-CONH_2$ group. [116]

A series of positively charged P_{11} peptides varying in polar amino acid were tested for their cytotoxicity using L929 murine fibroblast cell lines and the propensity for cell growth on the peptide gels was assessed using ATPlite assays. All peptides tested were found to be non-cytotoxic with their propensity to successfully support cell growth being dependent on the polar amino acid present (glutamine producing the best results) which is thought to be due to overall gel strength and stability.[117]

As well as soft tissue engineering, peptides may be of use in hard tissue engineering. For example, P_{11}-4 has been shown *in vitro* to increase the remineralisation of tooth enamel over a five day period as well as being capable of inducing hydroxyapatite nucleation.[118]

Another of the P_{11} series that has shown potential in regenerative medicine is P_{11}-9, which is a negatively charged serine based analogue of P_{11}-4. A series of peptides was investigated for the use as injectable lubricants for osteoarthritis and P_{11}-9 was found to perform better than hyaluronic acid in healthy static and dynamic friction testing models[88] indicating that self-assembling peptides could be developed as a therapeutic lubricant for early stage osteoarthritis.

β-Hairpins

The Schneider group have developed a group of peptides each adopting a β-hairpin structure, which are the building blocks for self-assembly. One such peptide can be seen in Figure 22.

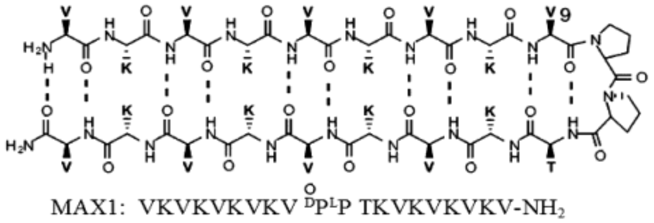

Figure 22 - Molecular structure of MAX1. Taken from Ozbas *et al*.[119]

MAX1 is a 20-residue peptide that was designed to have a β-hairpin secondary structure.[119] Figure 23 shows the self-assembly process occurring after intramolecular folding of the peptide, which is made possible by stimuli such as pH or temperature.[119,120]

Schneider *et al.* found that this design contradicts previous literature, which states that peptides composed exclusively of alternating positively charged and hydrophobic residues only form disordered precipitates and not organized gel scaffolds. However, MAX1 self-assembles without precipitating.[121]

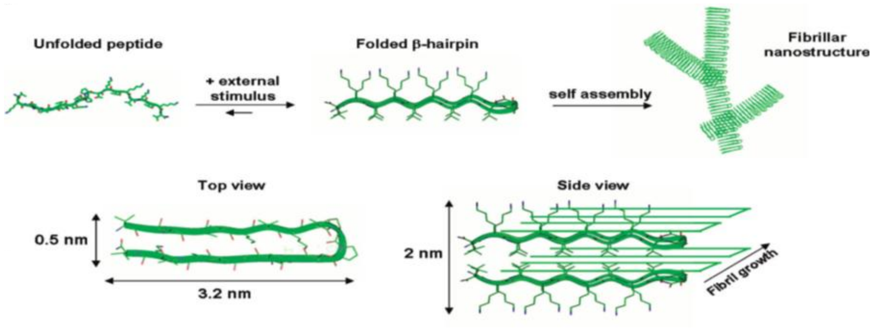

Figure 23 - Proposed self-assembly pathway. Taken from Branco *et al*.[120]

The self-assembly of the monomeric hairpins into fibrils is driven both sideways via H-bond formation between distinct hairpins and facially by hydrophobic association of the valine-rich faces of the amphiphilic folded peptide.[121] The resultant fibrils are composed of a bilayer of β-hairpins and have been found to be connected by noncovalent, interfibrillar junctions and entanglements. [119,121-123] If one hairpin is rotated relative to another in the bilayer, interfibril branching will occur and therefore will further self-assemble in two dimensions.[120]

The Schneider group have also designed a three stranded β-sheet that undergoes self-assembly in physiological-like conditions called TSS1.[124] The peptide undergoes a thermally induced folding, which results in a three stranded β-sheet amphiphilic monomer that self-assembles into a network of fibrils, 3 nm in width, forming a hydrogel (Figure 24).

As with MAX1 in the folded state, TSS1 self-assembles in a facial manner to form a bilayer sheltering its hydrophobic valine residues, as well as in a lateral manner forming a network of hydrogen bonds to give the long axis of a fibril.[123,124]

The peptide MAX1 can use pH as a trigger for self-assembly. At a pH of below 5.5, it exists as a random coil, whereas on increasing the pH to 9 a reversible β-sheet transition and gelation occur. [121,123] Temperature also plays a part in this triggerability, at pH 9 folding is only favoured above 25 °C. If this pH is decreased, folding no longer occurs, whereas if it is increased to pH 9.7 the transition temperature decreases. This shows that the net charge of MAX1 plays a vital role and requires less energy to fold the β-haripin when the overall charge is small.[121]

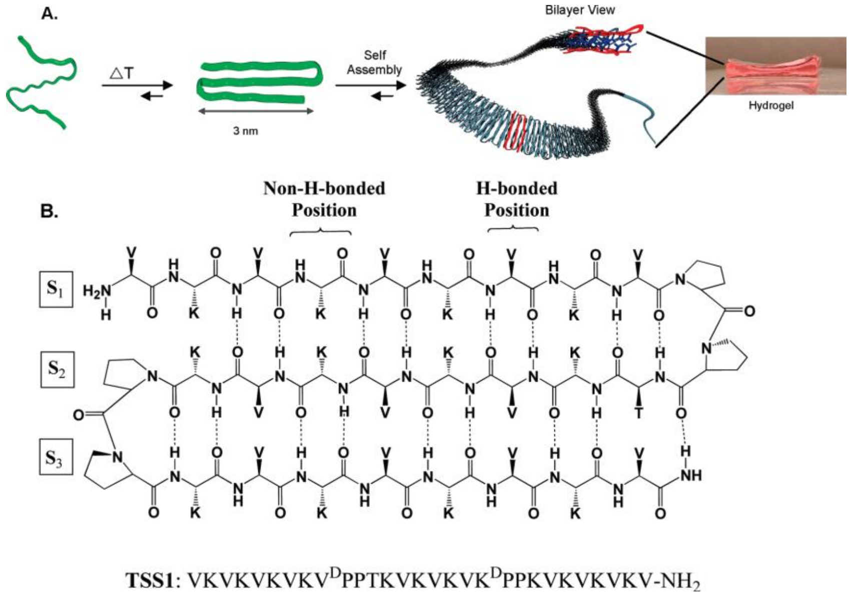

Figure 24 - A) Proposed mechanism of folding and self-assembly of TSS1, B) Structure of TSS1. Taken from Rughani *et al*.[124]

For the TSS1 peptide, folding and subsequent self-assembly and gelation in physiological conditions can be triggered by raising the temperature from 5^{o}C to 37^{o}C.[124]

The MAX1 peptide has been shown to form a hydrogel, whose surface is antibacterial with broad spectrum-activity against both Gram-negative and -positive bacteria, whilst being nonhaemolytic toward human blood cells. During co-culture experiments, MAX1 gels inhibited bacterial proliferation, yet allowed mammalian NIH3T3 fibroblast cell adhesion and proliferation.[125,126]

The TSS1 peptide has been proven to be noncytotoxic to mesenchymal stem cells when cultured on a gel surface for 24 hours. The peptide hydrogel surface supported cell adhesion and allowed cell migration, as well as allowing the cells to adopt typical morphologies.[124]

Schneider *et al.* have recently simplified their β-hairpin peptide and have designed a class of short amphiphilic peptides that undergo triggered self-assembly into β-sheet fibrils with alternating hydrophobic and hydrophilic amino acids along a linear sequence (e.g., (XZ)n). In a study into the effect of length, they found 13 residues to be optimum. They went on to investigate the rheological properties and influence of hydrophobicity and charge on this new class of XZ13 peptides.[127] LK13 undergoes saline triggered self-assembly and was found to provide the most rigid hydrogel (G' = 795 ± 105 kPa) with fast gelation kinetics. LK13 has shear thin-recovery behaviour, allowing its delivery by syringe and was assessed to be cytocompatible with murine C3H10t1/2 mesenchymal stem cells.[127]

Most of the β-peptide systems mentioned up until now are still at the design stages, however, the injectable therapeutic octapeptide lanreotide (Figure 25), which self-assembles in water into hollow and monodisperse β-sheet nanotubes (Figure 26)[128] was approved for sale in the United States by the FDA in 2007.

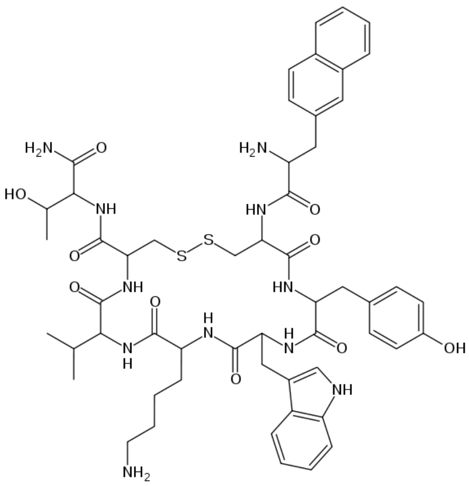

Figure 25 - Chemical structure of Lanreotide

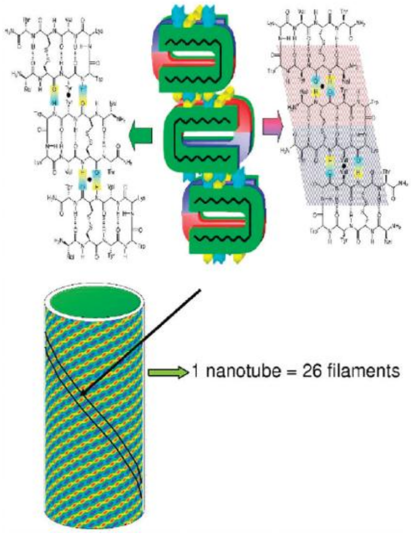

Figure 26 - (b) Molecular and supramolecular stacking of lanreotide in the nanotube wall. Colour code: green, hydrophilic; red, aromatic hydrophobic; and blue, aliphatic hydrophobic surface of the peptide. Partially taken from Pouget *et al*.[129]

Lanreotide is sold under the trade name of Somatuline[130] for an injectable treatment of acromegaly, which is a syndrome resulting from an excess in growth hormone.[131] It has also been indicated in the treatment for the relief of symptoms associated with neuroendocrine (particularly carcinoid). tumours[132]

The self-assembly of lanreotide nanotubes has three stages, i) peptide dimerisation, which occurs at low concentrations through a balance of hydrophobic interactions and electrostatic forces, ii.) ribbon growth then begins after a critical concentration up to a critical size and iii.) nanotube closure.[129]

Aromatic short peptides

Gazit and his fellow researchers, discovered that diphenylalanine (Figure 27), the core recognition motif of the β-amyloid polypeptide, forms discrete and hollow nanotubes in solution.[133] Self-assembly of this system is driven by π-stacking interactions, as well as the hydrophobic effect and hydrogen bonding.[86]

This dipeptide motif has been further developed by linking it to aromatic groups such as fluorenylmethoxycarbonyl (Fmoc) (Figure 28), resulting in structures with fibrillar morphology.[86,134-136]

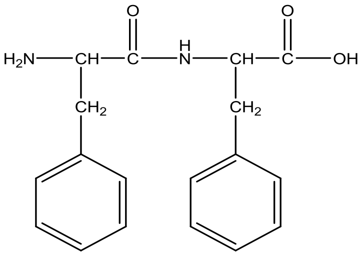

Figure 27– Molecular structure of diphenylalanine

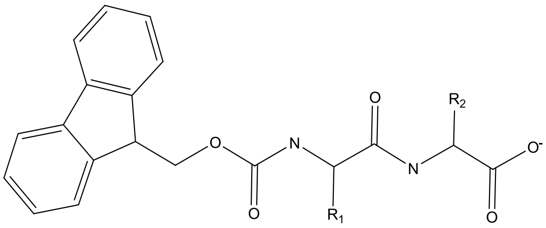

Figure 28 - Molecular structure of Fmoc-dipetides

In 1995 Vegners *et al.* reported the formation of hydrogels with Fmoc-protected peptides[137] and since it has been found that the Fmoc diphenylalanine building blocks self-assemble under physiological conditions. A molecular model has been proposed for this process, which is based on the two main features of anti-parallel β-sheets and π-stacked fluorenyl groups,[134] with the driving force for assembly being hydrogen bonding and π-π stacking.[86] The aromatic interactions also provide order and directionality to the self-assembly process.[138] The β-sheets are stabilized by the fluorenyl groups, which are on alternating sides within the fibrillar structures.[134] The Fmoc-diphenylanine along with other combinations of dipeptides have been identified to form hydrogels that are stable under cell-culture conditions and have dimensions similar to that of the fibrous components of the extracellular matrix.[86,138]

The advantage of this peptide is that it is simple and therefore cheap to produce. However, the disadvantages are that it again contains a hydrophobic section, which could be toxic to lipid bilayers, as well as it not being composed entirely of naturally occurring chemical groups. The cell cytotoxicty of various Fmoc-short peptides was investigated by growing Chinese hamster ovary cells on the surface of the gels formed and was found to be very structure dependent, with the highest viability observed in peptides containing the well known cell adhesion motif RGD and the lowest in peptides containing synthetic amino acids.[138] Chinese hamster ovary cells grown on a hydrogel scaffold made of Fmoc-diphenylamine peptide were found to have the same proliferation, viability and morphology as those grown as a control on a plastic culture plate.[139] In addition to this, the RGD motif has been attached to the Fmoc-FF peptide

(Fmoc-FFRGDF) to evaluate its biocompatibility and potential use in ophthalmology. The peptide showed good biocompatibility with minimal inflammation, when injected into the eye of Japanese albino rabbits both through clinical follow up and histology.[140]

Peptide Amphiphiles

As already detailed in the previous section, there is a class of peptide building block containing non-peptide segments that drive or influence to some extent the self-assembly process. Another such peptide design is the peptide-based amphiphiles (PA). These building blocks have two separate sections: one hydrophobic and one hydrophilic. The hydrophilic part is usually a peptide with its role being mainly bioactive rather than driving self-assembly and the hydrophobic section is usually aliphatic with its role being the driving force of self-assembly.[69] It has been discovered that an amphiphile with 16 carbon atoms in its alkyl tail attached to an ionic peptide will self-assemble in water into cylindrical micelles, due to the amphiphile's conical shape.[87] Stupp and his researchers have worked on a family of peptide amphiphiles that self-assemble into elongated nanostructures under physiological conditions and can display bioactive peptide epitopes.[87,141-143] One such peptide amphiphile building block was designed by Stupp *et al.* to direct mineralization of hydroxyapatite (Figure 29).[87]

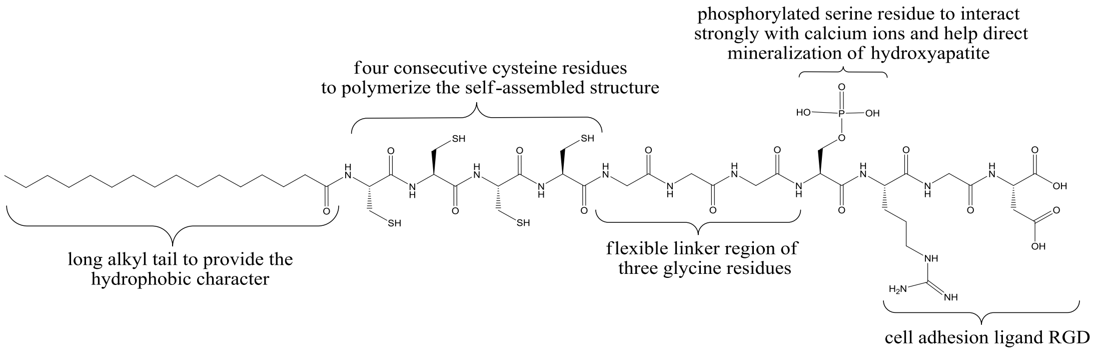

Figure 29 - Stupp *et al.* peptide amphiphile. Adapted from Hartgerink *et al*.[87]

The peptide section was designed to incorporate the RGD sequence, which has been found to play an important role in integrin–mediated cell adhesion.[87,144] The peptide amphiphile behaves as a surfactant in the self-assembly process and the surfaces of the micelles formed are the peptide section of the amphiphiles and therefore are bioactive (Figure 30).

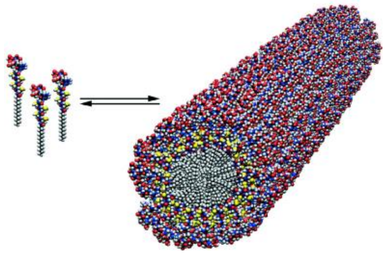

Figure 30 - Schematic showing the self-assembly of PA molecules into a cylindrical micelle. Taken from Hartgerink *et al*.[87]

A possible disadvantage with this form of building block is that the hydrophobic component of these molecules means that they cannot be delivered *in vivo* as monomers, because they may be toxic to lipid bilayers. Many of the currently reported self-assembling peptide systems are either amphiphilic or hydrophobic, which can create problems for tissue engineering, e.g. by interfering with cell membranes or natural folded protein. Cell membranes in particular are amphiphilic and so the amphiphilic or hydrophobic peptides may disrupt them. Stupp *et al.* have included cysteine residues into their peptides, which will form covalent disulphide bridges and therefore lock the self-assembled structure by cross-peptide linking, preventing free monomers escaping and causing cell death.[80] The disulphide bonds that are formed are enthalpically favourable, and assist with self-assembly. [54]

This Stupp peptide amphiphile utilises the self-assembly trigger of pH by self-assembling into cylindrical micelles forming self-supporting gels once the pH is lower than 4 and reversibly disassembles upon raising the pH.[87] It was found that with oxidation this reversibility was removed, however, upon reduction the pH reversibility was once again restored. This is thought to be due to the formation and breaking of disulphide bridges.[145] Stupp *et al.* also showed that the shape of nanostructures is pH dependent. [145]

Shorter peptide amphiphiles are also able to change morphology with a change of pH. The peptides P1 (Fmoc-VRGDV-COOH) and P2 ($C_{11}H_{19}O$-NH-VRGDV-COOH) of the Zhuo group both form interwoven fibres at pH 4; however, as the pH is increased they form large vesicle structures.[146]

Negative peptide amphiphiles analogous to that in Figure 29 have been designed to take advantage of electrostatic attractions between molecules of opposite charge, resulting in a self-assembly mechanism that can be triggered by the presence of metal ions, such as those found in tissue fluids and cell culture medium.[147] It was observed that gels prepared with transition metals had a higher modulus than those with earth metals and that polyvalent ions were much more effective initiators than monovalent ions.

The Stupp group have used their peptide amphiphiles, which have a high density of bioactive domains on their surface, to promote cell growth and differentiation leading to enamel regeneration within an *in vivo* cell and organ culture system.[148] They have also shown that, when injected in the spinal cord of mouse models, the peptide amphiphile incorporating the neuroactive domain IKVAV reduced scar formation and cell death. Moreover, this treatment increased axon regeneration after degeneration of the injected material, leading to an improvement in hind limb movement.[149]

Further to this, they have used a heparin binding peptide amphiphile that forms nanofiber gel networks *in vivo* and binds heparan sulphate like glycosaminoglycans.[150] The resultant heparan-sulphate containing peptide gels stayed within the tissue for up to 30 days and showed excellent biocompatibility. In addition to this, as the gel degraded, vascularised connective tissue formed.[150]

Interestingly, in another study, it was noted that MC3T3-E1 cells entrapped within negatively charged peptide amphiphile gels prepared using metal ion mediated self-assembly, not only survived and proliferated but also internalized the nanofibres. This suggests that not only were the nanofibres non-cytotoxic but that the cells were able to utilize the peptide molecules in their metabolic pathways and use the nanofibres as a source of nutrients.[147]

The Hartgerink laboratory has developed a self-assembling peptide system arranged in a block sequence, ABA, with the B block consisting of alternating hydrophilic and hydrophobic residues driving self-assembly and the A block consisting of charged residues e.g. MDP1 KK-SLSLSLSLSLSL-KK.[151] In aqueous solutions, this results in a facial peptide amphiphile being created.[151] The peptides first self-assemble as dimers stabilized by hydrophobic packing of the leucine residues. These dimers then go on to form fibres stabilized by anti-parallel β-sheet hydrogen bonding along the axis of the fibre. The charged end A blocks provide water solubility and to work against fibre assembly through electrostatic repulsions, thus allowing for fibre assembly and length to be controlled by A block design.[152] Multivalent ions with an opposite charge to the A block can then be used to trigger physical cross linking, fibre elongation and gelation.[153]

MDP1 was modified to include both an enzyme cleavage site and a cell adhesion motif (K-SLSLSLRGSLSLSL-KGRGDS) to increase its compatibility to living cells and enhance its role as a tissue engineering scaffold. Both of these modifications together lead to good cell proliferation and increased migration into the assembled hydrogel of human mesenchymal stem cells from teeth.[151]

Another peptide amphiphile was designed to include an enzyme-cleavable site as well as a cell adhesion motif (GTAGLIGQERGDS). This peptide formed a nanofibrous hydrogel which was found to support two adult tooth derived mesenchymal cell lines. Within the gel the cells were able to proliferate, remodel the gel by enzymatic degradation, and differentiate.[154]

The use of self-assembling peptide-amphiphiles containing the IKVAV domain as a cell culture scaffold has also been investigated by Zou *et al..* They have demonstrated their biocompatibility and bioactivity towards rat dorsal root ganglion neurons.[155]

Further to this, another group of dipeptide-based cationic amphiphiles have been developed by Kumar Das *et al.*, which are lethal to microbial cells, whilst having low to no cytotoxic effects on various human cancer cells. [156]

It becomes obvious from the cited examples above, that because of their intrinsic ability to self-assemble into fibrous and gelatinous materials; much effort has been directed so far towards β-structured systems. However, in recent years researchers have also been increasingly exploring α-helical structured systems.

α-helix/coiled coil systems

The α-helix motif tends not to be favourable for the construction of self-assembling nanostructures of increased stability due to weak intermolecular interactions stabilising the aggregates: the intramolecular hydrogen bonding on the helical peptide backbone means that intermolecular backbone hydrogen bonding is not available; therefore, for the enthalpic gain of self-assembly to override the entropic loss, the α-helical peptide typically has to be significantly longer (and thus more expensive to produce) compared to its β-sheet counterparts.

The coiled coil motif is a structure consisting of two or more α-helices that are wrapped around each other in a superhelical manner. The building block has a heptad repeat of hydrophobic and polar residues which are often designated **abcdefg** (Figure 31).[157]

When in an α-helix conformation, the hydrophobic residues at **a** and **d** are brought together to form an amphipatic structure. It is then through these hydrophobic faces that two or more helices can associate together to form a helical fibre. The number of helices in a coiled-coil is determined by the packing of the core residues. Stabilizing interstrand salt bridges can be formed if complementary charged residues are placed at positions **e** and **g**.

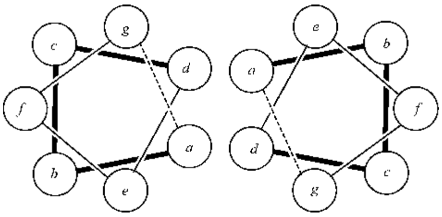

Figure 31 - Schematic representation of a coiled coil structure using a helical wheel. The letters indicate the different residue positions. Taken from Lowik *et al*.[90]

The Woolfson group have designed peptides based on α-helical building blocks and have elucidated design principles to drive the self-assembly of the building blocks into helical coiled-coil fibres. In the early 2000s work began on a dual peptide system, which comprised of two complementary short peptides that assembled to form an offset or sticky ended dimer in water. Using various solution-phase biophysical methods and microscopy, they were able to determine the pathway of self-assembly for an α-helical fibre. The self-assembly process is nucleated, with nucleation involving the aggregation of six or more partially helical dimers. After nucleation, the initial growth is somewhere between 2.5 and 3-dimensional with the fibres first growing as thick cylinders, then, as they reach an equilibrium width, further growth occurs only through elongation (Figure 32). An important consideration with this peptide design is that all faces of the helical building block are used in the self-assembly process. Therefore it can be quite challenging to incorporate additional functional domains without disrupting the self-assembling nanostructures.

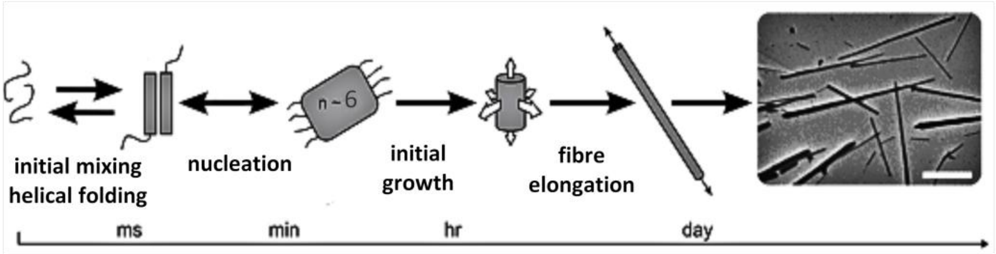

Figure 32 - Schematic of self-assembly pathway. Taken from Bromley *et al*.[158]

More recently, the Woolfson group’s work has been on a single designed peptide that assembles into stable ordered α-helical fibres, which has been named the MagicWand.[159] The MagicWand again has a basic heptad repeat **abcdefg** with hydrophobic residues at positions **a** and **d** and polar residues elsewhere. Isoleucine was placed at position **a** and leucine at position **d** as this pattern strongly promotes coiled coil dimers (Figure 33). To maximize the thermodynamic stability of MagicWand and to favour the staggered alignment of helices, charged residues were used at position **e** and **g**.[159] The self-assembled fibres of this peptide in phosphate buffered saline solution are microns long and tens of nanometres thick. The fibres are straight and do not branch, and form at sub-micromolar peptide concentrations.[159]

As with the β-structured peptides, the folding and unfolding of coiled coils, and hence their self-assembly, can be controlled by physical triggers. pH can be used to induce folding or unfolding of coiled coils by the (de)protonation of side chains. With the coiled coil peptides, (de)protonation of amino acid residues at positions **e** and **g** leads to the disruption of interchain salt bridges and therefore destabilizes the coiled coil.[157]

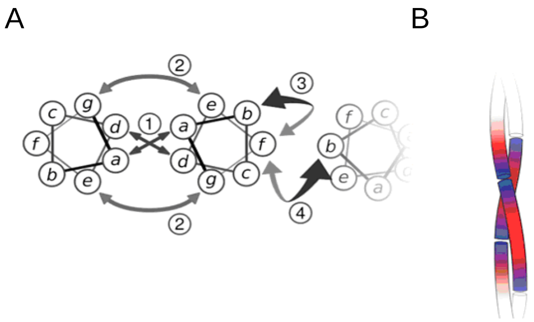

Figure 33 **- (A) Helical-wheel representations for two R-helices showing various coiled-coil interactions: 1, hydrophobic packing; 2, charge-charge interactions; and intrahelical; 3, interhelical; 4 cation-π interactions. (B) Cartoon of the coiled-coil target structure. Taken from Gribbon et al.**[159]

It is also possible to observe a structural rearrangement of a coiled coil peptide by increasing the ionic strength of solution through the addition of NaCl from 2 mM to 150 mM at pH 7.[160] An increase in temperature has been used to trigger the α-helix to β-sheet switch in a range of short coiled coil peptides.[161,162]

Hydrogels based on purely α-helical structures with a >99 % water content have been used as substrates in cell culture of rat adrenal pheochromocytoma cells. The hydrogels not only supported cell proliferation and differentiation but also maintained a similar appearance of the cells to ones seeded on the widely used ECM extract, Matrigel.[163] The coiled coil system used has the advantage of having two peptide components and therefore only gels upon mixing, offering considerable control.

1.5.2 Discussion and future perspectives

All the examples outlined above show the potential for self-assembling peptides to act as scaffolds for tissue engineering and show great promise in regenerative medicine. The use of “smart” materials that are externally responsive makes them favourable for minimally invasive treatments and 3D cell culture scaffolds. The optimisation of these smart materials to include cell adhesion motifs takes their potential even further.

Even though the field is in its infancy, it is already very difficult to compare the biocompatibility of the different peptide systems due to the numerous different tests and cell lines used. Further to this, the different systems have been used as tissue engineering scaffolds for different cell lines, and contrasted to different controls, again making comparisons between the different peptide materials virtually impossible. Standard tests and cell lines to use in all cases would be of great benefit to take this field further into understanding the key design principles that would lead to even more impressive scaffolds, more closely fulfilling the specific needs of individual applications.

Due to the inherent complex nature of these systems, one of their potential issues when it comes to their application is the reproducibility of their properties. The lack of reproducibility sometimes observed in self-assembling peptides has many origins; one of them is related to slow kinetics as demonstrated by the P_{11}-12 peptide.[117] This is one of the reasons why it is so essential to study the fundamental principles to truly understand peptide self-assembly prior to application.

Another factor often partly overlooked, that can lead to irreproducible behaviour is peptide purity, including HPLC purity, but equally important and largely ignored percentage peptide content, and type of non-peptide impurities. It is important to complete a full quality control of the peptides (including those purchased from companies and certified to be pure), prior to their usage to ensure that the peptides are not only free from impurities, but are also producing samples with correct peptide concentration taking into account possible counter ions.

One concern that has arisen over the use of peptides for biomedical applications is that they often have a fibre assembly process reminiscent of amyloid fibrils, which are associated with numerous diseases such as Alzheimer's. Simple tests with amyloid dyes such as congo red and thioflavin T can be carried out, however these are not conclusive because the dyes bind through aromatic interactions. So it can be hypothesised that many peptides containing aromatic residues, whether amyloidogenic or not, will bind to these dyes. Although this dye method was used by Gazit to confirm the completely different amyloidogenic potential of nearly identical peptide fragments,[164] the only real way to test for amyloid nucleation is to carry out in vivo studies using appropriate animal models. Westermark *et al.* have investigated the seeding specificity in amyloid growth induced by heterologous fibrils and the results showed that in general seeding of fibril elongation is highly specific, being exquisitely sensitive to point mutations at certain positions in the amyloidogenic peptide.[165] They have also investigated the possible amyloidogenicity of RAD16-I and found it to be amyloidogenic when the fibrils were made by dilution of the peptide in DMSO but not when dissolved directly in water, suggesting that that subtle variations in secondary and tertiary structure can alter the efficacy of cross-seeding.[166]

This said there have been many important milestones for the use of self-assembling peptides for biomedical applications. β-sheet based polypeptide silk fibres have been used in medicine for many years, as well as the lanreotide β-sheet peptide, which has received FDA approval. These peptides, as well as others that are in the process of entering the market, pave the way for the establishment of self-assembling peptide nanostructures as innovative medical devices for regenerative medicine, with, no doubt, many more to follow.

1.6 Summary

Disc degeneration is one of the major causes of back pain especially in the lower back. At present, late stage interventions have poor long term outcomes. A potential earlier stage treatment is nucleus augmentation, however current devices are not optimal, in particular often failing due to expulsion.

Although the devices in development at the moment are beginning to tackle the problems associated with disc degeneration, the lack of standard mechanical and biological models and tests hinders their development. It is difficult to compare the devices as different models and tests have been used throughout. A greater understanding of disc behaviour in a healthy and degenerated state is needed to fully develop suitable models for the testing of such devices. With better models the high expulsion levels seen in the early clinical trials for some of these devices may have been avoided.

Self-assembling peptides are a new class of materials with the potential application as biomaterials. They are starting to be investigated for their use in regenerative medicine and are already showing good biocompatibility. As yet the use of self-assembling peptides for nucleus augmentation has not been evaluated. All of the reasons that make peptides logical building blocks for tissue engineering scaffolds stand true for a nucleus pulposus replacement material, e.g. their chemical versatility, biocompatibility and triggerability.

The P_{11} series of β-sheet tape forming peptides are particularly advantageous as they are based on entirely natural amino acids and are shorter than other equivalent families, therefore being easier and more cost effective to make. They also undergo 1D hierarchical β-sheet self-assembly that can be controlled through the use of triggers such as pH, temperature and ionic strength. The ability to change the polar uncharged group offers them great versatility in terms of not only their chemical, but also mechanical properties. By using peptides with entirely natural amino acids, maximum biocompatibility is expected. However, as peptides are very versatile in their chemistry, if it is found that certain types of amino acids or a certain size of peptide elicits an immune response *in vivo*, they can be immediately modified.

The behaviour and self-assembly mechanism of the P_{11} peptides have not been fully characterised in physiological conditions, in particular the design criteria needed to make them suitable candidates for biomedical applications. For nucleus augmentation, ideally the material produced will undergo a transition from being soluble outside the human body to a gel after injection into the body. In other words, a suitable peptide will need a chemical trigger to undergo self-assembly: for example, a change of pH or ionic strength to that of physiological conditions. This will enable the therapy to be minimally invasive and reduce the potential for expulsion from the treatment site. The use of charge on the peptides should not only help to provide a self-assembly trigger, but also mimic the high charge found in the natural disc, which is crucial to maintaining the swelling pressure of the disc.

Aims and Objectives

The aim of the work presented in this thesis is to investigate peptide building blocks that self-assemble into β-sheet tapes and give rise to self-supporting gels in physiological conditions, with a particular focus on their application as a biomaterial for use in nucleus augmentation.

The investigation of these simple peptides can provide a deep insight into the forces and principles that guide self-assembly of biological peptides and β-sheet motifs in nature. It can also lead to the production of exciting new nanomaterials for a wide range of applications.

The three main objectives are to:

1. characterise the peptide self-assembly in physiological conditions;
2. optimise the peptides for the application of nucleus augmentation;
3. assess the ability of the hydrogel to restore disc mechanics and remain within the disc.

1. Characterisation

The self-assembly mechanism model of β-sheet tapes in pure water and methanol has previously been established and provides a starting point for understanding the β-sheet tape motif. In this work, the same process will be studied but in physiological-like conditions, which has never been done before. This research will investigate if the hierarchical model is also followed in physiological-like conditions.

Three pre-designed peptides will be studied initially that are the same in terms of primary structure, i.e. length and hydrophilicity, and differ only in overall charge. By studying the self-assembly curves of these simple model peptides as a function of peptide concentration, the effect of peptide charge on self-assembly in physiological-like solutions can be determined.

These three peptides will then be compared with other peptide analogues studied in parallel within the Aggeli group that have the same charge profiles but differ in a systematic way in hydrophilicity and polarity, to determine the effects of polar side chains on peptide self-assembly in physiological like solutions.

2. Optimisation

Once an insight has been gained into the basic scientific principles of the effect of peptide charge and polar side chains on the self-assembly of these building blocks in physiological-like solutions, the peptide system can be further optimised for biomedical applications.

Optimisation of the simple peptide systems may be achieved through creating new hybrid peptide materials by the interaction between the peptide material and a charged bio-polymer such as the GAG chains found within the disc. The addition of GAG chains may not only provide the high charge found in the natural tissue, but may also help to improve the self-assembling and rheological properties of the resulting gels to mimic the mechanical function and properties of the healthy nucleus pulposus

3. Nucleus augmentation

In this project, the focus will be on studying new peptidic materials for use in the replacement of the nucleus pulposus in degenerated intervertebral discs in the spine. Once the optimum peptide system has been determined, *ex vivo* mechanical loading and compression testing will be carried out to ascertain how the chosen material behaves within the disc. A model will be developed in order to act as a tool for comparing the best candidate gels.

A leakage study will also be performed to assess the ability of the chosen peptide to hold the GAGs *in situ*.

Chapter 2

2 Experimental procedures

2.1 Materials

2.1.1 Chemicals

Deuterated sodium 3-(trimethylsilyl)propionate-2,2,3,3-d_4 (TMSP) manufactured by Cambridge Isotope Laboratories was purchased from Goss Scientific Instruments Ltd., Great Baddow, Essex, UK.

Sodium hydroxide pellets, deuterium oxide, deuterated sodium hydroxide, deuterated hydrochloric acid, concentrated hydrochloric acid, sodium azide, sodium carbonate, citric acid, 1,9 dimethylene blue, formic acid, Dulbecco’s phosphate buffered saline (PBS) without calcium chloride or magnesium chloride sterile filtered, and Dulbecco's Modified Eagle's Medium (DMEM), were purchased from Sigma-Aldrich Ltd., Gillingham, Dorset, UK.

Sodium di-hydrogen orthophosphate, di-sodium hydrogen orthophosphate, ethanol, sodium formate, hydrochloric acid and sodium hydroxide were purchased from VWR International, Lutterworth, Leicestershire, UK.

Acrylic denture materials – rapid repair liquid, type 2 class 1 and acrylic denture materials old cire A31 purchased from WHW plastics, Hull, UK.

All water was ultrapure water (18.2 MΩ cm^{-1} resistivity), unless otherwise stated.

2.1.2 Peptides

P_{11}-4, P_{11}-7, P_{11}-8, P_{11}-9, P_{11}-12, P_{11}-13, P_{11}-14, P_{11}-28 and P_{11}-29 were purchased from CPC Scientific, NeoMPS or the Polypeptide Group. These peptides were analysed in house to check their content and purity using mass spectrometry, HPLC, amino acid analysis, elemental analysis and UV spectroscopy (see Appendix B for full details).

Manufacturer peptide content values were confirmed using the UV procedure as described in section 2.2.6., except for the solutions were prepared at 1 mg/ml and the pH adjust to a value known to make the peptides fully monomeric and therefore soluble. The in-house peptide content value from UV spectroscopy was calculated using Equation 1:

$$Peptide\ content = \frac{Molarity\ measure\ by\ UV}{Molarity\ measure\ by\ \frac{mass}{volume}\ ratio}$$

Equation 1

Peptides were stored in a freezer in a lyophilised state, and prior to use left to thaw at room temperature.

2.1.3 Glycosaminoglycan, GAG, chains

Chondroitin-6-sulfate sodium salt from shark cartilage was purchased from Sigma-Aldrich Ltd., Gillingham, Dorset, UK.

2.1.4 ^{1}H Nuclear Magnetic Resonance Spectroscopy, NMR

NMR 500 MHz borosilicate glass tubes were obtained from chemistry stores (University of Leeds).

2.1.5 Transmission Electron Microscopy, TEM

Hexagonal mesh copper grids size 400, mica sheets used for carbon film preparation and round copper quanntifoil 300 mesh carbon support films were obtained from Agar Scientific, Stansted, Essex, UK.

2.1.6 Circular Dichroism Ultra-Violet Spectroscopy, CD UV, and Ultra-Violet Spectroscopy, UV

Quartz SUPRASIL 10 mm, 1 mm and demountable cells were obtained from Hellma, Southend on Sea, Essex, UK.

2.1.7 Quantification of glycosaminoglycan leakage, DMB assay

Flat bottom 96 well plates were purchased from Nunc, Roskilde, Denmark.

2.2 Sample preparation and collection of data

This section summarises the typical procedure used to prepare all peptide solutions in this thesis. Any exceptions to these procedures are detailed in the appropriate section for each technique.

2.2.1 Weighing

All solids were weighed out on a Mettler AE240 balance.

2.2.2 Dissolution

Gilson micropipettes were used to add solvent to weighed peptide. The sample vials were sealed with Parafilm® and vortexed for ≈30 seconds (Scientific Industries Vortex Genie 2 vortexer), following this, the samples were sonicated for ≈30 minutes (Bandelin Sonorex RK52H sonicator).

2.2.3 pH measurement and adjustment

All samples were adjusted to a pH or pD (pH in deuterated solutions) of range 7.4 ± 0.1, unless otherwise specified. Measured pD values quoted here are those following the addition of a 0.4 correction value added to the pH meter reading.[167]

Sample pH was determined using either a WPA CD720 meter and a CMW711 semi-micro single junction probe, or a Sartorius Docu-pH meter and a VWR sympHony semi-micro combination double junction probe. Both probes were filled with, and stored in, 3.5 M KCl solution.

Prior to use, the WPA meter was calibrated using two of the pH 4, 7 and 10 standards (from pH 4, 7 and 10 Sigma-Aldrich reference standard buffers, each within ±0.01 pH units at 25^{o}C) that were closest to the final desired pH. At least two of the three buffers were used to calibrate the Sartorius meter dependent on the most appropriate pH range.

The pH of solutions was altered using microlitre aliquots of 0.1, 0.5 or 1 M HCl or NaOH (for deuterated solutions, DCl or NaOD were used). After each addition of acid or base, the solution was vortexed for ≈10 seconds, and its pH or pD rechecked.

2.2.4 Warming

After pH adjustment samples were sealed with PTFE tape and Parafilm® and then warmed on a hotplate at 80^{o}C, either until cloudy solutions became clear or bubbles began to appear at the bottom of the vial. After cooling, samples were stored in a closed cupboard at room temperature.

2.2.5 Storage

After sample preparation and between sample measurements, samples were stored in a closed dark cupboard at room temperature.

2.2.6 Molarity measurement by Ultra-Violet Spectroscopy, UV

2.2.6.1 Background

Solution molarity is normally calculated from, Equation 2:

$$molarity = \frac{moles\ of\ solid}{volume\ of\ solvent}$$

Equation 2

Unfortunately, for peptides this approach is not always suitable due to the material used having less than 100% peptide content due to the counter-ions bound during purification, such as, trifluoroacetic acid or ammonium salts.

For peptides containing the tryptophan residue the UV absorption spectra can be used to calculate the molar concentration. The wavelength of 279 nm corresponds to the electronic excitation of the indol side chain of the tryptophan residue. When the spectra are collected in a 1 cm path length cell, the molar concentration of the peptides can be determined by Equation 3 :

$$[peptide]M = \frac{Abs_{279}}{5600}$$

Equation 3

Where 5600 $M^{-1}cm^{-1}$ is the molar extinction coefficient of the tryptophan residue at 279 nm.

For samples which appeared turbid, an optical approach is less practical. In these cases, molarity was estimated from mass and volume, correcting the mass using an average of in-house measured and manufacturer recorded peptide content values (see Appendix B).

2.2.6.2 Method

UV spectra were recorded at 279 nm using a Perkin-Elmer Lambda 2 UV/visible 2.3. spectrometer, controlled by Perkin-Elmer UV WinLab 2.85.04 software. Peptide solutions were pipetted into Hellma 110-QS quartz SUPRASIL® cuvettes with a 1 mm path length for measurement. Before measuring solution absorbance, the spectrometer was autozeroed using two cuvettes filled with blank solvent. An average of 10 absorbance measurements was taken.

2.3 ^{1}H Nuclear Magnetic Resonance Spectroscopy, NMR

2.3.1 Background

The proton has nuclear spin I = 1/2 and may adopt one of two orientations, m_I = +1/2 and m_I = –1/2, in the presence of an applied magnetic field, B_0. As demonstrated in Figure 34, the two spin states (either aligned or opposed to the applied magnetic field) differ in energy by $h\gamma B_0/2\pi$ (where h = Planck's constant, γ = magnetogyric ratio for the proton) and it is the transitions between these two states that are observed in ^{1}H NMR spectroscopy.

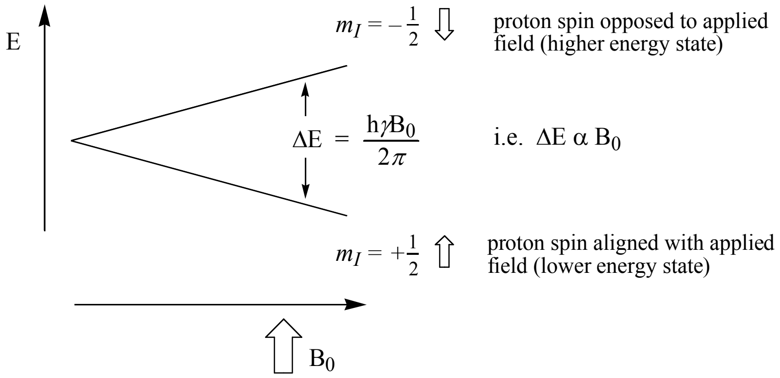

Figure 34 - The basic principles of ^{1}H NMR spectroscopy.

The familiar NMR parameters used to characterise organic compounds are also relevant to the study of proteins and peptides.[168] Previous work has shown that NMR can be used to study the self-assembly of peptides in the solution phase.[169-171]

When peptide samples are placed in a static magnetic field (B_o) and irradiated, initially the net macroscopic magnetization (M) is in the direction of the static field. When the field is applied at 90^o to the B_o field, this pushes M perpendicular to B_o. The transverse magnetization precesses due to the static magnetic field, which, in turn produces an electrical current in the detector. The free induction decay (FID) signal is observed whilst the system returns to its equilibrium state. It is this FID, which is observed by the NMR and is exploited when studying self-assembly. A Fourier transform algorithm is performed on this time domain signal, which in turn produces the conventional, frequency domain NMR spectrum.[172,173]

To measure self-assembly, the line width broadening of the NMR spectra is exploited. The line width broadening is associated with two parameters known as spin lattice or longitudinal (T_1) and spin-spin (T_2) relaxation times. Relaxation depends on two factors[174]:

1. magnetic interaction
2. molecular motions

T_1 is the time taken in which the magnetization reorientates itself back into the B_o plane and back into thermodynamic equilibrium after the application of the radio frequency pulse. T_1 is essentially associated with the tumbling of the molecule in solution. Subsequently it has a loose affinity to the self-assembled state of the molecule resulting from the intermolecular association between peptides. T_2 is the decay rate of the magnetization perpendicular to B_o. For non viscous liquids T_1 and T_2 are almost equal.[174] Often, due to the short relaxation time of $T_{2,}$ the NMR lines for macromolecules are broad compared to small molecules and further line broadening is seen after aggregation or increase of viscosity.[172] Essentially as every nucleus has several neighbours, the NMR line of each spin is split as each nucleus interacts with one another. In a stable self-assembled aggregate this pattern is averaged out over all of the possible orientations, resulting in a single featureless peak. The width is related to the spin-spin relaxation time via the Equation 4: [172,173]

$$\Delta\nu = \frac{1}{\pi . T_2}$$

Equation 4

Where Δv is the linewidth and T_2 is the relaxation time.

In a monomeric state, the coupling interaction between each nucleus is fast, subsequently this molecular motion reduces the dipolar broadening and line widths become well defined. The more closely the molecules are held the shorter the T_2 relaxation time, i.e. when in a self-assembled state. The relaxation time increases when the molecules have a greater intermolecular freedom.[173]

Self-assembly is measured by integrating the splitting pattern arising from the aromatic region and normalising it with respect to the peak observed due to a known standard. Plotting the integral with respect to the concentration, the fraction of monomer of the peptide can be measured. Below c*, the integral intensity is dependent on the concentration of peptide present. The fraction of monomer is observed as a positive linear function with a gradient that is dependent on the number of aromatic residues present. At and above c*, the gradient is no longer linear.[173]

2.3.2 Measurement

2.3.2.1 Sample preparation

Solutions of peptides P_{11}-7, P_{11}-9, P_{11}-12, P_{11}-13/14 and P_{11}-28/29 were prepared directly in D_2O, containing 130 mM NaCl and 0.125 mM of the NMR internal reference standard (2,2,3,3-d4)-trimethylsilyl-3-propionic acid, TMSP.

2.3.2.2 Method

Nuclear magnetic resonance spectroscopy was carried out using a Bruker DPX300 300 MHz spectrometer at room temperature, operating at 300 MHz (5 mm probe, spectral width 5995 Hz), controlled by XwinNMR software. Spectra were recorded with an automatic largest solvent peak presaturation programme and 1024 scans/spectrum. Samples were placed in 500 MHz borosilicate glass tubes. The areas of the aromatic peaks of the peptides were normalised against the area of a sharp constant control peak of 0.125 mM 3-trimethylsilylpropionate occurring at 0 ppm. MestReNova

(Mestrelab Research, Santiago de Compostela, Spain) was used to Fourier transform and measure NMR peak integrals, and Origin 8.6 (OriginLab Corporation, Massachusetts, USA) was used to process and plot the results.

The aromatic multiplet at chemical shift ~7.3-7.5 ppm was integrated, relative to the reference peak. To determine the estimated monomer concentration, the integral of the aromatic peak was divided by the slope of peptide concentration vs. integral, for the monomer/linear regime.[115] The line widths of the aromatic region and chemical shifts of the peaks in this region were also measured to check whether they undergo any change as peptide concentration increases.

The self-assembly curves were constructed by subtracting the estimated monomer concentration (derived from the aromatic integral) from the total peptide concentration to give the β-sheet concentration.

P_{11}-9

The solution peptide concentration was calculated by UV above 100 μM and below 500 μM. The sample concentration above 500 μM was calculated from the weighed peptide, multiplied by an average of the net peptide content from in house UV data and company data. The samples were analysed over 2.5 years at various time points, to establish equilibrium conditions. Once equilibrium conditions were believed to have been reached, the 3 mM sample was diluted down and studied at various time points once more, to confirm the equilibrium conditions. Diluted concentrations were calculated in the same way as above and then multiplied by the dilution factor.

P_{11}-12

The solution peptide concentration was calculated from the weighed peptide, multiplied by an average of the net peptide content from in house UV data and company data. The samples were analysed over 1.5 years at various time points, to establish equilibrium conditions.

P_{11}-7

The solution peptide concentration was calculated from the weighed peptide, multiplied by an average of the net peptide content from in-house UV data and company data. The samples were analysed over a month at various time points, to establish equilibrium conditions.

P_{11}-7 aggregates in the solution conditions used for this study were insoluble and form a white precipitate. This not only makes UV difficult, but also dilutions inaccurate. Although there was precipitate in the solutions, this was not thought to be a problem with NMR, as this technique measures the monomer concentration and the precipitate was believed to be the aggregated form.

P_{11}-13 and P_{11}-14

P_{11}-13 and P_{11}-14 NMR samples were prepared separately in molar ratios to one another as stated in 2.3, apart from the pD was adjusted to 6.5 ± 0.5 for P_{11}-14 and 8 ± 0.5 for P_{11}-13 to ensure totally monomeric solutions. P_{11}-14 was then pipetted into the relevant P_{11}-13 solution and vortexed for approximately 30 seconds using a Scientific Industries Vortex Genie 2. The solution peptide content was calculated for each peptide separately from the weighed peptide, multiplied by an average of the net peptide content from in-house UV data and company data, then an average taken for the P_{11}-13+14 mix. The samples were analysed over four months at various time points to establish equilibrium conditions.

P_{11}-28 and P_{11}-29

P_{11}-28 and P_{11}-29 NMR samples were prepared separately in molar ratios to one another as stated in 2.3, apart from the pD was adjusted to 6.5 ± 0.5 for P_{11}-28 and 8 ± 0.5 for P_{11}-29 to ensure totally monomeric solutions. P_{11}-28 was then pipetted into the relevant P_{11}-29 solution and vortexed for approximately 30 seconds using a Scientific Industries Vortex Genie 2. The solution peptide content was calculated for each peptide separately from the weighed peptide, multiplied by an average of the net peptide content from in house UV data and company data, then an average taken for the P_{11}-28+29 mix. The samples were analysed over a month at various time points to establish equilibrium conditions.

2.4 Transmission Electron Microscopy, TEM

2.4.1 Background

The transmission electron microscope works on the same basic principles as the light microscope but uses electrons as its ‘light source’. As electrons are used rather than light, it is possible to get a resolution thousands of times better than with a light microscope as the de Broglie wavelength of an electron is much lower than that of light, therefore nanometer sized structures can be resolved.[175] A schematic of a TEM is shown in Figure 35.

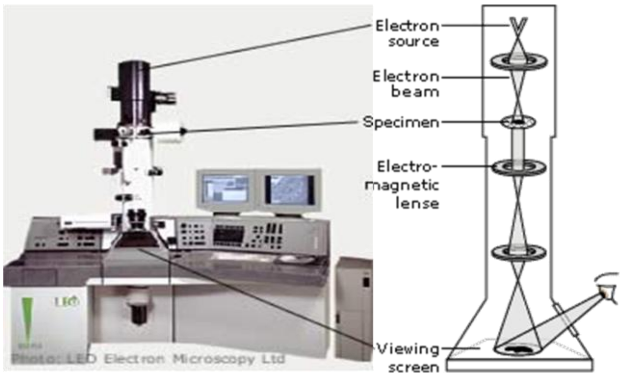

Figure 35 – TEM schematic. Taken from http://www.nobelprize.org/educational/physics/microscopes/tem/index.html.[175]

Electrons from a source at the top of the microscope travel as a beam through the vacuum in the column of the microscope. The beam is focussed by electromagnetic lenses and the beam passes through the sample. The sample will interact with the electron beam and depending on the density of the sample electrons can be scattered as back scattered electrons, elastically and inelastically scattered electrons and be lost as secondary electrons. X-rays and light will also be given off and can be used to gather elemental and chemical information. The transmitted electrons are used for imaging. At the bottom of the microscope they hit a fluorescent screen, resulting in a shadow image of the sample, with its different parts displayed in varied darkness according to its density.[175,176] The TEM provides information on the internal structure of a material as the image is a 2D projection of the structure.

2.4.2 Sample preparation

Solutions of peptides P_{11}-7 and P_{11}-9 were prepared directly in H_2O, containing 130 mM NaCl, and 0.02% NaN_3 (w/w) to prevent bacterial growth.

Solutions of peptide P_{11}-12 and peptide:GAG were prepared directly in PBS containing 0.04 % NaN_3 as stated in 2.8.1.2.

2.4.3 Method

Transmission electron microscopy was carried out using a Philips CM10 electron microscope. Electron microscope (EM) grids (copper 300 mesh) were coated with carbon prior to use by the flotation of a carbon film from a mica sheet onto the grids, these EM grids were glow discharged using an Edwards 306 A high vacuum coating unit fitted with ionic bombardment arms. These pass high tension, HT, through a partial vacuum to create a glow discharge on the grids, which aids with the adhesion of the sample. Peptide samples were quickly diluted by various factors in pure water where stated and the freshly glow-discharged, carbon coated TEM copper grids (hexagonal mesh size 400) were exposed immediately to the peptide solutions. The peptide solutions remained in contact with the grids for one minute, the excess was then removed. The grids were negatively stained by absorption of uranyl acetate at 4% (w/w) in water for 20 seconds. The excess was removed and left to air dry. Images were obtained quickly to avoid artefacts and destruction of the sample with the TEM operating at 80 kV accelerating voltage.

2.5 Circular Dichroism Ultra-Violet Spectroscopy, CD UV

2.5.1 Background

Circular dichroism UV spectroscopy, CD, works by measuring the difference in absorption between left and right handed circular polarised light as it passes through a sample, through the change in its electric field, E.[177,178] A periodic variation in the polarization of the light beam is induced by the polarization modulator through all ellipticities from left circular through elliptical, unchanged linear and elliptical to right circular. This polarized light passes through the sample to a photomultiplier detector.[178] With the introduction of a chiral sample, a preferential absorption is seen during one of the polarization periods and the intensity of the transmitted light now varies during the modulation cycle[177,178] The variation is directly related to the circular dichroism of the sample at that wavelength. Successive detection is performed at various wavelengths and leads to the generation of the full CD spectrum. The spectral bands can be assigned to certain structural components of a molecule.[178]

As the bands in CD are normal electronic absorption bands in the UV region, in an asymmetric molecule, the CD signal is zero if the molecule is not chiral.[178] The absorbance for left-circularly polarised light can be defined as, Equation 5:

$$A_l = log_{10}\left(\frac{I_l^0}{I_l}\right) = \varepsilon_l Cl$$

Equation 5 - Absorbance for left-circularly polarised light.[173]

Where A_l = absorbance for left-circularly polarised light, I_l^0 = intensity of left-circularly polarised incident light on the sample, I_l = intensity of left-circularly polarised light after travelling through the sample, ε_l = molar extinction coefficient of the solute for left-circularly polarised light / $dm^3.mol^{-1}.cm^{-1}$ and C = concentration of the sample /$mol.dm^{-3}$.

The absorbance of right-circularly polarised light can be formulated with a similar definition. CD is then defined as the difference between the absorbencies, Equation 6.[173,178,179]

$$\Delta A = A_l - A_r = \varepsilon_l Cl - \varepsilon_r Cl = \Delta\varepsilon Cl$$

Equation 6

Where $\Delta\boldsymbol{\varepsilon} = \boldsymbol{\varepsilon_l} - \boldsymbol{\varepsilon_r}$.

CD is reported either in units of ΔE, the difference in absorbance of E_r and E_l by an asymmetric molecule, or in degrees ellipticity, which is defined as the angle whose tangent is the ratio of the minor to the major axis of the ellipse. [θ], the molar ellipticity in deg cm^2 dmol^{-1} = 3,298ΔE.[177]

If molecules absorb light they undergo a transition from a lower to a higher energy state. Evaluation of peptide/protein secondary structure using CD analysis is a well established approach.[180] Absorption in the region below 240 nm for proteins is mainly due to the peptide bond.[178] The regular secondary structure in proteins and peptides results in a characteristic CD spectrum in the far UV. The amide group on the peptide is associated with two distinct electronic excitations. The first is a weak but broad $n \rightarrow \pi^*$ transition at around 220 nm: this is the excitation of electrons from a non-bonding (lone pair) orbital on the carbonyl oxygen to an anti-bonding π orbital.[178] The second is a more intense transition $\pi \rightarrow \pi^*$ around 190 nm and is the excitation of electrons from a bonding to an anti-bonding π orbital on the carbonyl double bond.[178]

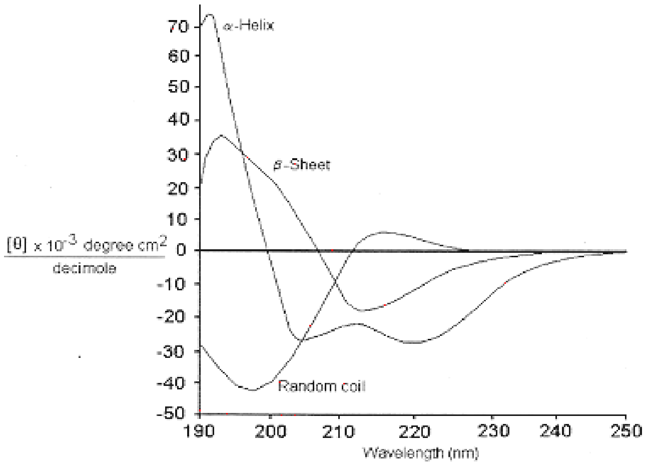

Figure 36 - Far UV CD spectra with various types of secondary structure.[181]

As shown in Figure 36, α-helical proteins have negative bands at 222 nm and 208 nm, and a positive band at 193 nm. Proteins with well-defined antiparallel β-pleated sheets have negative bands at 217 nm and positive bands at 195 nm, whereas random coils have very low ellipticity above 210 nm and negative bands near 195 nm.[177]

The acquisition of good quality CD UV spectra in physiological-like conditions is challenging. Therefore work was first carried out to establish the optimal conditions for the CD UV runs, as described in Appendix C. These conditions were then used for the experiments described here.

2.5.2 Solution preparation

Solutions of peptides P_{11}-9 and P_{11}-12 were prepared directly in H_2O, containing 43 mM Na_2HPO_4 and 0.02% NaN_3 (w/w) to prevent bacterial growth.

2.5.3 Method

CD spectra were recorded using a Jasco J-715 spectrometer using 1 mm and demountable quartz cuvettes at 20^oC. Spectra were recorded with a step resolution of 1 nm, a scan speed of 50 nm/minute, a sensitivity of 50 mdegs and a response time of 1 second. Far and near UV spectra were recorded over the wavelength range 300-190 nm and were the average of a number of scans, dependant on their smoothness. Each spectrum collected had the solvent spectrum subtracted. A first order smoothening was performed and finally an optical constant calculation converted the data to a mean residue molar ellipticity $[\theta]$/deg cm^2 $dmol^{-1}$

2.6 Fourier Transform Infra-Red Spectroscopy, FTIR

2.6.1 Background

Fourier transform infrared, FTIR is the measurement of wavelength and intensity of absorption of IR radiation by a sample. In FTIR the light (typically 4000-400 cm^{-1}) is split into two beams and either one beam or both are passed through the sample. Usually one beam has a longer path than the other and when the two beams are recombined they produce an intereference pattern. By systematically changing the difference in the two paths an interferogram can be produced and Fourier transformation of this interferogram results in the spectrum.[182]

Infrared light is absorbed by a molecule when the oscillating dipole moment interacts with the oscillating electric vector of the infrared beam.[182] A bond within a molecule can undergo different types of oscillations depending on the energy between its ground state and its excited state. The amount of energy that is absorbed is dependent on changes in the dipole moment and therefore weak absorption is seen by bonds that are non-polar and a strong absorption is seen for polar bonds such as C=O. A complex molecule will have a large number of vibrational modes; however, some of these will be the vibrations of individual bonds or functional groups and are known as localized vibrations and the various types are demonstrated in Figure 37.

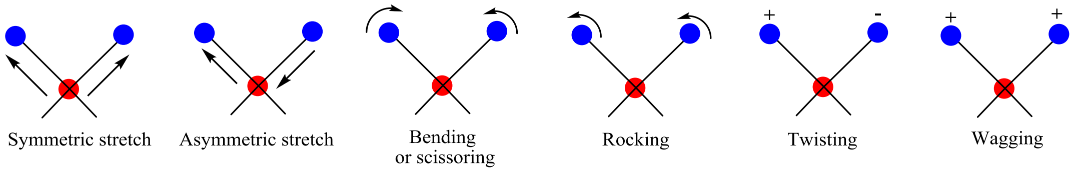

Figure 37 - Localized infrared vibrational modes.[182]

FTIR is a well established technique for the study of protein and peptide secondary structure. Both solution and dry state FTIR have been used to good effect in the examination of peptide conformation. Nine characteristic absorption bands (amide A, B, I, II, III, IV, V, VI, VII) allow the study of peptide secondary structure (Table 3).

Amide Band	Wavenumber /cm^{-1}	Origin
A	~3300	NH stretching
B	~3100	NH stretching
I	1600-1690	C=O stretching
II	1480-1575	CN stretching, NH bending,
III	1229-1301	CN stretching, NH bending,
IV	625-767	OCN bending mixed with other nodes
V	640-800	Out-of plane NH bending
VI	537-606	Out-of plane C=O bending
VII	~200	Skeletal torsion

Table 3 – Characteristic infrared bands of the peptide.[183]

The amide I, II, III bands are the most prominent and sensitive to conformation of the peptide backbone and so are the most useful for probing secondary structure. The amide II band is the least sensitive of the three to conformation, and the amide III band is relatively weak and is affected by other vibrations, therefore the amide I band is the most often used. The amide I stretch is affected by the different hydrogen bonding patterns that the peptide backbone is involved in, thus manifests itself as a featureless peak (occurring at 1700-1600 cm^{-1}) due to the overlap of component bands. The complex overlapping patterns of the peptide bands can also be masked by H-O-H bending at 1645 cm^{-1} whose intensity is an order of magnitude higher than the amide I band.[184] For this reason, all samples were run in deuterated solvents.

The exact frequencies of the vibrations in the amide I band depends on the nature of the hydrogen bonding involving the C=O and NH groups, which varies for the different secondary structures of a peptide backbone. If spectra have been recorded in D_2O, the amide bands have a prime symbol attached to them e.g. amide I'. The peak positions corresponding to the various secondary structures are presented in Table 4.

amide I' band (cm^{-1})	**secondary structure assignment**
1613-1630	β-sheet
1642-1649	unordered
1649-1655	a-helix
1658-1674	Turn
1673	TFA
1682-1690	β-sheet
1694-1697	Turn

Table 4 - Secondary structural assignments of amide I' infrared bands.[185-187]

To obtain semi-quantitative information from the amide I' region using FTIR, firstly the second derivative of the absorption spectrum in the region of 1700 - 1600 cm^{-1} is calculated. This ascertains the number and positions of individual component bands.

Secondly, the amide I' line shape is band fitted, from which, the assignment of the amide I' component bands can be correlated to different types of component bands. Amino acid side chains exhibit characteristic absorption frequencies in the amide I region and must be considered during the assignment of spectroscopic bands. However, the IR molar absorption coefficient for most side chains is a lot weaker compared to that of the peptide bond. A summary of amino acids that affect this region can be found in Table 5.

Another feature of the IR spectrum to be aware of is the TFA band is located at 1673 cm^{-1}. In the purification of peptides by reverse phase HPLC trifluoroacetic acid is used, which leads to it being present in the peptide material as a counter ion bound to the positively charged residues.[188] The amount of TFA present depends on the number of positively charged residues in the peptide, e.g. samples of peptides with greater numbers of arginine and ornithine residues will contain more TFA.

Amino Acid	Wavenumber /cm^{-1}	Origin
Aspartic acid	1715	C=O stretch
	1585	COO$^-$ asymmetric stretch
Glutamic acid	1710	C=O stretch
	1565	COO$^-$ asymmetric stretch
Glutamine	1620-1640	ND$_2$ stretch
	1670	C=O stretch
Arginine	1580	CN stretch
	1610	CN asymmetric stretch
Histidine	1600, 1625	ionised ring
	1620	non-ionised ring
Phenylalanine	1596,1607	ring
Tyrosine	1500,1575	ionised ring
	1517,1590,1615	non-ionised ring
Tryptophan	1545	ring

Table 5 - Infrared bands of amino acid side chains.[183]

2.6.2 Sample preparation

Solutions of peptides P$_{11}$-9 and P$_{11}$-12 were prepared directly in D$_2$O containing 130 mM NaCl. Any peptide concentrations given for the FTIR studies were values multiplied by an appropriate factor to account for the actual percentage peptide content.

2.6.3 Method

Samples were placed between CaF$_2$ crystals and their spectra acquired with a Thermo Scientific Nicolet 6700 FTIR spectrometer. Spectra were averages of 32 scans recorded at room temperature whilst purging with dry air. Blank solvent spectra were subtracted from the sample trace, the baseline corrected and the spectra smoothed. Processed spectra were band fitted using the Peak Resolve routine in OMNIC 7.3 SP1 (Thermo Electron Corporation, Loughborough, UK).

Once the fitted peaks in the amide I’ region had been assigned secondary structure the proportion of the peptide adopting a particular secondary structure was determined from its relative areas, Equation 7:[189,190]

$$\%\, secondary\ structure = 100\ x\ \frac{motif\ total\ peak\ area}{total\ secondary\ structure\ peak\ area}$$

Equation 7

2.7 Rheology

2.7.1 Background

When stressed, solids deform and liquids flow. Rheology involves applying a stress to a sample and measuring how much it deforms or how fast it flows. There are two basic kinds of flow with relative movement of adjacent particles of liquid; they are called shear and extensional flows. In shear flows, liquid elements flow over or past each other, while in extensional flow, adjacent elements flow towards or away from each other and all flows are resisted by viscosity.[191] There are three general flow behaviours; Newtonian, shear-thinning and shear-thickening (Figure 38).

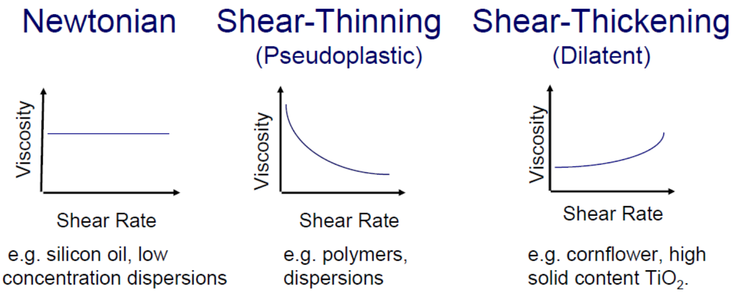

Figure 38 - General flow behaviours[192]

To determine the elasticity (resistance to deformation) of a material its modulus is measured. The modulus is a measure of shear stress divided by the strain, or the pushing force divided by the amount it moves. A rotational rheometer (Figure 39) can measure the modulus of a sample by oscillating back and forth, and so can show properties under deformation before flow. It can do this two different ways:

1. Controlled stress – oscillate the top plate with a set force and measure its displacement;
2. Controlled rate – oscillate the top plate with a set displacement and measure the force.

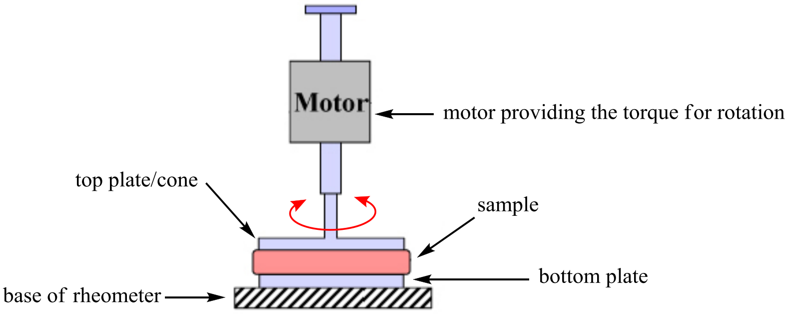

Figure 39 - Schematic diagram of a rotational rheometer.[193]

Different types of material have a different lag/phase angle, δ, between the input stress and measured strain (Figure 40).

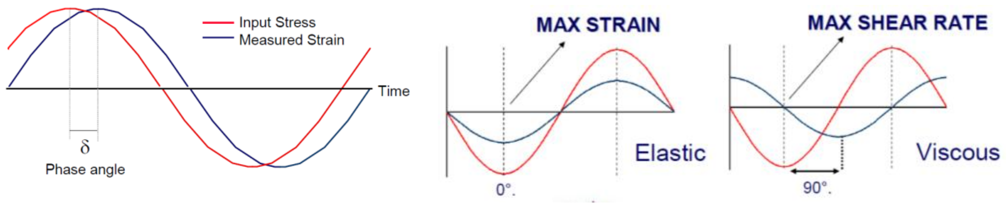

Figure 40 - Origin of the phase angle and its relationship to viscous and elastic materials.[192]

For a purely elastic material (solid-like behaviour), the stress and strain would be exactly in phase and therefore the phase angle would be zero. For a purely viscous material (liquid-like behaviour), however, the stress and strain would be ¼ of a cycle out of phase and therefore the phase angle would be 90° (Figure 40).

The complex modulus, G*, is a measure of the stiffness of a material and is calculated from how much a sample moves (shear strain) for a given force (shear stress). It can be broken down into its component parts:

1. Storage (elastic) modulus – G’ = G*cos δ
2. Loss (viscous) modulus – G” = G*sin δ

If G’>G’’ the phase angle will be less than 45° and so have solid-like behaviour, whereas if G”>G’ the phase angle will be more than 45° and so have liquid-like behaviour.

In all structured liquids, there is a natural rest state of the microstructure that represents a minimum energy state. Thermodynamic forces work to restore this state when the liquids are deformed. This restoring force increases linearly at first with the distance that any deformation takes the material away from the state of rest, however eventually non-linearity will occur. A steady state condition where the elastic force becomes constant is reached at very large deformations and the microstructure becomes anisotropic.[191] As well as the elastic forces, viscous forces will be present due to the dissipation and in proportion to the rate of deformation. Together these two forces produce viscoelastic effects. The viscoelastic profile of a material can be measured by applying an oscillating stress or strain as an input to the sample and monitoring the resulting oscillatory strain or stress output. The same repetitive sinusoidal straining motion recurs over and over again, with each cycle taking a certain time, and having a frequency that is inversely proportional to that time.[191] This can be used to study the microstructure and therefore predict a material's behaviour. There are fundamentally two parts of the oscillation that can be controlled:

1. Amplitude, stress or strain – an amplitude sweep experiment is carried out to determine the linear viscoelastic region (LVER);
2. Frequency, oscillation time scale – a frequency sweep experiment is run to determine the response to different timescales and is carried out within the LVER.

There are three general material behaviours: viscoelastic solid where the phase angle at rest (0 Hz) tends towards 0°; gel where the phase angle is independent of frequency; and viscoelastic liquid where the phase angle at rest tends towards 90° (Figure 41).

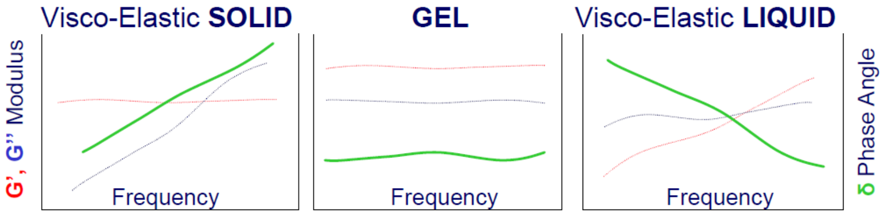

Figure 41 – General material behaviours in terms of the phase angle and storage and viscous moduli.[192]

An understanding of the rheological properties of hydrogels is extremely important, especially at the design stage for specific applications. The frequency dependence, gelation kinetics and gel stiffness are all critical hydrogel characteristics that can directly impact the final uses of the materials.[194] Shear-thinning and self-healing hydrogels can be excellent candidates for injectable materials.[194] Rheology has been used to probe peptide and protein based hydrogels, from understanding the fundamental mechanisms of gelation of globular peptide based hydrogels,[195] to measuring the effects of cross-linking fibrous protein based hydrogels.[196] Previously within the Aggeli group, the rheological properties of polypeptide K24 have been studied, determining that at a low concentration in 2-chloroethanol, a hydrogel is formed with an elastic modulus of around 300 Pa.[111] Rheology can be used to not only look at the bulk mechanical properties of peptide hydrogels, but also gelation mechanisms and the behaviour of the gels during and after flow. Rheometers can also be used to mimic the mechanical processes of specific applications such as the shearing effect of injection.

2.7.2 Sample preparation

2.7.2.1 P_{11}-4, P_{11}-8, P_{11}-9, P_{11}-12 control samples

Approximately 20 mg/ml of peptide was weighed into a sample vial, to which 2 ml of PBS containing 0.04 % NaN_3 was added.

2.7.2.2 P_{11}-13/14, P_{11}-28/29 control samples

Approximately 20 mg/ml of peptide was weighed into separate sample vials, to which 2 ml of PBS containing 0.04 % NaN_3 was added. The solutions were vortexed for 20 seconds using a Scientific Industries Vortex Genie 2, and then sonicated in a Bandelin Sonorex RK52H sonicator for 20 minutes. Solution pH was measured and adjusted to 6.5 ± 0.5 for P_{11}-14 and P_{11}-28, and 8 ± 0.5 for P_{11}-13 and P11-29, using a calibrated pH meter (Sartorius Docu-pH+). Any adjustment of pH, if necessary, was made with minimal μL volumes of 0.1, 0.5 or 1 M HCl and/or 0.1, 0.5 or 1 M NaOH. Finally, solution vials were closed, sealed with PTFE tape, and then warmed to approximately 80^{o}C for around five minutes until samples were a clear liquid to maximise peptide solubility.

2.7.3 Method

All the rheological measurements were performed on a Malvern Kinexus Pro rheometer with a cone-plate geometry (cone angle: 1^{o}, diameter: 50 mm, gap: 0.033 mm). All the tests were performed at 25^{o}C, utilizing a solvent trap and the atmosphere within was kept saturated to minimize evaporation of the peptide samples.

To ensure the measurements were made in the linear viscoelastic regime (LVER), amplitude sweeps were performed in a shear strain controlled mode from 0.01-100%. Two amplitude sweeps were carried out for each sample (1 Hz and 20 Hz) and a strain level was chosen at which the elastic modulus (G’) and viscous modulus (G’’) were independent of strain amplitude at the two different frequency levels.

The dynamic moduli of the hydrogels were measured as a frequency function with the sweeps carried out between 1 and 20 Hz. Peptide samples were allowed to equilibrate for 15 minutes once loaded prior to the start of testing (this was determined to be adequate following preliminary testing of P_{11}-9 Appendix D). Fresh samples were used for the amplitude and frequency sweeps.

After the frequency sweeps, two more amplitude sweeps (1 Hz and 20 Hz) were carried out in a stress controlled mode to confirm the testing was performed within the LVER. The stress range was chosen based on the stress values from the frequency sweeps at 1 and 20 Hz: if these two values were then independent of stress amplitude, then this confirmed that testing was within the LVER.

In order to check the reproducibility of the results, the same experiments were run on two different samples for P_{11}-4, P_{11}-28/29 and P_{11}-12, the results of which can be found in APPENDIX D.

rSpace for Kinexus 1.10 (Malvern Instruments) was used to control the rheometer and to export the raw data and Origin 8.6 (OriginLab Corporation, USA) was used to process and plot the results.

2.8 GAG mixing study

It was hypothesised that the charged glycosaminoglycan, GAG, chains of chondroitin-6-suplate, CS, would interact electrostatically with the charged peptides. In order to establish whether such an interaction was possible, a simple mixing study was carried out. The concentration of peptide was kept the same for each sample and the molar ratio of GAG subunit to one peptide was increased. The samples were named by the number of GAG subunits to each peptide present e.g. P_{11}-12:GAG 1:10 = one P_{11}-12 peptide monomer to ten GAG dimer subunits.

2.8.1 Sample preparation

2.8.1.1 GAG control (equivalent concentration of GAG in 1:10 sample)

0.034 g of chondroitin-6-sulphate was weighed into a sample vial, to which 0.5 ml of PBS was added containing 0.04% $NaN_{3.}$ The solution was then vortexed (20 secs) and sonicated (20 mins) before pH adjusting to 7.4 ± 0.1.

2.8.1.2 P_{11}-4, P_{11}-8, P_{11}-9, P_{11}-12, P_{11}-13/14 and P_{11}-28/29 :GAG

Approximately 20 mg/ml of peptide was weighed into a sample vial, to which 0.5 ml PBS was added containing 0.04% NaN_3. The solutions were then vortexed (20 secs) and sonicated (20 mins) before pH adjusting to 7.4 ± 0.1. After warming and whilst the solutions were still warm, a premeasured amount of chondroitin-6-sulphate was added and the mixture vortexed and heated again to approximately 80^oC to ensure complete mixing of the monomers.

2.8.1.3 P_{11}-13:GAG + P_{11}-14

P_{11}-13 and P_{11}-14 peptide solutions were prepared as above in 2.8.1.2, however the premeasured amount of chondroitin-6-sulphate was only added to the P_{11}-13 solution. The P_{11}-13:GAG mix was then vortexed and heated again to approximately 80^oC to ensure complete mixing of the monomers and the sample left overnight. The following morning the mix was heated once more, P_{11}-14 was pipetted into the P_{11}-13:GAG mix and the solution was then vortexed.

2.8.1.4 P_{11}-14:GAG + P_{11}-13

Prepared as above in 2.8.1.2, however the chondroitin-6-sulphate was added to the P_{11}-14 peptide sample and left over-night. The following morning, the mix was heated once more, P_{11}-13 was pipetted into the P_{11}-14:GAG mix and the solution was then vortexed.

2.8.1.5 P_{11}-28:GAG + P_{11}-29

P_{11}-28 and P_{11}-29 peptide solutions were prepared as above in 2.8.1.2, however the premeasured amount of chondroitin-6-sulphate was only added to the P_{11}-28 solution. The P_{11}-28:GAG mix was then vortexed and heated again to approximately 80^{o}C to insure complete mixing of the monomers and the sample left overnight. The following morning, the mix was heated once more, P_{11}-29 was pipetted into the P_{11}-28:GAG mix and the solution was then vortexed.

2.8.1.6 P_{11}-29:GAG + P_{11}-28

Prepared as above in 2.8.1.2, however, the chondroitin-6-sulphate was added to the P_{11}-29 peptide sample and left over night. The following morning, the mix was heated once more, P_{11}-28 was pipetted into the P_{11}-29:GAG mix and the solution was then vortexed.

2.8.2 Method

Visual observations were recorded including time for the gel to form and appearance of samples.

For peptides P_{11}-9 and P_{11}-12, a TEM study was carried out on representative GAG ratios as well as the peptide control and GAG samples. The TEM protocol described in 2.4.3 was followed.

A rheological study was carried out on representative GAG ratios for all peptides under investigation: the procedure described in 2.7.3 was followed.

2.9 Ex vivo investigation

The methods for the ex vivo investigation including the chondroitin-6-sulphate leakage study and the static loading study presented in Chapter 5 are detailed within the chapter as they rely on results from the previous chapters and do not follow standard protocols.

Chapter 3

3 Self-assembly and morphology of peptide nanostructures and mechanical properties of their hydrogels

3.1 Self-assembling peptides

3.1.1 Introduction

The class of peptides used herein are from the Aggeli group and are β-sheet tape forming peptides, which self-assemble in one dimension into a hierarchy of well defined structures. They are based on entirely natural amino acids and are 11 amino acids long. They are shorter than other equivalent families and therefore are inherently easier and more cost effective to make. Figure 42 shows the generic structure of this class of peptide.

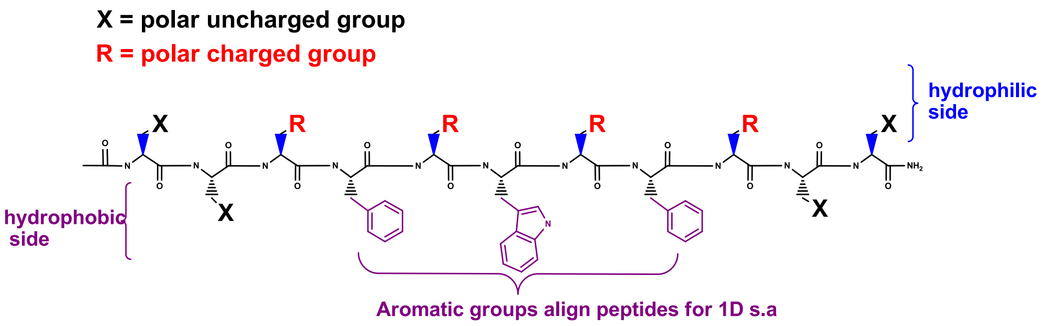

Figure 42 - Generic β-sheet tape forming peptide structure

All the peptides studied have a hydrophilic side and a hydrophobic side to help drive the self-assembly and an aromatic core recognition region to align the peptides for one dimensional self-assembly. This class of peptides is very versatile because the polar groups, R and X in Figure 42, can be changed to provide self-assembled molecules with different structures and therefore material properties.

3.1.2 Peptide design criteria

The design criteria for self-assembly for this class of peptide in organic solvents and pure water has been experimentally verified and is explained by a model suggesting hierarchical self-assembly.[110] The intension here was to study the self-assembly behaviour of a range of differing peptides, and to take the design criteria already established within the Aggeli group to optimise the peptides further to suit the application of a nucleus pulposus replacement.

The first design criterion for this particular application was that the peptide should have a low critical concentration (c*) because it was hypothesised that this would provide as strong and stable a gel as possible, as well as resulting in a low background monomer concentration and therefore reducing possible leakage from the injection site. Finally, it would lead to a more cost effective medical device.

Secondly, the peptide should be able to form a gel in basic physiological conditions (130mM NaCl, pH 7.4) and more complicated physiological conditions, such as cell media, and do so with short gelation times. The gels formed were also required to have good strengths and mechanical properties mimicking that of the natural tissue.

On top of needing to have similar mechanical properties to the natural tissue, the gels needed to have similar biofunctionality, i.e. to provide a high swelling pressure within the disc, ideally through water binding similar to that found naturally.

In order for the therapy to be minimally invasive, a trigger for self-assembly needed to be incorporated, so that the peptide could be injected as a liquid and form a gel once *in situ*.

Finally, because the intended application is within the body, it was vital that the chosen peptides are biocompatible.

To establish the design criteria to give a low c*, the versatility of this class of peptides was explored.

Three pre-designed peptides (Table 6) were studied initially that are the same in terms of primary structure i.e. length and hydrophilicity and differ only in overall charge. By studying the self-assembly curves of these simple model peptides as a function of peptide concentration, the effect of peptide charge on self-assembly in physiological like solutions could be determined.

Peptide Name	**Net Charge at pH 7.5**	**Polar Amino Acid**	**Peptide Structure**
P_{11}-7	0	Serine	CH_3CO-S-S-R-F-S-W-S-F-E-S-S-NH_2
P_{11}-9	-2	Serine	CH_3CO-S-S-R-F-E-W-E-F-E-S-S-NH_2
P_{11}-12	+2	Serine	CH_3CO-S-S-R-F-O-W-O-F-E-S-S- NH_2

Table 6 – Peptide structures of P_{11}-7, P_{11}-9 and P_{11}-12

The peptides investigated here were then compared with other peptide analogues (Table 7) studied in parallel within the Aggeli group by Dr Steven Maude.[189] These have the same charge profiles but differ in a systematic way in hydrophilicity and polarity, so would enable the effects of polar side chains on peptide self-assembly in physiological-like solutions to be determined.

Peptide Name	**Net Charge at pH 7.5**	**Polar Amino Acid**	**Peptide Structure**
P_{11}-2	0	Glutamine	CH_3CO-Q-Q-R-F-Q-W-Q-F-E-Q-Q-NH_2
P_{11}-4	-2	Glutamine	CH_3CO-Q-Q-R-F-E-W-E-F-E-Q-Q-NH_2
P_{11}-8	+2	Glutamine	CH_3CO-Q-Q-R-F-O-W-O-F-E-Q-Q-NH_2

Table 7 - Peptide structures for P_{11}-2, P_{11}-4 and P_{11}-8

The intention was to study the self-assembly behaviour as a function of peptide concentration, because this had not previously been studied before with these peptides under physiological-type solution conditions and also to enable fitting to the theoretical data. A systematic ^{1}H NMR study was chosen as a starting point because a wide range of concentrations could be studied, the complementary techniques of CD UV, FTIR and TEM were then used to confirm the NMR data.

3.1.3 Results: Studies on peptide self-assembly and morphology

3.1.3.1 P_{11}-9

^{1}H Nuclear Magnetic Resonance Spectroscopy, NMR

To examine the self-assembly behaviour at equilibrium, various different concentrations were prepared one by one and observed as a function of time. To establish if a linear region was visible at lower peptide concentrations and a plateau at higher concentrations, the total peptide concentration vs. estimated monomer peptide concentration using this technique was plotted (Figure 43).

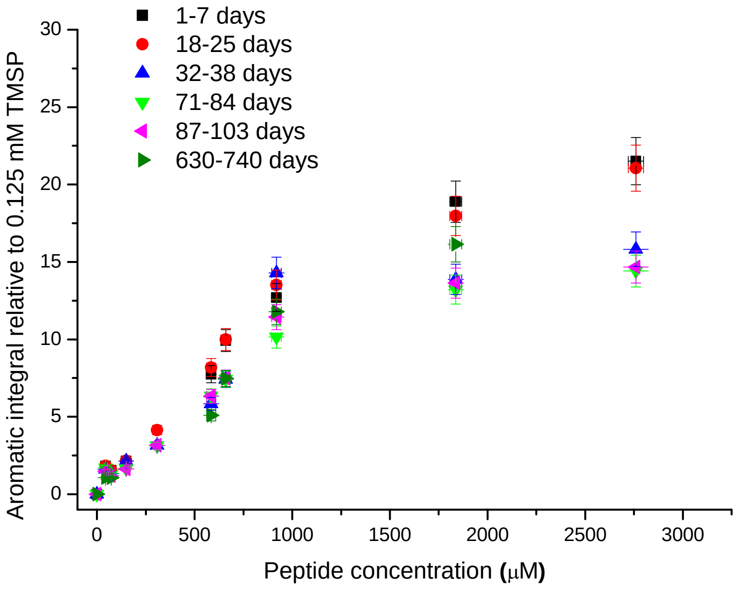

Figure 43 - ^{1}H NMR aromatic region integral of P_{11}-9 relative to integral of 0.125 mM TMSP reference peak as a function of increasing total peptide concentration and time from sample preparation.

The samples were analysed over 2.5 years at various time points, to establish equilibrium conditions. This study revealed that the peptide solutions reached equilibrium slowly after approximately one month with the biggest changes in the solutions taking place after two weeks, as can be seen in Figure 43 and Figure 44. Below c*, equilibrium was reached quickly, whereas above c*, equilibrium took much longer to attain as illustrated in Figure 44.

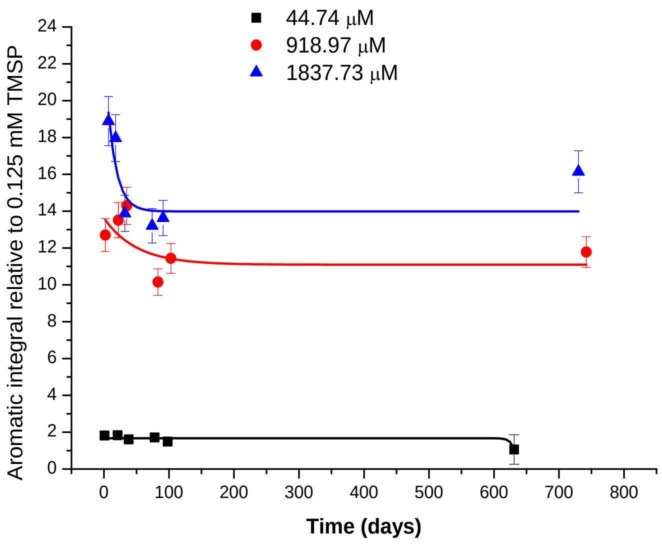

Figure 44 - Time variation of aromatic integral and of peptide concentration in monomeric state in P_{11}-9 solutions at three concentrations. Guidelines are first order decay fits created in OriginPro 8.6.

The line widths of the aromatic region and chemical shifts of the peaks in this region were also measured to check whether they underwent any change as peptide concentration increased. From Figure 45 a.) and b.), it can be seen that there was no change, implying that the molecular states that gave rise to the NMR signals plotted in Figure 43 are the same, i.e. monomeric random coils, irrespective of the total peptide concentration.

Once equilibrium conditions were believed to have been reached, the 3 mM sample was diluted down and studied at various time points once more, to confirm the equilibrium conditions (Figure 46).

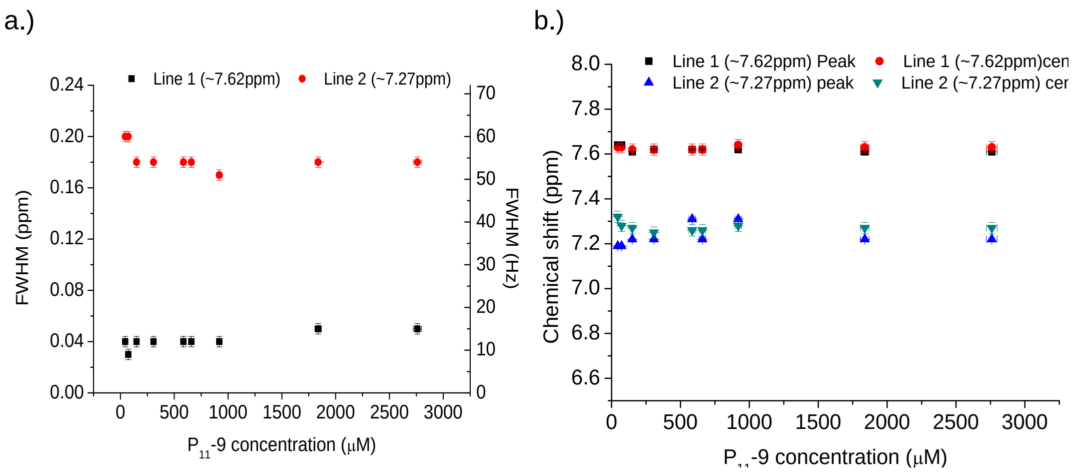

Figure 45 – a.) Line widths of aromatic peaks b.) Chemical shift of aromatic peaks in P_{11}-9 ^{1}H NMR spectra as a function of increasing total peptide concentration, samples 87-103 days old.

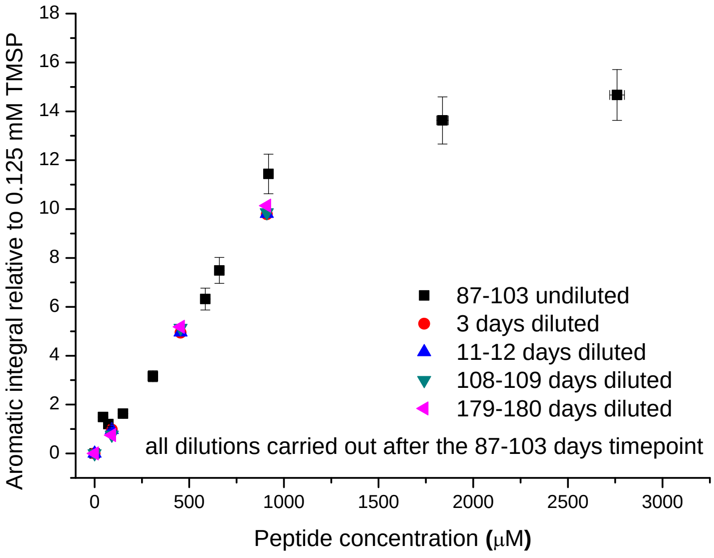

Figure 46 - ^{1}H NMR aromatic region integral of P_{11}-9 relative to integral of 0.125 mM TMSP reference peak as a function of increasing total peptide concentration and time from sample preparation.

The diluted data and the time-point data showed good concordance suggesting that equilibrium conditions had been met.

Determination of c using surfactant model*

From Figure 43, it can be seen there was a linear region up to ~1000 μM, where the aromatic integral varied linearly with P_{11}-9 concentration, this suggests that the peptide in solution remained monomeric. Any large peptide aggregates should have undergone rapid relaxation after NMR excitation, therefore not contributing to the integral. The c* was determined using the surfactant model as detailed in section 1.4 and is defined as the point at which the linear and the plateau region cross. Below, the c* was determined using only the data that was believed to be at equilibrium i.e. after 32 days (Figure 47).

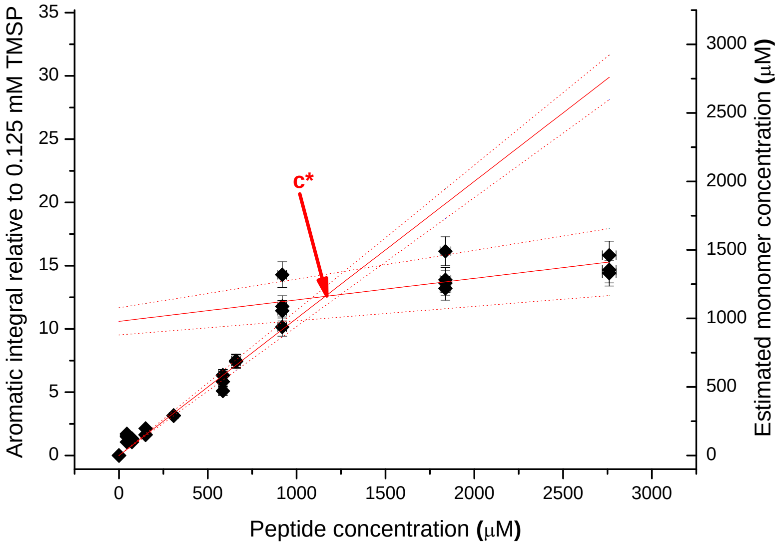

Figure 47 - Equilibrium NMR data used to determine c* value for P_{11}-9. Estimated concentration axis derived from P_{11}-9 linear gradient of 0.01083 μM^{-1}. The plateau region was taken to be a linear fit through the highest three concentrations, whereas the monomer/linear region was taken to be a linear fit through the rest of the concentrations.

From Figure 47, and using the surfactant model, the c* for P_{11}-9 was estimated as 1160 ± 175 μM. The right hand estimated monomer concentration axis for the plot was calculated from the aromatic integral divided by the slope of the linear monomer region of the plot. As the peptide concentration increased and as the aggregates increased in length, they formed a network of entanglements ultimately leading to self-supporting gels above a concentration of 3-6 mM.

Estimated self-assembly curve

From the above results of the P_{11}-9 NMR data, the self-assembly curve for the equilibrium data was constructed (Figure 48).

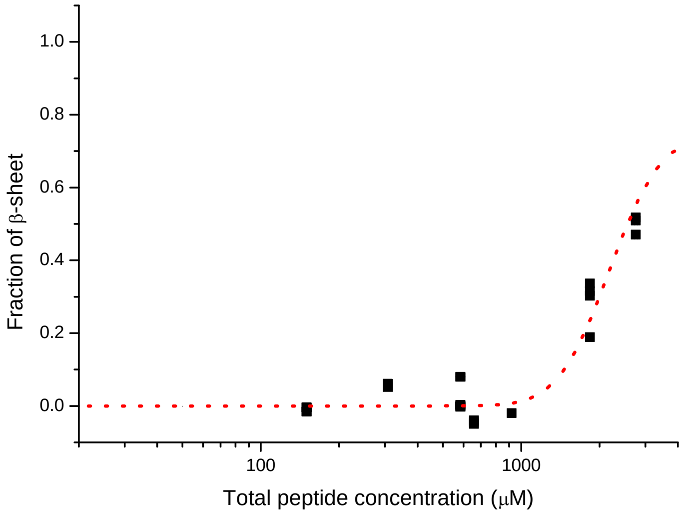

Figure 48 - Estimated equilibrium self-assembling curve for P_{11}-9, i.e. fraction of peptide in self-assembled state as a function of increasing total peptide concentration. Dotted line = sigmoidal SGompertz fit.

The self-assembly curve was constructed by subtracting the estimated monomer concentration (derived from the aromatic integral) from the total peptide concentration to give the β-sheet concentration. This was then divided by the total peptide concentration to produce the fraction of aggregate. From the above plots and from the data gathered so far it can be seen that the transition for monomer to aggregate is broad, this is thought to be due to either the precise magnitudes of ε_{tape} and ε_{trans} that are unknown at this time, or due to the ionised state of the charged peptides being affected slightly by changes in pH, which in turn can slightly affect the self-assembly behaviour.

This NMR technique has been validated against FTIR and CD data previously, showing that it is a good technique for the systematic study of self-assembling peptides.[70,114] From the work carried out by Carrick *et al*.[114] it was found that in the pD range of 6 – 8, the c* values may not differ too greatly, as can be seen in Figure 49.

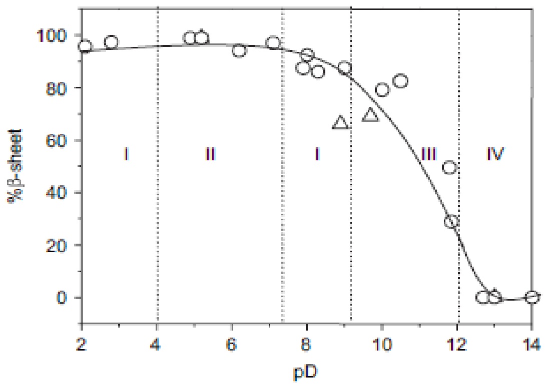

Figure 49 - Percentage β-sheet of P_{11}-9 (concentration = 7 mM) as determined by FTIR (O) and NMR (Δ) as a function of pD in 130 mM NaCl in D_2O: I: nematic gel, II: flocculate, III: nematic fluid, IV: isotropic fluid.[114]

The physiological pD region falls in the middle of this stable area and so small differences between sample pD may not greatly affect the construction of the true self-assembly curve. However, from other work carried out within the Aggeli group, it has been found that the deprotonation of glutamic acid (γ-COOH), arginine (δ-guanidinium) and ornithine (δ-NH_3^+) charged residues occur over wide bands of up to 5 pH units.[89] Therefore the charged peptides can have a complex range of ionisation states over a range of pH values. As ε_{tape} is strongly influenced by the direct electrostatic forces between the charged side chains, the c* for the charged peptides will be dependent on the ionised state of the side chains.[89] The pD values as measured straight after sample preparation ranged from a pD value of 7.34 to 7.54.

This NMR study was systematic; however, it was necessary to employ other complementary techniques to try to confirm the actual c* value and establish the nature of the conformational transition. These questions were addressed using circular dichroism UV and Fourier transform infra-red spectroscopies.

Circular Dichroism Ultra-Violet Spectroscopy, CD UV

The CD UV spectra for a range of concentrations of P_{11}-9 were obtained to confirm the c* value determined from the above NMR and to establish the peptide secondary structure (Figure 50).

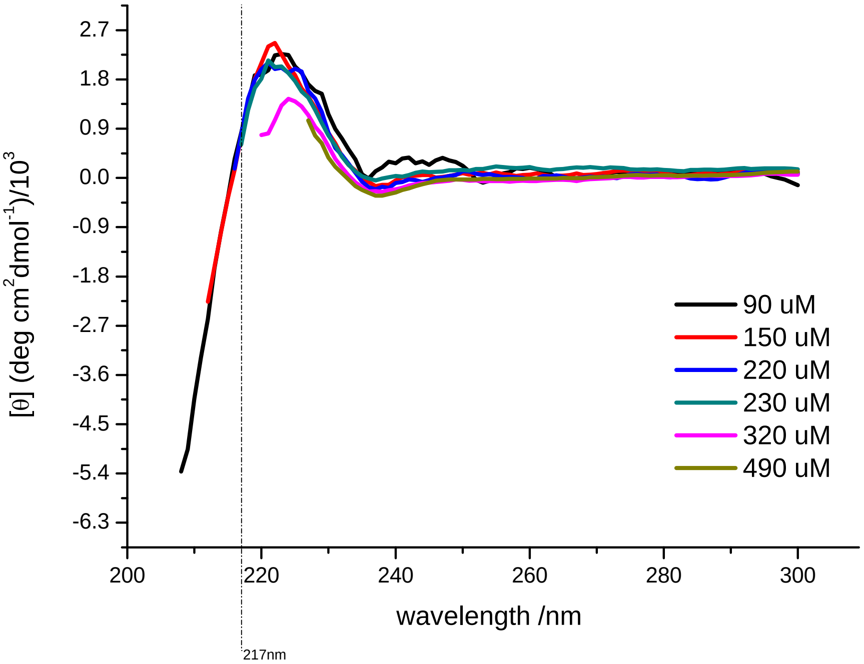

Figure 50 - CD Spectra for P_{11}-9 in 43mM Na_2HPO_4, 0.02% wt/wt NaN_3, H_2O, pH 7.4, with a high tension voltage cut off of 700 V. Concentrations calculated using UV. Samples 7 days old.

A higher concentration than 500 μM could not be examined due to a high tension (HT) voltage cut off being at a higher wavelength than that of interest for peptide secondary structure features. It can be seen that below 230 μM, the spectra corresponds to a predominantly random coil conformation, because there was a slightly positive band around 220 nm and what appeared to be a negative band forming around 195 nm. The percentage concentration of random coil appeared to decrease slightly in the final two spectra above a peptide concentration of 320 μM, as can be seen by the decrease of molar ellipticity of the positive band at around 220 nm. However, this decrease was minimal and is thought to be due to a broad rather than sharp c* transition. It is also possible that this small decrease in random coil may be due to an artefact of the high HT voltage cut off value. It is also important to note that the samples were analysed at 7 days old, and, from the subsequent NMR data gathered (Figure 43), this would suggest that it is not true equilibrium behaviour that is being observed.

This preliminary CD work agrees qualitatively with the NMR data (Figure 43). In particular, the NMR data shows that all the peptide was in a monomeric state in solutions of low peptide concentration and up to seven days old; the CD shows that under the same conditions the peptide was in a predominantly random coil, i.e. monomeric state.

To further confirm the c* for P_{11}-9 and to provide information on the conformational transition, the technique of FTIR was employed because it is complementary to CD UV as samples of higher concentrations can be studied.

Fourier Transform Infra-Red Spectroscopy, FTIR

Examination of the FTIR spectra of P_{11}-9 provided further evidence for the NMR findings. Three concentrations above the believed c* from the ^{1}HNMR study for P_{11}-9 were analysed and the amide I' region of the spectra was band fitted (Figure 51 and Figure 52).

For the two highest concentrations studied, the spectrum was dominated by β-sheet components located at 1613 cm^{-1} and 1625 cm^{-1}; weak peaks at higher wavenumbers of 1682 cm^{-1} and 1698 cm^{-1} implied antiparallel arrangement of the β-sheet structure. There was also a broad peak centred around 1650 cm^{-1} coexisting with the β-sheet bands, suggesting a small presence of monomeric peptide even at the highest concentrations studied by FTIR.

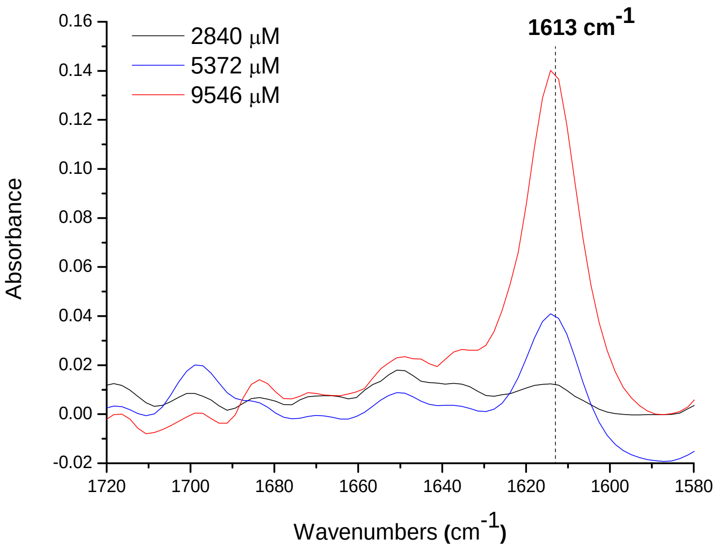

Figure 51 - FTIR amide I’ bands for P_{11}-9 solutions at three peptide concentrations in 130 mM NaCl, D_2O, pD 7.4, two weeks after sample preparation.

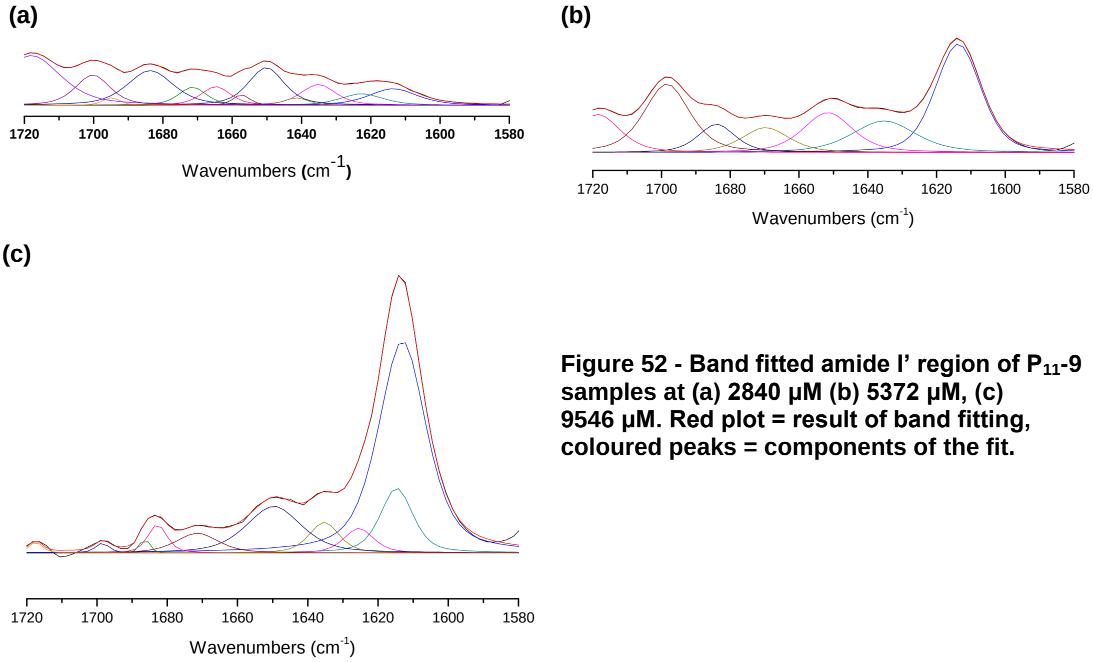

Figure 52 - Band fitted amide I’ region of P_{11}-9 samples at (a) 2840 μM (b) 5372 μM, (c) 9546 μM. Red plot = result of band fitting, coloured peaks = components of the fit.

The spectrum for the lowest concentration studied, 2840 μM, was not dominated by β-sheet components at 1613 cm^{-1} and 1622 cm^{-1}, however, they were still present alongside the peaks at higher wavenumbers implying an antiparallel arrangement once more. The random coil peak centered around 1650 cm^{-1} was of similar size to that of the β-sheet components, suggesting that neither peptide in an aggregated or monomeric state is the majority species.

The fitting data (Table 8) for the highest concentration investigated here was used to calculate a β-sheet content of 85.4%.

Peak Type	**Center X**	Height	FWHH	Other	Area	**Assignment**
Gaussian/Lorentzian	**1613.1**	0.1117	16.1368	0.4577	2.405	**β-sheet**
Gaussian/Lorentzian	**1614.7**	0.0342	10.8807	0.4927	0.4909	**β-sheet**
Gaussian/Lorentzian	**1625.5**	0.013	9.9377	0.4984	0.17	**β-sheet**
Gaussian/Lorentzian	**1635.3**	0.0163	9.9492	0.4977	0.2129	**β-sheet**
Gaussian/Lorentzian	**1649.6**	0.0246	18.4526	0.5017	0.5953	**α-helix**
Gaussian/Lorentzian	**1671.4**	0.0104	14.304	0.5052	0.1942	**TFA**
Gaussian/Lorentzian	**1682.8**	0.015	6.4159	0.5052	0.1264	**β-sheet**
Gaussian/Lorentzian	**1686.4**	0.0076	3.1721	0.5057	0.0316	**β-sheet**
Gaussian/Lorentzian	**1698.5**	0.0051	4.7792	0.5057	0.0323	**β-sheet**

Table 8 – Peaks found on analysing the amide I’ band of P_{11}-9 (9546 μM) spectrum at two weeks old, recorded in D_2O containing 130 mM NaCl

Again, like the CD work, the FTIR analysis was not carried out under equilibrium conditions. However it still agrees with the NMR data at the same timepoint of two weeks, concluding that below 2840 μM there was a conformational transition from monomeric peptide to anti-parallel β-sheet peptide.

Transmission Electron Microscopy, TEM

TEM was employed to study the morphology of the self-assembled aggregates. From Figure 53, it can be seen that the majority of the peptide was in thin aggregates, which can be seen forming a gel network covering the background of the grid. These aggregates vary in width from 2 to 4 nm, have an approximate persistence length of 10 to 21 nm and are at least 20 to 68 nm long. The properties of these aggregates imply they are most likely ribbons rather than fibrils, which would be expected to be wider and much more rigid than observed.[110]

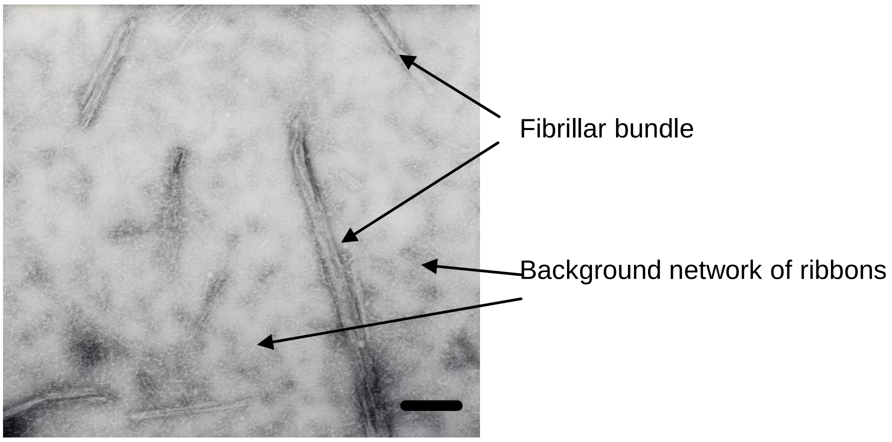

Figure 53 - TEM image of 0.5 mM P_{11}-9 in H_2O with 130 mM NaCl at pH 7.4. Magnification = 52000x. Sample = 3 months old. Scale bar = 200 nm

The ribbon network was random, however, there were parts that were less dense and these would be the pores in the gel. There was no well defined structure and the ribbons were seen to associate in a loose manner forming bundles of fibril-like structures, which vary in width from 78 to 102 nm. The individual fibril-like structures varied in width from 7 to 12 nm with lateral striations with widths of 2 to 4 nm, meaning that the fibril-like structures are formed from around 2 to 6 loosely packed ribbons.

Due to the high energy given off from the technique, often only the higher hierarchical structures such as the fibrils survived, and other structures like the ribbon were fragmented.

Here it was found that the presence of the serine residues in the peptides favours the formation of ribbons rather than fibrils in physiological-like conditions. This may be due to the low magnitude of ε_{fibril} for peptides that contain serines. This is in agreement with previous work carried out by the Aggeli group[114], where it was established that peptides that contain serines favour ribbon formation rather than fibrils in pure water conditions.

Interestingly, aggregates were seen in the TEM images at a concentration below that of the c* value determined by NMR. This may be due to a high level of monomer present resulting in aggregate formation during the drying process. The fact that they do not resemble well formed fibrils therefore suggests they are rapidly formed fibrils instead.

This study was only preliminary, therefore in order to truly gain an understanding of the aggregates formed in solution, more concentrations need to be investigated alongside different dilutions. Another hypothesis is that the fibrils may be present at a lower concentration than expected from the previous data due to the c* being a broad rather than abrupt transition.

To further study the effect of the basic scientific principle of charge on self-assembly, the same experimental method for the study of P_{11}-9 was carried out on the positively charged peptide P_{11}-12.

3.1.3.2 P_{11}-12

^{1}H Nuclear Magnetic Resonance Spectroscopy, NMR

As with the P_{11}-9 NMR study, the intention was to study the equilibrium self-assembly behaviour of this peptide because this had not previously been studied under these solution conditions and it would also enable fitting to the theoretical data. To try to examine this behaviour, the various different concentrations were prepared one by one and observed as a function of time. To establish if the linear region was visible using this technique, the solution peptide concentration vs. solution monomer concentration was plotted in Figure 54.

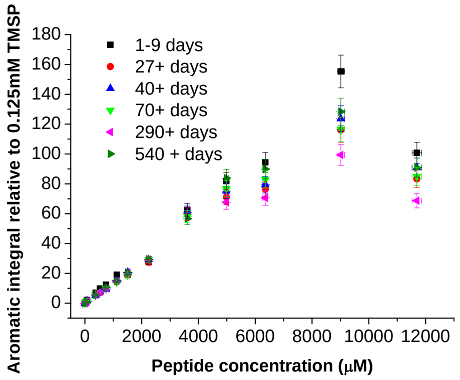

Figure 54 -^{1}H NMR aromatic region integral of P_{11}-12 relative to integral of 0.125 mM TMSP reference peak as a function of increasing total peptide concentration and time from sample preparation.

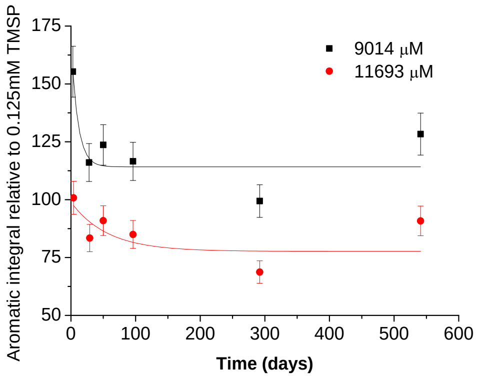

Figure 55 - Time variation of aromatic integral and of peptide concentration in monomeric state in P_{11}-12 solutions at two concentrations. Guidelines are first order decay fits created in OriginPro 8.6.

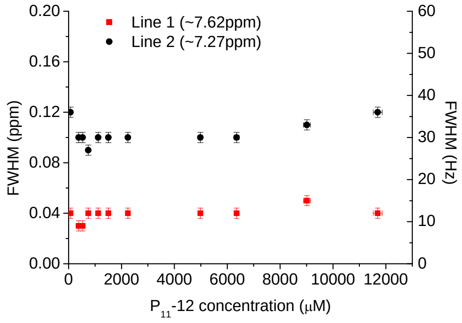

Figure 56 - Chemical shifts of aromatic peaks in P_{11}-12 ^{1}H NMR spectra as a function of increasing total peptide concentration.

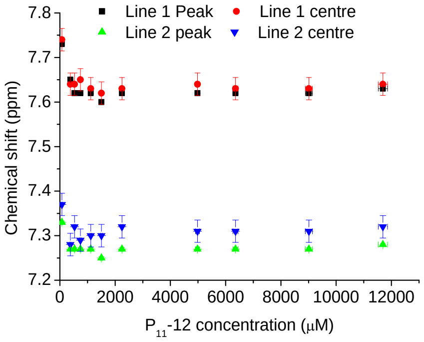

Figure 57 - Line widths of aromatic peaks in P_{11}-12 ^{1}H NMR spectra as a function of increasing total peptide concentration.

From Figure 54, it can be seen that the time to reach equilibrium conditions was within two months, with the main changes occurring in the first month. This is very slow, which is consistent with that of the charged peptide P_{11}-9. Solutions below c* were again seen to reach equilibrium rapidly, as the monomeric random coil solutions of P_{11}-9, whilst solutions above c* achieved equilibrium over the course of two months (Figure 55). It was important to be aware of such behaviour of self-assembling peptide materials for two reasons; firstly in order to obtain equilibrium data, one needs to wait a sufficient amount of time; secondly the use of gels in various applications requires consistency and reproducibility of their behaviour *in vitro* and *in vivo*; this may not always be possible unless materials in an equilibrium state are used.

The chemical shifts and line widths of the P_{11}-12 NMR lines, plotted in Figure 56 and Figure 57, did not appear to undergo any change as peptide concentration increased. This implies that the molecular states that give rise to the NMR signals plotted in Figure 54 are the same i.e. monomeric random coils, irrespective of the total peptide concentration.

Determination of c using the surfactant model*

Again, as with P_{11}-9, the surfactant model was employed to determine the c* value for P_{11}-12 (Figure 58). Only the equilibrium data above 27 days was used.

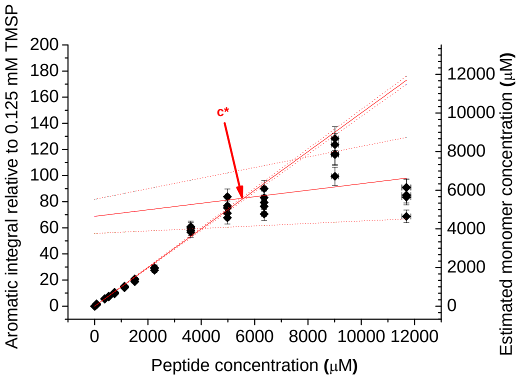

Figure 58 - Equilibrium NMR data used to determine c* value for P_{11}-12. The estimated monomer concentration scale was derived from the gradient of the linear region fit of 0.01479 μM^{-1}. The plateau region was taken to be a linear fit through the last four concentrations, whereas the monomer/linear region was taken to be a linear fit through the rest of the concentrations.

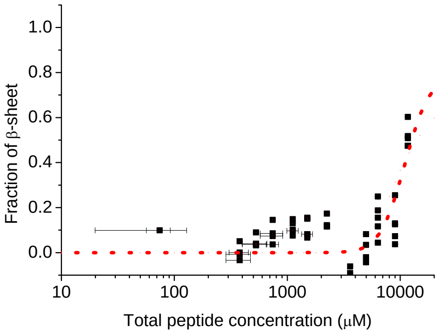

Figure 59 - Estimated equilibrium self-assembling curve for P_{11}-12, i.e. fraction of peptide in self-assembled state as a function of increasing total peptide concentration. Dotted line = sigmodal SGompertz fit created in OriginPro 8.6.

From Figure 58, and using the surfactant model, the c* for P_{11}-12 was estimated as 5600 ± 1750 μM. The right hand estimated monomer concentration axis for the plot was calculated from the aromatic integral divided by the slope of the linear monomer region of the plot.

From the results of the P_{11}-12 NMR data, the linear regime and plateau regime cross at 5600 ± 1750 μM and so the assumption could be made that peptide at a concentration less than this was 100% monomeric. Typically c* for self-assembly is a lot lower than c* for gelation. However, P_{11}-12 exhibits unusual behaviour, in that the c* for self-assembly seems to coincide with c* for gelation. This is possibly because the c* for self-assembly is so high that as soon as aggregation starts, the solution immediately reaches the semi-dilute regime and the start of gelation is observed; this concentration is 2300 ± 750 μM. From this information, and following the same method used for P_{11}-9, the self-assembly curve was constructed (Figure 59).

From Figure 59, it can be seen that the self-assembly curve is broad as is the case with P_{11}-9, this is thought to be due to either the precise magnitudes of $\varepsilon_{\text{tape and}}$ $\varepsilon_{\text{trans}}$ that are unknown at this time, or due to the ionised state of the charged peptides being affected slightly by changes in pH, which in turn can slightly affect the self-assembly behaviour.

From work previously carried out on this peptide under physiological like conditions by Carrick *et al.*,[114] it was observed that there is an extremely abrupt transition region between pD 6-8, as can be seen in Figure 60.

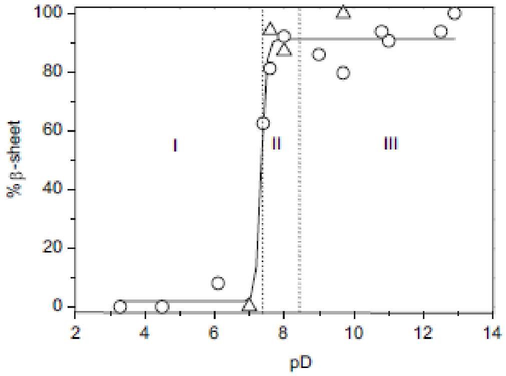

Figure 60 - Percentage β -sheet of P_{11}-12 (concentration = 7.1 mM) as determined by FTIR (O) and NMR (Δ) as a function of pD in 130 mM NaCl in D_2O: I: isotropic fluid,II: weakly nematic viscous fluid, III: weakly nematic gel.[114]

This would mean that a slight change of pD for the samples in the physiological range would results in very different c* values. The pD values for this study were measured straight after sample preparation and the samples range from a pD value of 7.34 to 7.54. This would result in samples belonging to different self-assembly curves because they have different c* values dependent on the pD of the solution. For this reason, it is not appropriate to carry out an accurate study of the self-assembly curve because it is not justifiable to fine tune the pD of each sample to within two decimal places. This may also explain the broadness of the observed curve.

As with P_{11}-9, additional techniques to NMR were used to assist with the understanding of the self-assembly process of P_{11}-12. CD UV and FTIR were used to reinforce where the c* is and to determine the conformational transition.

Circular Dichroism Ultra-Violet spectroscopy, CD UV

The CD UV spectra for a range of concentrations were obtained to confirm the c* value determined using ^{1}H NMR (Figure 61).

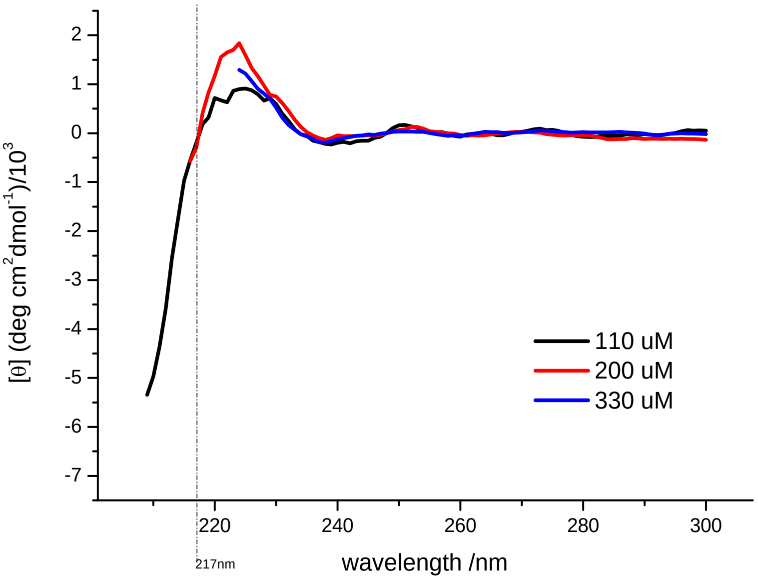

Figure 61 - CD Spectra for P_{11}-12 in 43 mM Na_2HPO_4, 0.02% wt/wt NaN_3, H_2O, pH 7.4, with a High Tension Voltage cut off of 700 V. Concentrations calculated using UV. Samples 7 days old. Sample pH as measured straight after preparation: 110 µM = 7.43, 200 µM =7.44, 330 µM = 7.44

As with P_{11}-9, a higher concentration than 500 µM could not be examined due to a HT voltage cut off being at a higher wavelength than that of interest for peptide secondary structure features. It can be seen that for all the solution concentrations studied the spectra corresponds to a predominantly random coil conformation, because there was a slightly positive band around 220 nm and the start of a negative peak that was centred at much lower wavelengths. Based on these data, the apparent c* is above 330 µM. The red and blue spectra were a little distorted due to the HT voltage; however, there were enough data to observe a random coil conformation. The samples were analysed at 7 days old, and the subsequent NMR data gathered (Figure 54) would suggest that it was not equilibrium behaviour that was being observed.

This preliminary CD work agrees qualitatively with the NMR data (Figure 54). In particular, the NMR data shows that all the peptide was in a monomeric state in solutions of low peptide concentration and up to 7 days old; the CD shows that under the same conditions the peptide was in a predominantly random coil, i.e. monomeric state.

Fourier Transform Infra-Red Spectroscopy, FTIR

The FTIR spectra for a range of concentrations are shown in Figure 62 and their band fitting in Figure 63.

At the lowest concentration of around 3000 µM, the percentage of β-sheet infra-red bands centered around 1615 and 1636 cm^{-1} was minimal and the spectrum was dominated by a broad band at 1650 cm^{-1}, suggesting a majority monomeric state. However, at higher peptide concentrations of nearly 5700 µM and over, the peaks characteristic of an anti-parallel β-sheet peptide became increasingly the most prominent feature of the spectra, with the main peak centred around 1614 cm^{-1} and smaller peaks at ca. 1625 cm^{-1} and 1635 cm^{-1}. Weak peaks observed at higher wavenumbers of 1684 and 1698 cm^{-1} imply antiparallel arrangement of the β-sheet structure. In all spectra, a large broad peak centred around 1650 cm^{-1} coexisted with the β-sheet bands. This suggests the presence of significant amount of peptide in non-β-sheet state even at the highest concentration studied by FTIR. A prominent peak centred at 1672 cm^{-1} present in all spectra is again attributed to residual TFA.

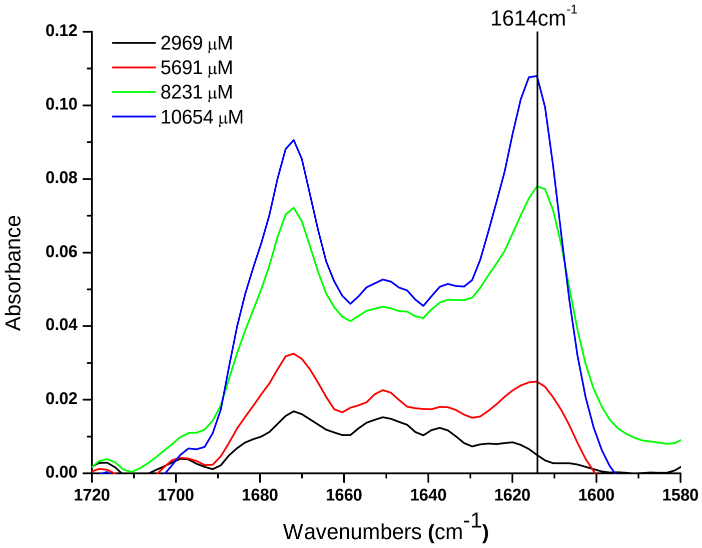

Figure 62 - FTIR amide I' bands for P_{11}-12 solutions with a range of peptide concentrations in 130 mM NaCl, D_2O, pD 7.4, two weeks after sample preparation.

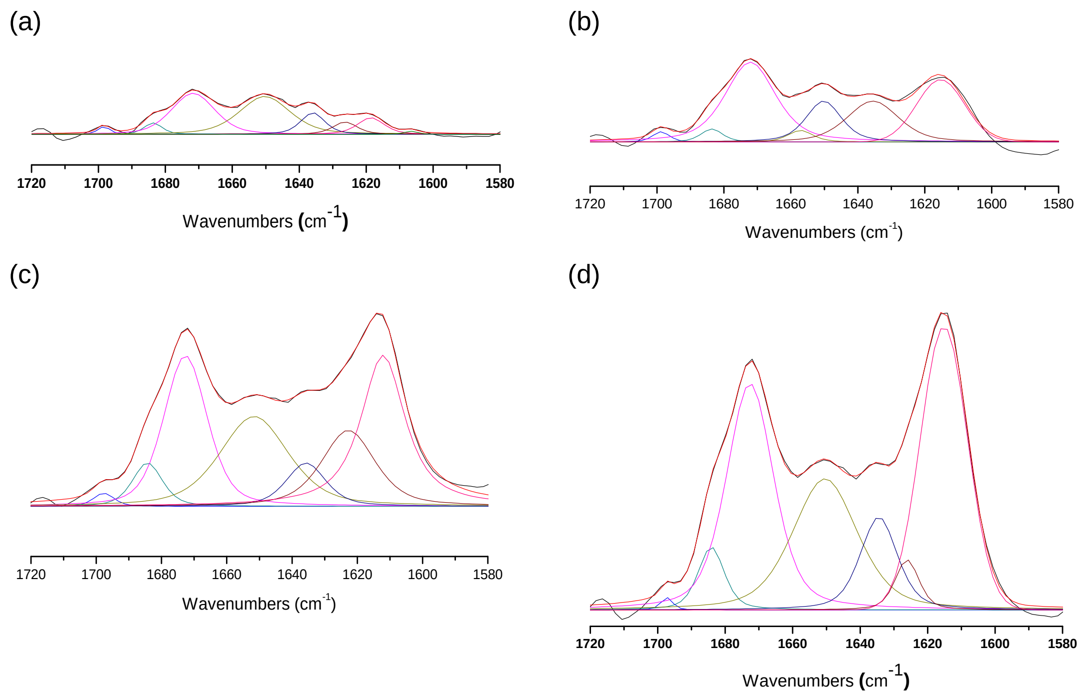

Figure 63 - Band fitted amide I’ region of P_{11}-12 samples at (a) 2969 μM, (b) 5691 μM, (c) 8231 μM, and (d) 10654 μM.

A table of the typical peaks present in the spectra for P_{11}-12 is shown in Table 9.

Peak Type	**Center X**	Height	FWHH	Other	Area	**Assignment**
Gaussian/Lorentzian	**1615.2**	0.1067	16.4752	1	1.8719	**β-sheet**
Gaussian/Lorentzian	**1626.1**	0.019	8.3789	0.5516	0.2051	**β-sheet**
Gaussian/Lorentzian	**1634.5**	0.0351	12.9454	0.5346	0.5889	**β-sheet**
Gaussian/Lorentzian	**1650.4**	0.0494	22.6382	0.5852	1.4204	**α-helix**
Gaussian/Lorentzian	**1672.6**	0.0853	16.3756	0.5922	1.7722	**TFA**
Gaussian/Lorentzian	**1684.2**	0.0237	9.2004	0.5225	0.2848	**β-sheet**
Gaussian/Lorentzian	**1697.3**	0.0047	4.159	0.5074	0.0255	**β-sheet**

Table 9 - Peaks found on analysing the amide I’ band of P_{11}-12 (10654 μM) spectrum at 2 weeks old, recorded in D_2O containing 130 mM NaCl.

The peak area and assignments from the fitting data were used to calculate the % β-sheet content within the samples studied here (Table 10).

Sample concentration (μM)	**% β-sheet (±10%)**
2969	46
5691	74
8231	71
10654	68

Table 10 – P_{11}-12 % β-sheet content as determined by FTIR

Again, like the CD work, the FTIR analysis was not carried out under equilibrium conditions. From the NMR data alone, a c* value of 5600 ± 1750 μM was estimated, however, a lower c* value of 2300 ± 750 μM was determined when visually observing gelation. The FTIR data confirmed that there is a broad conformational transition from monomeric peptide to anti-parallel β-sheet peptide below a concentration of 3000 μM.

Transmission Electron Microscopy, TEM

TEM was once again used to study the morphology of the peptide aggregates. From Figure 64 and Figure 65, it can be seen that P_{11}-12 tends to form loose bundles with a width of 10 to 20 nm. The individual thin subunits had a width of approximately 2 nm. In Figure 64 the amorphous aggregates feeding the fibrillar bundle formation can be observed, as well as the background network of ribbons.

These TEM images were taken four days after samples were prepared (Figure 64 and Figure 65). To see if the morphology of the peptide is the same for equilibrium conditions, samples were studied after 7.5 months (Figure 66, Figure 67 and Figure 68).

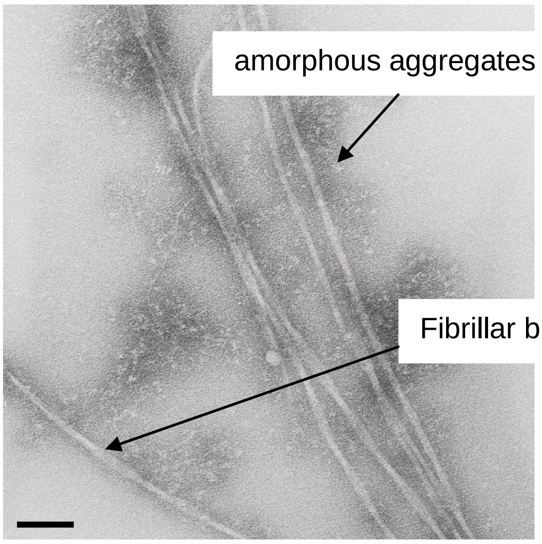

Figure 64 - TEM image of P_{11}-12 at 14 mM (20 mg/ml) in phosphate buffered saline solution, 73000x magnification, diluted to approximately 3.6 mM (5 mg/ml), sample 4 days old, scale bar = 100 nm.

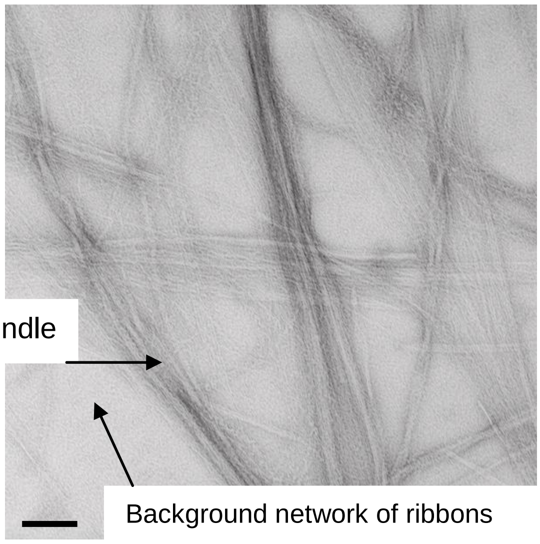

Figure 65 - TEM image of P_{11}-12 at 14 mM (20 mg/ml) in phosphate buffered saline solution, 73000x magnification, observed undiluted, sample 4 days old, scale bar = 100 nm

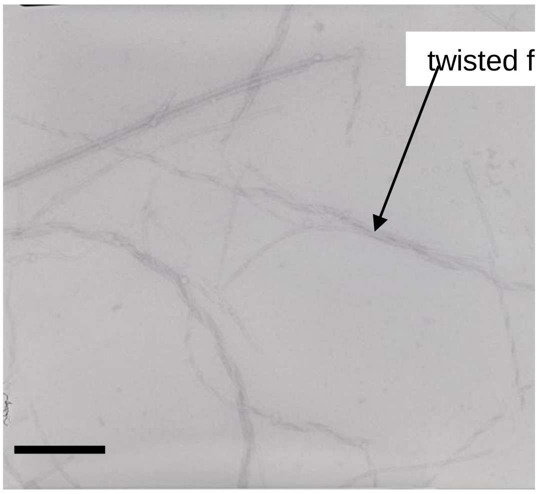

Figure 66 - TEM image of P_{11}-12 at 14 mM (20 mg/ml) in phosphate buffered saline solution, 39000x magnification, diluted to approximately 20 µM, sample 7.5 months old, scale bar = 400 nm.

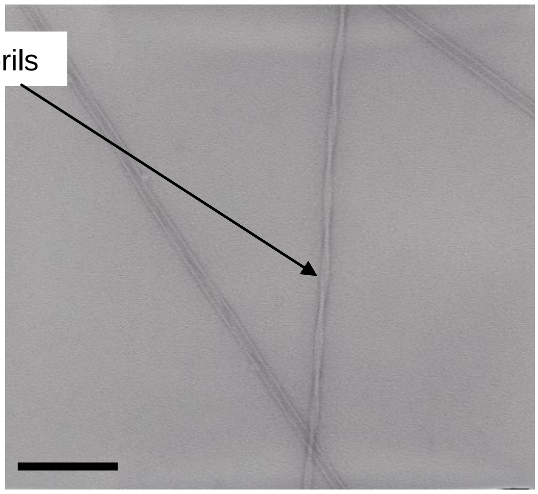

Figure 67 – TEM image of P_{11}-12 at 14 mM (20 mg/ml) in phosphate buffered saline solution, 73000x, magnification, diluted to approximately 20 µM, sample 7.5 months old, scale bar = 200 nm.

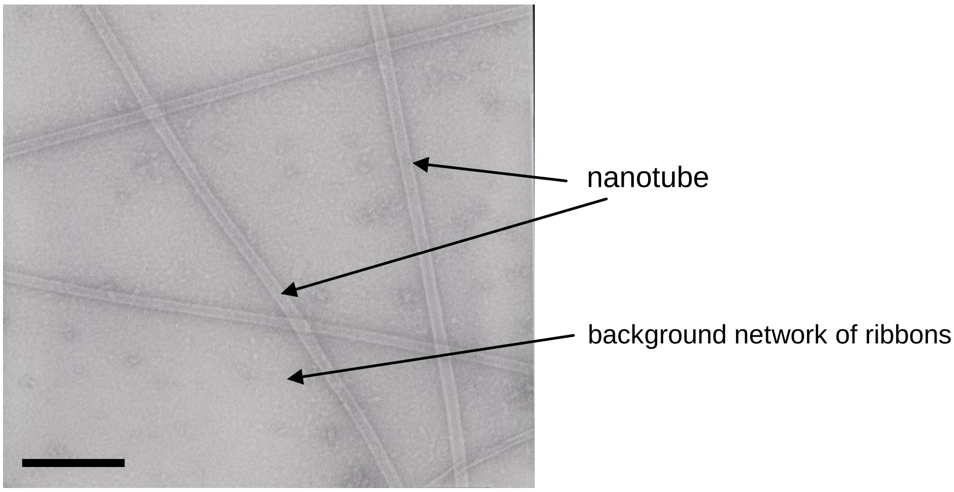

Figure 68 - TEM image of P_{11}-12 at 14 mM (20 mg/ml) in phosphate buffered saline solution, 73000x magnification, diluted to approximately 5 mM (7 mg/ml), sample 7.5 months old, scale bar = 200 nm.

As can be seen in Figure 66 and Figure 67 once again the majority of the peptide was in thin aggregates forming a background network of ribbons 2-4 nm wide. There was also a presence of highly twisted fibrils varying in width between 15 and 40 nm with a twist pitch from 100 – 250 nm.

Interestingly, there also appeared to be another self-assembled structure present in this sample, which can be described as a nanotube and is visible in Figure 68. It is believed that nanotube formation occurs via edge to edge interactions of β-sheet ribbons to form helical structures, whose width is a multiple of the width of an individual ribbon. The external width of the nanotubes was between 19 and 30 nm.

Previously in the Aggeli group, it has only been possible to form nanotubes in the presence of hexafluoroisopropanol (HFIP), which is a very strong polar solvent. HFIP enhances the edge to edge interactions of ribbons by interacting with the faces of the ribbons and preventing them from stacking on top of one another to form fibrillar structures.[197]

To complete the study of the effect of charge on self-assembly, the same experimental method for the study of P_{11}-9 and P_{11}-12 was carried out on the net neutrally charged peptide P_{11}-7.

3.1.3.3 P_{11}-7

The charged peptides P_{11}-9 and P_{11}-12 were soluble in physiological like conditions, so they underwent a transition from clear solutions to clear gels with an increase in concentration. In contrast, the net neutrally charged peptide P_{11}-7 did not form soluble self-assembled structures in the same conditions and so as the concentration increased the amount of insoluble white precipitate increased with it. However, to enable a full understanding of the basic scientific principle of charge it was necessary to compare it with the positively and negatively charged peptides above.

^{1}H Nuclear Magnetic Resonance Spectroscopy, NMR

A ^{1}H NMR method has already been established in this project and so the same was applied here. To examine the self-assembly behaviour, various different concentrations were prepared one by one and observed as a function of time (Figure 69).

This study revealed that the neutrally charged peptide has faster kinetics than the two charged peptides. From Figure 69 and Figure 70, it can be seen that the peptide has reached apparent equilibrium behaviour between one and two weeks, with not much movement between the time-point curves.

The chemical shifts and line widths of the P_{11}-7 NMR lines plotted in Figure 69 do not appear to undergo any significant change as peptide concentration increases (Figure 71 and Figure 72). This implies that the molecular states that give rise to the NMR signals plotted in Figure 69 are the same, i.e. monomeric random coils, irrespective of the total peptide concentration.

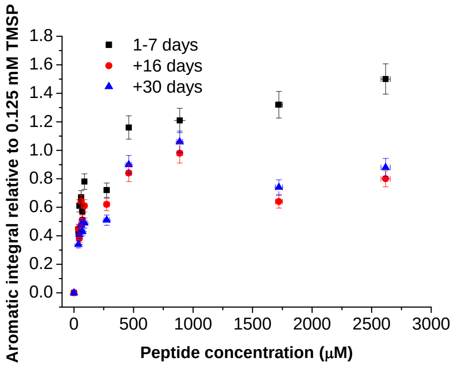

Figure 69 - ^{1}H NMR aromatic region integral of P_{11}-7 relative to integral of 0.125 mM TMSP reference peak as a function of increasing total peptide concentration and time from sample preparation.

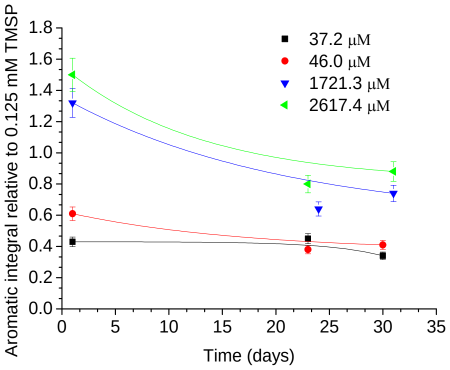

Figure 70 - Time variation of aromatic integral and of peptide concentration in monomeric state in P_{11}-7 solutions at four concentrations. Guidelines are first order decay fits created in OriginPro 8.6.

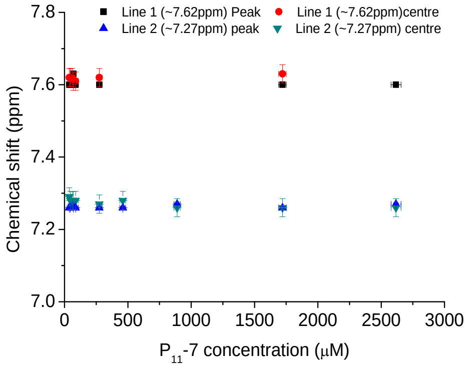

Figure 71 - Chemical shifts of aromatic peaks in P_{11}-7 ^{1}H NMR spectra as a function of increasing total peptide concentration.

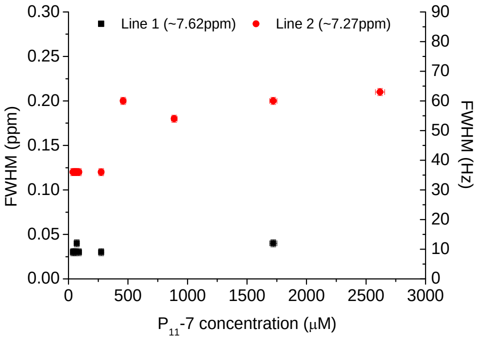

Figure 72 - Line widths of aromatic peaks in P_{11}-7 ^{1}H NMR spectra as a function of increasing total peptide concentration.

From Figure 73, and using the surfactant model, the c* for P_{11}-7 was estimated as 110 ± 20 μM. The right hand estimated monomer concentration axis for the plot was calculated from the aromatic integral divided by the slope of the linear monomer region of the plot.

From the above data, the self-assembly curve, Figure 74, showing the fraction of solution peptide in an aggregated state as a function of increasing peptide concentration in solution, was constructed.

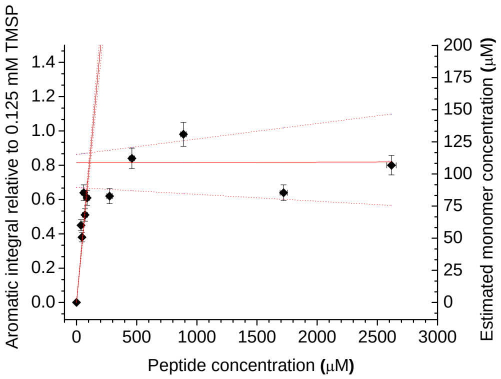

Figure 73 - Equilibrium NMR data used to determine c* value for P$_{11}$-7. The estimated monomer concentration scale is derived from the gradient of the linear region fit of 0.00749 μM^{-1}. The plateau region was taken to be a linear fit through the last five concentrations, whereas the monomer/linear region was taken to be a linear fit through the rest of the concentrations.

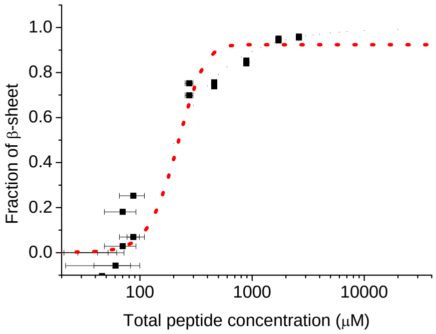

Figure 74 - Estimated equilibrium self-assembling curve of P$_{11}$-7, i.e. fraction of peptide in self-assembled state as a function of increasing total peptide concentration. Dotted line = OrginPro 8.6 sigmoidal SGompertz fitting.

Due to this peptide not forming soluble aggregates, it was deemed not suitable for a CD UV study due to light scattering effects resulting in possible nonsensical spectra.

Transmission Electron Microscopy, TEM

Previously, it has been found that the peptide P$_{11}$-7 has a low ε_{fibril} in pure water and so has a tendency to favour the formation of ribbons rather than fibrils.[173] It has been found here that this is the same for physiological like conditions, as is demonstrated in Figure 75. The majority of the peptide was in ribbons, which were seen forming a network covering the background of the grid; these structures varied in width from 2 to 5 nm. There was no well defined structure and the ribbons associated in a loose manner forming fibril-like bundles, which varied in width from 10 to 23 nm, meaning that they are formed from around 3 to 6 loosely packed ribbons with a width of 2 to 5 nm. These loosely packed fibrils bundles are the start of phase separation/formation of precipitate, which is what leads this peptide to be insoluble.

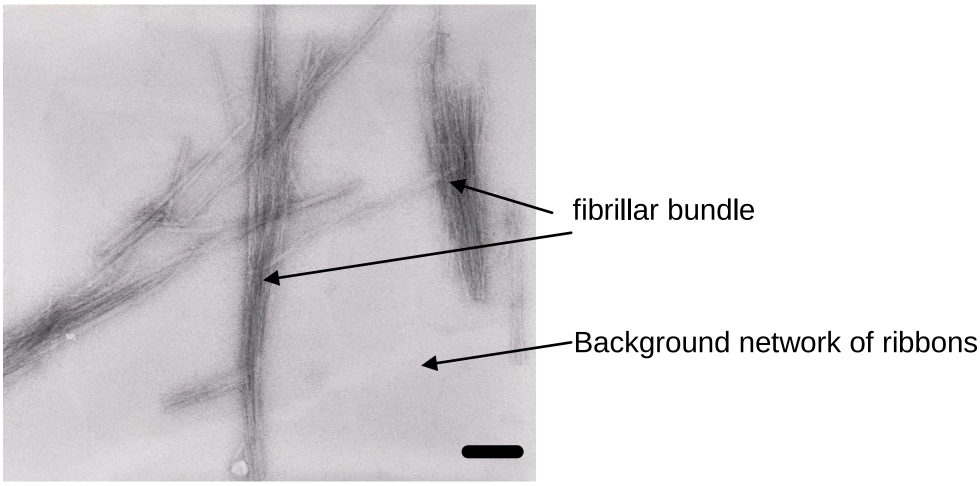

Figure 75 - TEM image of 3 mM P_{11}-7 in H_2O with 130 mM NaCl at pH 7.4. Samples 25 days old. Magnification = 39000x. Scale bar = 200 nm

There was also further evidence that is indicative of a peptide that preferentially forms ribbons, and this was the presence of ring structures with a diameter of 4 to 8 nm. A ring is formed when a ribbon is long enough to curl around and “bite its own tail” but not so long that the entropic penalty would be too great. Fibrils are too rigid to form rings and the lower hierarchical structures are not long enough.

Now that an insight had been gained in the basic scientific principles of the self-assembly of these peptide building blocks in physiological-like solutions, it was possible to optimise the peptide system further for biomedical applications, in particular for use in the treatment of disc degeneration.

P_{11}-13 and P_{11}-14 are glutamine-based peptides (Table 11) and have been designed to have complementary electric charges such that when mixed, fibril self-assembly and subsequent gel formation occurs spontaneously. P_{11}-13 has an overall charge of -6 and P_{11}-14 has an overall charge of +4 and so once mixed they have a net charge of -2. As these peptides prior to mixing do not favour self-assembly, they could potentially be used as an injectable biomaterial. Also, as they benefit from very large enthalpic gains from the electrostatic interactions, they have a low c* and therefore a low concentration of peptide in the monomeric state, which should benefit biocompatibility as well as help them to remain at a treatment site.

Peptide Name	**Net Charge at pH 7.5**	**Polar Amino Acid**	**Peptide Primary Structure**
P_{11}-13/14	-2	Glutamine	CH_3CO-E-Q-E-F-E-W-E-F-E-Q-E-NH_2 CH_3CO-Q-Q-O-F-O-W-O-F-O-Q-Q-NH_2
P_{11}-28/29	+2	Glutamine	CH_3CO-O-Q-O-F-O-W-O-F-O-Q-O-NH_2 CH_3CO-Q-Q-E-F-E-W-E-F-E-Q-Q-NH_2

Table 11 - Peptide structures of P_{11}-13/14 and P_{11}-28/29.

3.1.3.4 P_{11}-13 and P_{11}-14

^{1}H Nuclear Magnetic Resonance Spectroscopy, NMR

The NMR method already established in this project was also applied to these peptides. To examine the self-assembly behaviour, the various different concentrations were prepared one by one and observed as a function of time.

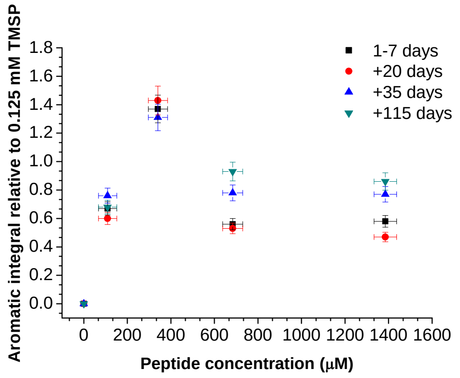

Figure 76 - ^{1}H NMR aromatic region integral of P_{11}-13+14 relative to integral of 0.125 mM TMSP reference peak as a function of increasing total peptide concentration and time from sample preparation.

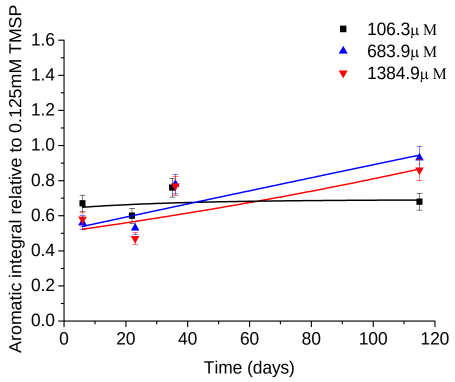

Figure 77 - Time variation of aromatic integral and of peptide concentration in monomeric state in P_{11}-13+14 solutions. Guidelines are first order decay fits created in OriginPro 8.

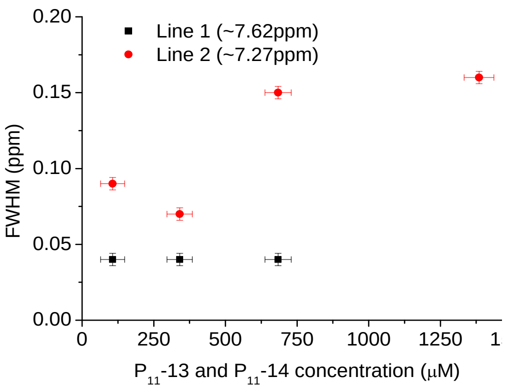

Figure 78 - Line widths of aromatic peaks in P_{11}-13+14 ^{1}H NMR spectra as a function of increasing total peptide concentration.

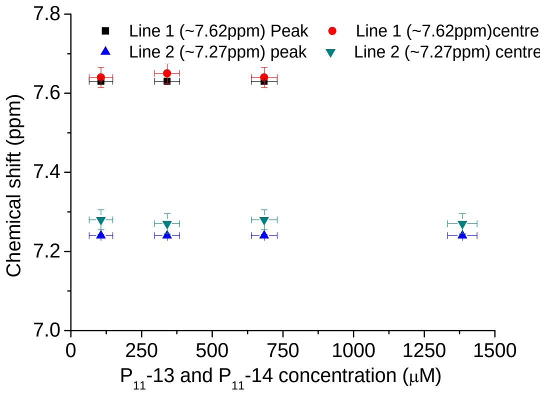

Figure 79 - Chemical shifts of aromatic peaks in P_{11}-13+14 ^{1}H NMR spectra as a function of increasing total peptide concentration.

From the data gathered (Figure 76), it was not possible to see a linear region, which would suggest that all the concentrations studied were above c*. Equilibrium conditions were reached much faster for these complementary peptides than for the single peptides previously studied (Figure 77). This is thought to be due to the strong electrostatic interactions between the two peptides driving self-assembly.

The line widths of the aromatic region and chemical shifts of the peaks in this region were also measured to check whether they undergo any change as peptide concentration increases (Figure 78 and Figure 79). There was no change in chemical shifts, however, at a concentration of around 700 μM and greater, the line width increased, which is thought to be due to the onset of gelation.

*Determination of c**

Due to there being no visible linear monomer region visible in the NMR plot (Figure 76), the surfactant model could not be employed here to determine the c* of P_{11}-13/14. However, the plateau region visible in the plot could be thought of as the background monomer concentration. To estimate the monomer concentration, the integral was divided by the slope of the monomer linear line for P_{11}-4 (0.0218 μM^{-1})[189] because this had the same hydrophobicity and overall charge as P_{11}-13/14, so is believed to be the closest representation. The c* for this complementary peptide was estimated as the point at which the plateau region for P_{11}-13/14 crosses the monomer line for P_{11}-4. Therefore, from this information, c* for P_{11}-13/14 was estimated as 28 ± 7 μM.

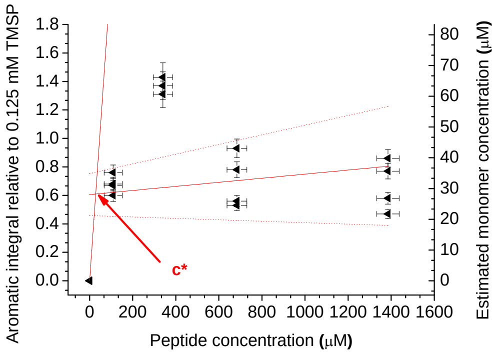

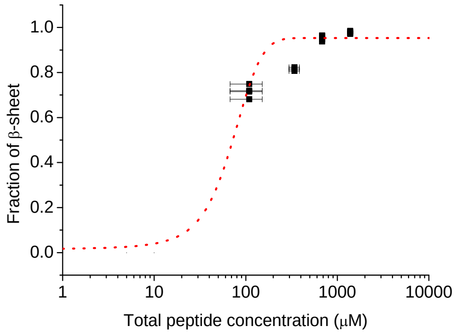

Figure 80 - Equilibrium NMR data used to determine c* value for P_{11}-13/14.

Figure 81 - Estimated equilibrium self-assembling curve for P_{11}-13/14, i.e. fraction of peptide in self-assembled state as a function of increasing total peptide concentration. Dotted line = OriginPro 8.6 sigmodal SGompertz fitting.

From the above data, the self-assembly curve (Figure 81), showing the fraction of solution peptide in an aggregated state as a function of increasing peptide concentration in solution, was constructed, following the same method as used for the previous peptides.

To establish the effect of charge for the complimentary peptides, another complimentary pairing was investigated using P_{11}-28 and P_{11}-29 peptide analogues to P_{11}-13 and P_{11}-14. P_{11}-28 has an overall charge of +6 and P_{11}-29 has an overall charge of -4 and so once mixed they have a net charge of +2. Again, because these peptides do not favour self-assembly prior to mixing, they can potentially be used as an injectable biomaterial.

3.1.3.5 P_{11}-28 and P_{11}-29

^{1}H Nuclear Magnetic Resonance Spectroscopy, NMR

The NMR method already established in this project was also applied to these peptides. To examine the self-assembly behaviour, the various different concentrations were prepared one by one and observed as a function of time.

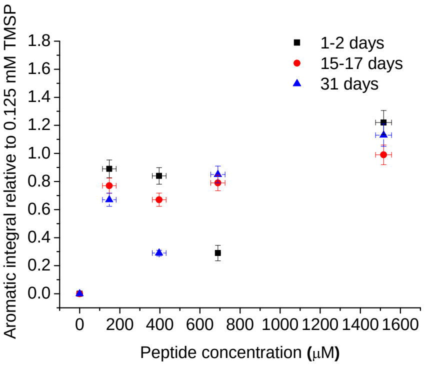

Figure 82 - ^{1}H NMR aromatic region integral of P_{11}-28+29 relative to integral of 0.125 mM TMSP reference peak as a function of increasing total peptide concentration and time from sample preparation.

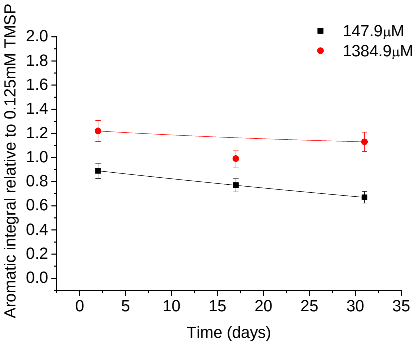

Figure 83 - Time variation of aromatic integral and of peptide concentration in monomeric state in P_{11}-28+29 solutions. Guidelines are first order decay fits created in OriginPro 8.6.

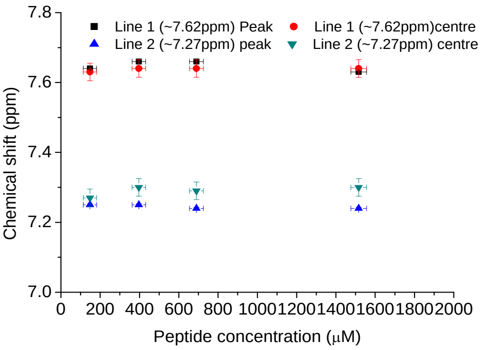

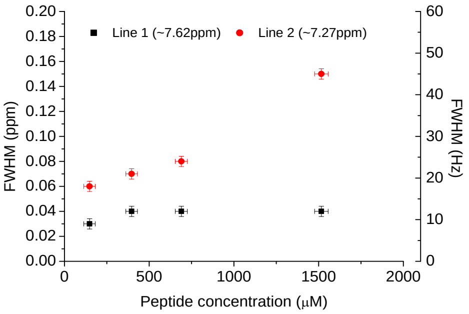

Figure 84 - Chemical shifts of aromatic peaks in P_{11}-28+29 ^{1}H NMR spectra as a function of increasing total peptide concentration.

Figure 85 - Line widths of aromatic peaks in P_{11}-28+29 ^{1}H NMR spectra as a function of increasing total peptide concentration.

As with P_{11}-13+14, from the data gathered (Figure 82) it was not possible to see a linear region, which would suggest that all the concentrations studied were above c*. Equilibrium conditions were reached much faster for these complementary peptides than for the single peptides previously studied (Figure 83). This is thought to be due to the strong electrostatic interactions between the two peptides driving self-assembly.

The line widths of the aromatic region and chemical shifts of the peaks in this region were also measured to check whether they undergo any change as peptide concentration increases (Figure 84 and Figure 85). There was no change in chemical shifts. However, for the aromatic peak at 7.27 ppm, there was an increase in line width with concentration, which is thought to be due to local or global gelation in the sample.

*Determination of c**

Due to there being no visible linear monomer region visible in the NMR plot (Figure 82), the surfactant model could not be employed here to determine the c* of P_{11}-28/29. The plateau region visible in the plot could be thought of as the background monomer concentration. To estimate the monomer concentration, the integral was divided by the slope of the monomer linear line for P_{11}-8 (0.0200 μM^{-1})[189] because this has the same hydrophobicity and overall charge as P_{11}-28/29, so was believed to be the closest representation. The c* for this complementary peptide was estimated as the point at which the plateau region for P_{11}-28/29 crosses the monomer line for P_{11}-8. (Figure 86) From this information, the c* value for P_{11}-28/29 was estimated as 29 ± 11 μM.

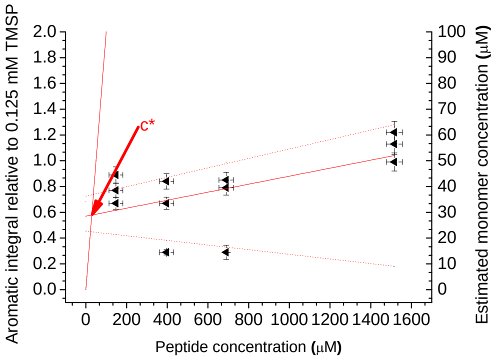

Figure 86 – Equilibrium ^{1}HNMR data used to determine c* value for P_{11}-28/29. The estimated monomer concentration scale is derived from the gradient of the linear region fit of P_{11}-8, 0.0200 μM^{-1}. The plateau region is taken to be a linear fit through the all the concentrations whereas the monomer/linear fit is taken to be a theoretical linear fit of the P_{11}-8 monomer line.

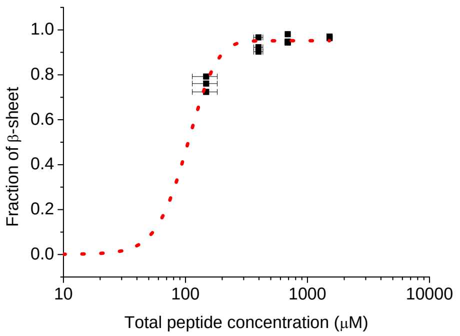

Figure 87 - Estimated equilibrium self-assembling curve for P_{11}-28/29, i.e. fraction of peptide in self-assembled state as a function of increasing total peptide concentration. Dotted line = sigmodal SGompertz fit created in OriginPro 8.6.

From the above data the self-assembly curve, Figure 87 showing the fraction of solution peptide in an aggregated state as a function of increasing peptide concentration in solution, was constructed.

3.1.4 Discussion

3.1.4.1 The effect of net peptide charge on self-assembly

It has been found previously within the Aggeli group that overall peptide charge can play an important role in peptide self-assembly, with even a single increment of peptide charge magnitude resulting in large increases in the amount of free monomer present in equilibrium with aggregates, and the concentration at which aggregation occurs.[189] It was also observed that the polarity of the charge had no effect; this hypothesis was tested again in this work by comparing the negatively charged P_{11}-9 with the positively charged P_{11}-12 and with the neutrally charged P_{11}-7 peptide.

The c* for P_{11}-7 is lower than the c* values for the two charged peptides as is demonstrated in Figure 88, with the background monomer concentration being largest for P_{11}-12.

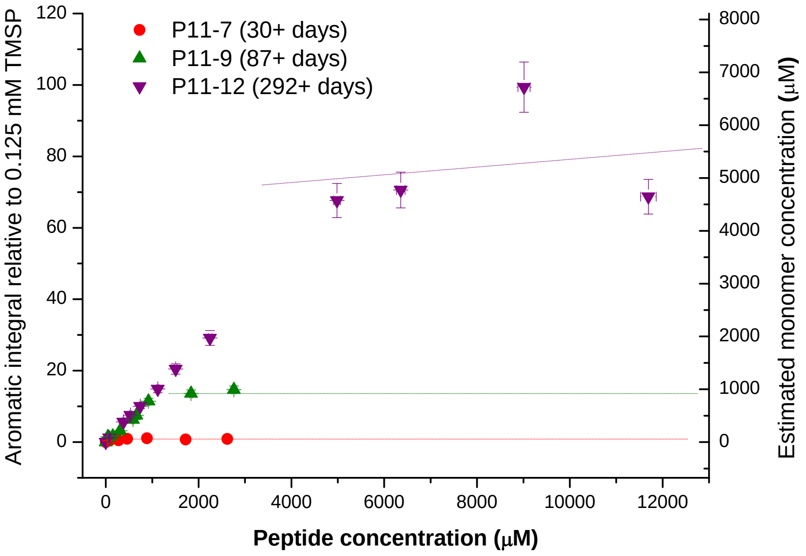

Figure 88 - Concentration of peptide in the monomeric state vs. solution peptide concentration, after a month for P_{11}-7, after 3 months for P_{11}-9 and after around 10 months for P_{11}-12. The estimated monomer concentration scale is derived from the gradient of the linear region fit of 0.01479 μM^{-1} for P_{11}-12.

The magnitude of c* is governed by the thermodynamic parameters involved, tape energy (ε_β) and transformation energy (ε_{trans}) (Equation 8):

$$c* = \frac{1}{v_\beta}\exp\left(\varepsilon_{trans} - \varepsilon_\beta\right)$$

Equation 8 - Critical concentration

Where c* is the critical number density concentration of the peptide in number of molecules/m^3, v_β is the effective volume of bonds between neighbouring peptides, ε_{trans} is the transformation energy (entropy lost) and ε_β is the tape scission energy (enthalpy gained).

The tape energy for all three peptides should be similar because it is dependent on the length of the chain, and number and quality of non-covalent interactions, which is the same for P_{11}-7, 9 and 12 with them only differing in charge. Therefore the difference in c* for these three peptides is due to the transformation energy, which is entropic in nature and is dependent on the straightening out of the highly flexible peptide chain and the immobilisation of counter ions and salts. In order for the charged peptides P_{11}-9 and P_{11}-12 to form a fibril they need to be neutralised to overcome the electrostatic repulsions from the peptides inside the fibril being closer than their debye length. However, this neutralisation comes at an entropic cost because these counter-ions are also bound inside the fibrils therefore becoming more ordered. The difference in the c* of the three serine-based peptides is demonstrated by comparing their self-assembly curves (Figure 89).

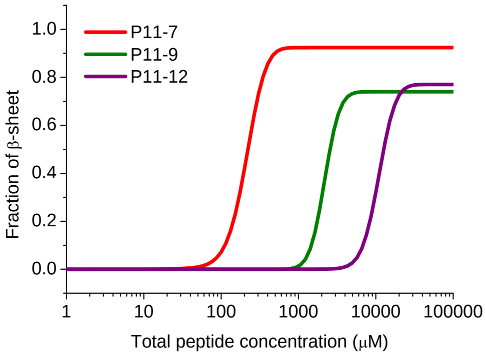

Figure 89 - Estimated self -assembly curves for P_{11}-7, P_{11}-9 and P_{11}-12. Lines = OriginPro 8.6 sigmodal SGompertz fitting.

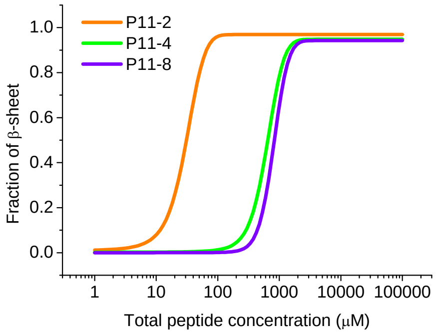

Figure 90 - Estimated self -assembly curves for P_{11}-2, P_{11}-4 and P_{11}-8. Lines = sigmodal SGompertz fits created in OriginPro 8.6. (Data from S. Maude).[189]

This same trend of the neutrally charged peptide having the lowest c* followed by the negatively charged peptide then the positively charged peptide having the highest c* is also true for the glutamine analogues P_{11}-2, P_{11}-4 and P_{11}-8 (Figure 90). However, the effect is not as dramatic as the glutamine polar zipper effect dominates over the charge effect.

It is hypothesised that the differences in the peptides' isoelectric point may explain the difference between the positively charged P_{11}-12 and negatively charged P_{11}-9. The positively charged peptide may in physiological-like conditions have a net overall charge of 2, whereas the negatively charged peptide may only have a net overall charge of 1.5, therefore resulting in fewer counter-ions being immobilised inside the fibril for the negatively charged peptide, leading to a lower entropic penalty.

The increase in c* for the positively charged P_{11}-12 may also be due to the positively charged ornithine residues having longer side chains than the negative glutamate residues (replacing the ornithines) in the P_{11}-9 peptide. The longer side chain of ornithine will create a greater steric hindrance to two peptides self-assembling as well as there being a greater entropic energy loss upon self-assembly.

Fitting of the experimental data for P_{11}-2, P_{11}-4 and P_{11}-8 has been carried out by Steven Maude, using the model described by Nyrkova *et al.*[198] set up as a Mathcad program (Figure 91). The parameters entered into Mathcad were: the volume of hydrogen bonds, the number of tapes in a fibril and c*, the critical aggregation concentration. *(Steven Maude and Irina Nyrkova personal communications, unpublished data)*

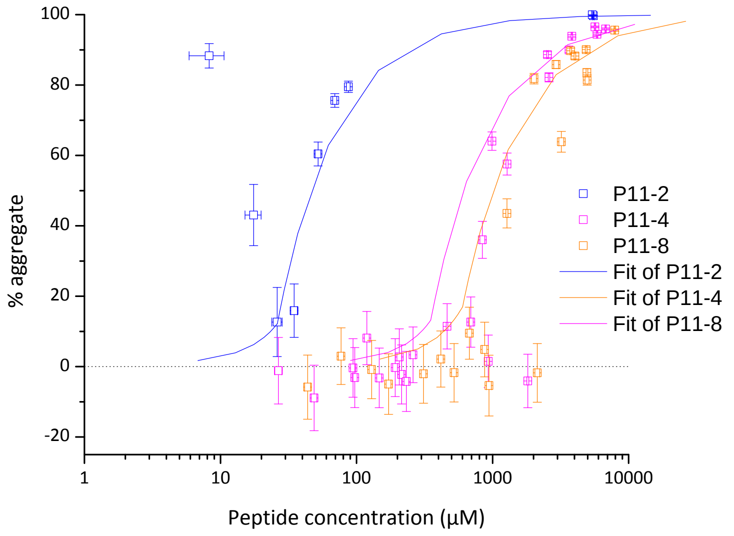

Figure 91 – Plot of P_{11}-2, P_{11}-4 and P_{11}-8 Mathcad fits. (*Steven Maude personal communications, unpublished data)*

As a starting point, the parameters derived for P_{11}-2 in pure water were used,[110] namely ε_{trans} = 3 ± 1 k_BT and ε_{ribbon} = 0.6 ± 0.3 k_BT.

ε_{ribbon} was estimated to be similar for all of these peptides (and similar to the value used for P_{11}-2 in water) because it originates from the hydrophobic pairing of tapes. The residues on the hydrophobic face are identical (QFWFQ) for all of the peptides studied and so these interactions should be comparable.

The fitting of the experimental data yields a tape scission energy, ε_β (k_BT), and predicted equilibrium lengths. The tape scission energy is calculated for the inputted energetic parameters using Equation 9, which is derived from Equation 8:

$$\varepsilon_\beta = \varepsilon_{trans} - \varepsilon_{ribbon} - \ln(\nu_\beta \times C\,*)$$

Equation 9

Where ε_{trans} is the free energy change of a monomer from random coil to rod, ε_β is the enthalpic tape energy or the energy required to break a tape apart and ε_{ribbon} is the energy required to break a ribbon apart and ν_β is the effective volume of hydrogen bonds.

From this information, the free energy change, △G can be calculated for a peptide monomer when a monomer becomes incorporated inside a fibril using Equation 10:

$$\Delta G = \varepsilon_{trans} - \varepsilon_{\beta} - \varepsilon_{ribbon}$$

Equation 10

The fibril scission energy, $\varepsilon_{fibril,}$ is the energy required to break a fibril and this can be calculated by Equation 11:

$$\varepsilon_{\mathrm{fibril}=}\varepsilon_{\boldsymbol{\beta}} * \mathrm{p}$$

Equation 11

Where p is the number of tapes per fibril.

The average equilibrium lengths are determined from the fits and given in units of number of peptides, therefore to find the total length this is multiplied by the width of one peptide, 0.47 nm.

The energies and average lengths for peptides P_{11}-2, P_{11}-4 and P_{11}-8 produced from the fitting carried out by Steven Maude are listed in Table 12.

Peptide (charge at pH 7)	P_{11}-4 (-2)	P_{11}-2 (0)	P_{11}-8 (+2)
p (number of tapes per fibril)	8	6	8
ε_{tr} (k_BT)	3.10	3.05	2.95
ε_{ribbon}(k_BT)	0.65	0.60	0.60
ε_{β} (k_BT)	23.36	25.74	21.52
ΔG of peptide monomer to peptide in (middle of) fibril	-51.6 kJ mol^{-1}	-58.0 kJ mol^{-1}	-50.3 kJ mol^{-1}
Scission energy for fibril (tape scission energy * p)	461.3 kJ mol^{-1}	382.9 kJ mol^{-1}	449.4 kJ mol^{-1}
Average length at 18 mM (approx. 30 mg ml^{-1})	2.35 * 10^7 km	2.35 * 10^5 km	1.41 * 10^6 km

Table 12 – Peptide fitting parameters and energies and lengths derived from the fits. (1 k_BT = 2.479 kJ.mol^{-1}) ***(Unpublished data, Steven Maude, University of Leeds, 2012).***

The predicted fibril lengths are extraordinarily long. At approximately 30 mg ml^{-1}, for peptides with net charges of 0 to 2, these are estimated to be hundreds of thousands, or even millions, of kilometers long (c.f. Earth's circumference of 40000 km). However, these lengths are the equilibrium lengths, therefore these values would be approached as the number of fibril seeds tends to one. Considering restricted volumes and fibril breakage this means that many seeds, rather than a single one exist, reducing the ultimate length achieved. Fibril lengths therefore are dependent both on how fibrils are prepared (number of seeds) and handled (sonication, vortexing break up existing fibrils). There is also a large entropic barrier to having one fibril.

The tape energy ε_{β} is the free energy change accompanying the association of two monomeric β-strands to form a β-sheet (and is similar to the scission energy of the tape) and although mainly enthalpic in nature the differences in the values for each of the peptides can be attributed to the loss of entropy from not only the binding of the β-strand peptide monomers in the fibril structures but also the binding of the counter ions, which is required for the fibrils to be internally neutral and to allow the peptides to overcome their Debye distances. The counter-ions are closely bound and ordered in fibrils, relative to their solution state surrounding peptide monomers. As the differences in ε_β for the different charged peptides are far more than for ε_{tr}, it can be concluded that ε_β has the largest impact on the total free energy change of monomers.

The tape scission energy for these peptides is roughly 2.5 times greater than the strength of hydrogen bond in water (23 kJ.mol^{-1}),[199] whereas the fibril scission energy is around 19 times greater.

Fibrils are, for the most part, internally electroneutral, since any excess charges are balanced by counter-ions present in the salt solution and the charge effect largely manifests in ε_β, so the effect of charge in destabilising fibrils, i.e. $\varepsilon_{fibril,}$ is minimal.

From the energetics calculated here it is even more evident that charge has an effect on the self-assembly of the peptides. The neutral P_{11}-2 peptide has a higher ε_β and therefore more favourable free energy change for fibril formation than those of the charged peptides P_{11}-4 and P_{11}-8. For P_{11}-2, only two peptide monomers are needed to form a dimer, whereas for P_{11}-4 or P_{11}-8 to form a dimer, not only are the two peptide monomers required, but four counter-ions to neutralise the charge. In this case, this process has a higher overall order of reaction than for P_{11}-2 and may explain the effect of charge on the kinetics of self-assembly.

3.1.4.2 The effect of polar amino acid residues on self-assembly

The effect of polar amino acids on self-assembly in physiological like conditions is one of the design principles that was set out to be established by this work. The greater the electronegativity difference between atoms in a bond, the more polar the bond. Side chains, which have functional groups such as acids, amides, alcohols, and amines will impart a more polar character to the amino acid. To gain an insight into the role of polar side chains as another design principle for peptide self-assembly and gelation in a physiological environment the self-assembly curves of the three serine-based peptides P_{11}-7, P_{11}-9 and P_{11}-12 were compared with the three charged analogous glutamine-based peptides P_{11}-2, P_{11}-4 and P_{11}-8 (work carried out by S Maude) (Table 13).[117]

Peptide	**Polar residue**	**Charge**	**c^*_{sa} (μM)**	**c^*_{gel} (μM)**
P_{11}-2	Q	0	14 ± 3.2	-
P_{11}-7	S	0	110 ± 20	-
P_{11}-4	Q	-2	310 ± 72	2000 ± 600
P_{11}-9	S	-2	1160 ± 175	4500 ± 1500
P_{11}-8	Q	+2	400 ± 100	2000 ± 600
P_{11}-12	S	+2	5600 ± 1750	2300 ± 750

Table 13 - Peptide c* values (where c^*_{sa} = critical self-assembly concentration, as determined by ^{1}HNMR and c^*_{gel} = gelation concentration).

Comparing all of their estimated self-assembly curves (Figure 92) shows that the charge effect has a greater dominance on the serine analogues.

It is apparent from this study that the type of polar neutral side chain greatly affects peptide self-assembly in physiological solutions. The peptides based on serine side chains exhibit much higher c* values for self-assembly than the peptides based on glutamine side chains. The higher c* of the serine peptides implies that the intermolecular interactions between serine side chains are much weaker compared to those between glutamine side chains. This observation is consistent with the “polar zipper” effect of glutamines known from previous studies.[200] The much higher c* for self-assembly means that gels of the serine peptides contain a higher concentration of peptide in the monomer random coil state than glutamine gels (e.g. for P_{11}-12, it is around five times higher than for P_{11}-8. P_{11}-12 and P_{11}-8 start self-assembling at 2,300 and 440 μM respectively).

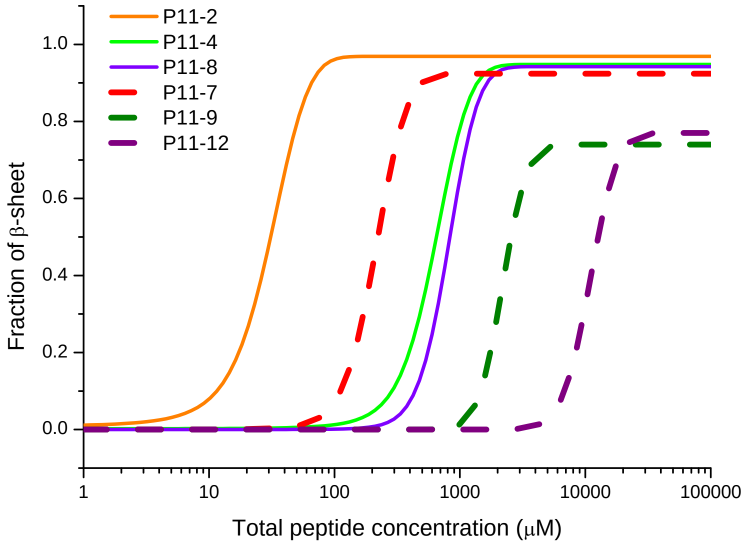

Figure 92 - Estimated self-assembly curves for all serine (dash) and glutamine (solid) analogues. All lines are sigmoidal SGompertz fits created in OriginPro 8.6.

The self-assembly of peptides relies on weak non-covalent interactions and it is clear from this data that the glutamine residues provide stability and strength to the aggregates resulting in a lower c*. Therefore, as we convert from glutamine to serine, for example with P_{11}-2 and P_{11}-7, the transformation energy is unaffected, but the tape energy is modified and the number and quality of hydrogen bonds and hydrophobic interactions is changed. Two glutamine residues contain two hydrogen acceptor sites and two hydrogen donor sites (see Figure 93) and therefore can form four intermolecular hydrogen bonds, which is enthalpically favourable; this is termed the polar zipper effect. In contrast two serine residues only have one hydrogen acceptor site and one hydrogen donor site (see Figure 94) and so can only form two intermolecular bonds, which is less enthalpically favourable.

The hydroxyl functional group of serine also has a high affinity to hydrogen bond to water, resulting in water competing for the hydrogen bond interactions with the peptides containing serine residues, which may in turn cause self-assembly to be less favourable. All of these factors should result in a higher c* for the peptides containing serine residues instead of glutamine residues, as observed here.

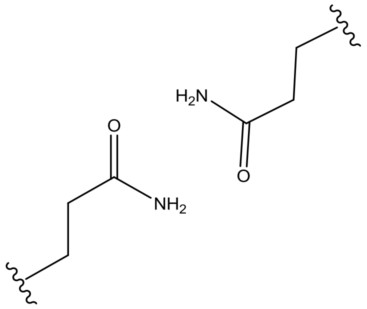

Figure 93 - Two glutamine residues

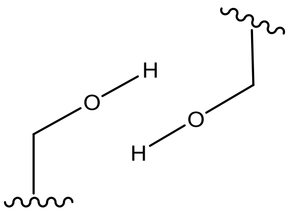

Figure 94 - Two serine residues

Thus it becomes obvious that self-assembly of peptide tapes in physiological solutions follows a similar behaviour to the self-assembly of peptide tapes in simpler solvents (pure water and organic solvents) that were studied previously,[110,111,113] i.e. it is nucleated self-assembly characterised by the presence of a critical concentration for self-assembly from monomeric random coil to β-sheet tape. This observation is also important because it implies it is possible to use the same theoretical model previously developed,[110] in order to fit the experimental data obtained in physiological solutions. This makes it possible to gain quantitative information on the magnitudes of energetic parameters and intermolecular interactions that govern peptide self-assembly in physiological conditions and how they are affected by peptide modifications. This is essential not only because it can shed light into the intermolecular interactions that stabilise protein aggregates *in vivo* in general, but it also allows us to start learning how to better control peptide self-assembly and materials properties by peptide design.

To date, the Nyrkova model fitting has only been applied to P_{11}-2, P_{11}-4 and P_{11}-8 in physiological conditions. However, considering the energetic parameters obtained for these three peptides, we can estimate approximate values for ε_{β}, $\triangle$G and average equilibrium lengths for P_{11}-7, P_{11}-9 and P_{11}-12 using the estimated c* values determined with ^{1}H NMR, and ε_{tr} and ε_{ribbon} values based on their glutamine analogues P_{11}-2, P_{11}-4 and P_{11}-8 respectively (Table 14).

Peptide (charge at pH 7)	**ε_{tr} (k_BT)**	**ε_{ribbon} (k_BT)**	**ε_{β} (k_BT)**	**ΔG of peptide monomer to peptide in (middle of) fibril**	**Average length at 18 mM (~ 30 mg/ml)**
P_{11}-9 (-2)	3.10	0.65	22	-19 k_BT = -48 kJ mol^{-1}	1.18 * 10^5 km
P_{11}-4 (-2)	*3.10*	*0.65*	*23.36*	*-51.6 kJ mol^{-1}*	*2.35 * 10^7 km*
P_{11}-7 (0)	3.05	0.60	24	-22 k_BT = -54 kJ mol^{-1}	2.35 * 10^3 km
P_{11}-2 (0)	*3.05*	*0.60*	*25.74*	*-58.0 kJ mol^{-1}*	*2.35 * 10^5 km*
P_{11}-12 (+2)	2.95	0.60	21	-19 k_BT = -46. kJ mol^{-1}	3.05 * 10^3 km
P_{11}-8 (+2)	*2.95*	*0.60*	*21.52*	*-50.3 kJ mol^{-1}*	*1.41 * 10^6 km*

Table 14 – Approximate peptide fitting parameters and estimated energies and lengths derived from the Nyrkova theoretical model.

From comparing the energetics derived from the model for the serine and glutamine-based peptides, it is found that by converting from glutamine to serine that the tape scission energy is decreased. In turn, the Gibbs free energy is increased. This means that aggregation is more favourable for the glutamine-based peptides, as suspected due to the polar zipper effect. As well as the energetics being affected, the average equilibrium tape lengths are also a lot shorter for the serine-based peptides.

3.1.4.3 Effect of having a complementary pair over a single peptide system on the self-assembly

By comparing the self-assembly curves (Figure 95) for the complementary peptides P_{11}-13/14 (Q,-2) and P_{11}28/29 (Q,+2) with their single peptide analogues P_{11}-4(Q,-2) and P_{11}-8(Q,-2) (work carried out by S. Maude)[189] it can be observed that, by moving to a complementary system, the c* value is greatly reduced (Table 15). As the c* is greatly reduced, so too is the background concentration of monomer that exists in equilibrium with aggregates above this critical concentration.

The decrease in c* for the complementary peptides compared to their single analogue is due to a gain in their tape energy through the gain in enthalpy from the electrostatic interactions between the two complementary peptides and also a decrease in the loss of entropy, due to each peptide in a complementary pair only having a net charge of one therefore, resulting in less counterions being immobilised during aggregation.

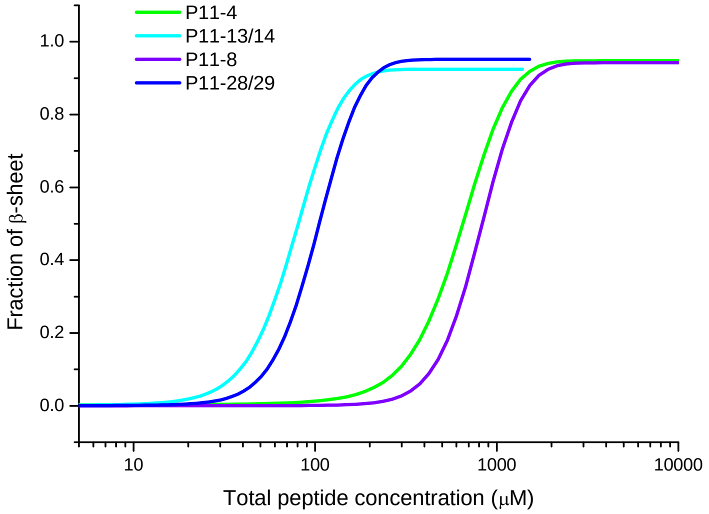

Figure 95 - Self-assembly curves for P_{11}-4, P_{11}-8, P_{11}-13/14 and P_{11}-28/29. All lines are sigmoidal SGompertz fits created in OriginPro 8.6.

Peptide	**Polar residue**	**Charge**	**c*$_{sa}$** (μM)	**c*$_{gel}$**
P_{11}-13/14	Q	-2 (-6,+4)	28 ± 7	350-680
P_{11}-4	Q	-2	310 ± 72	2000±600
P_{11}-28/29	Q	+2 (+6,-4)	29 ± 11	300-600
P_{11}-8	Q	+2	400 ± 100	2000±600

Table 15 - Peptide c* values.

As stated at the outset of this chapter, it is important to have a low c* because this means that there will be less background monomer present, which should mean less issues of toxicity, and slower gel dissolution rates.[117] Based on the theory of surfactant self-assembly the amount of monomer present at any concentration below c* will be 100 % and above c* will be the equivalent concentration to c*. This means that a peptide with a high c* will have a higher amount of monomer always present than for a peptide with a low c*. This is demonstrated in Figure 96 which shows that the glutamine peptides at this stage would be the best candidates for use in nucleus augmentation.

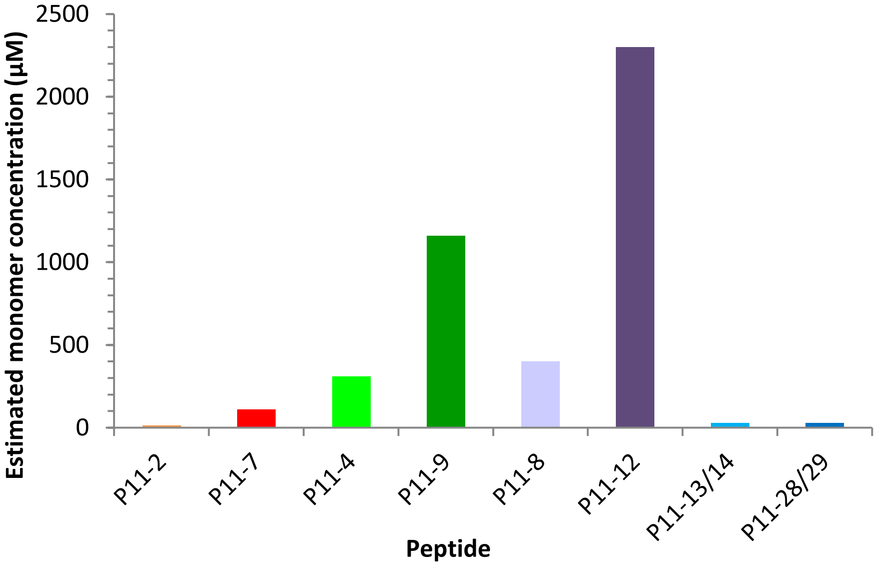

Figure 96 – Plot of concentration of monomeric peptide present in a 20 mg/ml (~13 mM) sample, based on peptide c* values.

3.2 Mechanical and material properties of peptide hydrogels in physiological conditions

If the correct design criteria are chosen, peptide aggregates will form that are long enough to become a network of entangled aggregates, for example fibrils. This entanglement of polymers can result in a self-supporting gel (Figure 97).

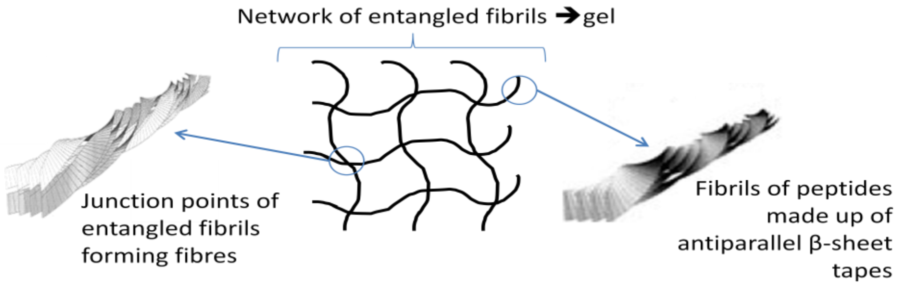

Figure 97 - Schematic representation of an entangled network of peptide aggregates in a gel.

Once the fundamental principles underlying the design of self-assembly peptides for use in physiological like conditions have been understood, an optimum peptide system could be used in a biomedical application. For this use, it is essential to understand not only the chemical and thermodynamic behaviour of the peptide, but also its mechanical and rheological properties, i.e. its viscoelastic characteristics and how it behaves under shear loading. Such information can be obtained using rheological measurement methods. An initial study of the material properties of the above peptides was undertaken and is reported in this section. The details of the protocol used are described in section 2.7. The amplitude sweeps carried out after the frequency sweeps to confirm the experiment was carried out in the linear viscoelastic region (LVER) are presented in APPENDIX D.

3.2.1 Results

3.2.1.1 P_{11}-9

During the preparation of the higher concentration NMR samples, it was observed that P_{11}-9 forms clear self-supporting gels above a concentration of ca. 3 to 6 mM.

Figure 98 - P_{11}-9 self-supporting gel, 20 mg/ml (14 mM) 1 month old a.) in DMEM cell culture medium, b.) in PBS

P_{11}-9 gels at a concentration of 6 mM were not birefringent, whereas at 12 mM they were birefringent. Birefringence is a property of nematic gels, which have macroscopic directional organisation of the peptide aggregates in domains. It is this anisotropy that is visualised by the many colours seen in the birefringent samples when crossed polarised light is passed through it. The nematic ordering is a property of semi-rigid rods. The peptide aggregates behave like semi rigid rod-like objects and at a certain concentration C_{IN}, their solution undergoes a transition from an isotropic to a nematic state.[110] The concentration at which this transition will take place depends on the width and rigidity (i.e. persistence length) of the specific aggregate type. Thus solutions of peptide fibrils tend to have a very low C_{IN} because they are very rigid. Solutions of ribbons would be expected to have much higher C_{IN}, because they are more flexible than fibrils.[110] P_{11}-9 not only forms gels in physiological like solutions (130mM NaCl, pH 7.4), but also forms gels in solutions closer to that found in the body, such as in the cell culture medium DMEM, as well as in phosphate buffered saline (PBS) solutions (Figure 98a and b). The rheological studies conducted here were carried out in PBS.

A 20 mg/ml control sample was prepared as described in section 2.7.2 and produced a clear self-supporting gel that became a viscous liquid upon light shaking (Figure 98b).

From the amplitude sweeps (Figure 99), a strain value of 0.5% was chosen within the LVER to carry out the frequency sweep. The frequency sweep spectrum for P_{11}-9 is presented in Figure 100. The phase angle remained constant at around an average of 33°.

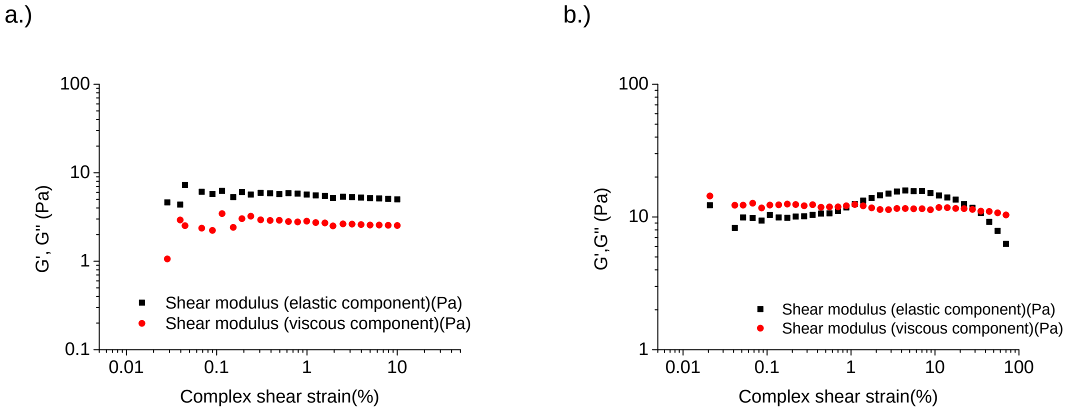

Figure 99 – P_{11}-9 Elastic and viscous modulus vs. shear strain. Starting shear strain 0.01%, end shear strain: 100%, Temp 25°C, a.) Frequency: 1 Hz and b.) Frequency: 20 Hz

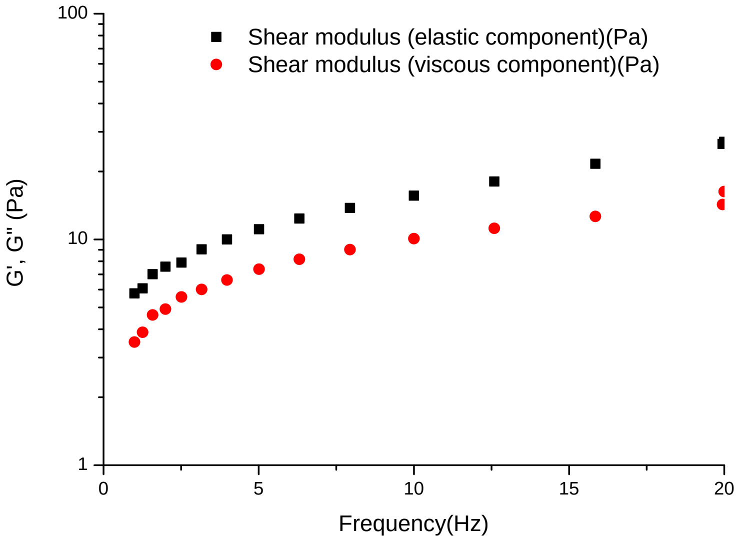

Figure 100 - Elastic and viscous modulus vs. frequency. Starting frequency 1 Hz, end frequency: 20 Hz, Strain controlled: 0.5%, Temp: 25°C.

To examine the effect of changing the peptide's polar amino acid on the rheological properties of the self-assembled gel P_{11}-4 was compared to P_{11}-9.

3.2.1.2 P_{11}-4

A 20 mg/ml control sample was prepared as described in section 2.7.2 and produced a cloudy self-supporting gel that was observed to have a similar consistency to P_{11}-9 (Figure 101).

Figure 101 - P_{11}-4 20 mg/ml (12.5 mM) in PBS 20 days old.

From the amplitude sweeps (Figure 102), a strain value of 0.15% was chosen within the LVER to carry out the frequency sweep. The frequency sweep spectrum for P_{11}-4 is presented in Figure 103. The phase angle increased over the frequency range from 8.7-17.2°.

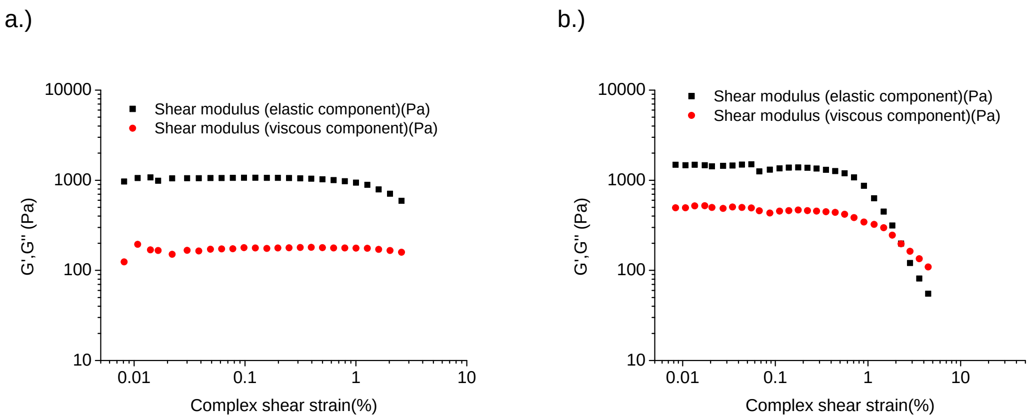

Figure 102 – P_{11}-4 Elastic and viscous modulus vs. shear strain. Starting shear strain 0.01%, end shear strain: 100%, Temp 25°C, a.) Frequency: 1 Hz and b.) Frequency: 20 Hz.

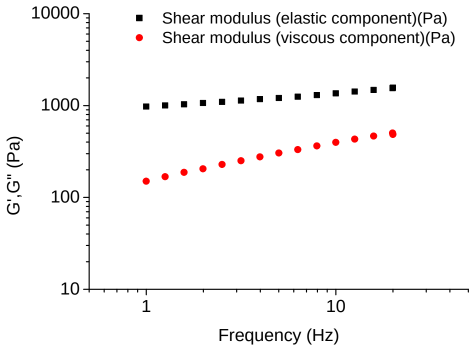

Figure 103 – P_{11}-4 Elastic and viscous modulus vs. frequency. Starting frequency 1 Hz, end frequency: 20 Hz, Strain controlled: 0.15%, Temp: 25°C.

3.2.1.3 P_{11}-12

During the preparation of the higher concentration NMR samples, it was observed that P_{11}-12 formed clear self-supporting gels above a concentration of ca. 4 to 8 mM, although gelation began at around 2300 μM. At a concentration of 16 mM in physiological-like conditions, P_{11}-12 formed a gel with a small amount of white precipitate as the peptide approached its solubility limit, upon reheating this precipitate became soluble again but only in a metastable manner. P_{11}-12 gels at concentrations of 8 mM, 12 mM and 16 mM were all birefringent. The birefringence shows that the gels were nematic meaning that the peptide aggregates have long range directional organisation in domains. P_{11}-12 not only formed gels in physiological like solutions (130 mM NaCl, pH 7.4) but also formed gels in solutions closer to that found in the body such as the cell culture medium DMEM (Figure 104) as well as in PBS solutions. The rheological study conducted here was carried out in PBS.

Figure 104 - P_{11}-12 self-supporting gel, 20 mg/ml (14 mM) in DMEM cell culture medium.

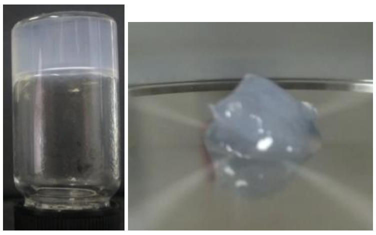

Figure 105 - P_{11}-12 20 mg/ml (14 mM) in PBS, 2 months old.

To look into the effect that changing the peptides charge had on the rheological properties of the self-assembled gel, P_{11}-12 was compared to P_{11}-9. A 20 mg/ml sample was prepared as described in section 2.7.2 and produced a cloudy self-supporting gel (Figure 105).

From the amplitude sweeps (Figure 106), a strain value of 0.25% was chosen within the LVER to carry out the frequency sweep.

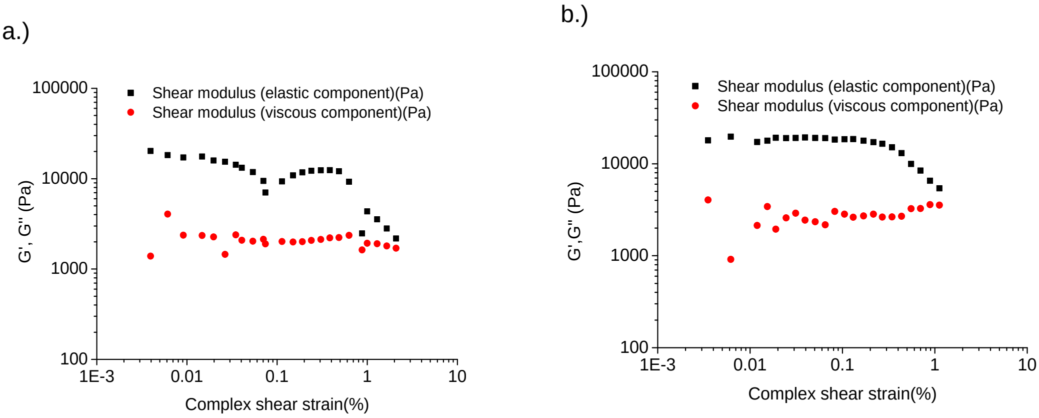

Figure 106 – P_{11}-12 Elastic and viscous modulus vs. shear strain. Starting shear strain 0.01%, end shear strain: 100%, Temp 25°C, a.) Frequency: 1 Hz and b.) Frequency : 20 Hz.

The frequency sweep spectrum for P_{11}-12 is presented in Figure 107. The phase angle remained constant at around an average of 8.8°.

It was observed when trying to unload the sample from the machine that the top cone could not be easily raised, suggesting the gel had a strong molecular structure that was difficult to break and hence pull apart.

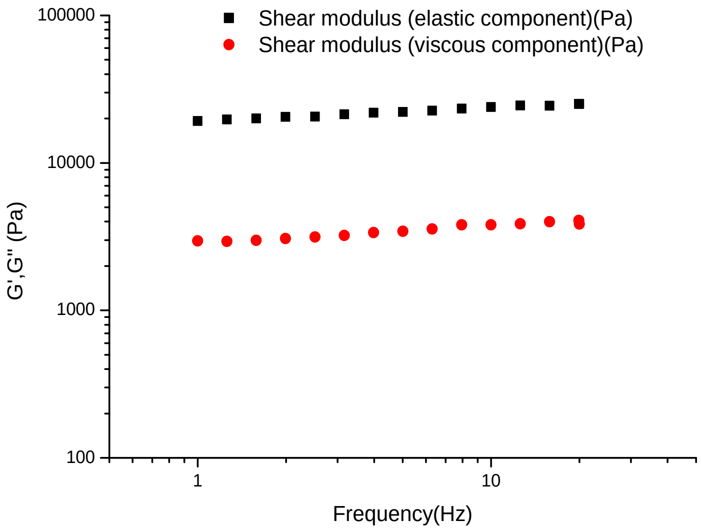

Figure 107 – P_{11}-12 Elastic and viscous modulus vs. frequency. Starting frequency 1 Hz, end frequency: 20 Hz, Strain controlled: 0.25%, Temp: 25°C.

In order to investigate the effect of charge on the rheological properties further and to see if the same effects are seen for the glutamine-based peptides, P_{11}-8 (+2) was compared to P_{11}-4 (-2).

3.2.1.4 P_{11}-8

A 20 mg/ml control sample was prepared as described in section 2.7.2 and produced a sample of two phases, one a clear liquid and the other a cloudy gel on the walls of the vial (Figure 108). The rheometry was primarily carried out on the gel phase.

It was noted during loading that the gel sample had a gritty texture and a lot was needed to cover the area under the top cone (Figure 109).

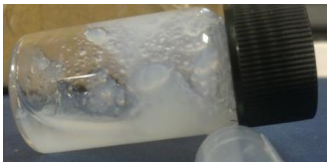

Figure 108 - P_{11}-8 13 mM (20 mg/ml) in PBS, 1.5 months old.

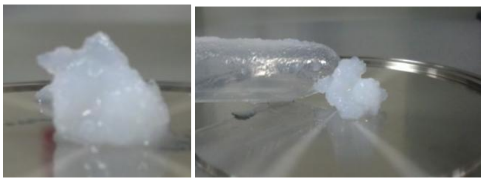

Figure 109 - P_{11}-8 13 mM (20 mg/ml) loading onto the rheometer.

It was also observed that, upon loading the rheometer, a large force was required to close the gap between the top cone and bottom plate, i.e. it struggled to compress the sample, which suggests a strong molecular structure and a material with a high modulus (Figure 110).

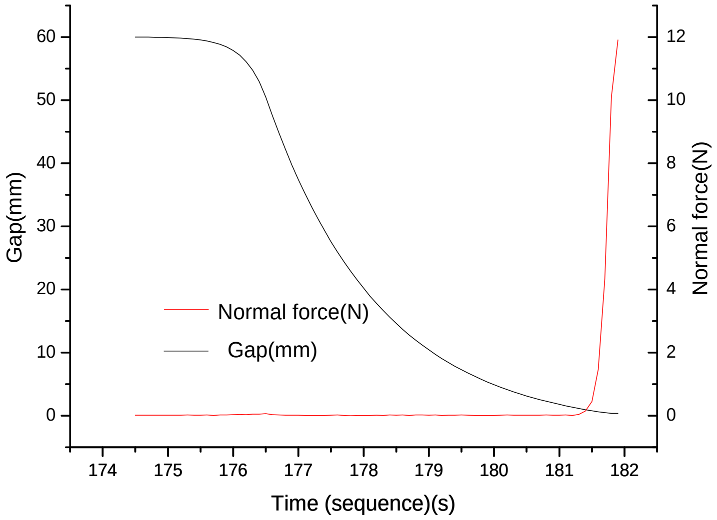

Figure 110 – P_{11}-8 raw data plot of Gap and Normal force Vs experiment time for loading to the predefined cone and plate gap.

It was observed that after running the experiments on the gel, the sample had split into two phases as illustrated in Figure 111.

Figure 111 - P_{11}-8 sample after experiments carried out.

Figure 112 - Waxy residue of P_{11}-8 gel after liquid phase is removed upon cleaning of the rheometer.

It was also observed that when the liquid phase was removed during sample unloading and cleaning of the rheometer, a very waxy residue was left (Figure 112).

From the amplitude sweeps (Figure 113), a strain value of 0.1% was chosen within the LVER to carry out the frequency sweep.

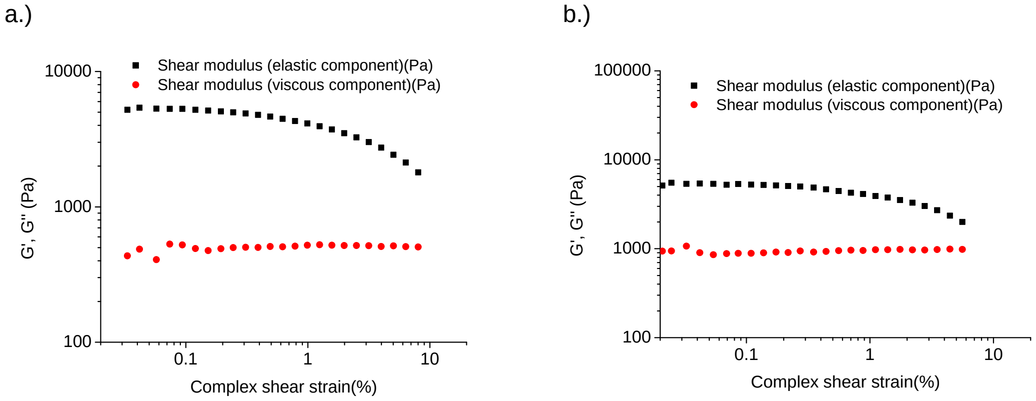

Figure 113 – P_{11}-8 Elastic and viscous modulus vs. shear strain. Starting shear strain 0.01%, end shear strain: 100%, Temp 25^{o}C, a.) Frequency: 1 Hz, b.) Frequency: 20 Hz.

The frequency sweep spectrum for P_{11}-8 is presented in Figure 114. The phase angle remained constant at around an average of 7.6º.

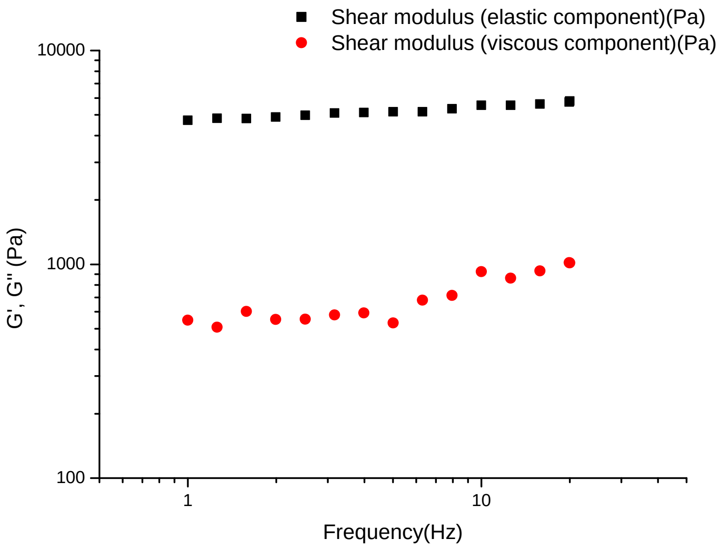

Figure 114 – P_{11}-8 Elastic and viscous modulus vs. frequency. Starting frequency 1 Hz, end frequency: 20 Hz, Strain controlled: 0.1%, Temp: 25^{o}C.

In order to complete the rheological study of the self-assembling peptides, the rheological methods established so far were applied to the two pairs of complementary peptides P_{11}-13/14 (-6, +4, overall -2) and P_{11}-28/29 (+6, -4, overall +2).

3.2.1.5 *P_{11}-13/14*

During the preparation of the NMR samples, it was observed that the P_{11}-13+14 mix formed clear self-supporting gels between a concentration of ca. 350-680 μM. Birefringence was seen in gels above a concentration of 1380 μM.

Figure 115 - P_{11}-13/14 20 mg/ml (13 mM) in PBS, 2 weeks old.

The sample prepared as described in section 2.7.2 formed a self-supporting gel (Figure 115), which upon light shearing became a viscous liquid that recovered into a self-supporting gel again within a minute. Under crossed polarised light the sample was birefringent, showing that the gel was nematic meaning that the peptide aggregates had long range directional organisation in domains.

From the amplitude sweeps (Figure 116) a strain value of 3% was chosen within the LVER to carry out the frequency sweep.

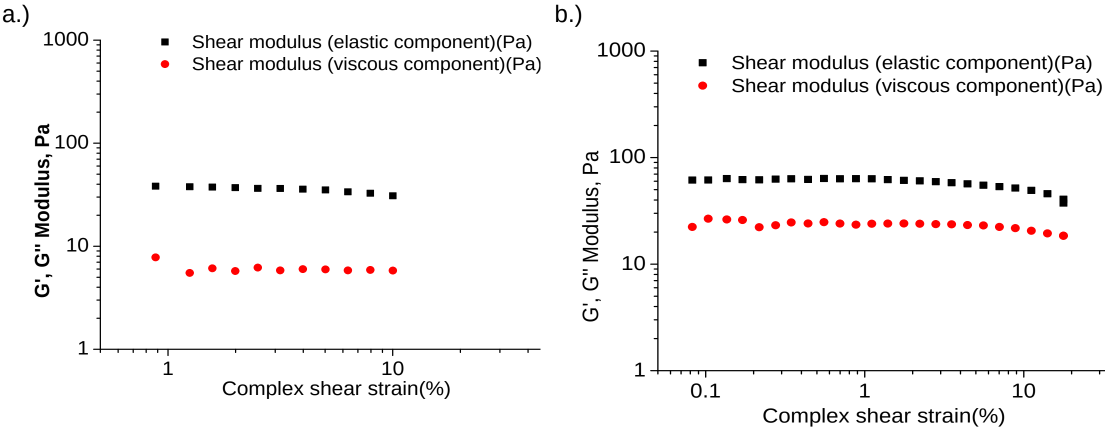

Figure 116 - P_{11}-13/14 Elastic and viscous modulus vs. shear strain. Starting shear strain 0.01%, end shear strain: 100%, Temp 25^{o}C, a.) Frequency: 1 Hz and b.) Frequency: 20Hz.

The frequency sweep spectrum for P_{11}-13/14 is presented in Figure 117. The phase angle increased over the frequency range studied from 11-23º.

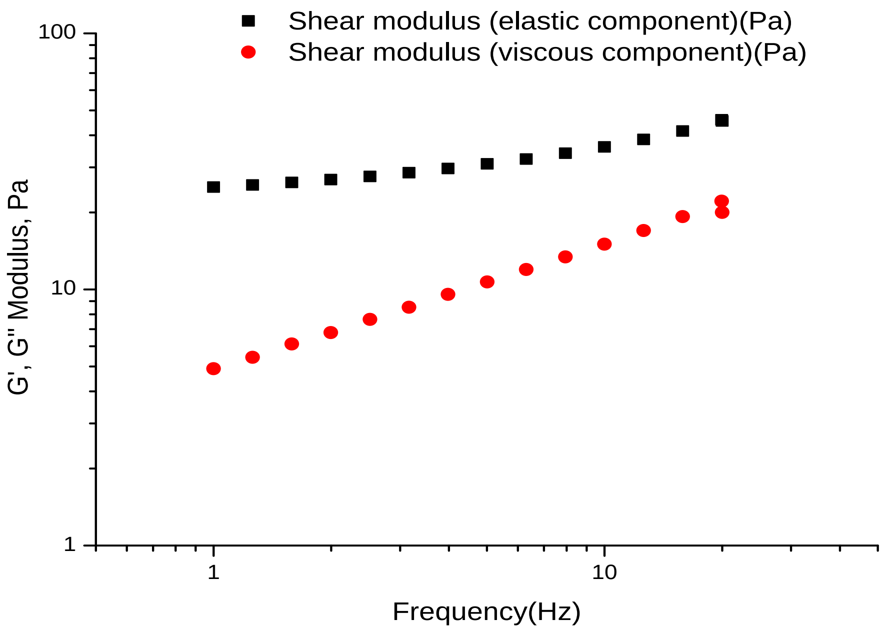

Figure 117 - P_{11}-13/14 Elastic and viscous modulus vs. frequency. Starting frequency 1 Hz, end frequency: 20 Hz, Strain controlled: 3%, Temp: 25^{o}C.

In order to see if there is a charge effect for the complementary peptides, P_{11}-13/14(-2) was compared with P_{11}-28/29 (+2).

3.2.1.6 P_{11}-28/29

During the preparation of the NMR samples, it was observed that the P_{11}-28+29 mix formed clear self-supporting gels between a concentration of ca. 300-600 μM. The gelation was spontaneous upon mixing.

A 20 mg/ml control sample was prepared as described in section 2.7.2 produced a cloudy self-supporting gel with a few bubbles. Sonication was then used to remove the bubbles but this led to the gel becoming cloudier in appearance (Figure 118).

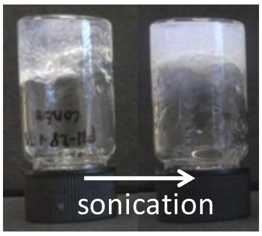

Figure 118 - P_{11}-28/29 20 mg/ml in PBS. 6 days old.

From the amplitude sweeps (Figure 119), a strain value of 0.25% was chosen within the LVER to carry out the frequency sweep.

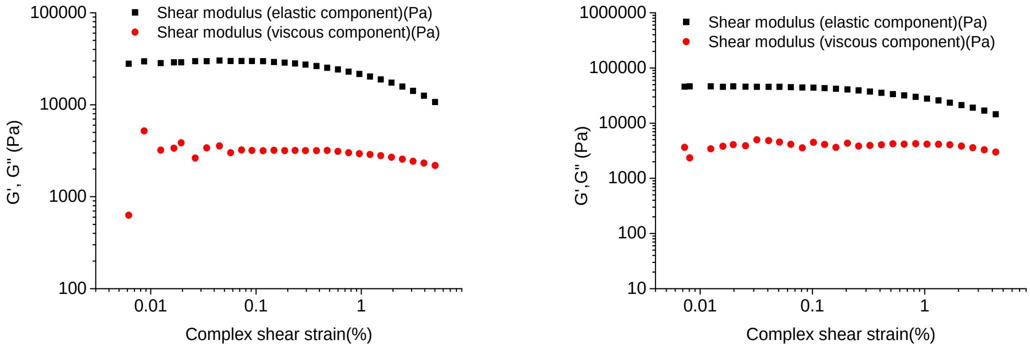

Figure 119 - P_{11}-28/29 Elastic and viscous modulus vs. shear strain. Starting shear strain 0.01%, end shear strain: 100%, Temp 25^{o}C, a.) Frequency: 1 Hz and b.) Frequency: 20 Hz.

The frequency sweep spectrum for P_{11}-28/29 is presented in Figure 120. The phase angle remained constant at around an average of 6.5º.

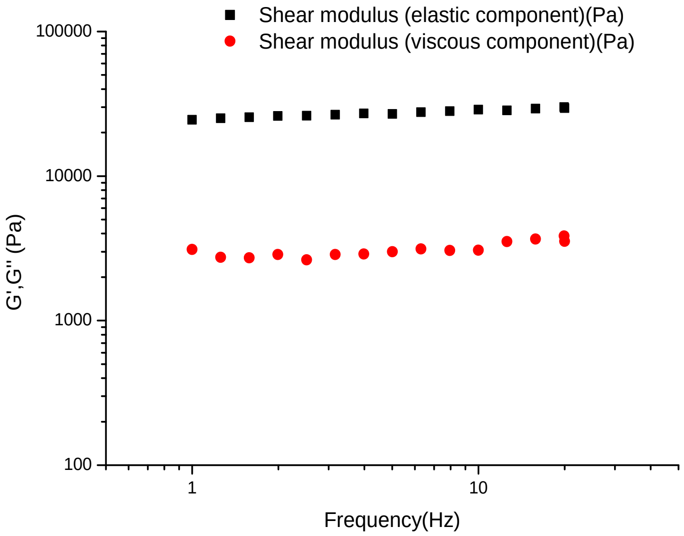

Figure 120 - P_{11}-28/29 Elastic and viscous modulus vs. frequency. Starting frequency 1 Hz, end frequency: 20 Hz, Strain controlled: 0.25%, Temp: 25^{o}C.

3.2.2 Discussion

3.2.2.1 Common rheological properties for self-assembled peptide gels

From the rheological experiments carried out here, some general rheological properties have been determined for this class of self-assembling peptide:

1. In all cases the elastic modulus was higher than the viscous modulus, suggesting that the samples had more solid-like than liquid-like behaviour. This was further confirmed by the typically low phase angles (~10º).

2. The shapes of the frequency sweeps were typical of gel-like behaviour over the frequency range studied and, with most peptides, this was confirmed with a constant phase angle. However, the increase in the phase angle for P_{11}-4 and P_{11}-13/14 is more typical of viscoelastic solid behaviour.

3. The mechanical spectra of the peptides studied was flat over the frequency range studied, suggesting that the dominant viscoelastic relaxations were at lower frequencies than measured i.e. the relaxation time of the networks were long (Figure 121). This is indicative of either very long and stable polymers that are highly entangled or strong non-covalent chemical crosslinks between highly stable polymers.

4. The reproducibility was investigated using P_{11}-4, P_{11}-9, P_{11}-12 and P_{11}-28/29 (see appendix D). For the second frequency sweep on same sample, the shape and position of the plots were almost identical to those of the first samples, showing good reproducibility.

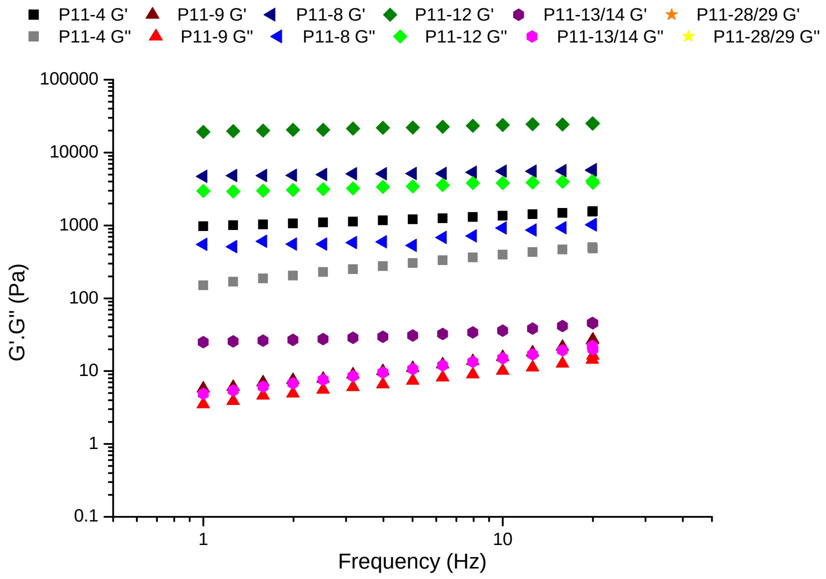

Figure 121 – Mechanical spectra of peptides studied over a frequency range of 1-20 Hz.

The class of self-assembling peptide studied here have similar rheological properties to other classes of self-assembling peptides studied by other groups. In a study by Genove *et al.* the RADA16-I peptide at a concentration of ~3 mM in PBS was found to have an elastic modulus higher than its viscous modulus, both of which remained relatively constant over the frequency range studied, suggesting a gel profile. It had an average G’ of 2.5 kPa at room temperature (Figure 122).[201] Sun *et al.* found that in pure water RADA16-1 had an elastic modulus of 7 Pa, however when exposed to DMEM medium the modulus increased to 4000 Pa both at 25°C.[202]

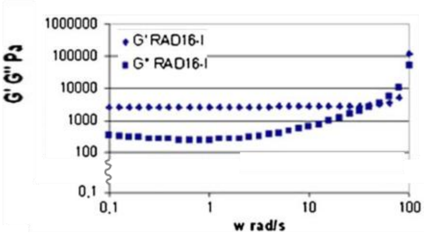

Figure 122 - Physicochemical characterization of peptides RAD16-I by rheometry: dynamic frequency sweep test for peptide scaffold at fixed strain of 0.01%. Taken from Genove *et al.*.[201]

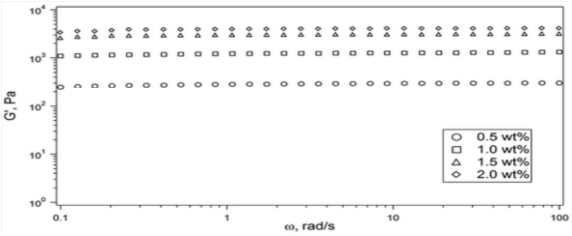

Figure 123 - Frequency sweep data showing the storage modulus (G’) for MAX8 hydrogels at pH 7.4, 50 mM BTP buffer, 150 mM NaCl, 20 °C. Taken from Hule *et al.*.[203]

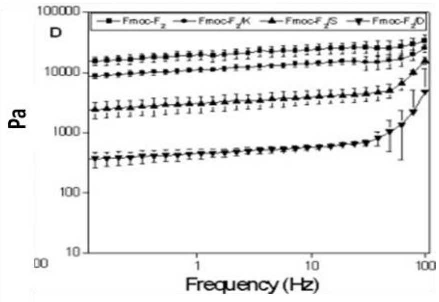

Figure 124 - Linear viscoelastic spectra for four Fmoc-FF analogues, 20 mM, 25 °C. Taken from Ozbas *et al.*.[204]

Numerous rheological studies have been carried out on the β-hairpin structures of the Pochan and Schneider group. They have found that like the peptides studied here the G' values are a magnitude higher than the corresponding G'' for all concentrations. Hydrogels of the MAX8 peptide have been found to have a G' in the region of 10^2-10^3 Pa dependent on concentration[203] (Figure 123). The authors have suggested that the rheological behaviour that they see for their peptides, i.e. a G'>G'' and both being insensitive to frequency, suggests that the crosslink points of the fibrils are permanent junction points and not simple entanglements, possibly due to the formation of a supramolecular fibril structure.[122] The same may be true for the P_{11} peptides studied here because they exhibited a similar behaviour.

Gelain *et al.* carried out frequency sweep tests assessing G' and G'' moduli of various functionalised ionic β-sheet peptide hydrogels and found that values (in the 1–100 Hz range) of the assembled scaffolds resided in the 70–400 Pa and 8–20 Pa ranges respectively.[205]

The Ulijn group have looked into the mechanical profiles of various Fmoc-FF analogues and they have elastic moduli in a similar range to the peptides tested here, with Fmoc-FF having an elastic modulus of 21.2 kPa.[204] Once again, the elastic moduli exceeded that of their viscous moduli (Figure 124).

3.2.2.2 The effect of polar amino acid residues on the rheological properties of the peptide hydrogels

As with the case of investigating the polar residue effect on the peptide self-assembly, the serine-based peptide gels can be compared with their glutamine analogues to determine their effect on the rheological properties.

The moduli for P_{11}-4 (Q) are higher than those of P_{11}-9 (S) by two orders of magnitude suggesting that a P_{11}-4 gel is stiffer than a P_{11}-9 gel (Figure 125).

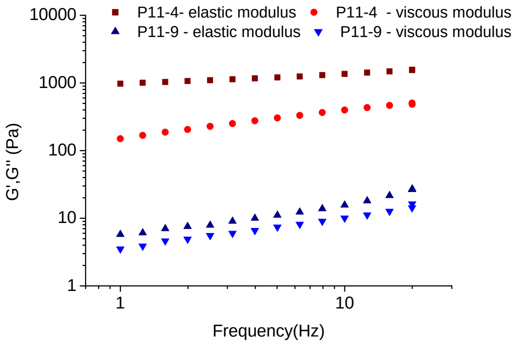

Figure 125 - Comparison of elastic modulus and viscous modulus of P_{11}-4 and P_{11}-9.

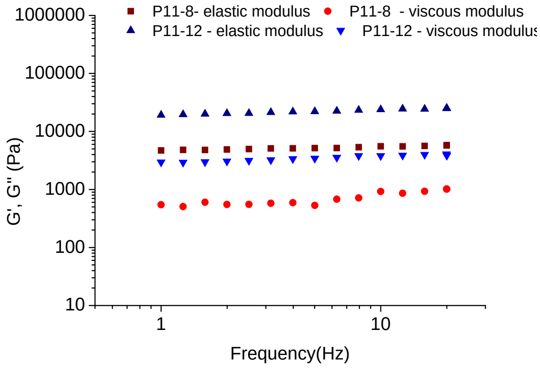

Figure 126 – Comparison of frequency sweeps of P_{11}-8 and P_{11}-12.

To investigate the polar amino acid effect further, P_{11}-8 (Q) can be compared directly to P_{11}-12 (S) because they have the same charge but different polar side chains (Figure 126).

Unlike the case with P_{11}-4 (Q) and P_{11}-9 (S), where the glutamine-based peptide had much higher elastic and viscous moduli and therefore was a stiffer gel, P_{11}-8 (Q) actually had a lower elastic and viscous moduli than serine-based P_{11}-12 (Figure 127). Therefore there seems to be no obvious trend in the effect of polar amino acid residues on the rheological properties of the peptide hydrogels.

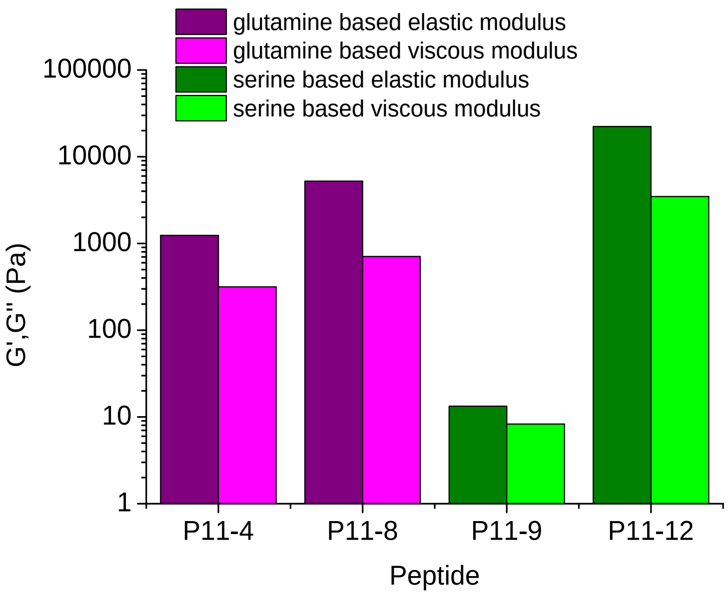

Figure 127 - Comparative plot for serine- and glutamine-based peptides of average modulus vs. peptide.

It was hypothesised that because the rheological properties of the peptide gels would be governed by the size, length and type of structures making up the bulk material, i.e. the aggregates, that similar trends in c* would be seen in the rheological data. However, this was not the case and the stiffness of the gels did not appear to be related to their c* values. This is due to the energetics that determine the c*, i.e. how the monomers interact with one another to form an aggregate will not be the same for how the aggregates interact with one another. The self-assembly of the peptides is governed by the energetic parameter ε_{tape} which dominates on a molecular level. However, gelation and the rheological properties are governed by other energetic parameters, which are small on a molecular level but must add up and become much more important at a bulk level.

3.2.2.3 Effect of having a complementary pair over a single peptide system on the rheological properties of the peptide hydrogels

The glutamine-based complementary pair P_{11}-13/14 with an overall charge of -2 can be compared to P_{11}-4 as its non complementary analogue (Figure 128). The moduli for P_{11}-4 are almost two times the magnitude of that of the complementary pair, suggesting that P_{11}-4 is the stiffer gel.

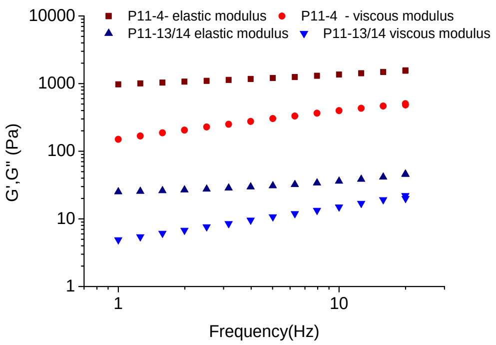

Figure 128 - Comparison of frequency sweeps for P_{11}-13/14 and P_{11}-4.

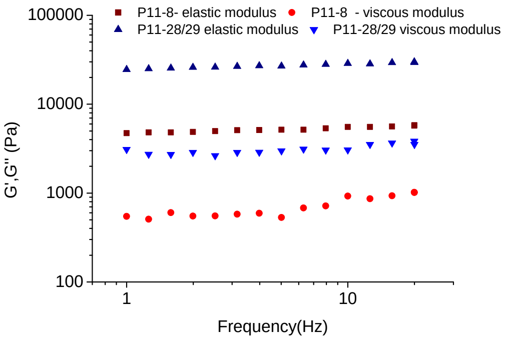

Figure 129 - Comparison of frequency sweeps for P_{11}-28/29 and P_{11}-8.

The complementary pair P_{11}-28/29 that has an overall charge of +2 and is glutamine-based can be compared to P_{11}-8 as its non complementary analogue (Figure 129) Unlike the comparison between P_{11}-13/14 and P_{11}-4, the complementary peptide P_{11}-28/29 has higher moduli than P_{11}-8 by one order of magnitude, suggesting in this case that the complementary peptide produces a stiffer gel.

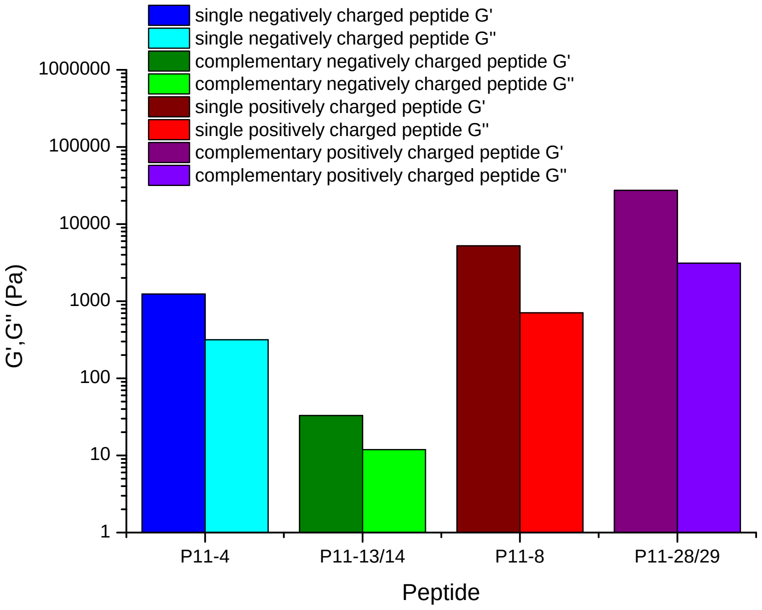

Figure 130 - Comparative plot for single and complementary glutamine-based peptides of average modulus vs. peptide.

Figure 130 shows there to be no consistent trend in the effect of going from a single to complementary peptide system. This further reinforces the hypothesis that there is no link between the peptide c* and its rheological properties.

3.2.2.4 The effect of net peptide charge on the rheological properties of the peptide hydrogels

By comparing the elastic and viscous moduli of the negatively charged peptides and the positively charged peptides, it would appear that charge has a large effect on the viscoelastic properties of their hydrogels (Figure 131).

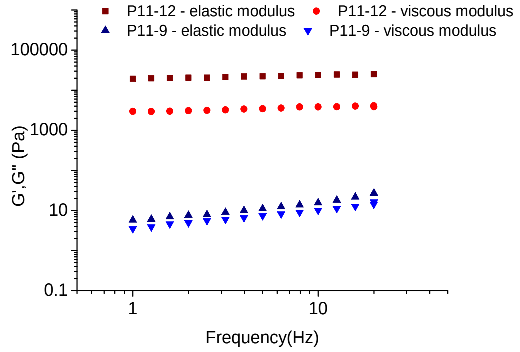

Figure 131 – Comparison of frequency sweeps for P_{11}-9 and P_{11}-12.

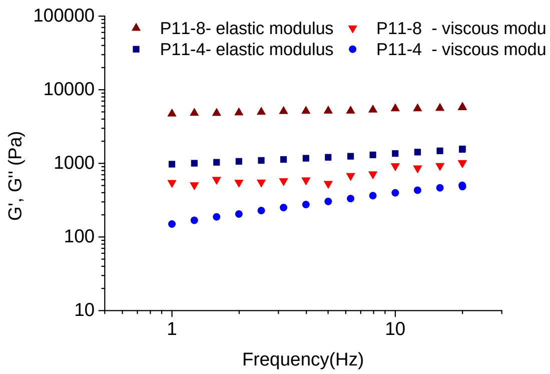

Figure 132 – Comparison of frequency sweeps of P_{11}-4 and P_{11}-8.

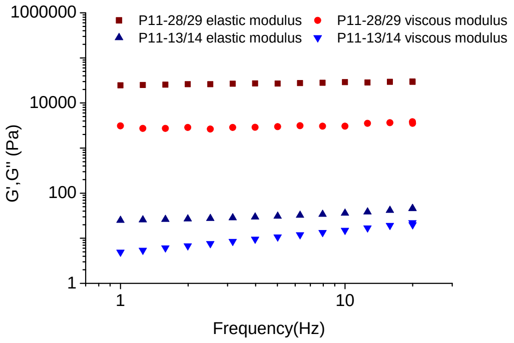

Figure 133 – Comparison of frequency sweeps for P_{11}-13/14 and P_{11}-28/29.

The elastic modulus of the positively charged P_{11}-12 was four times the magnitude of that of the negatively charged P_{11}-9, meaning that the P_{11}-12 gel was much stiffer (Figure 131). The elastic modulus, which can be thought of as the measure of stiffness, for P_{11}-12 was in the order of 20,000 Pa which is relatively high for a gel made of soft matter at concentration of only 2% w/v.

As with the serine-based peptides, for the glutamine-based peptides the positively charged P_{11}-8 has a greater elastic and viscous modulus than the negatively charged P_{11}-4, although the effect is not as pronounced (Figure 132).

This charge effect of a positive charge resulting in a stiffer gel is also true for the complementary peptides (Figure 133). The moduli for the positive P_{11}-28/29 are three times the magnitude of that of the negatively charged P_{11}-13/14.

The effect of a positive charge increasing the elastic and viscous modulus of the peptide gels is illustrated again in Figure 134

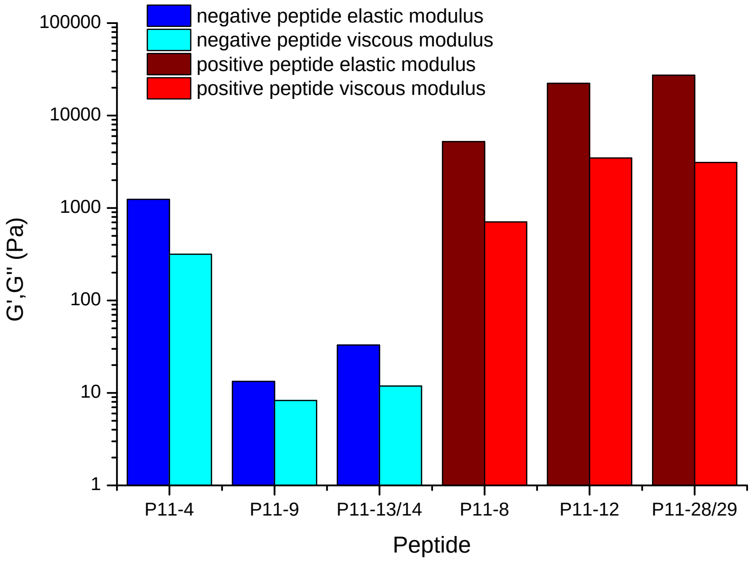

Figure 134 – Comparative plot for negative and positive peptides of average modulus vs. peptide.

This suggests that, as the positively charged peptides have a higher G', they must also have a higher density of entanglements. This may be due to them having a high affinity for entanglements, or they may have narrower longer chains and therefore a greater probability of junction points occurring. Future work combining the rheological data with microscopy data may help to shed some light on this effect further.

Based on the three discussion points so far, the sign of the peptide is the most important factor. The other effects are dominated by the charge effect and it is hard to pick out the trends in their effects, therefore the safest way to design a peptide with a high G' is to concentrate on controlling the charge.

The Schneider and Pochan group have also found that the effect of charge is important in the rheological properties of gels as well as in the gelation kinetics. When comparing two peptides MAX1 (+9 charge) and MAX1K15E (+7 charge), they found that the peptides with a lower net positive charge form gels more quickly than gels of higher positive charge. They also determined that gels with a higher net positive charge have a lower elastic modulus than those with a lower charge, 50 Pa and 600 Pa respectively.[123]

3.2.2.5 *Estimating the mesh size of the peptide network for the magnitude of the plateau elastic modulus.*

It has been shown that, for gels formed with semiflexible polymers, small changes in the crosslink density at constant volume fractions can dramatically alter the elastic modulus over a few orders of magnitude.[206,207] Using a model taken from the rubber-like elasticity theory developed by Aggeli *et al.*,[113] the magnitude of the plateau elastic modulus can be used to extract information about the mesh size of the peptide network and therefore the crosslink density. The lower limit distance (j) between two nearest entanglements or crosslinks in space is given by the following relationship:

$$j = \frac{g_n . f . k_B . T^{1/3}}{2G'^{o}_{N}}$$

Equation 12

Where g_N is a numerical factor not far from unity, f is the number of tapes attributed to each entanglement, k_B is the Boltzmann constant, T is the absolute temperature and $G'_N{}^{o}$ is the plateau elastic modulus.

The lower limit j values have been calculated for the above peptides using Equation 12 and are listed in Table 16.

From these values it is clear to see how the mesh size affects the mechanical properties of the gels. The stiffer gels have shorter distances between crosslinks and therefore a greater number of crosslinks in the network per unit volume.

Peptide	**G'^{o}_{N} (kg m^{-1} s^{-2})**	**j (nm)**
P_{11}-4	**1,240**	**18.8**
P_{11}-9	**13**	**85.2**
P_{11}-13/14	**33**	**64.0**
P_{11}-8	**5,221**	**11.6**
P_{11}-12	**22,285**	**7.2**
P_{11}-28/29	**27,302**	**6.7**

Table 16 - Plateau elastic modulus and lower limit of the distance between nearest cross links (j) in the peptide gels. (g_N = 1± 0.2, f ≥ 4, k_B = 1.38x10^{-23} m^2 kg s^{-2} K^{-1}, T = 298K) Negatively charged. Positively charged

3.3 Summary

Here the self-assembly and mechanical profiles of a series of P_{11} peptides were studied, and the results are summarised in Table 17. It is important to fully understand the underlying science of such systems in order to choose and optimise the best for biological applications such as the one in this thesis.

In summary, to achieve a self-assembled peptide gel, the peptide needs to have an overall ±2 charge. To acquire a gel with a low c* using a single peptide system, a negatively charged peptide should be used and one based on glutamine rather than serine will provide the lowest c*. Complementary peptides will provide lower c* values than the single peptide systems and they also have the advantage of reaching an equilibrium state in shorter timescales.

To achieve a stiff rather than weak hydrogel, a positively charged peptide should be used.

In order for a peptide gel to be used in regenerative medicine, other factors should also be considered such as the gel stability/lifetimes and biocompatibility.

For the application of nucleus replacement therapy, on top of needing to have similar mechanical properties to the natural tissue, the gels need to have similar biofunctionality, i.e. provide a high swelling pressure within the disc, ideally through water binding similar to that found naturally. In order for the therapy to be minimally invasive, a trigger for self-assembly needs to be incorporated. These two design criteria will be addressed in the next chapter.

Peptide	C* (μM)	C*gel (μM)	Time to gel 20mg/ml	Gel lifetime 20 mg/ml	G’ 20mg/ml (Pa)	G’’ 20mg/ml (Pa)	Phase angle	trigger	Gel appearance	Other properties/notes	Pros	Cons
P_{11}-7 (S,0)	110 ± 20	-	-	-	-	-	-		-		Low c*	Doesn’t form a gel
P_{11}-2 (Q,0)	14 ± 3.2	-	-	-	-	-	-		-		Low c*	Doesn’t form a gel
P_{11}-9 (S,-2)	1160 ± 175	4500 ± 1500	Minutes	>1yr 4mths	7.8	4.9	33	pH GAG addition	Clear, self-supporting gel		Gel stability	Weak gel
P_{11}-4 (Q,-2)	310 ± 140	2000 ± 600	Minutes-hours	>1mth	1,065	205	8.7-17.2	GAG addition	Slightly cloudy, self-supporting gel		Low c*	Long gelation time
P_{11}-12 (S,+2)	5600 ± 1750	2300 ± 750	Minutes	>1yr 11mths	20,510	3067	8.8	GAG addition	Cloudy, self-supporting gel	Had to reheat at 4mths to reform gel→ gel formed was then stable	Gel stability Gel strength	High c*
P_{11}-8 (Q,+2)	400 ± 100	2000 ± 600	Days	Still some self-supporting gel at 90 days but also liquid phase	4,881	552	7.6	GAG addition	Bitty, cloudy, self-supporting gel with some liquid phase	Liquid phase increases from 13 days	Poor gel lifetime	Long gelation time
P_{11}-13/14 (Q,[-6,+4] net -2)	28 ± 7	350-680	spontaneous	>10mth	27	7	11-23	Peptide mixing	Clear, self-supporting gel		Low c* Fast gelation	Weak gel
P_{11}-28/29 (Q,[+6,-4] net +2)	29 ± 11	300-600	spontaneous	>15 <41 days	25,980	2864	6.5	Peptide mixing	Cloudy, self-supporting gel		Low c* Fast gelation Strong gel	Poor gel lifetime

Table 17 - Summary of self-assembly and mechanical data for all peptides studied.

Chapter 4

4 Self-assembling peptide and glycosaminoglycan hybrid gels

4.1 Introduction

4.1.1 The biological role and importance of glycosaminoglycans

Glycosaminoglycans (GAGs) are long unbranched polysaccharides containing a repeating disaccharide unit and they are the most abundant heteropolysaccharides in the body.[208] They have molecular weights ranging from 5 to 5000 kDa.[209] GAGs are located mainly on the surface of cells or in the extracellular matrix.[210]

The majority of GAGs in the body are linked to core proteins forming proteoglycans.[209] The GAGs extend out from the core in a brush-like structure (Figure 135). The protein cores of proteoglycans are rich in serine and threonine residues, which allow multiple GAG attachments.[208]

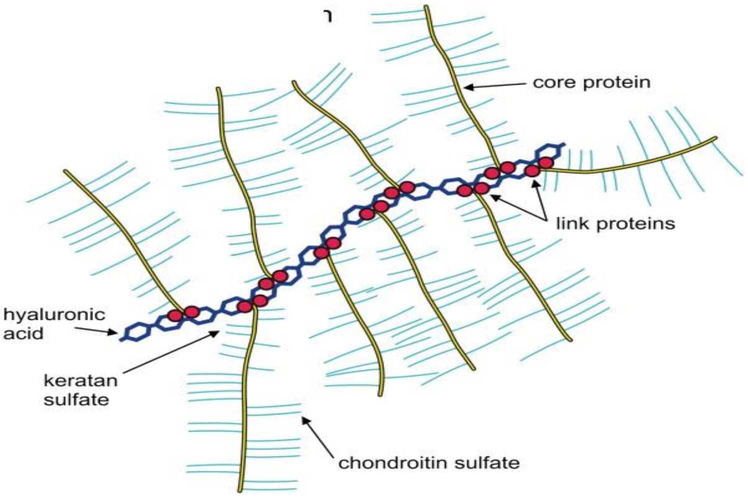

Figure 135 – Basic structure of aggrecan. The proteoglycans in the large aggrecan complex are feather-like structures composed of a number of regularly spaced GAGs, such as keratin sulphate and chondroitin sulphate (in light blue), which are covalently linked to a protein core (yellow). Taken from Oussoren *et al*.[211]

Proteoglycans and GAGs perform numerous vital functions in the body. The GAGs of significant importance are chondroitin sulphate, dermatan sulphate, heparan sulphate, heparin sulphate, hyaluronic acid and keratin sulphate. Chondroitin sulphate is the most abundant GAG in the body and is found within cartilage, bone, heart valves and the intervertebral disc.[212-216] Heparin sulphate has the highest negative charge density of any known biological molecule and is found lining the arteries of the lungs, liver and skin; it is well known for its role in preventing blood clotting.[208,209] Heparan sulphate, although less sulphated than heparin sulphate, contains higher acetylated glucosamine than heparin. Heparan sulphate is found in basement membranes and makes up components of cell surfaces. Hyaluronic acid is a particularly large polymer and often plays the role of shock absorber and so is often found in the extracellular matrix (ECM) of loose connective tissue, as well as in synovial fluid and vitreous humor.[217-221] Keratan sulphate is found in the cornea, bone and in an aggregated form with chondroitin sulphate in cartilage and intervertebral discs.[216,222-224] Finally, dermatan sulphate is located in the skin, blood vessels and heart valves.[208]

GAGs are highly negatively charged and have an extended conformation, which results in a high viscosity of the solution. Along with the high viscosity of GAGs comes low compressibility, making these molecules excellent for lubricating fluid in the joints.[208]

In terms of the application of self-assembling peptides in the treatment of disc degeneration, an important factor is the significant loss of water that occurs with degeneration. Therefore a replacement biomaterial needs to have high water content and be able to retain this water. The natural tissue achieves this by the presence of a large number of negative charges, which causes an influx of small cations to balance these charges. This high salt content results in a high osmotic pressure. The peptides studied so far in this project may be optimised for this application by mixing with another charged bio-polymer to create a peptide hybrid material.

The high negative charge density within the disc is due to the high concentration of proteoglycans and therefore GAG chains. Specifically within the disc tissue, these GAGs are chondroitin and keratin sulphate, with chondroitin sulphate being the most prevalent.

There are four different types of chondroitin sulphate differing at the site of sulphation; chondroitin-4-sulphate, chondroitin-6-sulphate, chondroitin-2,6-sulphate and chondroitin-4,6-sulphate, also sometimes known as chondroitin sulphate A, C, D and E respectively. Chondroitin sulphate B is the old name for dermatan sulphate. Both chondroitin-4-sulphate and chondroitin-6-sulphate are found within the disc, with their ratio varying with age.[225] A ratio of 2:1 chondroitin-6-sulphate:chondroitin-4-sulphate is found in young healthy discs, however, chondroitin-4-sulphate prevails in old degenerate discs.[226]

4.1.2 Peptide hybridisation and GAG selection

In this chapter, the effects of mixing a GAG with the peptides reported previously are investigated. It was hypothesised that the charged GAG chains would interact electrostatically with the charged peptides. To establish whether such an interaction was possible, visual observations of a simple mixing study was carried out as described in section 2.8.2, the morphology of the mixing studied using TEM as described in section 2.4.3 and the mechanical properties of a selection of the gels formed was investigated using rheometry as described in section 2.7.3. Throughout this work the terminology 1:n refers to the molar ratio of one peptide to n GAG subunits.

The GAG selected for the mixing study was chondroitin-6-sulphate (Figure 136). Chondroitin-6-sulphate was chosen as it is the most abundant GAG in the healthy disc, so the most likely candidate to provide mechanical and biological behaviour similar to that of the natural tissue.

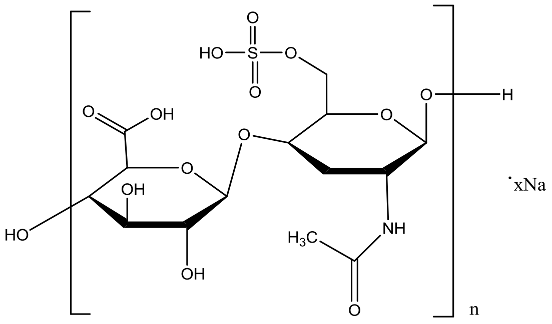

Figure 136 - One subunit of chondroitin-6-sulphate.

The concentration of peptide was kept the same for each sample (20 mg/ml) and the molar ratio of GAG subunit to one peptide was increased to see how the presence of another charged bio-polymer affected the propensity for the peptide to self-assemble and the morphologies of the self-assembled state. From this, an understanding of the mixing interactions could be gained.

Once the fundamental principles underlying the design of self-assembling peptides for use in physiological-like conditions and the interactions between the self-assembling peptides and GAGs have been understood, an optimum peptide hybrid system will be trialled in a biomedical application. For this use it is essential to understand not only the chemical and thermodynamic behaviour of the peptide, but also its mechanical and rheological properties i.e. its viscoelastic characteristics, how it behaves under shear loading, and the gel recovery times and profiles. Such information can be obtained using rheological measurement methods. An initial study into the material properties of the peptides and how these vary upon mixing with GAGs was undertaken and is reported in this chapter.

In the previous chapter, it was discussed that for the use in the treatment of degenerative disc disease, complementary peptides would be advantageous because they are triggerable, they form self-supporting gels and have low c* both for self-assembly and gelation. For this reason, a GAG mixing experiment was carried out on the single peptides and complementary pairs of peptides. It was envisioned that the order in which mixing occurred would potentially affect the observed outcomes, GAG peptide interactions and the peptides propensity to self-assemble. To ensure reproducible and complete mixing with the complementary peptides, mixing within the peptide monomer state is essential and so the GAG was mixed with one peptide before the addition of the other complementary peptide.

In this chapter, the main observations and findings from the mixing study are presented, but further details on individual observations including time for the gel to form and appearance of sample, are presented in Appendix E. The full results for the LVER checks performed for each peptide:GAG ratio during the rheological testing can also be found in Appendix E.

4.2 Results

4.2.1 P_{11}-9:GAG

Both P_{11}-9 and chondroitin-6-sulphate have an overall negative charge, and so the two molecules should repel each other, however, by mixing in physiological-like conditions it was hypothesised that the salts present might act as salt bridges enabling an ionic interaction to form.

4.2.1.1 *Mixing study observations*

Peptide:GAG ratios from 1:0.1 to 1:10 were investigated. Self-supporting gels were formed at all GAG molar ratios (Figure 137). However, as the GAG concentration was increased the quality of the gel differed and the gels became more turbid and “bitty”. The 1:10 sample was a very turbid milky gel. At a GAG ratio of 1:2 subunits and higher, a lot of heating and vortexing was needed to enable the GAG to dissolve. However, once the GAG was dissolved and the heating stopped, the gelation time of the samples was decreased from minutes to seconds even while the samples were still warm.

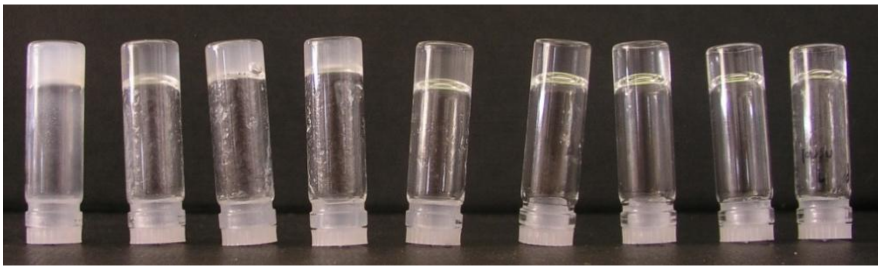

Figure 137 - Samples 3 days old. From left to right P_{11}-9:GAG 1:10, 1:4, 1:3, 1:2, 1:1, 1:0.5, 1:0.2, 1:0.1 and P_{11}-9 control.

After a few months, the gel quality again differed as the GAG concentration increased (Figure 138). The 1:10 sample was no longer a gel, but after reheating and cooling the self-supporting gel was restored, suggesting that the gel was metastable. After very light shearing, the P_{11}-9 control became a viscous liquid that given time would form a gel once more.

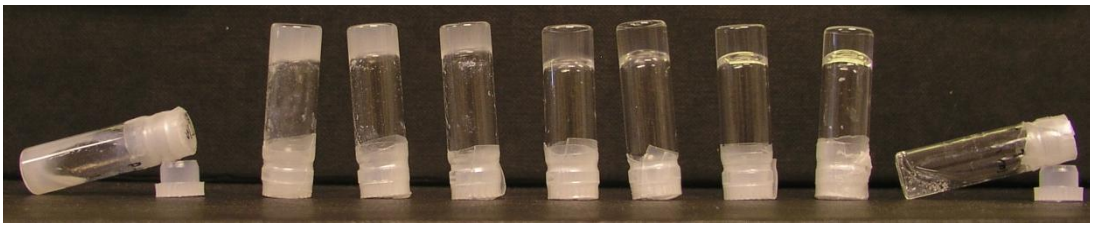

Figure 138 - Samples 3 months old. From left to right P_{11}-9:GAG 1:10, 1:4, 1:3, 1:2, 1:1, 1:0.5, 1:0.2, 1:0.1 and P_{11}-9 control.

From six months onwards, the lower GAG concentrations were still clear gels, the mid range GAG concentrations were easily broken bitty gels, while in the highest concentration GAG samples phase separation occurred and a precipitate was present.

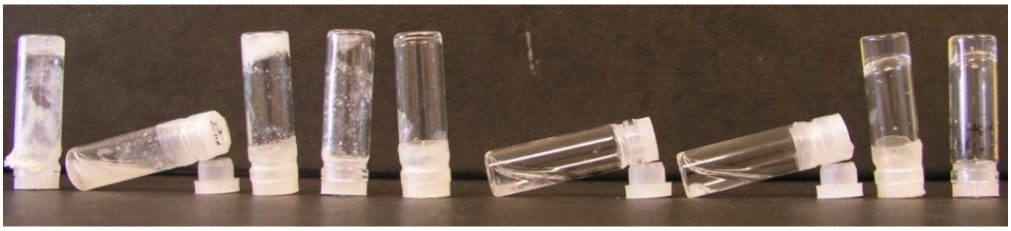

Figure 139 - Samples 1 year and 4 months old. From left to right P_{11}-9:GAG 1:10, 1:4, 1:3, 1:2, 1:1, 1:0.5, 1:0.2, 1:0.1 and P_{11}-9 control.

After a year, the P_{11}-9 control was still a self-supporting gel alongside the lowest GAG concentration. However, as the GAG concentration increased the gel quality was once again reduced. From a ratio of 1:0.2 and upwards phase separation occurred and a gel-like precipitate was observed alongside a clear liquid phase. At the higher ratios in some cases, such as 1:10 and 1:3, a large self-supporting gel phase was still visible.

4.2.1.2 Transmission Electron Microscopy (TEM)

After approximately four and a half months, three representative samples were chosen to be studied by TEM. Peptide:GAG ratios of 1:0.5, 1:2 and 1:10 were compared to the GAG and peptide control samples. Typical images are shown in Figure 140 to Figure 148.

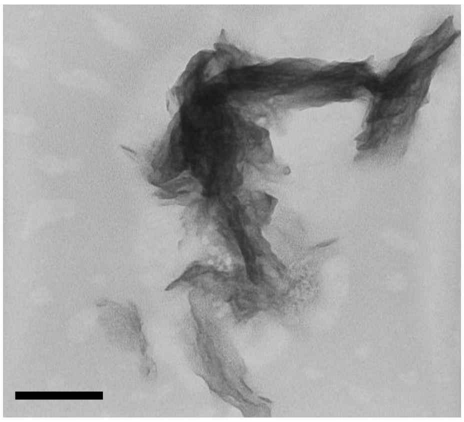

Figure 140 - GAG control, magnification = 73000x, scale bar = 100nm, diluted to approx 7 mg/ml.

In the GAG control sample, the main structures seen were amorphous with no well defined structures (Figure 140).

In the P_{11}-9 control sample a background carpet of ribbon structures was seen with ribbons having a width of 3-5 nm (Figure 141, Figure 145 and Figure 148).

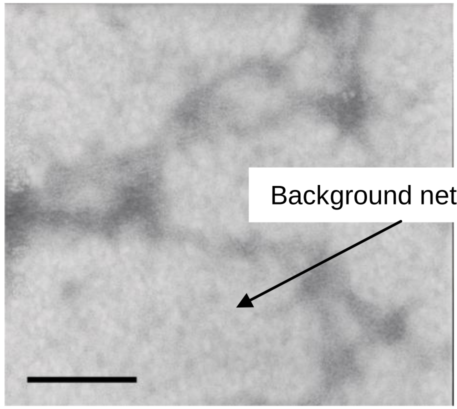

Figure 141 - P_{11}-9 control, magnification = 39000x, scale bar = 500 nm, diluted to approx 7 mg/ml

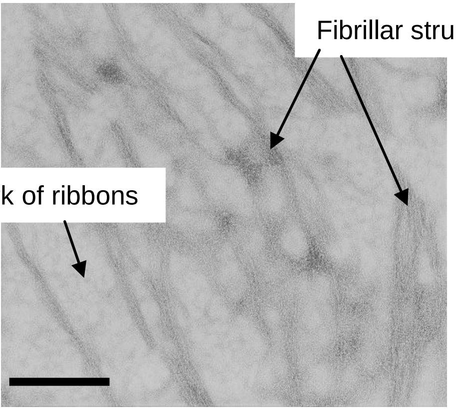

Figure 142 - P_{11}-9 1:0.5 GAG, magnification = 39000x, scale bar = 500 nm, diluted to approx 7 mg/ml.

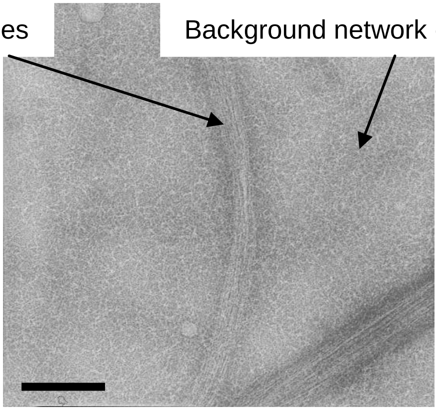

Figure 143 - P_{11}-9 1:2 GAG, magnification = 73000x, scale bar = 200 nm, no dilution.

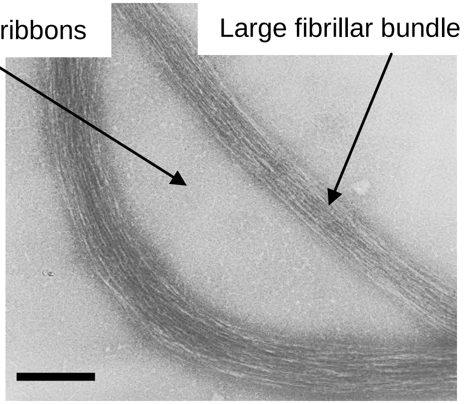

Figure 144 - P_{11}-9 1:10 GAG, magnification = 73000x, scale bar = 200 nm, diluted to approx. 7 mg/ml.

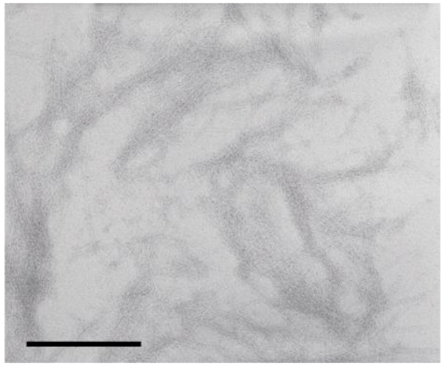

Figure 145 - P11-9 control, magnification = 105000x, scale bar = 200 nm, no dilution.

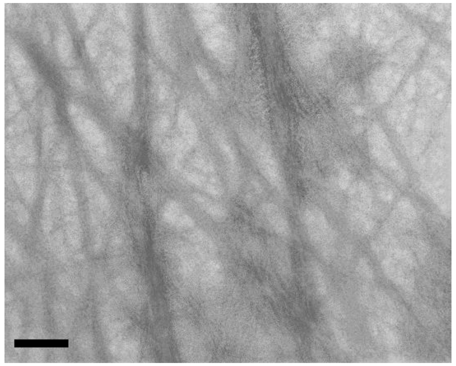

Figure 146 - P_{11}-9 1:0.5 GAG, magnification = 21000x, scale bar = 500 nm, no dilution.

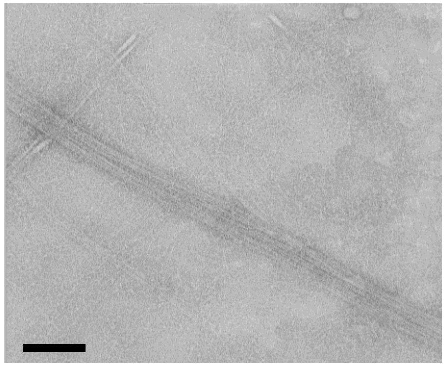

Figure 147 - P_{11}-9 1:2 GAG, magnification = 52000x, scale bar = 200 nm, no dilution.

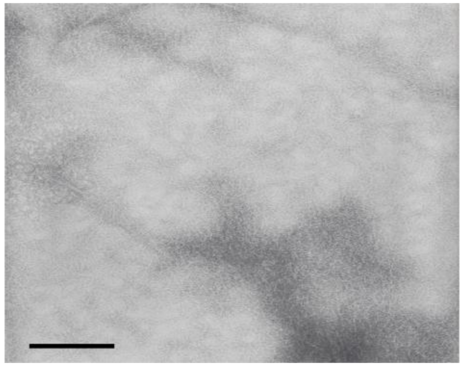

Figure 148 - P_{11}-9 control, magnification = 73000x, scale bar = 200 nm, diluted to approx. 7 mg/ml.

At a low GAG ratio of 1:0.5 (Figure 142), a ribbon network was observed in the background of the image with larger, undefined fibrillar structures visible. The widths of large bundles varied from around 60 to 75 nm, and the widths of the individual ribbons were around 5 nm. An image was also taken of the undiluted sample (Figure 146): although the finite structures could not be clearly identified, it was possible to identify the porous and intertwined structure of the gel.

At a medium GAG ratio of 1:2, again the ribbon network was observed in the background of the image with larger, undefined fibrillar structures visible (Figure 143 and Figure 147). The width of these larger bundles varied from 30 to 100 nm and the background ribbons varied in width between 2 and 6 nm.

In the high GAG ratio sample of 1:10, the background ribbon network was observed again with larger, undefined fibrillar structures visible (Figure 144). However, the larger bundles of ribbons were less commonly seen than with the lower GAG ratios. The width of these large bundles was around 100 to 130 nm and the width of the background ribbons was approximately 4 nm.

In summary, in the 1:0.5 sample there was a very high density of bundles of ribbons forming undefined fibril like structures. In the 1:2 sample, there was mainly a background network of ribbons with very long bundles ½ width of a TEM grid in length and again in the 1:10 sample there was mainly a background network of ribbons visible with fewer but larger bundles present.

As is the case with no GAG present, this peptide in the presence of GAG forms mainly ribbon structures with no well defined fibrils. However it was observed that the loose bundling of ribbons was reduced in the presence of GAG.

4.2.1.3 The effect of GAG addition on the gel mechanical properties

Rheometry was chosen to study the effect of increased GAG ratio on the mechanical properties of P_{11}-9. Three ratios from the mixing study in 4.2.1.1 were chosen to determine the effect, 1:0.5, 1:2 and 1:10.

The samples prepared for the rheological experiments coincided with the samples prepared for the mixing study having gels with similar appearances (Figure 149). It was also observed through polarised lenses that an addition of a small concentration of GAG actually led to the birefringence of the gel increasing (Figure 150).

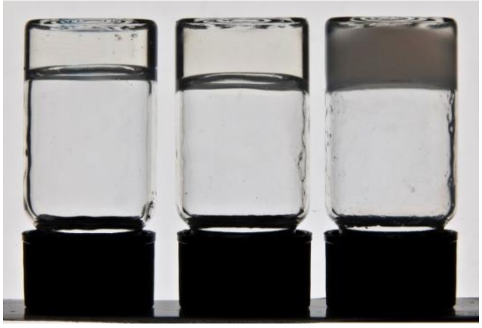

Figure 149 – Optical micrograph[*] From left to right P_{11}-9 control, P_{11}-9:GAG 1:0.5 and P_{11}-9:GAG 1:10.

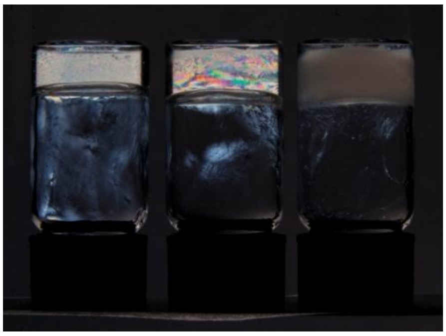

Figure 150 - Optical micrograph[*] taken through polarised lenses. From left to right P_{11}-9 control, P_{11}-9:GAG 1:0.5 and P_{11}-9:GAG 1:10.

The 1:0.5 sample was a clear self-supporting gel that did not turn to viscous liquid under light shaking; it also appeared stiffer and stronger to the touch than the P_{11}-9 control sample.

The 1:2 sample was a self-supporting gel. However, at one month old the 1:2 sample was a cloudy gel with clear liquid phase. There was still a small amount of self-supporting gel that had a very stretchy texture as demonstrated in Figure 151.

---

[*] Optical micrographs taken by Anthony Glossop (Leeds University Print and Copy Bureau)

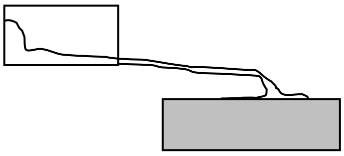

Figure 151 - Schematic of stretchy texture of P_{11}-9:GAG 1:2 sample at 1 month old.

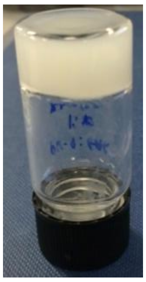

Figure 152 - P_{11}-9:GAG 1:10 in PBS, 1 month old.

The 1:10 sample at one month old was a cloudy self-supporting gel that also appeared to have a small amount of clear liquid phase and a cloudy gel bitty phase (Figure 152).

From the rheometry carried out on P_{11}-9 in the previous chapter, a strain value of 0.5% was chosen to carry out the frequency sweeps. For the 1:2 sample, the frequency sweep was carried out on the gel part of the sample, however, there may have still have been some heterogeneity to the sample. The frequency sweeps are shown in Figure 153 and compared to that of the P_{11}-9 control.

For all samples, the elastic modulus was higher than the viscous modulus, therefore the samples had more solid-like than liquid-like behaviour, except for the 1:2 sample. In the case of the 1:2 sample, the two moduli were very similar: This may be due to the inhomogeneous sample and so it is difficult to draw any true conclusions about its behaviour.

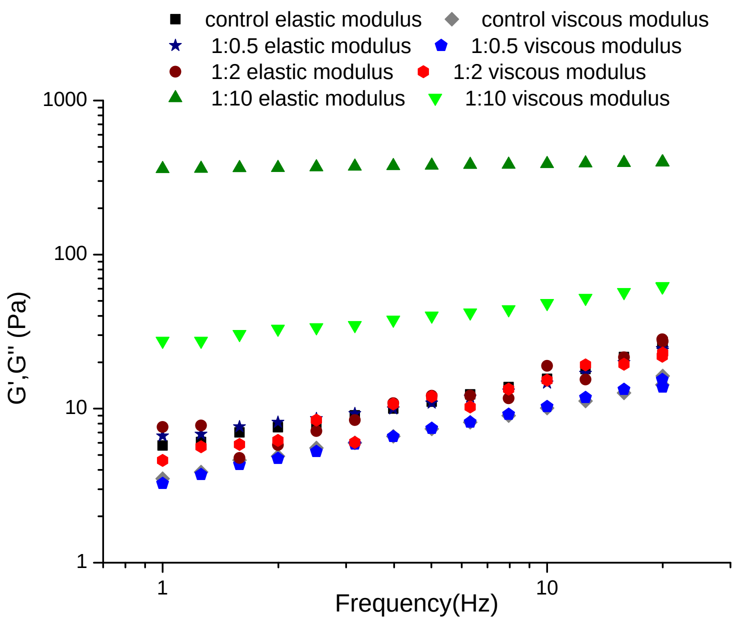

Figure 153 – P_{11}-9:GAG Elastic and viscous modulus vs. frequency. Starting frequency 1 Hz, end frequency: 20 Hz, Strain controlled: 0.5%, Temp: 25°C.

By adding a small amount of GAG (1:0.5) to the sample, the modulus of the material was not significantly changed from the control. This was also the case for the 1:2 sample, however from the visual observations alone it was clear that the material properties of the gel had changed. By adding a larger amount of GAG (1:10) to P_{11}-9, both the elastic and viscous moduli increased suggesting a much stiffer gel. The elastic component increased by around 50 times suggesting a much higher density of junction points. The bundles captured in the TEM study that form in the higher GAG samples may act as such junction points.

The shape of the plot of the 1:10 sample is typical of that of a gel (i.e. moduli independent of frequency), whereas the other samples are typical of that of a viscoelastic solid (i.e. viscous modulus increases with frequency). This was also confirmed by the phase angle measurements, where for 1:10 the angle was unaffected by frequency and remained at around 6.3°, whereas the 1:0.5 and 1:2 phase angles increased with frequency from 3-14° and 31-40° respectively.

4.2.2 P_{11}-12:GAG

P_{11}-12 has an overall charge of +2 and so the peptide and negatively charged GAGs should interact electrostatically directly with one another forming ionic bonds.

4.2.2.1 Mixing study observations

Peptide:GAG ratios from 0.1 to 1:100 were investigated. At all GAG ratios self-supporting gels were formed (Figure 154), although as the GAG concentration was increased the quality of the gel differed and the gels became less turbid and “bitty” over the mid range ratios. Once above 1:20 the gels became more turbid and bitty again with the 1:100 ratio being a very thick gel. The addition of a small ratio of GAG increased the gelation time from minutes to hours, but the addition of a GAG ratio of 1:1 and above took the gelation time down to seconds, with gelation in a ratio of 1:20 and above happening spontaneously upon mixing.

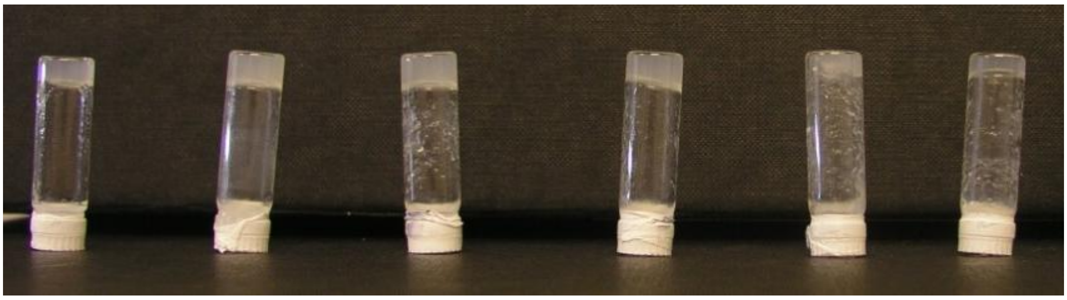

Figure 154 - Samples 1 week old. From left to right P_{11}-12 control 1:10, 1:4, 1:3 1:2, 1:1 and GAG control.

At two to four weeks, the quality of the gels observed again differed (Figure 155) with the lower and mid range GAG concentrations no longer being self-supporting gels, with the exception of the 1:0.5 ratio, which was still a self-supporting gel. At these lower GAG concentrations, there was a large amount of gel-like precipitate visible on the sides of the walls of the vials. At the higher GAG concentrations, the self-supporting gels remained intact although were “bitty” with the exception of the highest 1:10 ratio.

Figure 155 – From left to right GAG control, 1:10, 1:4, 1:3, 1:2, 1:1, 1:0.5, 1:0.2, 1:0.1, P_{11}-12 control. P_{11}-12 control, 1:1, 1:2, 1:3, 1:4, 1:10. GAG control samples all 1 month old and 1:0.1, 1:0.2, 1:0.5 samples 2 weeks old.

The samples that were no longer self-supporting gels (1:0.1, 1:0.2, 1:1, 1:2) were reheated and self-supporting gels reformed on cooling, suggesting that the gels that were first formed were only meta-stable. After a further 2.5 months, all gels were still self-supporting with the reheated sample gels being less bitty than when first prepared.

After eight to ten months, all samples were still self-supporting gels. The quality of the gel still differed with increasing GAG concentration, at the very low ratios precipitation was observed, whereas, at the medium ratios less precipitate was visible and the gels were less bitty, at the high GAG ratios the gels became much more homogenous.

After a year and five months, all samples were still self-supporting gels showing remarkable stability.

At nearly two years, all gels were still self-supporting. The midrange ratios had less bitty gels on the walls of the vials. The 1:100 was by far the thickest gel and showed a yellow colour due to the GAG (Figure 156).

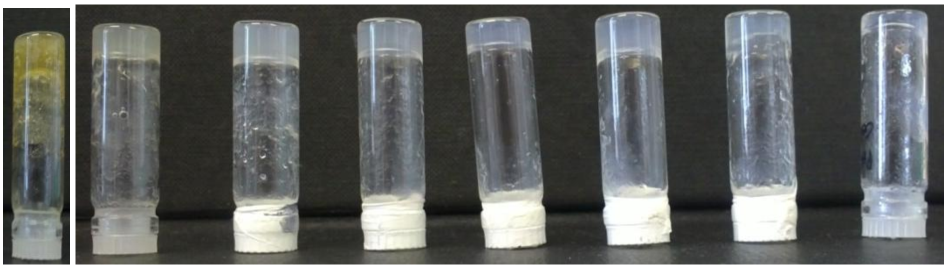

Figure 156 –From left to right, 1:100, 1:50, 1:20, 1:4, 1:3, 1:1, 1:0.2, 1:0.1, P_{11}-12 control. Samples 1:100, 1:50 and 1:20 6.5 months old; other samples 1 year and 11 months old.

4.2.2.2 Transmission Electron Microscopy

After approximately five and a half months, three representative samples were chosen to be studied by TEM. Peptide:GAG ratios of 1:0.5, 1:2 and 1:5 were compared to the GAG and peptide control samples. Typical images are shown in Figure 157 to Figure 170.

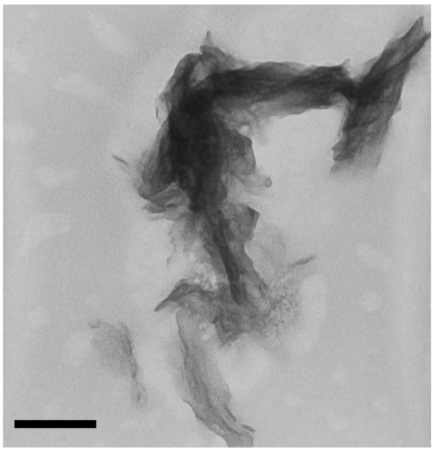

Figure 157 - GAG control, magnification = 73000x, scale bar = 100nm, diluted to approx 7 mg/ml.

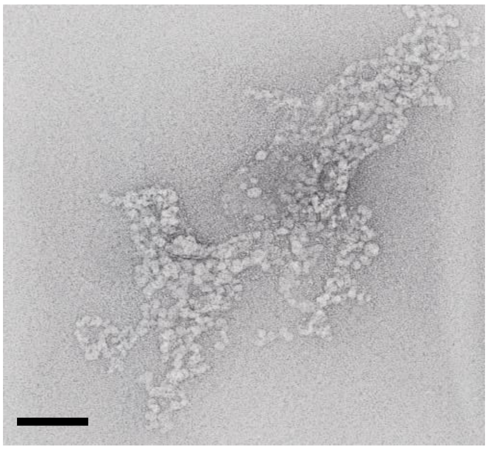

Figure 158 - GAG control, magnification = 105000x, scale bar = 100nm, diluted to 20 µM.

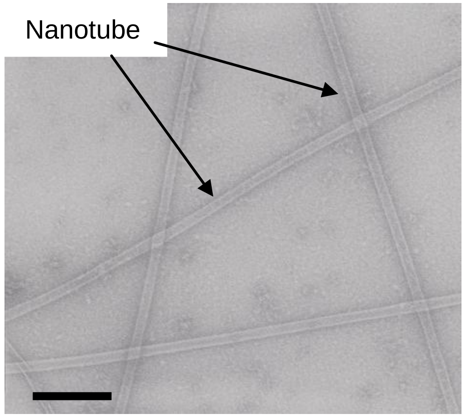

Figure 159 - P_{11}-12 control, magnification = 73000x, scale bar = 200 nm, diluted to approx 5000 µM.

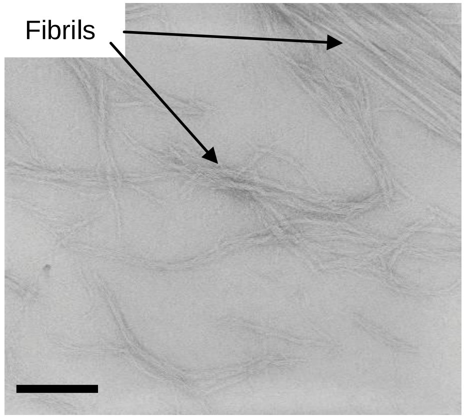

Figure 160 - P_{11}-12:GAG 1:0.5, magnification = 73000x, scale bar = 100 nm, diluted to approx 5000 µM.

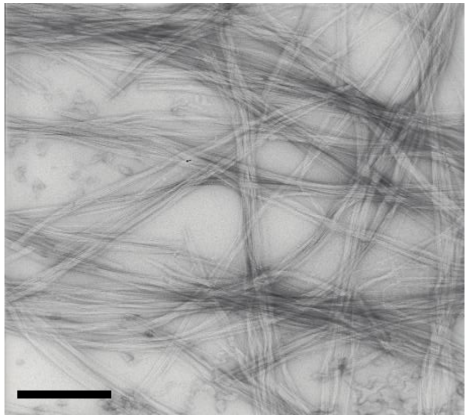

Figure 161 - P_{11}-12:GAG 1:0.5, magnification = 39000x scale bar = 400 nm, diluted to approx 5000 µM.

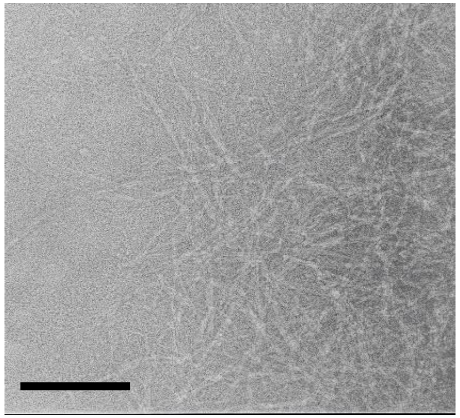

Figure 162 - P_{11}-12:GAG 1:10, magnification = 73000x, scale bar = 200 nm diluted to approx 5000 µM.

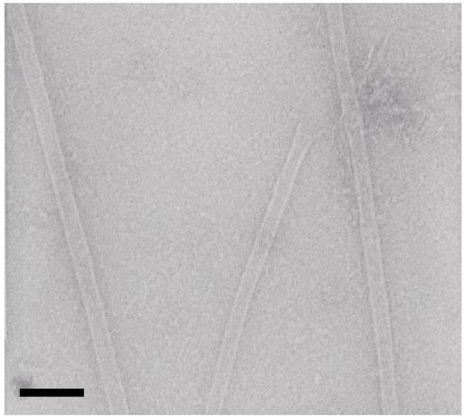

Figure 163 - P_{11}-12 control, magnification = 105000x scale bar = 100 nm, diluted to approx 5000 µM.

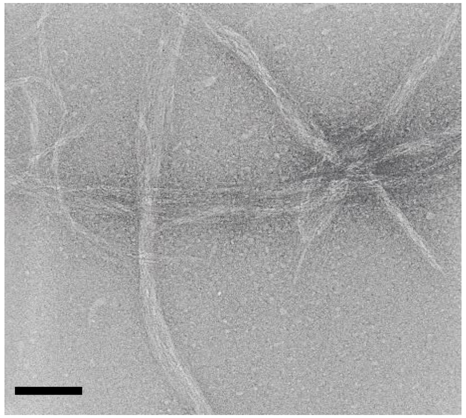

Figure 164 - P_{11}-12:GAG 1:0.5, magnification = 105000x scale bar = 100 nm, diluted to approx 5000 µM.

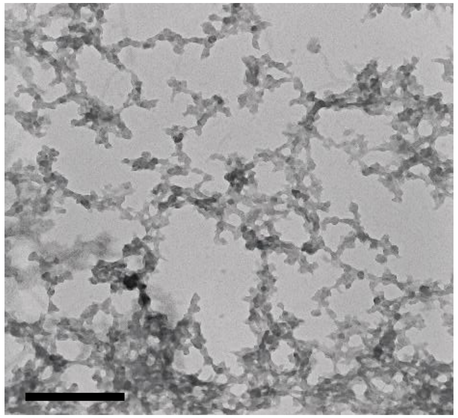

Figure 165 - P_{11}-12:GAG 1:0.5, magnification = 39000x scale bar = 400 nm, no dilution.

-

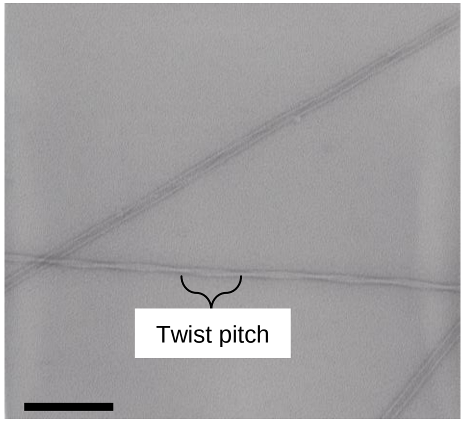

Figure 166 - P_{11}-12 control,, magnification = 73000x, scale bar = 200 nm diluted to approx 20 μM.

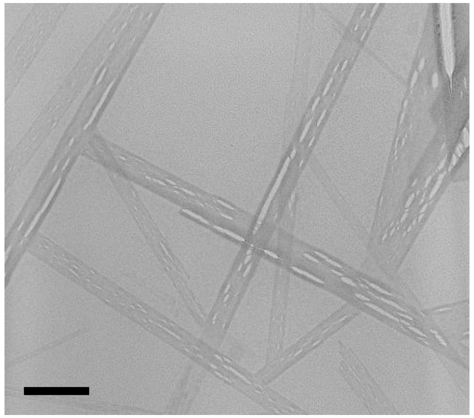

Figure 167 - P_{11}-12:GAG 1:2, magnification = 73000x, scale bar = 200 nm, diluted to approx 20 μM.

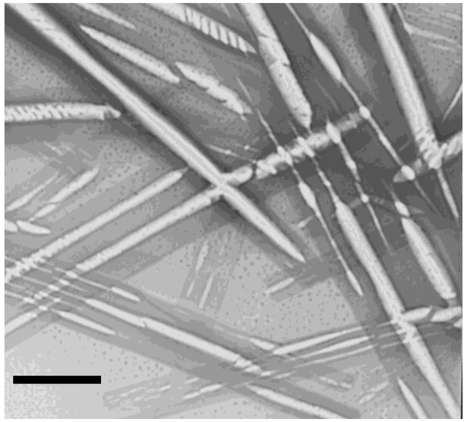

Figure 168 - P_{11}-12:GAG 1:10, magnification = 73000x, scale bar = 200 nm, diluted to approx 20 μM.

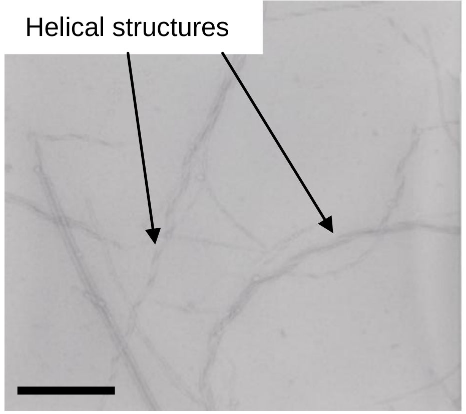

Figure 169 - P_{11}-12 control, magnification = 39000x scale bar = 400 nm, diluted to approx 20 μM.

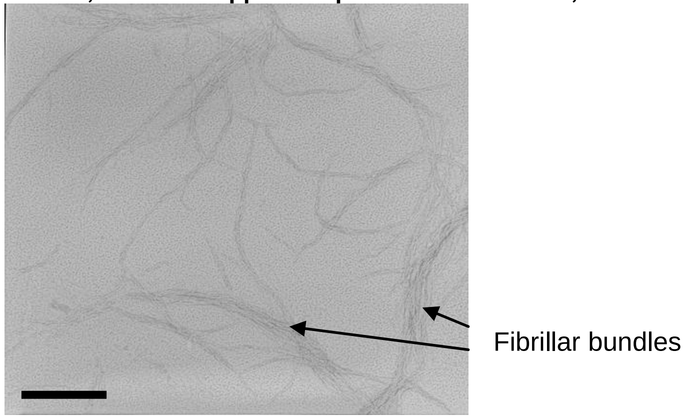

Figure 170 - P_{11}-12:GAG 1:2, magnification = 52000x, scale bar = 200 nm, diluted to approx 20 μM.

In the P_{11}-12 control sample diluted down to approximately 5000 µM (7 mg/ml), the main structures seen were nanotubes with an external diameter of 20 to 39 nm (Figure 159, Figure 163). In the P_{11}-12 control sample diluted down to approximately 20 µM, the main structures observed were again tubular structures with a width of 25 ± 2 nm and a twist pitch of ~165 nm, there was also a presence of helical structures with a twist pitch of approx 230 nm and a width of 15 to 40 nm (Figure 166 and Figure 169).

In the 1:0.5 ratio sample, fibril structures were observed with a width of 15 to 30 nm and a background network of ribbons of width 2 to 3 nm (Figure 160, Figure 161 and Figure 164). There was also the presence of an amorphous aggregate structure (Figure 165).

In the 1:2 sample, there was a background network of ribbons with an average width of around 4 nm with larger fibrillar bundles varying in width from 8 to 40 nm. There was also a presence of needle like structures with a very uniform width of 60 to 90 nm (Figure 167).

In Figure 162, the edge of a large fibril network can be seen. Once again, the presence of needle like structures could be seen that varied in width between 60 and 150 nm (Figure 168).

In the GAG control sample, the main structures seen were amorphous with no well defined structures (Figure 157 and Figure 158).

4.2.2.3 The effect of GAG addition to P_{11}-12 on the gel mechanical properties

The rheological properties of P_{11}-12:GAG samples were examined and compared to the rheological properties of P_{11}-12 determined in Chapter 3 to establish how the addition of GAG affected the material properties of the gels.

Four GAG ratios were chosen from the above mixing study for the rheological testing: 1:0.5, 1:2, 1:10 and 1:100. All samples prepared for the rheological testing were consistent in appearance with those prepared for the initial mixing study showing process reproducibility.

The 1:0.5 sample was a cloudy self-supporting gel similar to that of P_{11}-12 on its own (Figure 171). It was observed that, after the rheological experiment was carried out, the top cone of the rheometer could not be easily separated from the sample upon unloading. This suggests a sample with a strong molecular structure that is hard to pull apart.

Figure 171 - P_{11}-12:GAG 1:0.5, 2 months old.

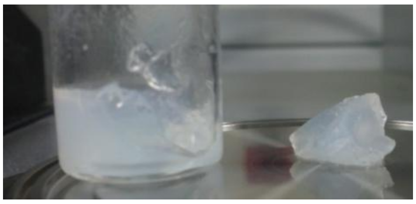

Figure 172 - P_{11}-12:GAG 1:2 in PBS, 2 months old.

The 1:2 sample was a cloudy self-supporting gel with a slightly gritty texture (Figure 172). Once again, the rheometer struggled to rise upon unloading, suggesting a strong molecular structure.

The 1:10 sample was a cloudy self-supporting gel (Figure 173). It was observed that the gel has a very slow relaxation time, even after 10 months the gel in Figure 174 had not relaxed from the position it was left in after some of the gel was removed from the vial for testing.

Figure 173 - P_{11}-12:GAG 1:2 in PBS, on day of preparation.

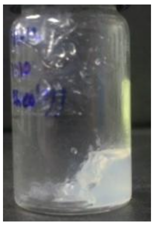

Figure 174 - P_{11}-12:GAG 1:2 in PBS, 1 month 20 days old.

The 1:100 sample produced a yellow, very thick self-supporting gel. It was observed when loading the gel onto the rheometer that the gel appeared to be very stretchy and not brittle at all, i.e. it flowed. It was also very sticky and resisted removal from the spatula being used for loading. It had an almost “wallpaper paste” or caramel-like texture. The top cone did not easily separate from the sample on unloading: upon cleaning, it was observed that the surfaces seemed to be greasy.

Amplitude sweeps were carried out to determine the linear viscoelastic region (LVER) for the 1:2 sample. From these a strain value of 0.1% was chosen for the 1:2 sample, 0.05% for the 1:10 sample, and 0.15% for the 1:100 sample for the frequency sweeps (Figure 175, Figure 176, Figure 177 and Figure 178). For the 1:0.5 sample, the strain value of 0.25%, deduced for P_{11}-12 in the previous chapter, was used for the frequency sweep.

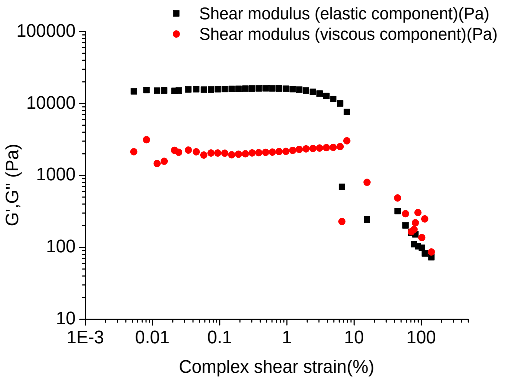

Figure 175 - P_{11}-12:GAG 1:2 elastic and viscous modulus vs. shear strain. Starting shear strain 0.01%, end shear strain: 100%, Frequency: 1 Hz, temp 25^{o}C. 2 months old.

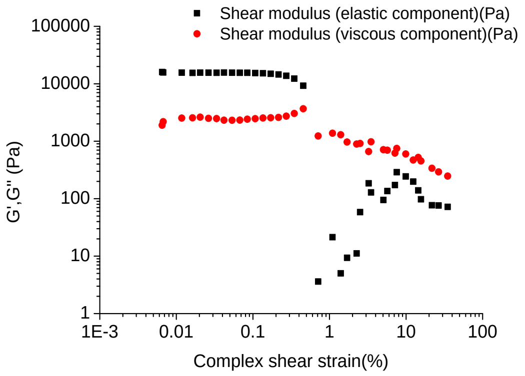

Figure 176 - P_{11}-12:GAG 1:2 elastic and viscous modulus vs. shear strain. Starting shear strain 0.01%, end shear strain: 100%, Frequency: 20 Hz, temp 25^{o}C. 2 months old.

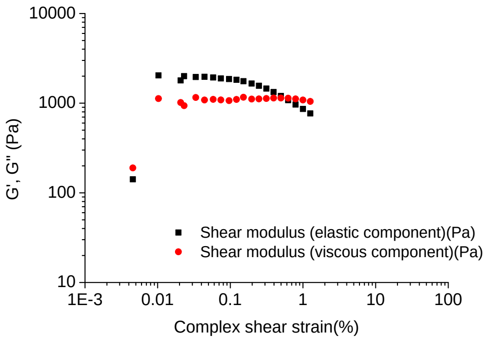

Figure 177 - P_{11}-12:GAG 1:100 elastic and viscous modulus vs. shear strain. Starting shear strain 0.01%, end shear strain: 100%, Frequency: 1 Hz, temp 25^{o}C. 6 days old.

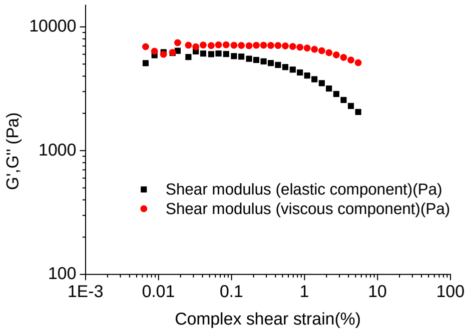

Figure 178 - P_{11}-12:GAG 1:100 elastic and viscous modulus vs. shear strain. Starting shear strain 0.01%, end shear strain: 100%, Frequency: 20 Hz, temp 25^{o}C. 6 days old.

The results of the frequency sweeps are presented in Figure 179.

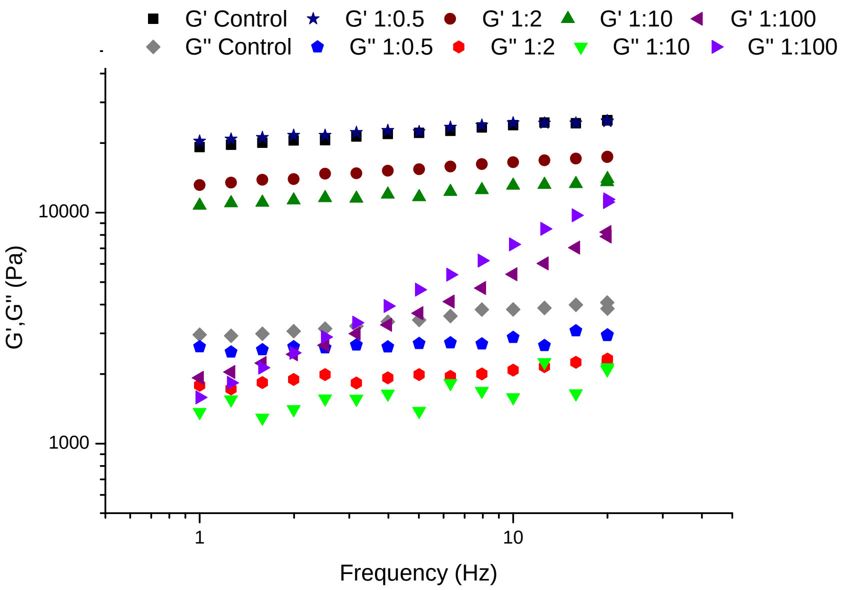

Figure 179 - P_{11}-12:GAG Elastic and viscous modulus vs. frequency. Starting frequency 1 Hz, end frequency: 20 Hz, Strain controlled: 0.25% (1:0.5), 0.1% (1:2), 0.05%(1:10), 0.15% (1:100), Temp: 25°C. 1:0.5, 1:2 and 1:10 2 months old and 1:100 6 days old.

The 1:0.5, 1:2 and 1:10 samples had similar shaped plots and so are considered first. In all cases, as with the P_{11}-12 control, the elastic modulus was higher than the viscous modulus suggesting more solid-like than liquid-like behaviour. The shape of the plots showed gel-like behaviour over the frequency range studied and this was confirmed by the phase angles being unaffected by the frequency (1:0.5 = 6.8°, 1:2 = 7.4° and 1:10 = 8°). The increase in the phase angle and decrease in elastic modulus as the amount of GAG is increased suggests that gels become weaker with increasing GAG ratios.

The 1:100 sample frequency sweep was very different to the others. At low frequencies, the gel was more solid-like, whereas at high frequencies it was more liquid-like. However, from looking at the combined moduli, the stiffness of the gel increased with frequency. In comparison to the other samples this sample also had a very high phase angle that increased from 39° to 55° over the frequency range, suggesting more liquid-like behaviour. The shape of the plot and the increasing phase angle was classic viscoelastic solid behaviour.

4.2.3 P_{11}-4:GAG

4.2.3.1 Mixing study observations

Peptide:GAG ratios from 1:2 to 1:10 were investigated. At all GAG ratios, self-supporting gels were formed. However, as the GAG concentration was increased, the quality of the gel differed and the gels became cloudier in appearance. The addition of GAG reduced the samples' gelation time from hours to seconds.

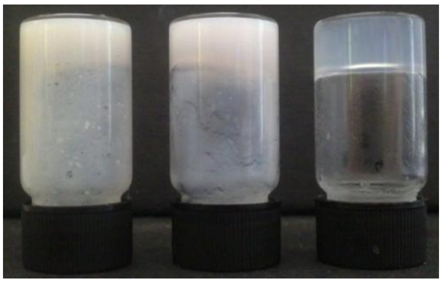

Figure 180 - Samples 2 days old. From left to right, P_{11}-4:GAG 1:10, 1:2 and P_{11}-4 control.

After two days, the gels were still self-supporting and did not appear to have changed since preparation. There was much more gel visible on the walls of the vial for P_{11}-4:GAG 1:2 and 1:10 than the control. This was thought to be due to the having to sonicate and heat during preparation to remove the bubbles formed upon mixing with the GAG (Figure 180).

At 10 and 20 days, the sample again appeared unchanged from the day of preparation with all gels remaining self-supporting. An increase in GAG concentration led to a more opaque gel.

4.2.3.2 The effect of GAG addition to P_{11}-4 on the gel mechanical properties

The rheological properties of P_{11}-4:GAG samples were examined and compared to those of P_{11}-4 determined in Chapter 3, to establish how the addition of GAG affects the material properties of P_{11}-4 gels.

The two GAG ratios (1:2, 1:10) prepared for the above mixing study were used for the rheological testing.

The 1:2 sample was a very cloudy/white self-supporting gel that differed from the P_{11}-4 control sample in that it appeared to be more liquid-like, i.e. runnier. The 1:10 sample formed a very white, almost opaque self-supporting gel with a more solid consistency than that of the 1:2 sample. It was observed upon loading that there were still some bubbles present in the sample from preparation; however, these were attempted to be removed before testing commenced.

First of all, amplitude sweeps were carried out at two frequencies to determine the LVER (Figure 181, Figure 182, Figure 183 and Figure 184).

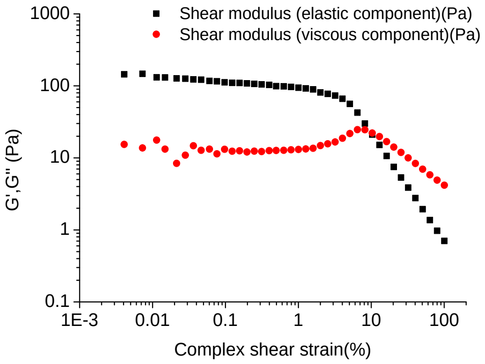

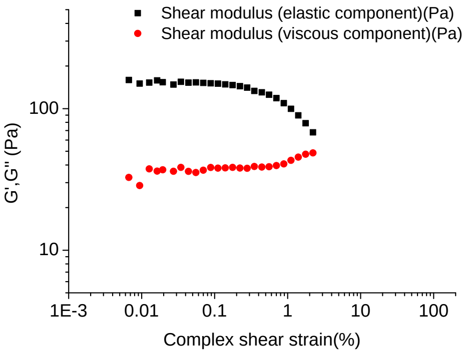

Figure 181 - P_{11}-4:GAG 1:2 elastic and viscous modulus vs. shear strain. Starting shear strain 0.01%, end shear strain: 100%, Frequency: 1 Hz, Temp 25°C. 20 days old.

Figure 182 - P_{11}-4:GAG 1:2 elastic and viscous modulus vs. shear strain. Starting shear strain 0.01%, end shear strain: 100%, Frequency: 20 Hz, Temp 25°C. 20 days old.

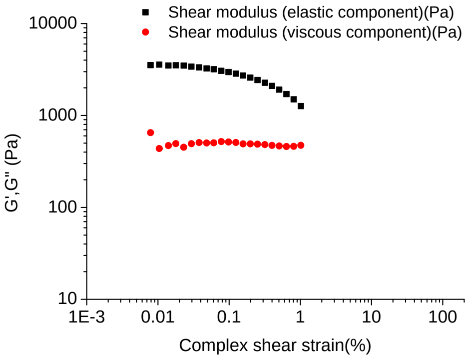

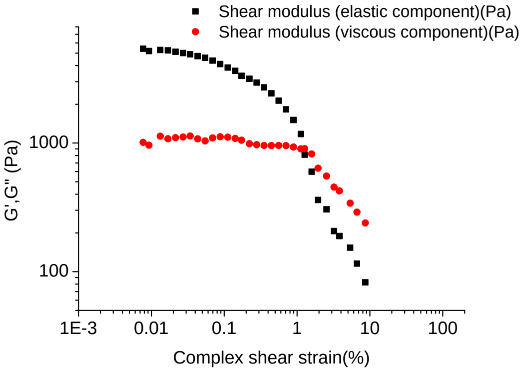

Figure 183 - P_{11}-4:GAG 1:10 elastic and viscous modulus vs. shear strain. Starting shear strain 0.01%, end shear strain: 100%, Frequency: 1 Hz, Temp 25°C. 20 days old.

Figure 184 - P_{11}-4:GAG 1:10 elastic and viscous modulus vs. shear strain. Starting shear strain 0.01%, end shear strain: 100%, Frequency: 20 Hz, Temp 25°C. 20 days old.

By comparing the amplitude sweeps for both samples it can be seen that the 1:2 gel has a slightly greater LVER indicating the gel could undergo higher strains before there was a breakdown in molecular structure, i.e. a “stretchier” gel.

From the amplitude sweeps above, a strain value of 0.175% was chosen within the LVER to carry out the frequency sweep for the 1:2 sample and 0.04% for the 1:10 sample. The frequency sweeps for these two samples are compared to the P$_{11}$-4 control in Figure 185.

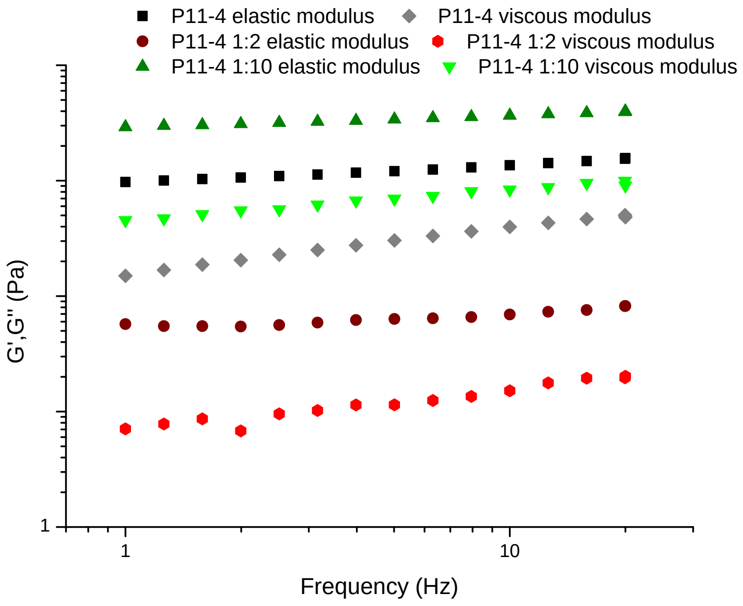

Figure 185 – P$_{11}$-4:GAG and viscous modulus vs. frequency. Starting frequency 1Hz, end frequency: 20 Hz, Strain controlled: 0.15 % (control), 0.175% (1:2) and 0.04% (1:10). Temp: 25^{o}C. 20 days old.

As with P$_{11}$-4 on its own, for both GAG ratios, the elastic modulus was higher than the viscous modulus, suggesting the sample had more solid than liquid-like behaviour. The shape of the plot is typical of that of a gel although the increase of the phase angle from 7-14^{o} for 1:2 and 9-13^{o} for 1:10 suggests viscoelastic solid behaviour.

The addition of a small amount of GAG (1:2) decreased the stiffness of the hydrogel formed. However, as the GAG concentration was increased further (1:10), the hybrid gels became stiffer than gels of the peptide alone.

4.2.4 P_{11}-8:GAG

4.2.4.1 Mixing study observations

Peptide:GAG ratios from 1:2 to 1:10 were investigated. The addition of GAG to P_{11}-8 led to faster gelation, with self-supporting gels forming on the day of preparation unlike the control sample which took days (Figure 186).

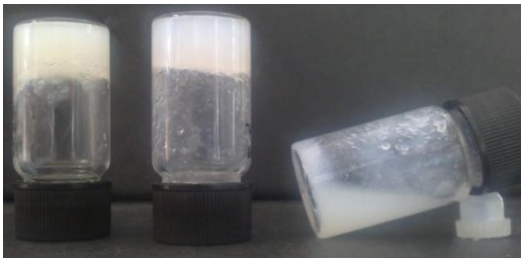

Figure 186 – Day of preparation. From left to right P_{11}-8:GAG 1:10, 1:2 and P_{11}-8 control.

After five days, all gels were cloudy self-supporting gels with the quality of the gel differing with an increase in GAG ratio. As the GAG concentration increased, the gels became less turbid and 'bitty'.

At 13 days, differences in the gel quality became even more obvious. All were still self-supporting gels, but the control sample was not as self-supporting as the rest as was observed by the gel starting to slip down the walls of the sample vial.

Again, at 40 days, all samples were still gels but with clear differences in their appearances.

4.2.4.2 The effect of GAG addition to P_{11}-8 on the gel mechanical properties

The rheological properties of P_{11}-8:GAG samples were examined and compared to those of P_{11}-8 determined in Chapter 3 to establish how the addition of GAG affects the material properties of P_{11}-8 gels.

The two GAG ratios (1:2 and 1:10) prepared for the above mixing study were used for the rheological testing.

The 1:2 sample was a cloudy self-supporting gel that appeared more similar to a P_{11}-12 gel than P_{11}-9 (Figure 187). It was observed that upon loading, the gel seemed to split into a liquid and gel phase as with the control. It was also noted that when trying to unload the sample from the machine, the top cone of the rheometer did not easily separate from the sample, suggesting a strong molecular structure that was difficult pull apart. Also when the gel was wiped off the rheometer with tissue, the gel formed a substance on the tissue, which looked and felt like candle wax.

Figure 187 - P_{11}-8:GAG 1:2 in PBS, 1.5 months old, on loading onto rheometer.

The 1:10 sample appeared much more liquid-like than the 1:2 gel and more similar to P_{11}-9 gel samples than, for example, a stiff P_{11}-12 gel.

First, amplitude sweeps were carried out at two frequencies to determine the LVER (Figure 188, Figure 189, Figure 190 and Figure 191).

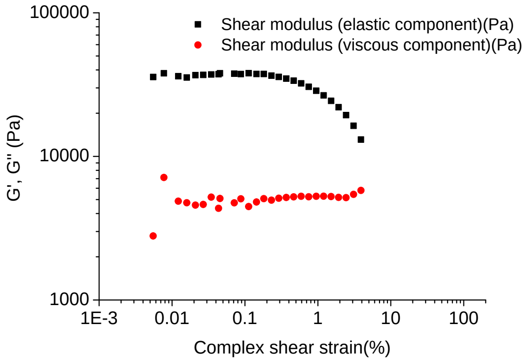

Figure 188 - P_{11}-8:GAG 1:2 elastic and viscous modulus vs. shear strain. Starting shear strain 0.01%, end shear strain: 100%, Frequency: 1Hz, Temp 25°C. 1.5 months old.

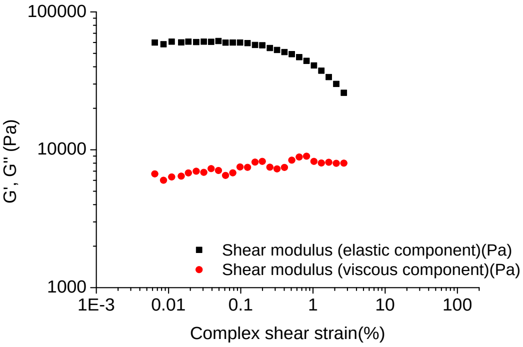

Figure 189 - P_{11}-8:GAG 1:2 elastic and viscous modulus vs. shear strain. Starting shear strain 0.01%, end shear strain: 100%, Frequency: 20 Hz, Temp 25°C. 1.5 months old.

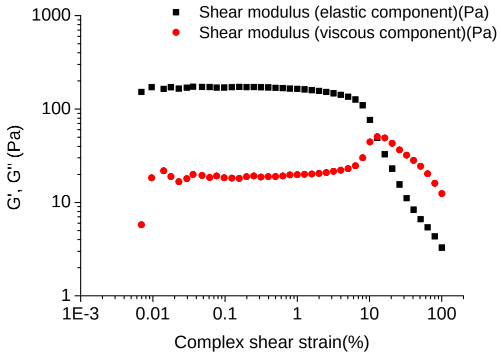

Figure 190 - P_{11}-8:GAG 1:10 elastic and viscous modulus vs. shear strain. Starting shear strain 0.01%, end shear strain: 100%, Frequency: 1Hz, Temp 25^{o}C. 1.5 months old.

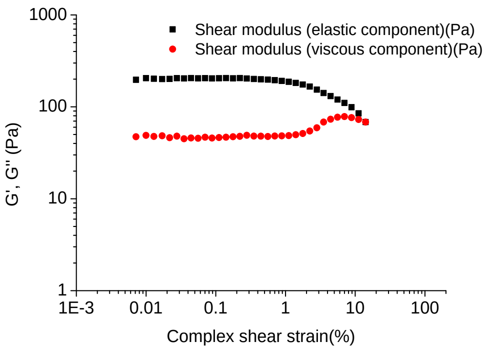

Figure 191 - P_{11}-8:GAG 1:10 elastic and viscous modulus vs. shear strain. Starting shear strain 0.01%, end shear strain: 100%, Frequency: 20 Hz, Temp 25^{o}C. 1.5 months old.

By comparing the amplitude sweeps for both samples, it was observed that the 1:10 sample had a slightly greater LVER indicating a stretchier gel. From the amplitude sweeps above, a strain value of 0.1% was chosen within the LVER for both the samples to carry out the frequency sweeps. The resulting frequency sweeps for these two samples are compared to the P_{11}-8 control in Figure 192.

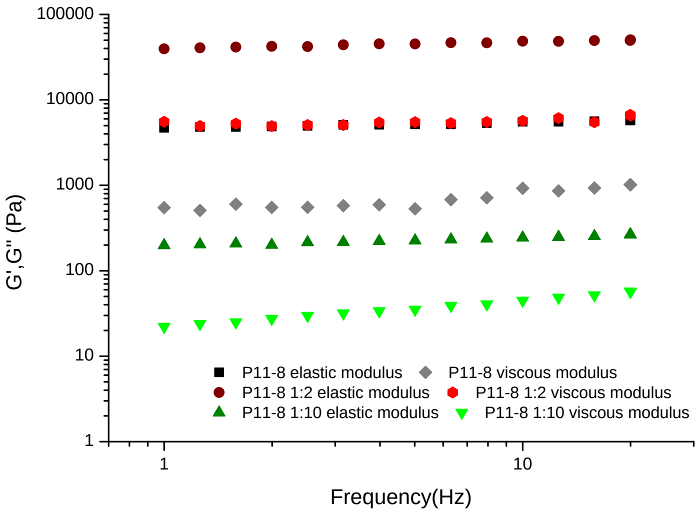

Figure 192 - P_{11}-8:GAG elastic and viscous modulus vs. frequency. Starting frequency 1 Hz, end frequency: 20 Hz, Strain controlled: 0.1% (control) 0.1% (1:2 and 1:10), Temp: 25^{o}C. 1.5 months old.

Once more, both the frequency sweeps showed the gels had solid-like behaviour with higher elastic than viscous modulus. The addition of a small amount of GAG (1:2) caused both moduli to greatly increase by over an order of magnitude. The elastic modulus for this peptide/GAG combination was the highest determined of those tested at nearly 50 kPa. The shape of this plot was typical for that of a gel and it had more solid-like than liquid-like behaviour with an average phase angle of ~7^o. However, as the GAG concentration was increased further (1:10), the gels actually became weaker than the peptide gel on its own. The increased viscosity was not only shown in the decreased moduli of the 1:10 sample, but also in the increase of its phase angle (~9^o) as well, again showing less solid-like behaviour (Figure 192).

4.2.5 P_{11}-13 + P_{11}-14:GAG

From the previous chapter it was discovered that this complementary pair did not form very stiff gels. Nonetheless, for some cases discussed above the addition of GAG to a peptide increased gel stiffness and therefore it was anticipated that this might be the case here too.

4.2.5.1 P_{11}-13:GAG+P_{11}-14 Mixing study observations

P_{11}-13 was mixed with GAG ratios from 1:0.1 to 1:20, left overnight and then P_{11}-14 in a molar ratio to P_{11}-13 was added to the peptide GAG mix, as described in section 2.8.1. Once again, the presence of the GAG chains did not inhibit self-assembly with self-supporting gels observed at all GAG ratios. At preparation and after a few days, all samples were clear self-supporting gels, except for the 1:10 sample, which was slightly cloudy. All gels seemed less turbid and bitty than seen with P_{11}-9 and P_{11}-12.

After a few weeks, the quality of the gels differed with increasing GAG concentrations and from first observed. At low to medium GAG ratios, the gels were turbid and upon light shearing and/or vortexing easily broke down into “bitty” viscous liquids. By contrast, upon vortexing and heating, the P_{11}-13+14 control did not break down, suggesting that a low concentration of the GAG chains diminished the gel properties. At the highest ratio of 1:10 the sample was no longer a self-supporting gel and instead was a cloudy liquid with precipitate on the walls. Interestingly, the 1:5 ratio was still a self-supporting gel and, much like the P_{11}-13+14 control, did not break down upon vortexing or heating, therefore suggesting that there is an optimum GAG concentration to produce the best gel (Figure 193).

Figure 193 - 19 days old. From left to right P_{11}-13/14:GAG 1:10, 1:5, 1:2, 1:1, 1:0.1 and P_{11}-13/14 control.

After a month, the presence of the low GAG concentrations still diminished the gel properties when compared to the control: the gels were very bitty in nature and were only found on the walls of the vials. The 1:5 sample was still a clear self-supporting gel, however. After 2 weeks, the 1:20 sample was also still a self-supporting gel.

Figure 194 – 6 months old. From left to right P_{11}-13/14:GAG 1:20, 1:10, 1:5, 1:2, 1:1, 1:0.1 and P_{11}-13/14 control.

After 6 months, the quality of the majority of the gels had greatly decreased. At the lower GAG ratios the gels were inhomogeneous, with a liquid phase and bitty gel particles covering the vial walls. The 1:5 ratio was still a self-supporting gel, however, there was a precipitate present and upon shearing it became viscous. The 1:10 ratio sample was similar to that of the lower GAG ratios and the highest 1:20 ratio was similar to that of the 1:5 ratio sample. The control sample was still a self-supporting gel that was not broken apart upon shearing and was not birefringent (Figure 194).

At the 6 month time point, all samples were heated, vortexed and then cooled again, resulting in cloudy self-supporting gels once more. At 10 months, all samples except for the 1:20 ratio were self-supporting gels with the control sample being the most homogeneous. The rest of the samples had bitty gel particulates covering the vial walls. The 1:20 ratio had some gel particles, however, a liquid phase was also present.

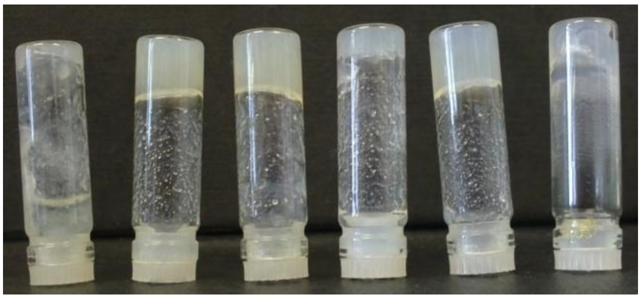

Figure 195 - 17 months old. From left to right P_{11}-13/14:GAG 1:20, 1:10, 1:5, 1:2, 1:1 and P_{11}-13/14 control. All samples heated, vortexed and then cooled after 6 months.

After 17 months, the appearance of the samples was similar to that at 10 months: all were still self-supporting other than the 1:20 ratio, which again had a liquid and bitty gel phase (Figure 195).

4.2.5.2 The effect of GAG addition to P_{11}-13/14 on the gel mechanical properties

The rheological properties of P_{11}-13/14:GAG samples were examined and compared to those of P_{11}-13/14 determined in Chapter 3 to establish how the addition of GAG affects the material properties of P_{11}-13/14 gels.

The two GAG ratios (1:2 and 1:10) prepared for the above mixing study were used for the rheological testing. However, the 1:10 sample had two phases: a clear liquid phase and cloudy viscous liquid gel phase, which was very hard to pull apart. The 1:10 sample was very different to the P_{11}-13+14 control and, due to the two phases, it was difficult to obtain consistent rheological data as the mechanical properties of the bulk material was dependent on how much of each phase was tested (Figure 196).

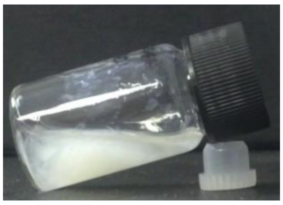

Figure 196 - P_{11}-13/14:GAG 1:10 2 weeks old.

The 1:2 sample was a slightly cloudy, self-supporting gel that appeared very similar to the control sample and so the strain conditions of 3% used for the control were also used in the frequency sweep for this sample (Figure 197).

The 1:2 sample, like the control, had a higher elastic than viscous modulus, and therefore had more solid-like than liquid-like behaviour. It behaved like a viscoelastic solid over the frequency range studied because the phase angle tended towards 0^o at rest ($17\text{-}30^o$). This means that over long timescales at low frequencies the sample was more liquid-like, but its stiffness increased to more solid-like over short timescales at high frequencies.

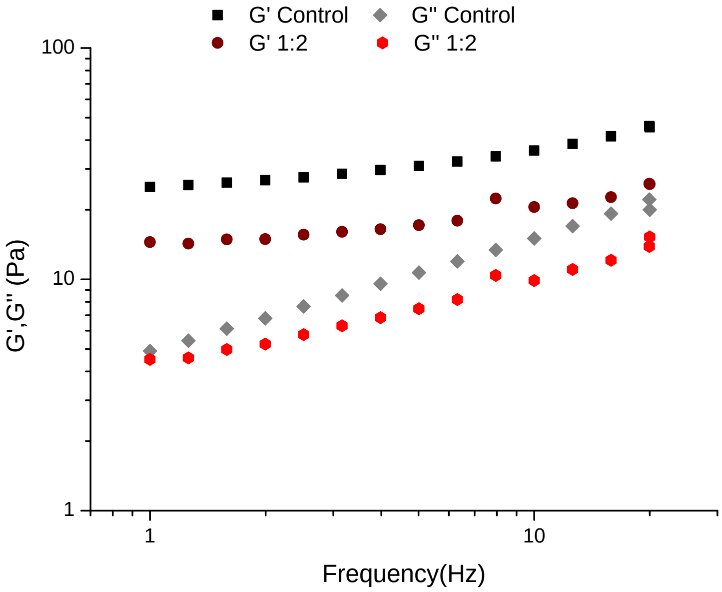

Figure 197 - P_{11}-13/14:GAG elastic and viscous modulus vs. frequency. Starting frequency 1Hz, end frequency: 20 Hz, Strain controlled: 3%, Temp: 25^oC. 2 weeks old.

4.2.6 P_{11}-14:GAG+P_{11}-13 mixing study observations

From the initial mixing studies of GAGs with P_{11}-9 and P_{11}-12, it was found that the best resulting gels were formed by mixing P_{11}-12 with the GAG. This may be due to favourable electrostatic interactions of the positively charged P_{11}-12 with the negatively charged GAG. Therefore, to try to mimic this with the complementary peptides, the GAG was mixed with the positive P_{11}-14 in the monomeric state, and then P_{11}-13 was added as described in section 2.8.1.

P_{11}-14 was mixed with GAG ratios from 1:1 to 1:20, left overnight and then P_{11}-13 in an equimolar ratio to P_{11}-14 was added to the peptide GAG mix. Again, the presence of the GAG chains did not inhibit self-assembly because self-supporting gels were seen at all ratios. However, as the GAG concentration was increased the gel quality differed and became milkier (Figure 198). At a ratio of 1:10, the GAG actually acted as a trigger to self-assembly and a gel was formed even before P_{11}-13 was mixed in. With the presence of the GAG chains, gel formation post P_{11}-13 addition was not as spontaneous as was the case with the control, the gel formed within seconds only upon vortexing and for all samples, further shearing resulted in a viscous liquid, which was again not the case with the control sample.

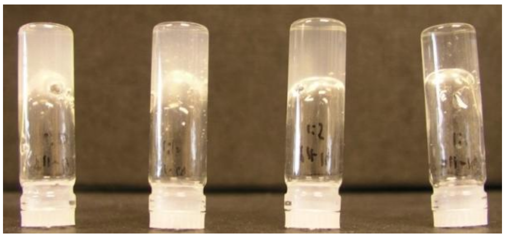

Figure 198 – Day of preparation. From left to right P_{11}-14:GAG+P11-13 1:20, 1:10, 1:5 and 1:1.

Figure 199 - 9 months old. From left to right P_{11}-14:GAG+P_{11}-13 1:20, 1:10, 1:5, 1:1 and P_{11}-13/14 control.

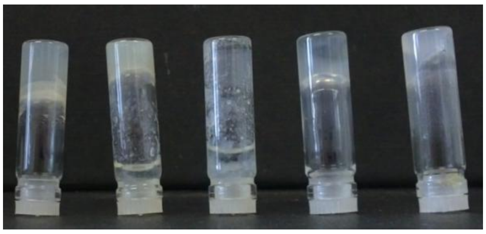

Figure 200 – 1 year and 3.5 months old. From left to right P_{11}-14:GAG+P_{11}-13 1:20, 1:10, 1:5, 1:1 and P_{11}-13/14 control.

After nearly two weeks, all the samples remained as self-supporting gels and were highly birefringent. With the lower GAG concentrations (1:1 and 1:5) the gels did not break apart upon vortexing, whereas with the higher (1:10 and 1:20) concentrations upon vortexing the gels were no longer self-supporting.

After five months, the lower GAG ratios were still self-supporting with the 1:5 ratio providing the best quality gel. As the GAG concentration was increased, the turbidity of the gel increased.

After nine months, the 1:10 ratio was no longer a self-supporting gel but was a liquid with some gel precipitate instead. The 1:20 ratio had some self-supporting gel and some liquid phase (Figure 199).

After approximately 16 months, the control and 1:1 ratios were unchanged, i.e. they were self-supporting gels, although the control was cloudier. The 1:5 ratio was a liquid with some precipitate, whereas the 1:10 was in two phases: one a liquid and one a self-supporting gel. Interestingly, the 1:20 sample had become a self-supporting gel once more (Figure 200).

4.2.6.1 The effect of GAG addition to P_{11}-14/13 on the gel mechanical properties

The rheological properties of P_{11}-14/13:GAG samples were examined and compared to those of P_{11}-14/13 determined in Chapter 3 to establish how the addition of GAG affects the material properties of P_{11}-14/13 gels.

Two GAG ratios (1:2 and 1:10) were chosen from the above mixing study for the rheological testing. The new samples were consistent with those prepared above, showing good reproducibility in the process.

The 1:2 ratio produced a clear, self-supporting gel with a stretchy texture that seemed to flow. The 1:10 sample was very similar to that of P_{11}-13:GAG+14 control in that it had two phases: a thick white gel inside a clear liquid phase. The gel was not self-supporting but was very stretching with an ability to flow. The rheometry was carried out on this gel phase.

First of all, amplitude sweeps were carried out at two frequencies to determine the LVER (Figure 201, Figure 202, Figure 203 and Figure 204).

By comparing the amplitude sweeps for both samples, it was observed that the 1:2 sample had a slightly greater LVER, indicating that higher strains were needed for a breakdown in molecular structure.

From the amplitude sweeps above, a strain value of 0.6% for the 1:2 ratio and 0.7% for the 1:10 ratio were chosen within the LVER to carry out the frequency sweeps. The frequency sweeps were then compared to that of the control (Figure 205).

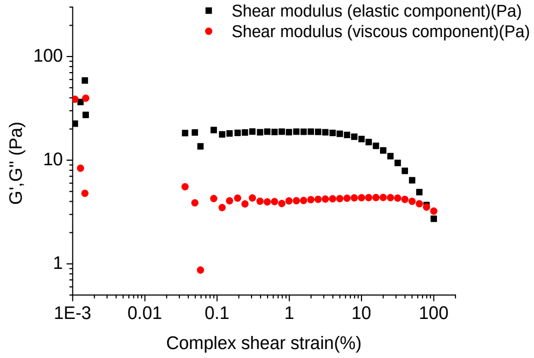

Figure 201 - P_{11}-14:GAG+P_{11}-13 1:2 elastic and viscous modulus vs. shear strain. Starting shear strain 0.01%, end shear strain: 100%, Frequency: 1Hz, Temp 25^{o}C. 2 days old.

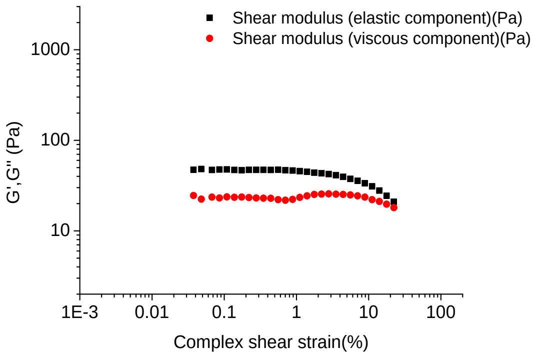

Figure 202 - P_{11}-14:GAG+P_{11}-13 1:2 elastic and viscous modulus vs. shear strain. Starting shear strain 0.01%, end shear strain: 100%, Frequency: 20 Hz, Temp 25^{o}C. 2 days old.

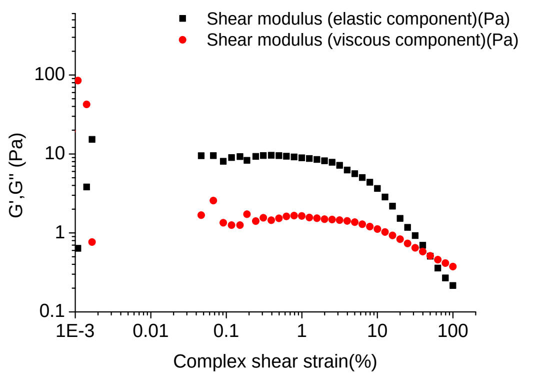

Figure 203 - P_{11}-14:GAG+P_{11}-13 1:10 elastic and viscous modulus vs. shear strain. Starting shear strain 0.01%, end shear strain: 100%, Frequency: 1 Hz, Temp 25^{o}C. 2 days old.

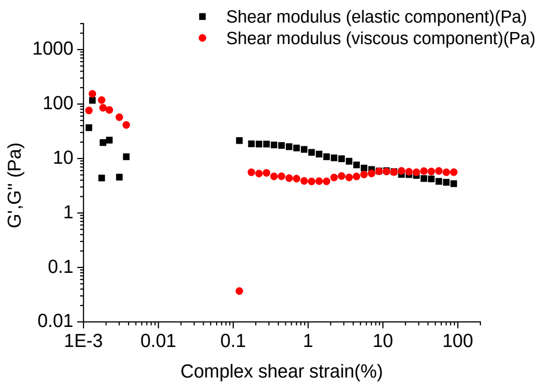

Figure 204 - P_{11}-14:GAG+P_{11}-13 1:10 elastic and viscous modulus vs. shear strain. Starting shear strain 0.01%, end shear strain: 100%, Frequency: 20 Hz, Temp 25^{o}C. 2 days old.

For both ratios, the elastic component was higher than the viscous component suggesting more solid than liquid-like behaviour as was the case with the control. Both samples had viscoelastic solid-like behaviour over the frequency range studied as the phase angle tended towards 0^{o} at rest (1:2 phase angle = $14\text{-}27^{o}$ and 1:10 phase angle = $9\text{-}16^{o}$). With the addition of a small amount of GAG, the moduli decreased resulting in a weaker gel. However, with a larger addition of GAG, the moduli were similar to that of the control. For both samples at low frequencies, the samples were more liquid-like, increasing their stiffness to more solid-like at higher frequencies.

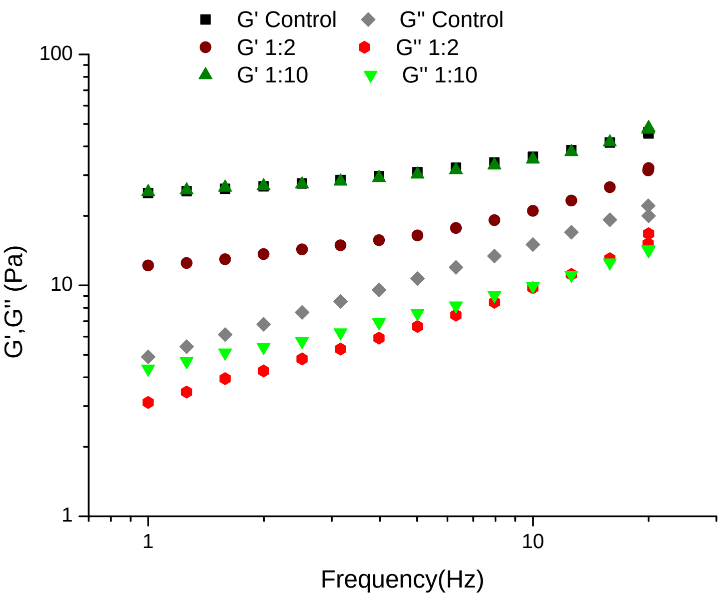

Figure 205 - P_{11}-14:GAG+P_{11}-13 elastic and viscous modulus vs. frequency. Starting frequency 1 Hz, end frequency: 20 Hz, Strain controlled: 3% (control), 0.6% (1:2) and 0.7% (1:10), Temp: 25^{o}C. 2 days old.

4.2.7 P_{11}-13/14 then GAG 1:10

In order to gain a full understanding of the effect of adding GAG to P_{11}-13 and P_{11}-14, the final stage was to add the GAG to an already prepared P_{11}-13 and P_{11}-14 gel.

The P_{11}-13/14 gel was prepared and left overnight (Figure 206). It was then sonicated and vortexed to attempt to break the gel apart. After 15 minutes of sonicating the gel was still self-supporting, but after around 30 seconds of vortexing it became a viscous liquid briefly before returning to the gel state (Figure 207). After the GAG was added, further vortexing was carried out to mix the GAG. Following a minute of vortexing, the clear gel turned into a cloudy viscous liquid (Figure 208). The sample was then left for three days, and was still a viscous liquid; however, at six days the sample was a cloudy self-supporting gel (Figure 209). After 25 days, the gel was still self-supporting; however, there was a very small amount of liquid phase present. At 57 days, the sample was still a cloudy self-supporting gel.

Figure 206 – P_{11}-13/14 gel on day after preparation.

Figure 207 - P_{11}-13/14 gel after sonication.

Figure 208 - P_{11}-13/14 gel after addition of GAG.

Figure 209 - P_{11}-13/14:GAG gel 6 days old.

4.2.8 P_{11}-28+P_{11}-29:GAG

To investigate the effect of adding GAG to an overall positively charged complementary peptide pair, the complementary peptides P_{11}-28 and P_{11}-29 were used. As with P_{11}-13/14, three different process methods were used.

4.2.8.1 *P_{11}-28:GAG+P_{11}-29 Mixing study observations*

P_{11}-28 was mixed with GAG ratios from 1:0.5 to 1:100, left overnight and then P_{11}-29 in a equimolar ratio to P_{11}-28 was added to the peptide GAG mix. The addition of GAG to P_{11}-28 resulted in gelation at very high GAG concentrations (1:100) (Figure 210). After 24 hours, all other ratios were still liquids except for the 1:100, which remained a self-supporting gel.

The addition of P_{11}-29 to the P_{11}-28:GAG samples led to gelation in all cases with the appearance of the gel becoming cloudier with increased GAG concentrations. The gels formed were self-supporting but all, except the 1:100 ratio, were weak gels and would flow down the sample vial within an observable time frame (Figure 211).

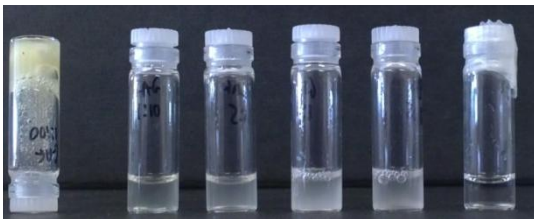

Figure 210 – P_{11}-28:GAG on day of preparation. From left to right 1:100, 1:10, 1:5, 1:2, 1:0.5, control.

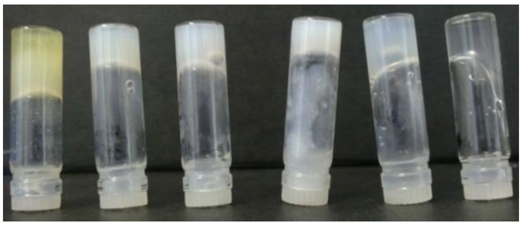

Figure 211 - P_{11}-28:GAG + P_{11}-29 on day of preparation. From left to right 1:100, 1:10, 1:5, 1:2, 1:0.5, control.

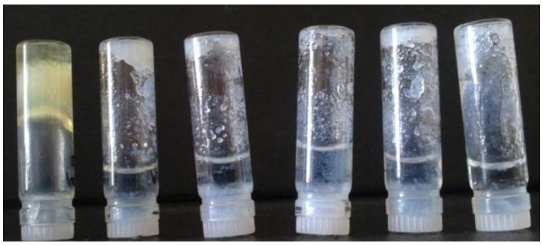

Figure 212 - P_{11}-28:GAG + P_{11}-29 40 days old. From left to right 1:100, 1:10, 1:5, 1:2, 1:0.5, control.

Figure 213 - P_{11}-28:GAG + P_{11}-29 1:100 81 days old.

At 20 days, the gel quality greatly differed with GAG concentration. The control sample was still a self-supporting gel, although some cloudy precipitate was present. At low to medium GAG ratios, the samples were no longer self-supporting gels, they were all liquids with some gel precipitate present on the vial walls. The 1:100 ratio, however, was still a gel, although it was inhomogeneous in colour, with some of the gel clearer than other parts.

After 40 days, the only sample left that was still a gel was the 1:100 ratio, suggesting that all the other gels that were formed were only metastable (Figure 212).

Even after vortexing, and then vortexing and heating, the samples did not reform gels. The 1:100 ratio sample, however, remained a gel even after 80 days (Figure 213), suggesting that at very high GAG concentrations the GAG helped to stabilise the gel formed.

4.2.8.2 The effect of GAG addition to P_{11}-28/29 on the gel mechanical properties.

The rheological properties P_{11}-28/29:GAG samples were examined and compared to those of P_{11}-28/29 determined in Chapter 3 to establish how the addition of GAG affects the material properties of P_{11}-28/29 gels.

Two GAG ratios (1:2 and 1:10) were chosen from the above mixing study for the rheological testing. The new samples were consistent with those prepared above showing good reproducibility in the process.

The 1:2 ratio produced a cloudy self-supporting gel with a small amount of clear liquid phase. It had a slightly gritty texture and was not stretchy (Figure 214).

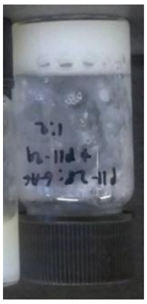

Figure 214 – P_{11}28:GAG + P_{11}-29 1:2 4 days old.

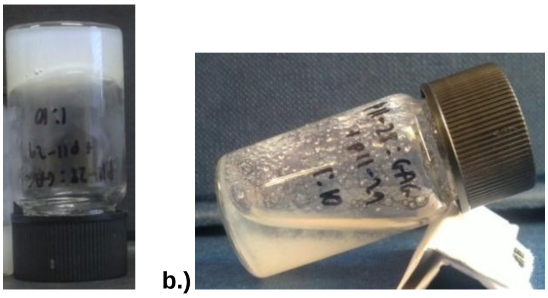

a.) b.)

Figure 215 – P_{11}28:GAG + P_{11}-29 1:10 a.) on day of preparation b.) 4 days old.

The 1:10 sample started as a cloudy self-supporting gel, but after 4 days it turned into a liquid with some precipitate, therefore rheological testing was not carried out on the sample (Figure 215).

First, an amplitude sweep was carried out at two frequencies to determine the LVER (Figure 216 and Figure 217).

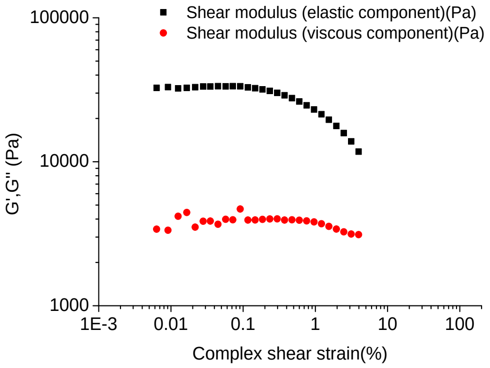

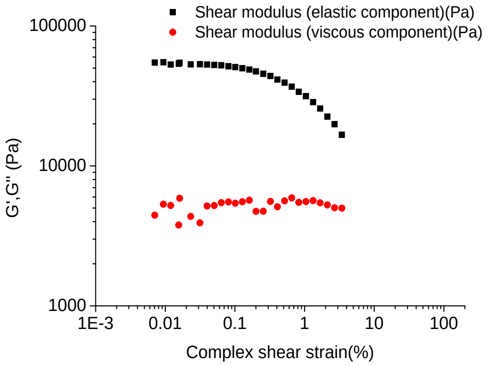

Figure 216 - P_{11}-28:GAG+P_{11}-29 1:2 elastic and viscous modulus vs. shear strain. Starting shear strain 0.01%, end shear strain: 100%, Frequency: 1Hz, Temp 25^{o}C. 4 days old.

Figure 217 - P_{11}-28:GAG+P_{11}-29 1:2 elastic and viscous modulus vs. shear strain. Starting shear strain 0.01%, end shear strain: 100%, Frequency: 20 Hz, Temp 25^{o}C. 4 days old.

From the amplitude sweeps above, a strain value of 0.14% was chosen within the LVER to carry out the frequency sweep. The frequency sweep was then compared to that of the control (Figure 218).

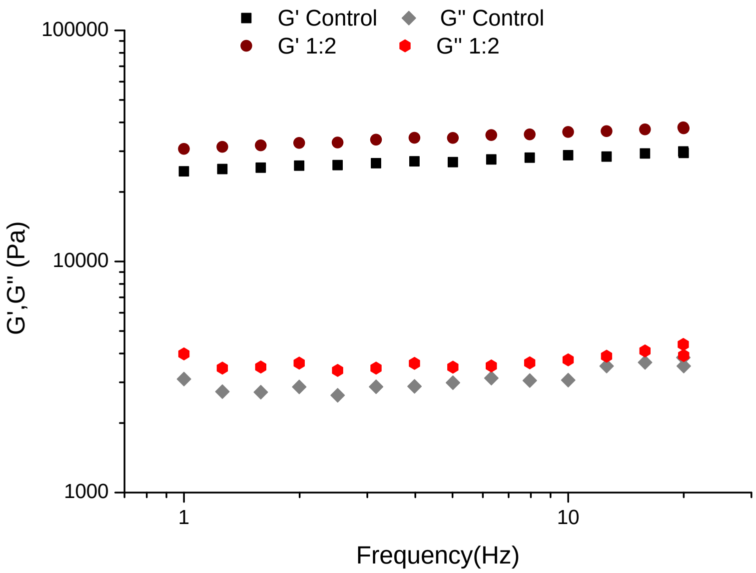

Figure 218 - P_{11}-28:GAG+P_{11}-29 elastic and viscous modulus vs. frequency. Starting frequency 1 Hz, end frequency: 20 Hz, Strain controlled: 0.25% (control), 0.14% (1:2), Temp: 25°C. 4 days old.

From the rheological data, it was observed that the 1:2 ratio had a higher elastic than viscous modulus, therefore it had more solid-like than liquid-like behaviour as was the case with the control. The phase angle for the 1:2 sample was independent of frequency (6°) and so had the material behaviour of a gel. The addition of a small amount of GAG to the sample increased the moduli of the gel slightly i.e. the gel became marginally stiffer.

4.2.9 P_{11}-29:GAG+P_{11}-28 Mixing study observations

P_{11}-29 was mixed with GAG ratios from 1:2 to 1:50, left overnight and then P_{11}-28 in a equimolar ratio to P_{11}-29 was added to the peptide GAG mix. On the day of preparation, the addition of GAG to P_{11}-29 did not result in gelation at any ratio. However, after 24 hours the 1:50 ratio had formed a self-supporting gel (Figure 219).

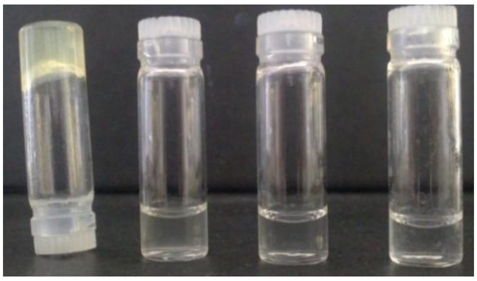

Figure 219 **- P11-29:GAG day after preparation. From left to right 1:50, 1:10, 1:2 and control**

Figure 220 - P_{11}-29:GAG+P11-28 day of preparation. From left to right 1:50, 1:10, 1:2 and control

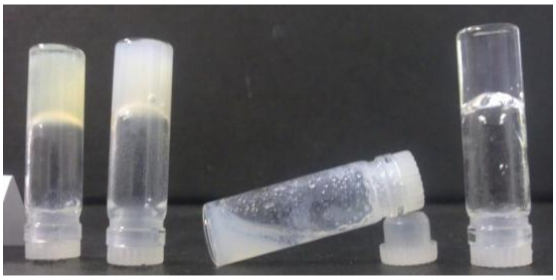

Figure 221 - P_{11}-29:GAG+P_{11}-28 15 days old. From left to right 1:50, 1:10, 1:2 and control.

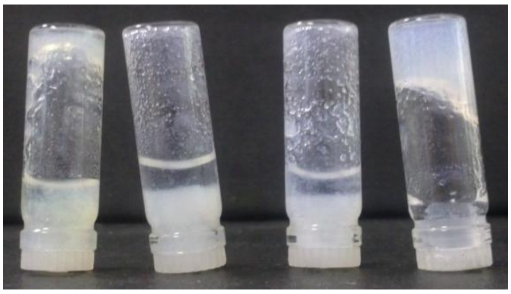

Figure 222 - P_{11}-29:GAG+P_{11}-28 41 days old. From left to right 1:50, 1:10, 1:2 and control.

Upon addition of P_{11}-28 to the samples, they all became self-supporting gels. The cloudiness of the gels increased with increasing GAG concentration (Figure 220).

After six days, all samples appeared as they were on the day of preparation with the transparency of the samples decreasing with increasing GAG. After 15 days, the gel quality differed with differing GAG concentrations, the lowest GAG ratio (1:2) was no longer a self-supporting gel and was instead a liquid with some gel precipitate. The higher GAG ratios however managed to maintain their gel integrity (Figure 221).

After 40 days, the gel quality of all the samples had decreased. The control was no longer clear, but was a cloudy gel: it was still self-supporting, but only weakly as can be observed in Figure 222, where it was flowing down the wall of the vial. All GAG ratios were no longer self-supporting gels, but liquids with gel precipitate: the 1:50 sample still had a small amount of self-supporting gel present (Figure 222).

4.2.9.1 *The effect of GAG addition to P_{11}-13/14 on the gel mechanical properties*

The rheological properties P_{11}-29/28:GAG samples were examined and compared to those of P_{11}-29/28 determined in Chapter 3 to establish how the addition of GAG affects the material properties of P_{11}- P_{11}-29/28 gels.

Two GAG ratios (1:2 and 1:10) were chosen from the above mixing study for the rheological testing. The new samples were consistent with those prepared above showing good reproducibility in the process.

The 1:2 ratio produced a cloudy self-supporting gel with some clear liquid phase (Figure 223).

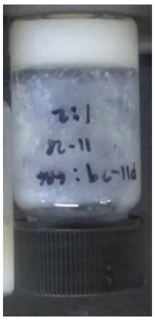

Figure 223 – P_{11}-29:GAG + P_{11}-28 1:2 4 days old.

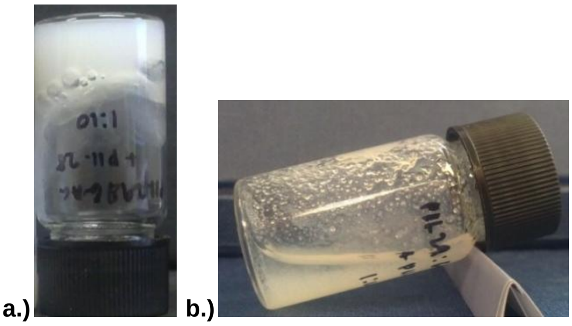

Figure 224 - P_{11}29:GAG + P_{11}-28 1:10 a.) on day of preparation b.) 4 days old.

As in the case of the P_{11}-28:GAG + P_{11}-29 1:2 sample, the P_{11}-29:GAG + P_{11}-28 1:10 started as a cloudy self-supporting gel, but after 4 days it was a liquid with some precipitate, therefore rheological testing was not carried out on the sample. (Figure 224)

First, an amplitude sweep was carried out at two frequencies to determine the LVER (Figure 225 and Figure 226).

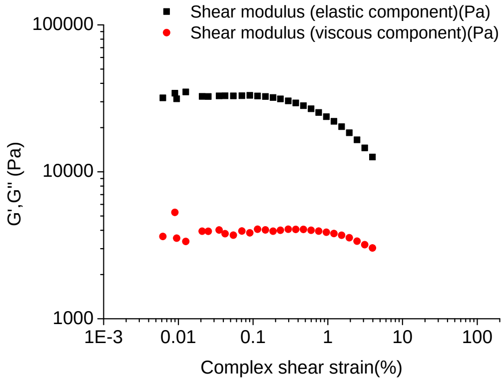

Figure 225 - P_{11}-29:GAG+P_{11}-28 1:2 elastic and viscous modulus vs. shear strain. Starting shear strain 0.01%, end shear strain: 100%, Frequency: 1 Hz, Temp 25^{o}C. 4 days old.

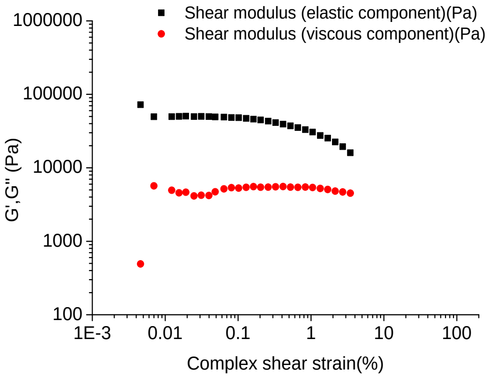

Figure 226 - P_{11}-29:GAG+P_{11}-28 1:2 elastic and viscous modulus vs. shear strain. Starting shear strain 0.01%, end shear strain: 100%, Frequency: 20 Hz, Temp 25^{o}C. 4 days old.

From the amplitude sweeps above, a strain value of 0.16% was chosen within the LVER to carry out the frequency sweeps. The frequency sweep was then compared to that of the control (Figure 227).

From the rheological data it was observed that the 1:2 sample had a higher elastic than viscous modulus, therefore had more solid-like than liquid-like behaviour, just as for the control and the P_{11}-28:GAG+P_{11}29 1:2 sample. The phase angle of the 1:2 sample was independent of frequency (6^{o}) and so had the material behaviour of a gel. The addition of a small amount of GAG to the sample slightly increased the moduli of the gel i.e. the gel became stiffer, even more so than when the GAG was added to the P_{11}-28 peptide first.

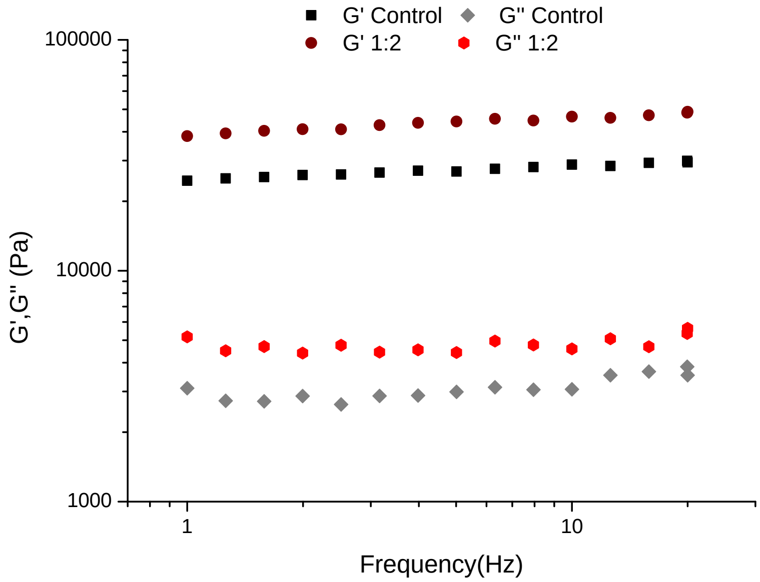

Figure 227 - P_{11}-29:GAG+P_{11}-28 elastic and viscous modulus vs. frequency. Starting frequency 1 Hz, end frequency: 20 Hz, Strain controlled: 0.25% (control), 0.16% (1:2), Temp: 25°C. 4 days old.

4.2.10 P_{11}-28/29 then GAG 1:10

In order to gain a full understanding of the effect of adding GAG to P_{11}-28 and P_{11}-29, the final stage was to add the GAG to an already prepared P_{11}-28 and P_{11}-29 gel.

The P_{11}-28/29 gel was prepared and left overnight (Figure 228). It was then sonicated and vortexed to attempt to break the gel apart: the gel was still self-supporting; however, there were areas of cloudiness visible in the clear gel (Figure 229). After the GAG was added, further vortexing was carried out to mix the GAG. After three minutes of vortexing, the clear gel turned into a cloudy viscous liquid that became a self-supporting gel once more within seconds of ceasing vortexing (Figure 230).

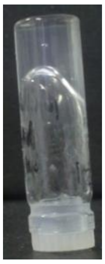

Figure 228 –P_{11}-28/29 gel on day of preparation.

Figure 229 - P_{11}-28/29 gel after sonication to break gel apart.

Figure 230 - P_{11}-28/29 after the addition of GAG on day of preparation.

Figure 231 - P_{11}-28/29:GAG 6 days old.

After six days, the sample was still a self-supporting gel (Figure 231). Even after 57 days, the gel was still self-supporting; therefore this method of preparation led to much more stable gels than mixing the GAG with one of the peptides first before mixing with the other.

4.2.10.1 The effect of GAG addition to P_{11}-28/29 on the gel mechanical properties

The sample prepared for the rheological testing was once again a cloudy self-supporting gel as above, suggesting good reproducibility in the process (Figure 232).

Figure 232 - P_{11}-28/29:GAG 1:10 in PBS 5 days old.

An amplitude sweep was carried out at two frequencies to determine the LVER (Figure 233 and Figure 234).

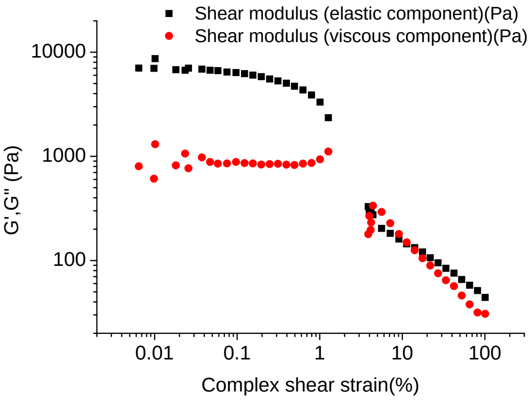

Figure 233 - P$_{11}$-28/29:GAG 1:10 elastic and viscous modulus vs. shear strain. Starting shear strain 0.01%, end shear strain: 100%, Frequency: 1Hz, Temp 25^{o}C. 5 days old.

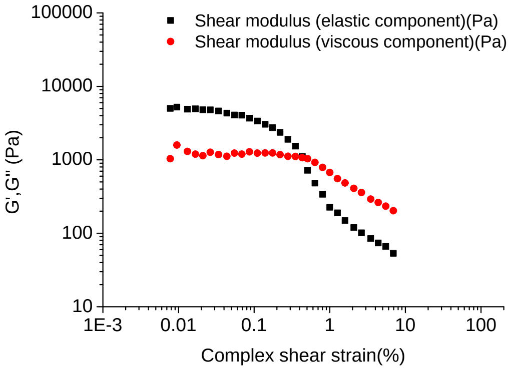

Figure 234 - P$_{11}$-28/29:GAG 1:10 elastic and viscous modulus vs. shear strain. Starting shear strain 0.01%, end shear strain: 100%, Frequency: 20 Hz, Temp 25^{o}C. 5 days old.

From the amplitude sweeps, a strain value of 0.15% was chosen within the LVER to carry out the frequency sweep. The frequency sweep was then compared to that of the control (Figure 235).

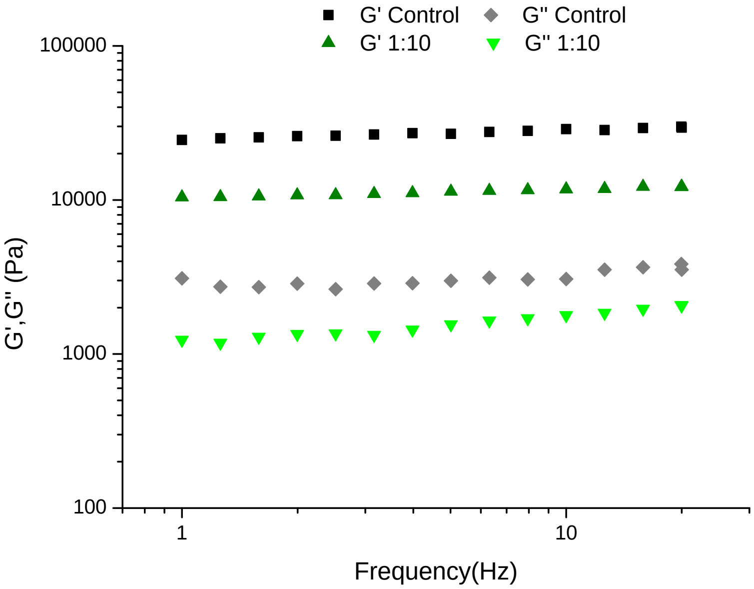

Figure 235 - P$_{11}$-28/29:GAG 1:10 elastic and viscous modulus vs. frequency. Starting frequency 1 Hz, end frequency: 20 Hz, Strain controlled: 0.25% (control), 0.15% (1:10), Temp: 25^{o}C. 5 days old.

As with the other P$_{11}$-28/29:GAG combinations, this sample had a higher elastic than viscous modulus and so was more solid-like than liquid-like. The shape of the plot was typical of that of gel behaviour, which was also confirmed by an average phase angle of 7.9°, which was unaffected by frequency. The moduli were lower than that of the control for the P_{11}-28/29:GAG 1:10 sample, suggesting a weaker gel than the control.

4.3 Discussion

From the evidence gathered so far, it is clear that there is an interaction between the GAG chains and the peptides because an increase in the GAG concentration affects not only the macroscopic properties of the gels formed, but also their microscopic structures.

The presence of a large amount of GAG does not inhibit self-assembly of the P_{11} peptides studied here and in some cases it actually enhanced rather than disrupted it, offering a trigger for gelation. Previous studies by Fraser *et al.* and Gelman and Blackwell have shown that GAGs can facilitate fibril formation and or stabilize aggregates of other β-sheet forming synthetic peptides.[227,228] In particular, the presence of chondroitin sulphates has been found to accelerate random coil to β-sheet transitions as well as prompting morphological changes such as extensive lateral aggregation leading to the formation of large bundles and precipitation of the fibrils.[229,230]

The gelation kinetics of all the peptides in this work were altered depending on the GAG ratio; for example, the addition of GAG to P_{11}-8 decreased the gelation time from days to seconds. P_{11}-9 and P_{11}-12 both had their gelation times reduced from minutes to seconds and even spontaneous gelation was seen in the case of P_{11}-12 at very high GAG ratios. However, with the complementary peptides, the gelation kinetics were slowed with gelation times increasing, for example from spontaneous to days with P_{11}-13/14 then GAG addition.

A modification of viscous moduli, elastic moduli and the resultant lower limit between two nearest entanglements, known as j values, is observed upon GAG addition to the peptides as summarised in Table 18.

For the negative peptides, all samples had a higher elastic modulus than the viscous suggesting solid-like behaviour (Figure 236). With P_{11}-4 and P_{11}-13/14 (not dependant on order of addition), an addition of a small amount of GAG (1:2) led to a decrease in both elastic and viscous modulus suggesting that the peptide alone resulted in a stiffer gel and therefore has a higher number of junction points. For P_{11}-9, the moduli for the 1:2 ratio and the control was similar, however, the 1:2 sample was stretchier. For P_{11}-4 and P_{11}-9, an addition of a large amount of GAG (1:10) resulted in an increase in the elastic and viscous moduli when compared to the control, suggesting a stiffer gel with a larger number of junction points. For P_{11}-14:GAG+P_{11}-13, a large addition of GAG (1:10) resulted in moduli similar to that of the control.

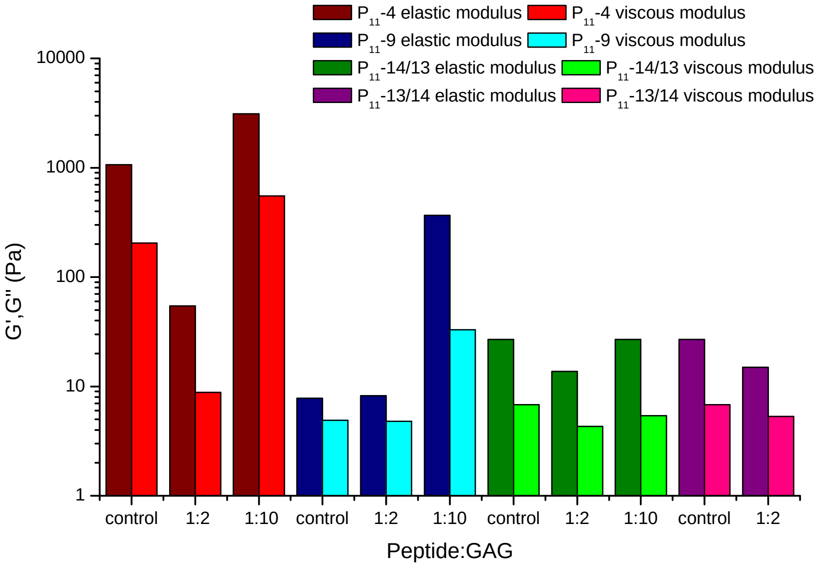

Figure 236 - Elastic and viscous modulus at 2 Hz (walking frequency) for the negative peptides.

Peptide:GAG	**G' (2 Hz) /Pa**	**G'' (2 Hz) /Pa**	**G'^{o}_{N} /Pa**	**Phase angle /^{o}**	**Behaviour from plot shape**	**j /nm**
P$_{11}$-4 control	1065	205.1	-	8.7-17.2	Visco-elastic solid	-
P$_{11}$-4 1:2	54.5	8.8	-	7-14	Visco-elastic solid	-
P$_{11}$-4 1:10	3105	551.4	-	9-13	Visco-elastic solid	-
P$_{11}$-9 control	7.8	4.9	13.3	32.4	Gel	85.2
P$_{11}$-9 1:0.5	8.2	4.8	-	3 - 14	Visco-elastic solid	-
P$_{11}$-9 1:2	5.8	6.2	-	31-40	Visco-elastic solid	-
P$_{11}$-9 1:10	366.4	32.9	379.4	6.3	Gel	27.9
P$_{11}$-8 control	4881	552	5221	7.6	Gel	11.6
P$_{11}$-8 1:2	42350	4931	45369	7	Gel	5.7
P$_{11}$-8 1:10	201	28	229	9.2	Gel	33
P$_{11}$-12 control	20510	3067	22285	9	Gel	7.17
P$_{11}$-12 1:0.5	21600	2626	22874	6.8	Gel	7.11
P$_{11}$-12 1:2	13960	1895	15463	7.4	Gel	8.1
P$_{11}$-12 1:10	11320	1407	12195	8	Gel	8.77
P$_{11}$-12 1:100	2471	2435		39-55	Unkown	-
P$_{11}$-13/14 control	26.8	6.8	-	11-23	Visco-elastic solid	-
P$_{11}$-13:GAG +P$_{11}$-14 1:2	14.9	5.3	-	17-30	Visco-elastic solid	-
P$_{11}$-14:GAG +P$_{11}$-13 1:2	13.7	4.3	-	14-27	Visco-elastic solid	-
P$_{11}$-14:GAG +P$_{11}$-13 1:10	26.9	5.4	-	9-16	Visco-elastic solid	-
P$_{11}$-28/29 control	25980	2864	27302	6.5	Gel	6.7
P$_{11}$-28:GAG +P$_{11}$-29 1:2	32580	3631	34532	6.2	Gel	6.2
P$_{11}$-29:GAG +P$_{11}$-28 1:2	41010	4402	43837	6.3	Gel	5.7
P$_{11}$-28/29 then GAG 1:10	10750	1347	11307	7.9	Gel	9

Table 18 - Summary of all peptide and peptide:GAG rheological data.

The addition of a small amount of GAG to the positive peptides P_{11}-8 and P_{11}-28/P_{11}-29 (not dependent on order of addition) resulted in an increase of the moduli when compared to the control, suggesting a small addition of GAG led to a stiffer gel with a greater number of entanglements. However, with P_{11}-12, a small addition of GAG led to a weaker gel. With all positive peptides, an addition of a larger GAG concentration (>1:10) led to a weaker gel than that of the control with fewer entanglements (Figure 237).

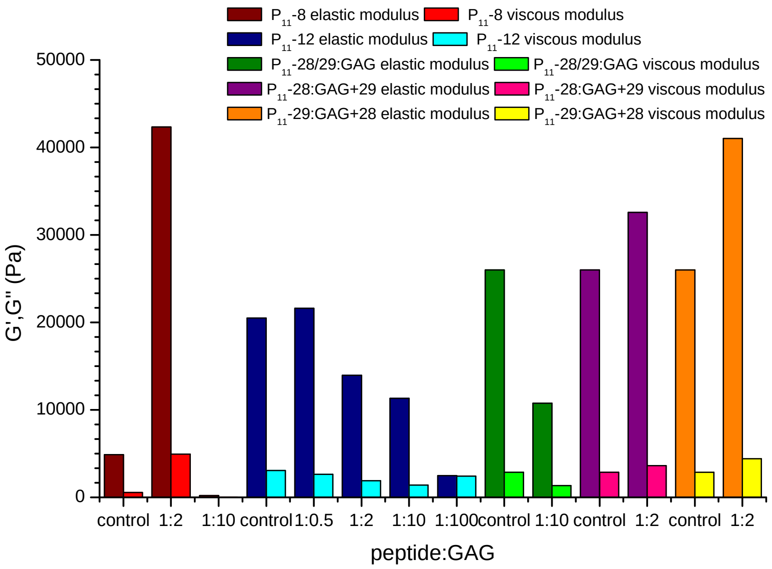

Figure 237 - Elastic and viscous modulus at 2 Hz (walking frequency) for the positive peptides.

The elastic modulus, or the stiffness of a material, is related to the number of junction points and the number of junction points is dependent on the:

- density of chains;
- width and length of chains;
- “cross linking” affinity at the junction points.

Therefore, if any of these three factors are altered, then G’ will be altered. The largest increase in elastic modulus due to an addition of GAG compared to the control was with P_{11}-8:GAG 1:2, which saw an increase of nearly 40,000 Pa. The largest decrease in elastic modulus due to the presence of GAG was with P_{11}-12:GAG 1:100, which saw a reduction of nearly 20,000 Pa. Various mechanisms for interactions between the peptides and GAGs can be considered to explain the increase or decrease in junction points, and therefore ultimately G’, such as those detailed in Figure 238.

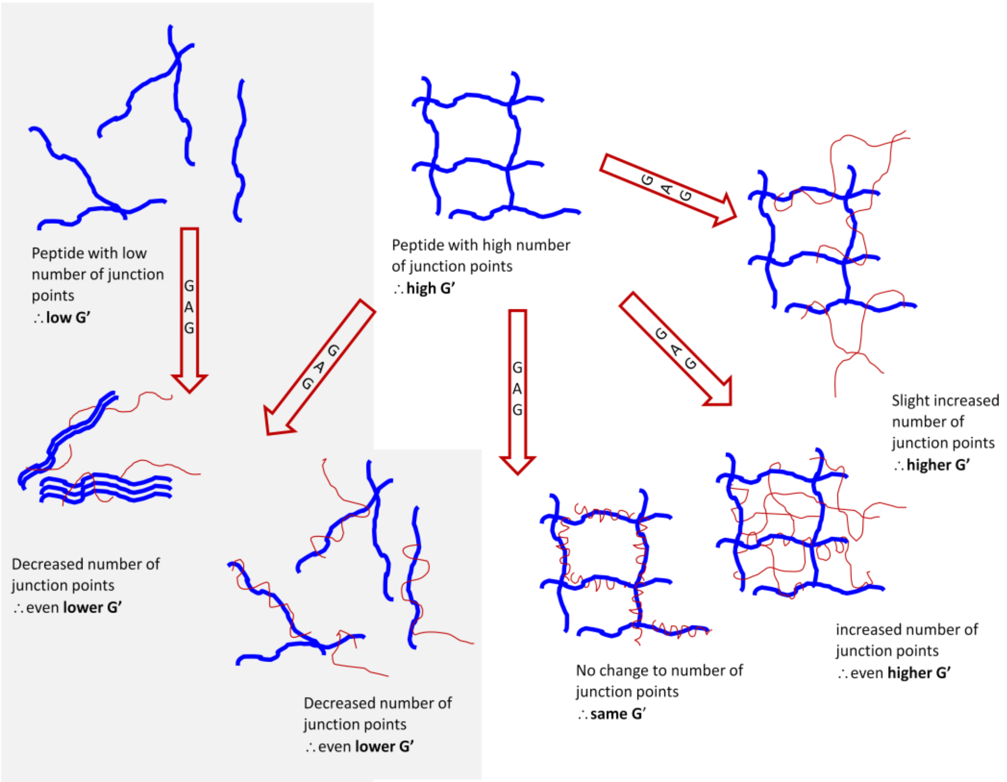

Figure 238 – Hypothesised mechanisms for peptide:GAG interactions.

It is thought that the negative GAG chains interact with the positive peptides via ionic bonding in a way similar to that demonstrated in the schematic diagram of Figure 239.

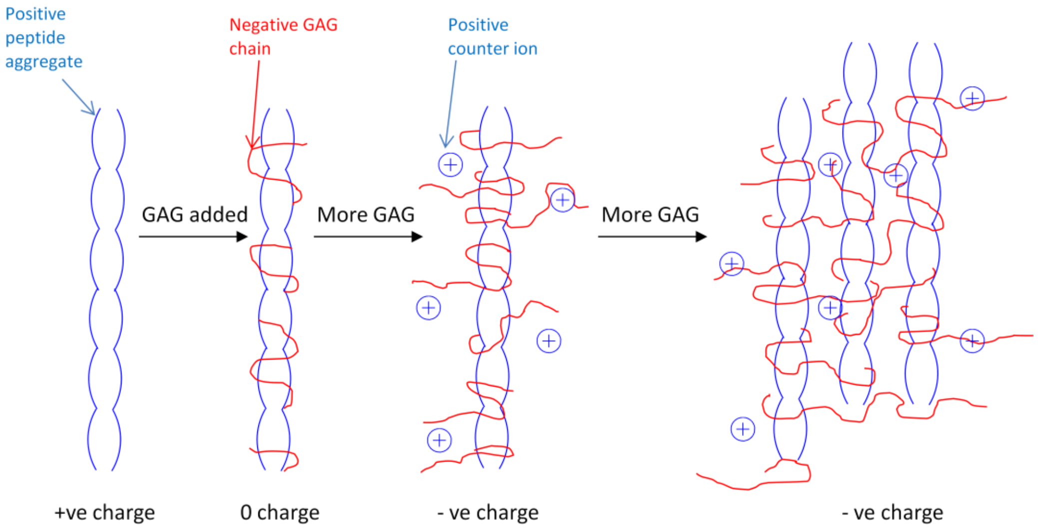

Figure 239 - Schematic diagram of possible GAG and P_{11}-12 interactions.

At the lower GAG ratios, a small amount of GAG mixes with the peptide and the negative charge of the GAG balances the positive charge of the peptide causing an overall neutral charge, which in physiological solutions results in a precipitated aggregated self-assembled state. As the GAG ratio is increased, the overall positive charge of the peptide becomes negative as the GAG chains wrap around the peptide exposing excess negative charges on the surface. Finally, at the highest GAG concentrations, as seen under the TEM for P_{11}-12, all the individual peptide chains become massive bundles, therefore the density of chains is decreased resulting in few junction points and a lower G'.

It is thought that the negative GAG chains interact with the negative peptides via positive ions acting as salt bridges in a way similar to that demonstrated in the schematic diagram of Figure 240.

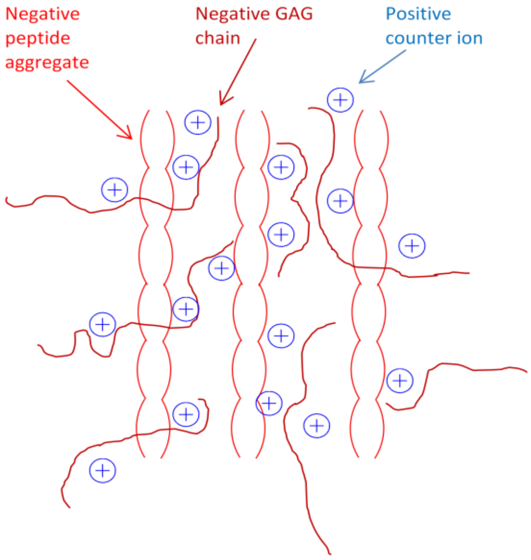

Figure 240 - Schematic diagram of possible GAG and P_{11}-9 interactions.

As the GAG concentration increases, these structures become larger, therefore increasing the turbidity of the gels as well as larger but fewer fibrillar bundles, as seen in the TEM images for P_{11}-9.

An interesting property that arose in some of the peptide:GAG gels was that there was a conversion from a rigid, brittle material to a stretchy material, due to an interaction between the rigid peptide and the flexible GAG chains. This was the case with an addition of a small amount of GAG (1:2) to P_{11}-9 and a large addition of GAG (1:100) to P_{11}-12.

One area that needs to be probed further is the exact intermolecular interactions between the peptides and GAGs and how this varies with polar residues. This may help to explain further the differing observed mechanical properties. It may be that, in addition to the differences in electrostatic interactions, the OH groups of the GAGs hydrogen bond with the hydroxyl group of the serine side chains better than with the amide group of the glutamine side chains. Also, the large glutamine side chains may provide more steric hindrance to the charged residues of the peptide, weakening the electrostatic interactions between the two charged biopolymers (Figure 241).

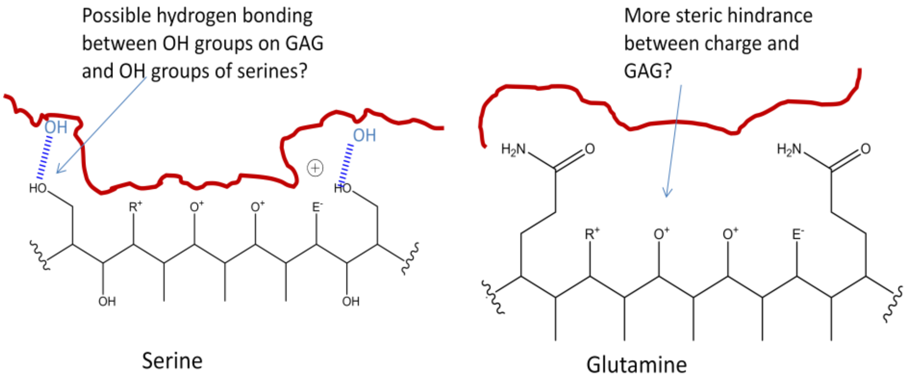

Figure 241 – Potential intermolecular interactions between serine and glutamine based peptides and GAGs.

A study on the effect of amino acid substitutions on peptide-GAG binding was carried out by McLaurin *et al*. [227] They suggested that GAG binding was more sensitive to changes in the secondary structure of the peptide than a loss of basic residues.[227] This suggests that there may be more than just ionic interactions involved, such as hydrogen bonding and van der Waals packing. These non-ionic interactions may also be another mechanism for interaction of the negatively charged peptides with the negatively charged GAG chains.

4.4 Summary

Here, work has been carried out into the formation of a new peptide hybrid material consisting of a mix of charged peptide and charged GAG chains. A systematic mixing study was carried out to determine the effect of the presence of GAG chains on peptide self-assembly and gel properties as a function of GAG concentration. The addition of GAG chains not only provided the high charge found in the natural tissue, mimicking the biological function of the nucleus pulposus, but also at an optimum ratio improved the self-assembling and rheological properties of the resulting gels.

At certain ratios, the GAG biopolymer was found to act as a trigger for self-assembly for all the single peptides apart from P_{11}-13 and P_{11}-28. The gelation kinetics were also enhanced; for example, for P_{11}-8, the gelation time was reduced from days to seconds.

The GAG also acted as an additive, improving the rheological gel properties and, in some cases, altering the gel stiffness of the peptides to that resembling the natural tissue. In particular, GAG inclusion decreased the gel stiffness of the positively charged peptides at high GAG concentrations but slightly increased the stiffness at low GAG concentrations. By contrast for the negatively charged peptides, gel stiffness was increased at high GAG concentrations, but the stiffness values were still lower overall than that for the positive peptides. An increase or decrease in the stiffness of the gels is a direct result of an increase or decrease in the number of junction points. In some cases the GAG chains not only provided junction points, but they also made the gels stretchier most likely due to the GAGs acting as flexible crosslinkers.

The order of mixing was found to be important when using the complementary peptides. By adding the GAG after the two peptides were mixed together, the best quality gels were formed. Mixing the positive peptide with the GAG before addition of the negative peptide seemed to produce more favourable gels than preparation vice versa.

In summary, new peptide:glycosaminoglycan hybrid materials have been developed with built-in triggerabilty and controllable mechanical properties. By the incorporation of chondroitin-6-sulphate and by choosing a ratio that provides the correct stiffness, the new material is anticipated to aid in the restoration of the mechanical and osmotic properties of disc post nucleus replacement. The ability of the peptide to maintain the GAG inside the disc alongside the ability of the gels to restore the biomechanics of the disc will be investigated in a preliminary study in the next chapter.

Chapter 5

5 Application of peptide/glycosaminoglycan hydrogels for nucleus pulposus replacement

5.1 Introduction

The ultimate goal for a nucleus pulposus replacement therapy is to maintain the motion and load bearing abilities of the functional spinal unit and prevent adjacent disc degeneration. Current total disc replacements aid in the preservation of some natural motion as well as disc height but, unlike the natural tissue, they are highly rigid because their composition is mostly metallic and high density polymeric components.[231] In 2005 the Orthopaedic and Rehabilitation Devices Advisory Panel of the US Food and Drug Administration (FDA) proposed that the introduction of less invasive surgical procedures earlier in the lumbar degenerative disease cascade could defer the need for fusion or disc replacements.[232]

Tissue engineered intervertebral disc (IVD) replacements are one option, with the intent to replace the degenerated tissue with a functional scaffold that promotes the growth of new healthy tissue. However, due to the lack of vascular network within the tissue, cells within the matrix can be 5 mm from the nearest blood supply. The disc is also oxygen and glucose deficient and has lower pH levels and higher osmolarity than found in most normal physiological tissues. Calcification of the endplate cartilage and degeneration of the underlying bone are common in disc degeneration and minimise nutrient and solute transport even further.[233] Even in a healthy natural disc, the cell density is low with the majority of the tissue consisting of the extra cellular matrix (ECM).[9] Therefore, another option for a successful treatment may be the use of a hydrogel that mimics the biological and mechanical function of the nucleus pulposus ECM, and that can be injected through the annulus fibrosus. As discussed in Chapter 1, there are a number of requirements for such a hydrogel. These include the need for the gel to have similar mechanical properties to the healthy nucleus so that it can restore the functional behaviour. The gel also needs to be injectable and undergo gelation *in-situ*.

Collagen gels have proven to restore disc height and some of the mechanical properties in bovine animal models.[231,234] Polyvinyl alcohol (PVA) and polyvinyl pyrrolidone polymer hydrogels have also been found to restore the compressive stiffness of denucleated discs when compared with equivalent conditions of the IVD.[235] However, one issue with injectable hydrogels is their propensity to leak out of the injection site before completely curing/gelling. There is also some controversy surrounding whether a puncture to the annulus fibrosus can cause further or accelerated degeneration. This has mainly come from concerns surrounding the diagnostic procedure of discography, where a needle is inserted into the nucleus pulposus and then a radiocontrast dye is injected into the disc to aid in morphologic analysis of the disc. There are currently no conclusions as to whether the increased degeneration observed in some cases is due to the puncture wound, to the cytotoxity of the injected reagents or the increased nucleus pressurisation.[236,237] Several studies have shown that the size of the needle compared to the relative size of the disc is important when assessing whether the puncture actually results in degeneration, with the smaller needles causing less perturbation of the annulus fibres.[238-241] A 16 G needle has been found to consistently cause degenerative changes, whereas needles of 18 G and higher were deemed to not cause predictable degeneration, with a 25 G needle and above causing minimal to no damage. [238,240-242]

In this chapter, a series of preliminary tests were undertaken using an ex-vivo model to investigate the potential of the peptide gels presented in the previous chapters to satisfy the basic mechanical and leakage-resistant requirements for a nucleus augmentation material.

The peptide:GAGs developed in Chapter 4 were designed to be injected as liquids and form a gel upon mixing *in situ*. This would enable injection through a narrow gauge needle, reducing damage to the annulus fibrosus and minimising the potential leakage. In this chapter, an investigation of GAG leakage through the disc was undertaken. The presence of the GAG in the new gel is key to restoring the swelling pressure and allowing the new gel to as closely mimic the natural tissue as possible. This would also be another tool for assessing how well the peptides interact with the GAG chains.

The intervertebral disc plays an important role in spinal biomechanics with the nucleus pulposus combined with the annulus fibrosus transmitting load and allowing motion. The disc is, in itself, aneural, and as the disc degenerates it is thought to be the change in biomechanics that can ultimately lead to patient pain. Therefore, it is vital to assess the biomechanical performance of any intervention. As a first step, the aim of the second study in this chapter was to investigate the capacity of the hydrogels to support static load in a denucleated disc model.

5.2 Peptide selection

In order to select the most likely candidates for a successful treatment from the hydrogels developed in the previous chapters, the advantages and disadvantages of each gel are compared in Table 19.

The ideal peptide:GAG hydrogel should have:

- a low c*, resulting in a low level of background monomer present and therefore minimising potential leakage from the treatment site;
- a trigger so that the gelation occurs *in situ* post injection;
- a similar gel stiffness to that of the natural nucleus pulposus;
- a short gelation time;
- a high GAG content;
- and good gel stability/lifetime.

The P_{11}-12:GAG 1:2 and 1:10 gels were chosen as the optimum at this stage because they had good gel stability, a similar elastic modulus to that of the natural tissue (Human G’ = 10 kPa, G’’ = 4.5 kPa)[243] and *in situ* gelation was possible due to a trigger in the form of the GAG addition. P_{11}-12:GAG 1:100 with its high GAG content was also considered because the osmotic swelling caused by the GAGs is a critical load-bearing mechanism in the natural tissue.[244]

Parallel to the work carried out in this project the biocompatibility of various P_{11} peptides has been examined. P_{11}-12 gels at 30 mg/ml have been assessed for their contact cytotoxity, and were found to be non-cytotoxic to L929 murine fibroblast cells,[117] i.e. the cells grew up to and in contact with the peptide gel. ISO standard extract cytotoxicty testing was also carried out using BHK and 3T3 cell lines and, again, P_{11}-12 was found to be non-toxic. This test is particularly useful as it examines the toxicity of anything that may have leached off the gels, e.g. monomers or soluble aggregates. In addition to this, P_{11}-12 gels have been found to be non-haemolytic to ovine red blood cells, to not have any effect on thrombus formation, and to have no inhibitory effect on complement activation, i.e. they don't cause red blood cells to rupture, they don't prevent or cause blood clotting, and they do not inhibit any natural immune responses (*Robert Guilliatt personal communication*).

Peptide	c* (μM)	c*$_{gel}$ (μM)	GAG ratio	Time to gel 20 mg/ml	Gel lifetime 20 mg/ml	G' at 2 Hz 20 mg/ml	G'' at 2 Hz 20 mg/ml	Trigger	Gel appearance	Main pros	Main cons
P$_{11}$-9	1160 ±175	4500 ± 1500	control	minutes	>1yr 4mths	8 Pa	5 Pa	pH	Clear self-supporting gel	Gel stability	Weak gel
			1:2	seconds	>1yr 4mths	8 Pa	5 Pa	GAG addition	Cloudy self-supporting gel	GAG triggers gelation	Weak gel
			1:10	Seconds	>1yr 4mths	366 Pa	33 Pa	GAG addition	Cloudy self-supporting gel	Gel strength increases with higher GAG	Weak gel
P$_{11}$-4	310 ± 140	2000 ± 600	control	mins-hours	>1mth	1,065 Pa	205 Pa	GAG addition	Slightly cloudy self-supporting gel	Low c*	Long gelation time
			1:2	secs-mins	>20 days	55 Pa	9 Pa	GAG addition	Cloudy self-supporting gel		Decrease in gel strength
			1:10	seconds	>20 days	3,105 Pa	551 Pa	GAG addition	Cloudy white self-supporting gel	Increase in gel strength GAG triggers gelation	
P$_{11}$-12	5600 ± 1750	2300 ± 750	control	minutes	>1yr 11mths	20,510 Pa	3067 Pa	GAG addition	Cloudy self-supporting gel	Gel stability Gel strength	High c*
			1:0.5	minutes	>1yr 5mths	21,600 Pa	2,626 Pa	Same as control	Slightly cloudy self-supporting gel	Gel strength slightly increases with small amount of GAG	

Peptide	c* (μM)	c^*_{gel} (μM)	GAG ratio	Time to gel 20 mg/ml	Gel lifetime 20 mg/ml	G' at 2 Hz 20 mg/ml	G'' at 2 Hz 20 mg/ml	Trigger	Gel appearance	Main pros	Main cons
P$_{11}$-12			1:2	seconds	>1yr 5mths	13,960 Pa	1,895 Pa	GAG addition	Cloudy bitty gel	Strong gel GAG triggers gelation Good gel lifetime	
			1:10	seconds	>4 mths	11,320 Pa	1,407 Pa	GAG addition	Cloudy self-supporting gel	Strong gel GAG triggers gelation	Gel strength decreases with higher GAG addition
			1:20	spontaneous	>6.5 mths	-	-	GAG addition	Cloudy self-supporting gel	Spontaneous gelation	
			1:50	spontaneous	>6.5 mths	-	-	GAG addition	Cloudy self-supporting gel	Spontaneous gelation	
			1:100	spontaneous	>6.5 mths	2,471 Pa	2,435 Pa	GAG addition	Cloudy self-supporting gel	High GAG content Spontaneous gelation	
P$_{11}$-8	400 ± 100	2000 ± 600	control	days	Still some self-supporting gel at 90 days but also liquid phase	4,881 Pa	552 Pa	GAG addition	Bitty cloudy self-supporting gel with some liquid phase	Poor gel lifetime	Long gelation
			1:2	seconds	>90 days	42,350 Pa	4,931 Pa	GAG addition	Cloudy self-supporting gel slightly bitty	Increased gel life Increased gel strength	Gel may be too stiff

Peptide	**c* (μM)**	**c^*_{gel} (μM)**	**GAG ratio**	**Time to gel 20 mg/ml**	**Gel lifetime 20 mg/ml**	**G’ at 2 Hz 20 mg/ml**	**G’’ at 2 Hz 20 mg/ml**	**Trigger**	**Gel appearance**	**Main pros**	**Main cons**
P_{11}-8			1:10	seconds	>90 days	201 Pa	28 Pa	GAG addition	Cloudy self-supporting gel	Increased gel life	Decreased gel strength
P_{11}-13/14	28 ± 7	350-680	control	spontaneous	>10 mths	27 Pa	7 Pa	Peptide mixing	Clear self-supporting gel	Low c* Fast gelation	Weak gel
			1:2	spontaneous	> 30 days	15 Pa	5 Pa	Peptide mixing	Clear self-supporting gel →cloudy over time	Fast gelation	Decreased gel strength
			1:10	spontaneous	> 30 days	-	-	Peptide mixing	Cloudy self-supporting gel	Fast gelation	
			1:20	seconds	>10 mths	-	-	Peptide mixing	Cloudy self-supporting gel	Fast gelation	Decreased gel time
P_{11}-14/13			1:2	seconds	>9 mths <1yr 4 mths	14 Pa	4 Pa	Peptide mixing	Cloudy self-supporting gel	Fast gelation	Decreased gel time
			1:10	seconds	<9 mths	27 Pa	5 Pa	GAG addition	Cloudy self-supporting gel	Fast gelation	Decreased gel life Decreased gel time
			1:20	seconds	>1yr 4mths	-	-	GAG addition	Cloudy self-supporting gel	Fast gelation	Decreased gel time
P_{11}-13/14 then GAG			1:10	3-6 days after GAG addition	>60 days	-	-	No trigger GAG added to gel	Cloudy self-supporting gel		Inhibits gelation Not injectable

Peptide	c* (μM)	c*$_{gel}$ (μM)	GAG ratio	Time to gel 20 mg/ml	Gel lifetime 20 mg/ml	G’ at 2 Hz 20 mg/ml	G’’ at 2 Hz 20 mg/ml	Trigger	Gel appearance	Main pros	Main cons
P$_{11}$-28/29	29 ± 11	300-600	control	spontaneous	>15 <41 days	25,980 Pa	2864 Pa	Peptide mixing	Cloudy self-supporting gel	Low c* Fast gelation Strong gel	Poor gel lifetime
			1:2	mins	<20 days	32, 580 Pa	3,631 Pa	Peptide mixing	Cloudy self-supporting gel	Increased gel strength	Lengthened gelation time Decreased gel life
			1:10	secs	4 days	-	-	Peptide mixing	Cloudy self-supporting gel	Fast gelation	Lengthened gelation time Decreased gel life
			1:100	spontaneous	>4 mths	-	-	GAG addition or peptide mixing	Cloudy yellow gel	Increased gel life	
P$_{11}$-29/28			1:2	secs	<15 days	41,010 Pa	4,402 Pa	Peptide mixing	Cloudy white gel	Increased gel strength	Lengthened gelation time Decreased gel life
			1:10	secs-mins	4 days	-	-	Peptide mixing	Cloudy white gel		Lengthened gelation time Decreased gel life

Peptide	c* (μM)	c*$_{gel}$ (μM)	GAG ratio	Time to gel 20 mg/ml	Gel lifetime 20 mg/ml	G' at 2 Hz 20 mg/ml	G'' at 2 Hz 20 mg/ml	Trigger	Gel appearance	Main pros	Main cons
P$_{11}$-29/28			1:50	spontaneous	>15 <41 days	-	-	GAG addition or peptide mixing	Cloudy yellow gel	Fast gelation	
P$_{11}$-28/29 then GAG			1:10	secs	>60 days	10, 750 Pa	1,347 Pa	No trigger GAG added to gel	Cloudy self-supporting gel	Increases gel life	Decreases gel strength Not injectable

Table 19 – Peptide:GAG summary

5.3 Materials and methods

5.3.1 Specimens

Ethical issues in using healthy juvenile human spinal segments for basic research required an alternative to be sought for testing. The selection of animal models to evaluate disc treatment methods is based on several factors - such as size, cost, disc geometry, biochemistry, cellularity, and biomechanics - with the choice ultimately being down to the question being asked.[245] For this study, bovine caudal discs were considered to be an adequate replacement, as those from C1 to C6 are representative of the size, biochemical makeup and elastic fibre organisation of healthy young human discs.[7,246,247] Bovine discs have previously been used in numerous studies as a source of disc tissue and were deemed an appropriate model for initial investigations because they would allow comparison with the 'healthy' state, which ideally the treatment would attempt to replicate.[20,248-255] Further to this, the relatively narrow age band of the specimens gave greater homogeneity in terms of size and material properties, reducing the inter-specimen variation.

Bovine tails were harvested from calves aged less than 30 months (typically 24-28 months) at a local abattoir. The specimens were transported to the laboratory and sealed in plastic bags within three days of slaughter. To avoid potential damage to the tissue, the discs were maintained at 2-8^{o}C prior to experimentation and were not frozen. The caudal discs were isolated from the tail and used experimentally.

5.3.2 Chondroitin-6-sulphate leakage study

5.3.2.1 Background

As a first step, the aim of this study was to investigate GAG leakage from the intervertebral disc through the annulus fibrosus and injection hole under zero load.

In order to quantify the GAG leakage from the discs the 1,9 dimethylmethylene blue (DMMB) assay was employed, which takes advantage of a colour change in the dye that can be monitored spectroscopically upon GAG and dye binding. Until the early 1980s, most assays for proteoglycans either measured carbohydrate constituents of the glycosaminoglycans, such as hexuronate or hexosamine, or measured the binding of cationic dyes to the glycosaminoglycan polyanionic moieties of the proteoglycans. However, in 1986, Farndale *et al*. developed a rapid spectrophotometric assay for proteoglycans based on the reaction of glycosaminoglycans with the DMMB dye.[256] This method was subsequently automated by Sabiston et al.[257] The assay using DMMB takes advantage of the metachromatic phenomenon[258] of GAGs and is more sensitive than that of alcian blue,[259] which is commonly used to stain for GAGs in histology.

The DMMB assay is now commonly used for the quantification of glycosaminoglycans in biological samples, from the measurement of sulphated glycosaminoglycan concentrations in synovial fluid to their measurement in cell cultures [260-263]

5.3.2.2 *Ex vivo model preparation*

Upon receipt of the specimens, the caudal intervertebral discs (C1-C6) were extracted with only the distal endplate still attached. They were placed in monosodium citrate solution (1.98g $NaHCO_3$, 3.93g $C_6H_8O_7$, 1000 ml distilled H_2O, pH adjusted to 7.4 (Jenway 3510 pH meter)) for 20 minutes to remove excess blood and through swelling pressures help differentiate the nucleus pulposus from the annulus fibrosus tissue. The discs were then removed from the solution and the nucleus pulposus tissue was excised. The disc and nucleus tissue were weighed prior to and post removal (Figure 242) (APPENDIX F).

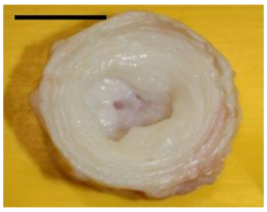

Figure 242 - Disc post nucleus pulposus removal. Scale bar = 10 mm.

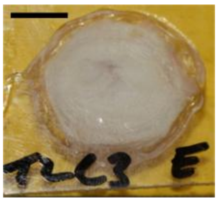

Figure 243 - Disc post endplate attachment. Scale bar = 10 mm.

The discs were then attached to lightly sanded artificial Perspex endplates (2x40x40 mm) using the adhesive Loctite 3090 (Henkel, Hatfield, United Kingdom) (Figure 243).

During analysis, special consideration must be given to the initial disc location, as the amount of GAG present naturally decreases from the proximal to distal caudal discs, i.e. C6 has less GAG present than C1.[264] Also, the size of the disc itself will give rise to different volumes of nucleus. The experiment was designed so that a range of discs were selected from C1 to C6 over the six tails, so that when an average was taken the effects of the change in background GAG content and disc size would be minimised.

The natural GAG leakage through the AF of discs with intact NP and denucleated NP were compared to that of denucleated discs with additional CS added. In turn, the presence of P_{11}-12 was investigated to determine whether this affected the added CS leakage.

For each GAG or P_{11}-12:GAG ratio investigated, discs were chosen from more than one tail over the range of C1 to C6 to try to eliminate variables in disc size, natural GAG levels and tail health. For each group studied, a control of no GAG injection to a denucleated disc was used to determine the average natural GAG leakage over all six tails. The exact tails and discs used for each group are listed in Table 20.

Group	**Tail and disc used**								
no injection	T1C1	T2C3	T1C5	T3C1	T4C3	T3C5	T5C1	T6C3	T5C5
1:2 GAG only injection	T2C1	T1C3	T2C5						
1:10 GAG only injection	T1C2	T2C4	T1C6						
1:100 GAG, CS added as dry powder and PBS injection	T4C2	T3C4	T4C6						
1:100 P_{11}-12:GAG, CS added as dry powder and P_{11}-12 injection	T3C2	T4C4	T3C6						
1:10 P_{11}-12:GAG injection	T4C1	T3C3	T4C5						
1:100 GAG, added as a gel	T5C2	T6C4	T5C6						
1:100 P_{11}-12:GAG, added as a gel	T6C2	T5C4	T6C6						
Natural NP placed back into disc	T6C1	T5C3	T6C5						

Table 20 - Tail and discs used for each group (T = tail, C = caudal disc), 1:n GAG only = the same amount of GAG there would be in a 1:n ratio peptide:GAG preparation.

One drawback to the bovine caudal model employed here was the use *of ex vivo* tissue. When cells begin to die, they release their own chemicals including matrix metalloproteinases (MMPs), which break down the matrix and the natural GAGs are cleaved proteolytically. Therefore, it was vital to compare any additional GAG leakage to the natural leakage of the tissue over the same time period. The DMMB assay used to detect the GAG leakage is not specific to the chondroitin-6-sulphate (CS) GAG injected and it stains for all GAGs present. Therefore, it was important to determine what level of added CS was detectable above the background.

5.3.2.3 Preparation of solutions and injection procedure

1:2 (0.0266 M CS) GAG only

1 ml of PBS was added to 0.01289 g chondroitin-6-sulphate (0.0266 M solution). The solution was vortexed for 1 min until all the powder was dissolved. 250 µl of solution

was then injected into a disc using a 25 G needle and syringe with a second 25 G needle as an air hole.

1:10 (0.133 M CS) GAG only

Prepared as the 1:2 solution, but using 2 ml of PBS added to 0.12688 g chondroitin-6-sulphate.

1:10 P_{11}-12:GAG

1 ml of PBS was added to 40 mg of P_{11}-12, and vortexed for 1 min with heating, until the solution was a clear liquid. 0.5 ml of PBS was added to 0.068 g of chondroitin-6-sulphate and the solution was vortexed for 1 min. 125 µl of the P_{11}-12 solution was then injected into each disc using a 25 G needle and syringe with a second 25 G needle as an air hole. This was followed by a 125 µl injection of the CS solution through the second 25 G needle, retaining the needle used for the P_{11}-12 injection as a new air hole.

1:100 (1.33M CS) GAG dry powder

A solution of CS in PBS at an equivalent ratio of 1:100 P_{11}-12:GAG resulted in a viscous liquid that was deemed to be too thick to inject through a narrow gauge needle. For a therapy to be successful, injection through a narrow gauge needle is necessary, but it was still considered important to investigate the GAG leakage and interaction with P_{11}-12 at a high GAG ratio. Therefore, to get around this injection drawback, the GAG was added to the disc as a dry powder prior to addition of the Perspex endplate (Figure 244).

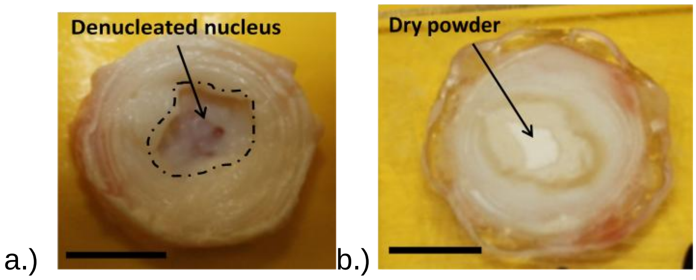

Figure 244 – a.) Disc prior to GAG powder addition b.) disc post GAG powder addition and endplate attachment. Scale bar = 10 mm

0.17 g of chondroitin-6-sulphate was weighed directly into the disc and packed down prior to endplate attachment. 250 µl of PBS was then injected into each disc after endplate attachment, using a 25 G needle and syringe with a 25 G needle as an air hole.

1:100 P$_{11}$-12:GAG dry powder

0.17 g of chondroitin-6-sulphate was weighed directly into the discs and packed down prior to endplate attachment. 1 ml of PBS was added to 40 mg of P$_{11}$-12. The solution was vortexed for 1 min and heated until the solution was a clear liquid. 125 µl of the P$_{11}$-12 solution was then injected into each disc after endplate attachment, followed by a 125 µl injection of PBS using a 25 G needle and syringe with a second 25 G needle as an air hole.

1:100 GAG gel

1 ml of PBS was added to 0.68 g of chondroitin-6-sulphate (1.33 M). The solution was vortexed for 1 min and resulted in a very viscous, gel-like liquid. The gel was then added to the disc prior to endplate attachment using a spatula and the disc weighed before and after to determine the amount added. The artificial endplate was then attached and the disc punctured with a 25 G needle to mimic the injection (Figure 245).

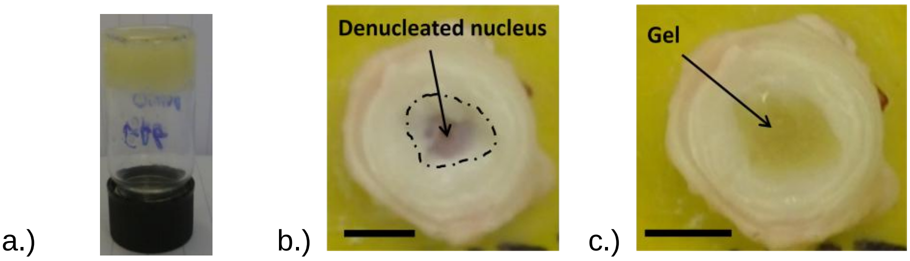

Figure 245 – a.) 1:100 GAG gel, b.) disc with nucleus pulposus removed. c.) disc with 1.33 M GAG gel added prior to endplate attachment. Scale bar = 10 mm.

1:100 P$_{11}$-12:GAG gel

2 ml of PBS was added to 0.04 g of P$_{11}$-12 (0.014 M). The solution was vortexed for 1 min and sonicated for 15 mins then pH adjusted to 7.4. The gel was then heated at 80^{o}C until the solution became a clear liquid and then 1.36 g of chondroitin-6-sulphate was added and vortexed. The gel was then added to the disc prior to artificial endplate attachment using a spatula and the disc weighed before and after to determine the

amount added. The artificial endplate was then attached and the disc punctured with a 25 G needle to mimic injection.

The injection procedure is illustrated in Figure 246. After the GAG or P_{11}-12:GAG additions to the discs were carried out, the discs were placed in 30 ml of PBS on a orbital shaker (Grant-Bio POS-300, Cambridge, UK) for 48 hours (Figure 247). 3 ml of PBS was removed at 24 and 48 hour timepoints.

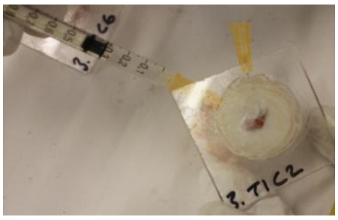

Figure 246 – Sample injected into disc through 25 G needle with a 25 G needle airhole.

Figure 247 – Discs placed in 30 ml PBS solution on an orbital shaker plate for 48 hours.

Further timepoints were not studied due to cell necrosis occurring from 5 days after animal slaughter, at which time MMPs are released resulting in matrix degradation. In order for further testing to be carried out a sterile hypoxic (<2% O_2) atmosphere would need to be maintained to retain cell viability and phenotype in the matrix and prevent contamination.

5.3.2.4 Quantification of glycosaminoglycan accumulation in PBS

In order to quantify the amount of GAG leaked from the discs over a 48 hour time period, the 3 ml PBS samples from each disc at the two timepoints were analysed with a DMMB assay via the following protocol:

SOLUTION PREPARATION

Assay buffer

137 ml of 0.1 M sodium di-hydrogen orthophosphate was combined with 63 ml 0.1 M di-sodium hydrogen orthophosphate. The solution was stirred using a magnetic stirrer

(Stuart Scientific CB161) and pH adjusted (Jenway 3510 pH meter) to 6.8 using 6 M hydrochloric acid or 6 M sodium hydroxide.

DMMB Dye solution

16 mg of DMMB was dissolved into 5 ml of ethanol and 2 ml of formic acid using a magnetic stirrer (Stuart Scientific CB161). 2 g of sodium formate was added and the volume increased to 1000 ml using distilled water. The pH was adjusted (Jenway 3510 pH meter) to 3.0 using formic acid.

Chondroitin sulphate standard stock

10 mg chondroitin-6-sulphate was diluted in 10 ml assay buffer to give a 1 mg/ml stock solution.

METHOD

Preparation of CS standards:

1 mg/ml stock CS was diluted with PBS to 50 µg/ml. Serial two-fold dilutions were performed to give a range of CS standards for the reference curve (50, 25, 12.5, 6.25, 3.13, 1.56, 0.78 and 0 µg/ml). 40 µl of each of the standards was added to a 96 well plate, in triplicate.

GAG measurement:

40 µl of each sample, diluted in PBS as necessary, was added to wells in triplicate. 250 µl DMMB solution was dispensed into all wells. The plate was left for 2 minutes and the absorbance read at 525 nm using a Multiskan spectrum microplate spectrometer (Thermo Scientific, Loughborough, United Kingdom).

Analysis of assay data

The average 0 µg/ml standard reading was subtracted from all other standards and sample readings to remove any background measurements. The CS standard sample concentrations were plotted against the absorbance, A_{525}. The sample A_{525} readings were then compared to the standard curve to determine the GAG concentrations and, where required, multiplied by a dilution factor to give the GAG concentration of the sample in μg/ml (for raw data and standard curves see APPENDIX F). In order to determine the percentage of added CS that leaked from the samples the following calculations were performed:

1. Calculation of CS concentration in 30 ml PBS if all the added amount of CS had leaked out of the disc (e.g. 0.01575 g of CS added *1000 *1000 /30 = 525 μg/ml).

2. The natural GAG leakage was determined from the discs with no GAG added (e.g. 12 ± 5 μg/ml at 24 hrs, 106 ± 6 μg/ml at 48 hours).

3. The natural GAG leakage (μg/ml) was subtracted from the sample GAG concentrations (μg/ml) to give the non-natural GAG leakage (e.g. at 24 hours 220 μg/ml – 12μg/ml = 208 μg/ml).

4. The non-natural GAG leakage was divided by the GAG concentration that would result if the entire added GAG had leaked out, and then multiplied by 100 to give the percentage (e.g. at 24 hours (208/525)*100 = 39 %).

Data sets were processed using GraphPad Prism 5 software (La Jolla, CA, USA). Values are reported as means ± standard error of the mean (SEM). Results of DMMB assays were analyzed by one-way ANOVA, followed by Tukey's multiple comparison test and were assessed for their statistical significance via paired t-tests (P values < 0.05 were considered as statistically significant). OriginPro 8.6 (OriginLab Corporation, USA) was used to plot the results.

5.3.3 Static loading study

5.3.3.1 Background

A number of studies have investigated the mechanical behaviour of the intervertebral disc using a range of testing methods.[235,244,265-268] However, as yet, there are no standardised test methods available for the evaluation of nucleus implants or injectable gels. In the current work, due to the need to extract one endplate to remove the nucleus, previously published methods were not applicable. Therefore, a basic new static test method was developed to undertake an initial comparison between discs with the nucleus removed, discs with the nucleus intact and discs augmented with the peptide gels.

5.3.3.2 Ex vivo model preparation

Four different groups were investigated as listed in Table 21. Four tails and six discs spanning from C1 to C6 were used for each group.

Group		**Disc and tail used**		
No NP	Nucleus pulposus removed	T1C1	T2C3	T1C5
		T3C2	T4C4	T3C6
NP	Nucleus pulposus intact	T2C1	T1C3	T2C5
		T4C2	T3C4	T4C6
1:10	P_{11}-12:GAG 1:10	T1C2	T2C4	T1C6
		T3C1	T4C3	T3C5
1:2	P_{11}-12:GAG 1:2	T2C2	T1C4	T2C6
		T4C1	T3C3	T4C5

Table 21 – Static loading study showing the tail (T) and caudal disc (C) used for each group

The tails were cleaned and the processes removed. The discs were then excised via a transverse cut between the disc and the proximal cartilage end plate and via a transverse cut through the vertebra leaving ~10mm of bone attached to the distal side of the disc, as illustrated in Figure 248.

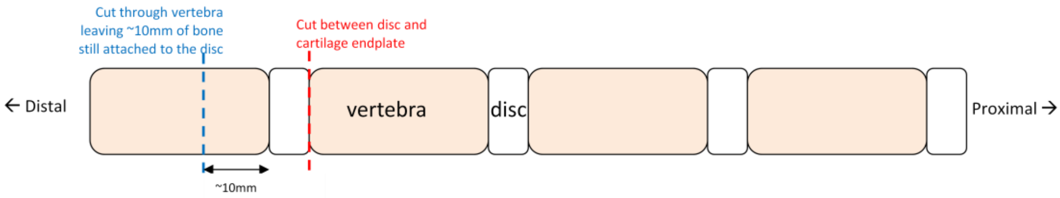

Figure 248 – Schematic diagram of disc removal

The discs were soaked in monosodium citrate for 20 minutes and then the nucleus pulposus was extracted from the discs to be used in groups No NP, 1:10 and 1:2. The discs were weighed pre and post removal (APPENDIX F). Artificial Perspex endplates (2x40x40mm) were then attached to all the discs with an adhesive (Loctite 3090, Henkel, Hatfield, UK) (Figure 249).

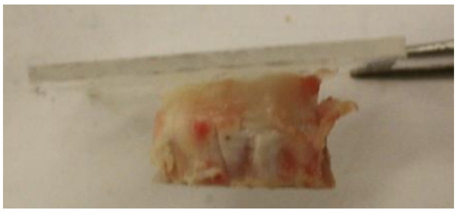

Figure 249 - Disc post endplate attachment.

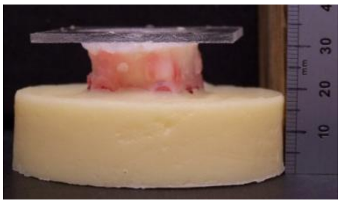

Figure 250 - Disc cast in PMMA cement ready for testing.

Discs for the 1:10 and 1:2 group were prepared in the following manner:

A solution of P_{11}-12 was prepared by adding 1 ml of PBS to 40 mg of P_{11}-12. The solution was vortexed for 1 min and heated until the solution was a clear liquid. It was injected into each disc using a 25 G needle and syringe with a 25 G needle as an air hole followed by a 125 µl injection of CS solution. The CS solution was prepared by adding 0.5 ml of PBS to 0.068 g of CS for the 1:10 group and 0.0137 g of CS for the 1:2 group. In both cases, the solution was then vortexed for 1 min. The CS injection was through the 25 G needle that had previously been used as the air hole and with the needle used for the P_{11}-12 injection as the new air hole

Following preparation, all discs were sealed in individual plastic bags with PBS soaked tissue paper to prevent samples drying and stored at 2-8^{o}C overnight. The distal vertebra section of each sample was then cast in 70 mm diameter polymethylmethacrylate (PMMA) cement to produce a flat surface that was parallel to the Perspex endplate as shown in Figure 250 and Figure 251. Once set, the samples were stored in individual sealed plastic bags containing PBS soaked tissue paper at 2-8^{o}C until testing.

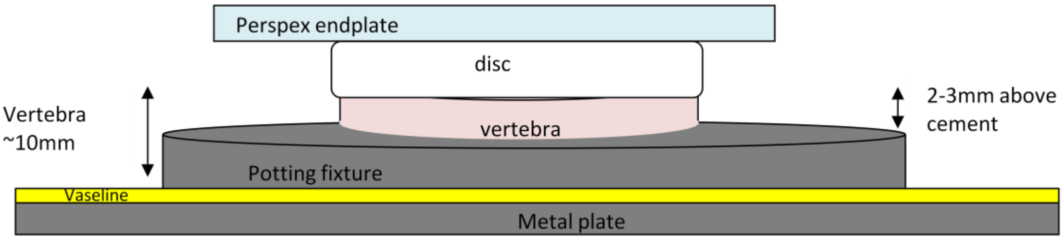

Figure 251 - Schematic diagram of casting procedure.

5.3.3.3 *Loading*

Prior to testing the disc heights and widths were recorded. (APPENDIX F).

All specimens underwent static axial compressive loading from 0 to 9 kN using displacement control at a low load rate of 1 mm/min. The experiments were carried out on an Instron 3366 materials testing machine with a 10 kN load cell (Instron, High Wycombe, Bucks, UK) (Figure 252).

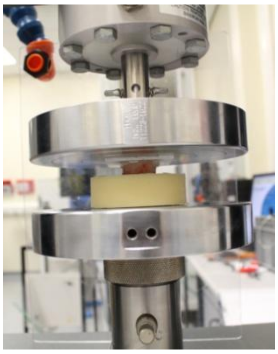

Figure 252 - Specimen loading on the Instron materials testing machine

It should be noted that at the start of each test, the fixture on the crosshead of the materials testing machine was brought into contact with the Perspex endplate until a load of 0.3 N was recorded. At this point, the displacement and load was then rezeroed and the test was started. Force/displacement data were collected using the Instron material testing software, Bluehill 2. The data were then plotted using Origin Pro 8.6.

In terms of analysing the resultant load-displacement curves, the stiffness of a physiologically relevant region was evaluated as well as the extent of the lax zone.

Calculation of the normalised stiffness

Stiffness is a measure of how much an object resists deformation in response to an applied force. It is also known as the rigidity of an object. The stiffness of an object can be calculated by Equation 13:

$$k = \frac{F}{\delta}$$

Equation 13

Where k = stiffness, F= force applied to the object, δ = the displacement produced by the force along the same degree of freedom.

In order to take into account the differences in the disc sizes when calculating their stiffness values, we can think of their stiffness in terms of their elastic modulus, Equation 14:

$$Elastic\ modulus = \frac{\sigma}{\varepsilon}$$

Equation 14

Where σ = stress and ε= strain.

This can also be written as Equation 15:

$$Elastic\ modulus = \frac{F/_{A}}{\delta/_{l}} = \frac{Fl}{A\delta}$$

Equation 15

Where F = force, A = area, δ = displacement and l= length.

In this study, the gradient of the linear part of the load vs. displacement plot was taken between 200-500 N (Figure 253) to give the stiffness F/δ = k.

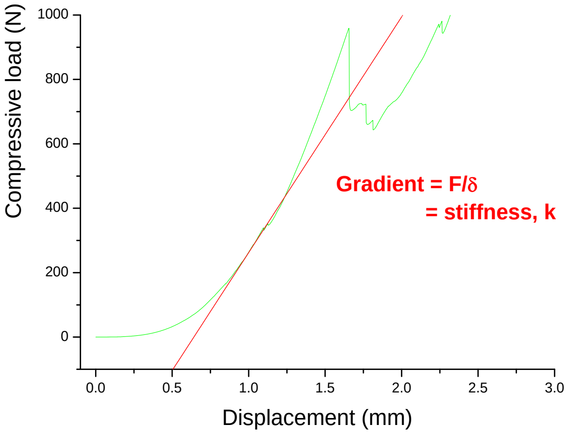

Figure 253 – Example of load vs. displacement plot for a disc. Red line = linear fit of curve from 200-500 N.

Then the normalised stiffness or elastic modulus for each disc in this load region was determined using Equation 16:

$$Normalised\ stiffness = \frac{kl}{A}$$

Equation 16

Where k = stiffness, A = area and l = length.

The areas and lengths were determined by taking measurements from photographs taken of each of each discs prior to testing (Figure 254) (APPENDIX F).

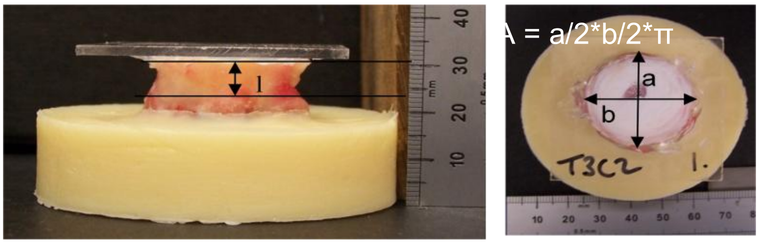

Figure 254 – Photographs of one of the disc used to determine l and A measurements.

The normalised stiffness value was calculated for each disc and then the average of the 6 discs for each sample type was taken.

Determination of the lax zone

When looking at the load-displacement plots for the individual disc specimens, it was observed that there were variations in the toe region of the plots, i.e. there was a plateau region prior to the linear region where an increase in the displacement required little change in the applied load. Here this plateau region is termed the lax zone. This non-linearity in the load displacement plot is due to a high flexibility around the neutral position and stiffening effect towards the end of the range of motion and is necessary for the proper functioning of the spinal system.[269] This lax zone is termed the 'neutral' zone in a spinal motion segment (disc with two vertebra attached as well as its ligaments).[269,270] To quantify this lax zone, the compressive displacement for the region from the preload 0 N to 1 N was determined, i.e. the displacement at which the curve went above 1 N as illustrated in Figure 255.

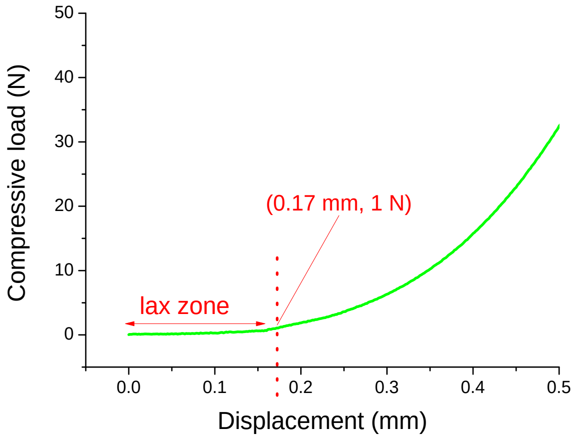

Figure 255 – Determination of the lax zone

5.4 Results and discussion

5.4.1 Assessment of GAG leakage through the annulus fibrosus and injection hole

5.4.1.1 Chondroitin sulphate only injection and leakage

No injection and CS injections of 1:2 and 1:10 GAG only

In order to determine what level of added chondroitin sulphate was detectable above the natural leakage/background, three groups were compared: those with no GAG injection, and those with 1:2 GAG only and 1:10 GAG only injections. (The latter two were used to represent the GAG concentrations in P_{11}-12:GAG 1:2 and 1:10 respectively, although in this case no peptide was used) (Figure 256).

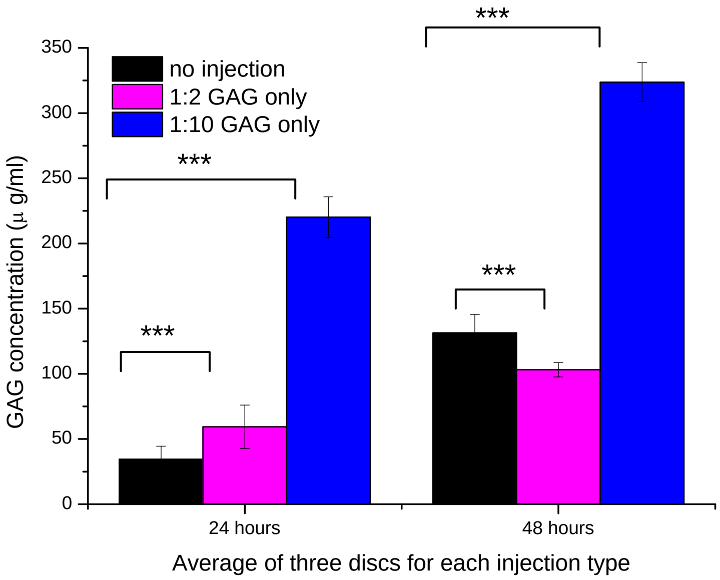

Figure 256 - Plot of the average GAG concentration leaked from discs with no injection, (i.e. natural leakage), 1:2 GAG only and 1:10 GAG only injections over a 48 hour time period. (error bars = SEM, n=3, One way ANOVA carried out using GraphPad Prism v.5, [unless stated difference is non-significant, *≥95%, **≥98%, *≥99% confidence that the means are significantly different.])**

At 24 and 48 hours no significant difference was found between a low concentration injection (1:2) of CS and no CS injected into the disc (i.e. background GAG leakage). However, for an injection of 1:10 CS there was a significant increase compared to no CS injected into the disc.

From this initial trial, it was determined that an addition of a lower GAG concentration of 0.0266 M (1:2) was not detectable above the background natural leakage of the disc. Therefore, in the following studies, a GAG concentration of 0.133 M (1:10) and above was used.

No injection and an injection of 1:100 GAG only (CS added as dry powder)

The results of the study comparing discs with no CS injection and discs containing 1:100 GAG only are presented in Figure 257:

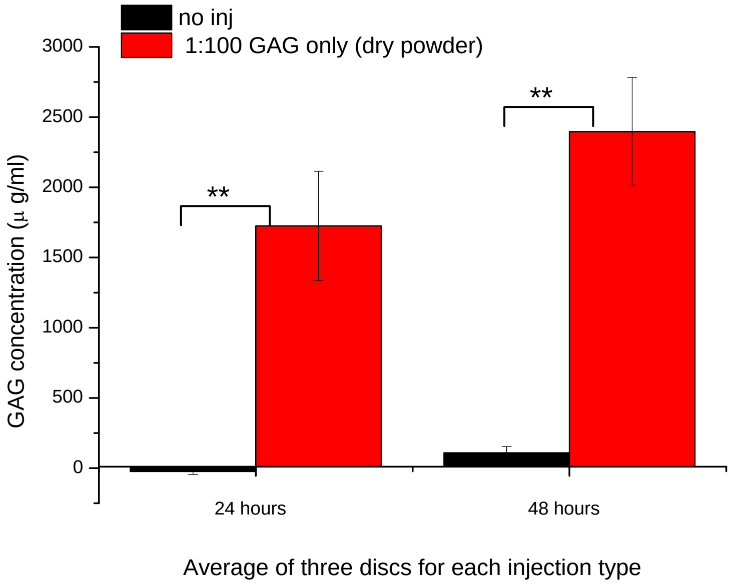

Figure 257 - Plot of the average GAG concentration leaked from discs with no injection, (i.e. natural leakage) and 1:100 GAG only added as a dry powder then injected with PBS over a 48 hour time period. (error bars = SEM, n=3, One way ANOVA carried out using GraphPad Prism v.5 [unless stated difference is non-significant, *≥95%, **≥98%, *≥99% confidence that the means are significantly different.])**

As can be observed in Figure 257, a significant difference was seen between the natural GAG leakage and the discs with 1:100 GAG only added, at both time points, suggesting a large leakage of GAG into the surrounding PBS solution. It was not truly understood if this large leakage was due to just the high levels of GAG added. The increase could also have been caused by inefficient mixing of the CS and PBS injection and therefore formation of the viscous liquid inside the disc.

No injection, 1:100 GAG only (CS added as gel) and dissected nucleus restored back in to the disc

The GAG leakage concentrations for no injection, 1:100 GAG only (added as gel) and the group with the nucleus dissected and reinserted into the disc are shown in Figure 258. A large amount of GAG was detected in the surrounding PBS solution for the 1:100 GAG only addition sample, however, it was less when added as a gel than when added as a dry powder (Figure 257), suggesting that the processing has a big part to play. There was a significant difference at both time points between the natural GAG leakage of the discs and the cases where a 1:100 GAG only gel was added. However, there was no significant difference between the two time points for the individual samples, suggesting that most of the leakage occurred in the first 24 hours.

In this trial, another group of discs were investigated where the natural nucleus tissue was first removed and then loosely packed back into the hole. It can be seen in Figure 258 that the GAG leakage when the denucleated discs and the reinserted nucleus discs are compared there is no significant difference between the amounts of GAG leaked. This confirmed that the cells have not yet began releasing matrix degrading enzymes, which would result in a breakdown of the proteoglycans leading to an increase in the natural GAG leakage. This is important as it shows that the experiment was carried out in a time window prior to detectable cell necrosis interference.

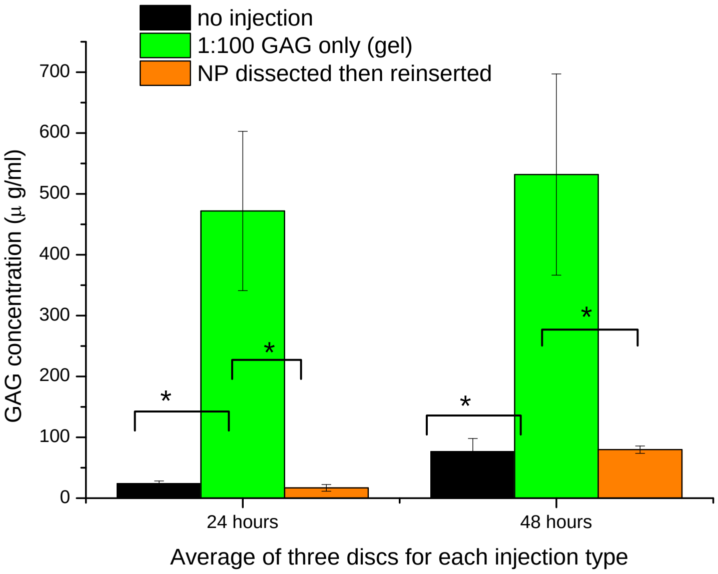

Figure 258 - Plot of the average GAG concentration leaked from discs with no injection, with the NP removed then placed back in the disc and 1:100 GAG only added as a premade gel over a 48 hour time period. (error bars = SEM, n=3, One way ANOVA carried out using GraphPad Prism v.5, [unless stated difference is non-significant, *≥95%, **≥98%, *≥99% confidence that the means are significantly different.])**

5.4.1.2 Chondroitin sulphate and P_{11}-12 injection and leakage

This study was to investigate the effect of the presence of P_{11}-12 on GAG leakage, i.e. whether the self-assembled peptide structure interacted in such a way with the GAG chains as to prevent them from leaking out of the disc.

The GAG concentration leakage is compared with that of the natural leakage of the tissue as before.

No injection, P_{11}-12:GAG 1:10 injection, P_{11}-12:GAG 1:100 (GAG added as dry powder)

The GAG concentrations found with no injection, P_{11}-12:GAG 1:10 injection, P_{11}-12:GAG 1:100 (GAG added as dry powder) are presented in Figure 259.

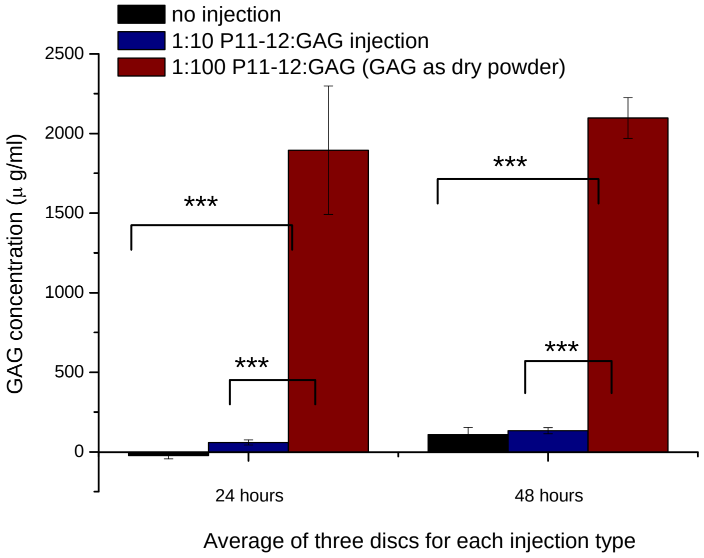

Figure 259 - Plot of the average GAG concentration leaked from discs with no injection, (i.e. natural leakage), with 1:10 P_{11}-12:GAG and 1:100 P11-12:GAG where the GAG was added as a dry powder to the disc prior to an injection of P11-12 over a 48 hour time period. (error bars = SEM, n=3, One way ANOVA carried out using GraphPad Prism v.5, [unless stated difference is non-significant, *≥95%, **≥98%, *≥99% confidence that the means are significantly different.])**

As can be seen in Figure 259, the 1:10 P_{11}-12:GAG injections show no significant GAG leakage compared to that seen in the discs with no additional GAG added. However, with the 1:100 P_{11}-12:GAG sample, there was a significant increase in the GAG leakage compared to that of the natural disc. This may have been an artefact of processing, i.e. complete mixing not occurring and therefore a homogeneous gel not forming, or due to the CS concentration reaching saturation of the P_{11}-12.

No injection, P_{11}-12:GAG 1:100 (GAG added as gel)

To overcome the potential processing issue as with the 1:100 GAG only sample above, the 1:100 P_{11}-12:GAG gel was prepared outside of the disc and then added prior to endplate attachment.

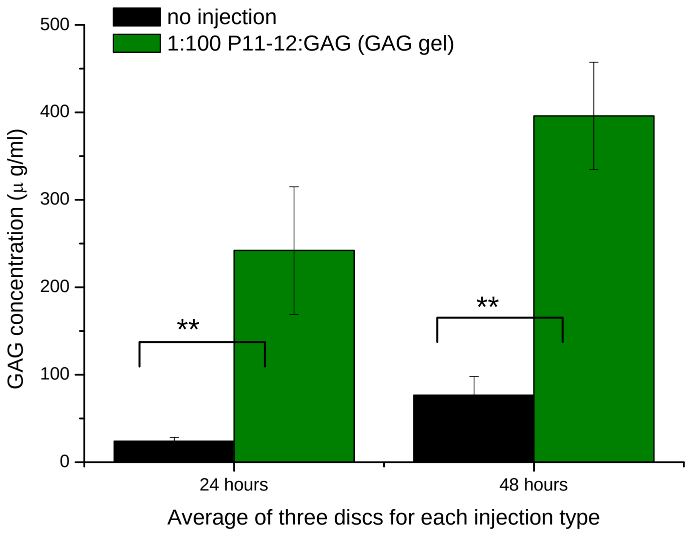

Figure 260 - Plot of the average GAG concentration leaked from discs with no injection, (i.e. natural leakage) and with 1:100 P_{11}-12:GAG where the gel was added to the disc rather than formed *in situ* over a 48 hour time period. (error bars = SEM, n=3, One way ANOVA carried out using GraphPad Prism v.5, [unless stated difference is non-significant, *≥95%, **≥98%, *≥99% confidence that the means are significantly different.])**

The GAG concentrations are shown in Figure 260. It can be seen that again there was significantly more GAG leakage than was seen naturally from the disc, but it was less than when the GAG was added in a dry powder form. There is no significant increase in GAG leakage over the second day, implying that the GAGs retained in the disc after one day have remained there.

5.4.1.3 The effect of the presence of P_{11}-12 on chondroitin sulphate leakage

In order for the effect of the presence of P_{11}-12 on GAG leakage to be truly understood from the data already presented, the percentage of added GAG leaked was determined using Equation 17:

$$Percentage\ GAG\ leakage = \left(\frac{GAG\ measured - natural\ GAG\ leakage}{total\ amount\ of\ GAG\ added\ to\ the\ disc}\right) * 100$$

Equation 17

Where GAG measured is the concentration of GAG measured in the 3 ml PBS aliquots for each of the groups and natural GAG leakage is the GAG measured concentration in the 3 ml PBS aliquots for the denucleated group with no additional GAG.

Peptide and GAG injected as liquids and gelation triggered in situ

In Figure 261, an injection of GAG only at a ratio of 1:10 is compared to an injection of P_{11}-12 and then GAG at a ratio of 1:10. The presence of P_{11}-12 significantly reduced the percentage of GAG added to the disc leaking out when taking into account the natural GAG leakage from the disc as well. This suggests that gelation and self-assembly were successful within the disc and that the P_{11}-12 aggregates were interacting with the GAG chains to hold them in place.

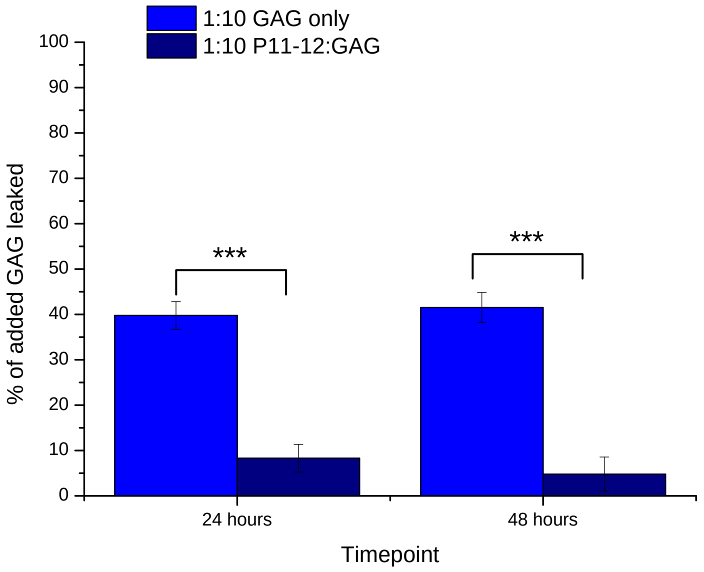

Figure 261 - Comparison of percentage of added GAG leaked (GAG concentration – natural leakage) from a disc when injected with 1:10 GAG only and 1:10 P_{11}-12:GAG over a 48 hour time period. (error bars = SEM of CS concentration detected then propagated, n=3, One way ANOVA carried out using GraphPad Prism v.5, [unless stated difference is non-significant, *≥95%, **≥98%, *≥99% confidence that the means are significantly different.])**

When looking into the effect of a higher GAG ratio, two different processing methods were used.

P_{11}-12 injected as liquid but GAG added to disc prior to injection as powdered form

Here the dry powder method was examined. As can be seen in Figure 262, the presence of P_{11}-12 has little to no effect on a high GAG concentration. This could be due to only a certain amount of GAG being able to interact with the P_{11}-12 aggregates and this may be at its optimum below a ratio of 1:100. Another possibility is that the processing method did not allow the GAG and the P_{11}-12 to fully mix within the disc cavity.

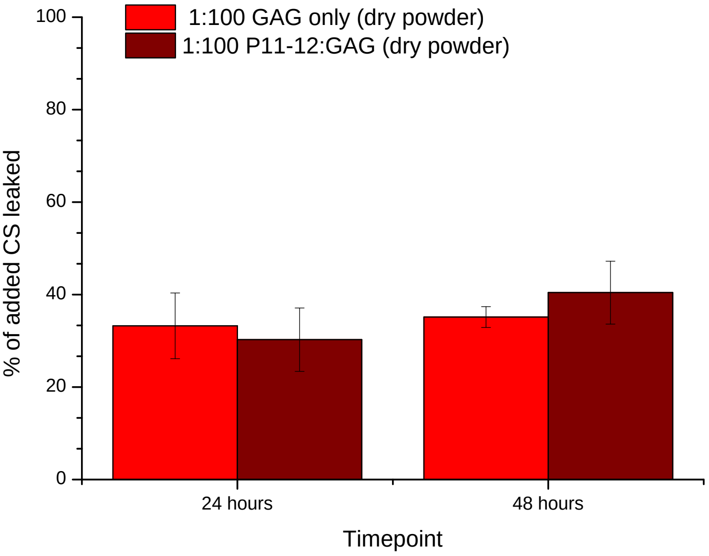

Figure 262 - Comparison of percentage of added GAG leaked (GAG concentration – natural leakage) from a disc when injected with 1:100 GAG only (GAG added to disc as dry powder prior to PBS injection) and 1:100 P_{11}-12:GAG (GAG added to disc as dry powder prior to P_{11}-12 injection) over a 48 hour time period. (error bars = SEM of CS concentration detected then propagated, n=3, One way ANOVA carried out using GraphPad Prism v.5, [unless stated difference is non-significant, *≥95%, **≥98%, *≥99% confidence that the means are significantly different.])**

P_{11}-12:GAG 1:100 gel prepared then placed in disc. Disc then punctured with 25 gauge needle to mimic injection

By preparing the 1:100 GAG only and P_{11}-12:GAG and then adding to the disc, again the presence of P_{11}-12 appears to have little effect on the overall GAG leakage when compared to that of the a GAG only gel (Figure 263). This suggests that there is an optimum ratio and that there was simply too high a level of GAG in this sample for the P_{11}-12 aggregates to interact with. However, it can be seen that this processing method leads to a reduced GAG leakage across both samples showing how important it is that the gel has mixed properly in situ.

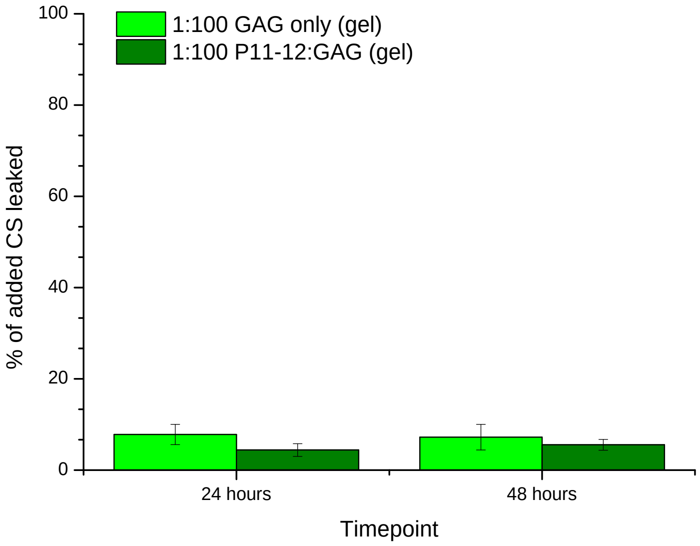

Figure 263 - Comparison of percentage of added GAG leaked (GAG concentration – natural leakage) from a disc when 1:100 GAG gel added and 1:100 P_{11}-12:GAG gel added over a 48 hour time period. (error bars = SEM of CS concentration detected then propagated, n=3, One way ANOVA carried out using GraphPad Prism v.5, [unless stated difference is non-significant, *≥95%, **≥98%, *≥99% confidence that the means are significantly different.])**

5.4.1.4 Natural GAG leakage with and without the NP

As three different trials were carried out, there were three batches of disc that had no GAG added. As an interesting side point, the variation in natural GAG leakage over 6 different tails is shown in Figure 264. There was no significant difference found between any of the three trials in the natural leakage. This is a positive result, because six different tails were used that could have had different degeneration/healthy states, which would have been dependent on many external factors. Also, due to the nature of using animal tissue obtained from an abattoir, the following could not be controlled:

- Exact age of the animal (~24-28 months)
- Breed of animal
- Time since slaughter (within 3 days)
- Sex (although not expected to have an effect until animals are much older)
- Diseases that may affect the health of the spine

The natural leakage from a denucleated disc can be compared to the natural GAG leakage from the disc when the nucleus is excised and then placed back in the disc. As illustrated in Figure 264, there was no significant difference over a 48 hour time period with or without the nucleus present.

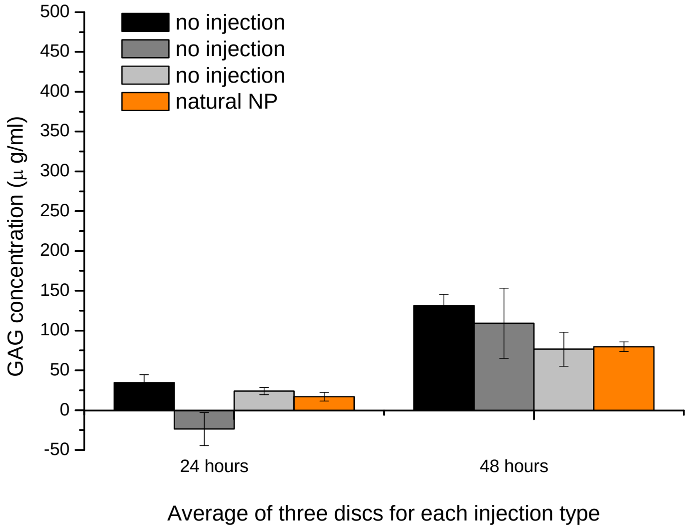

Figure 264 - Plot of the average GAG concentration leaked from discs with the NP excised (ie the no injection samples) compared to that with the natural NP excised and then placed back over a 48 hour time period. (error bars = SEM, n=3, One way ANOVA carried out using GraphPad Prism v.5, [unless stated difference is non-significant, *≥95%, **≥98%, *≥99% confidence that the means are significantly different.])**

5.4.2 Assessment of the capacity of the hydrogels to restore the disc biomechanics

5.4.2.1 Compressive loading of intervertebral discs

In order to gain an initial understanding of how these new peptide:GAG hybrid gels compared to the natural tissue, a very simple compressive loading experiment was designed.

The load-displacement curves for the 4 sample types tested are presented in Figure 265.

A comparison of the curves, (Figure 266) shows that there are some trends visible in the shapes and positions of the curves. The denucleated samples (red) are to the left-hand side of the plot suggesting that they do not deform as much for a given load in comparison to the samples with the nucleus intact (green), which are towards the right-hand side of the plot. The samples that have had their nucleus replaced with P_{11}-12:GAG gels fall somewhere between the two (Figure 266).

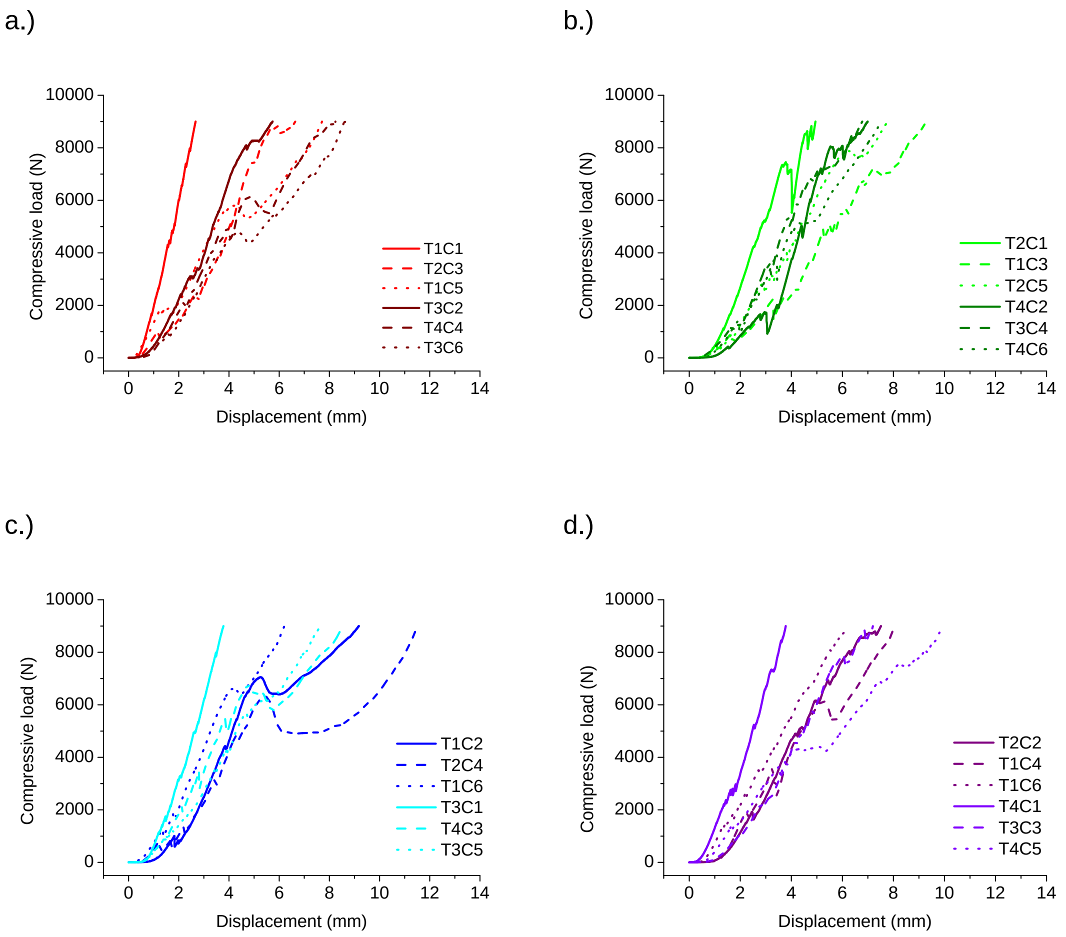

Figure 265 – Compressive load vs. displacement for 6 disc from 4 tails containing a.) denucleated, b.) nucleus pulposus intact, c.) nucleus pulposus removed and replaced with a 1:10 P_{11}-12:GAG gel, d.) nucleus pulposus removed and replaced with a 1:2 P_{11}-12:GAG gel.

From the load-displacement plots (Figure 266 b.), the normalised stiffness values for each group were calculated. These values are presented in Figure 267. The two control groups (No NP and NP) were significantly different from one another. The 1:2 sample showed no significant difference to the disc with the natural nucleus intact and was significantly different to the denucleated disc; however the 1:10 sample showed the opposite behaviour.

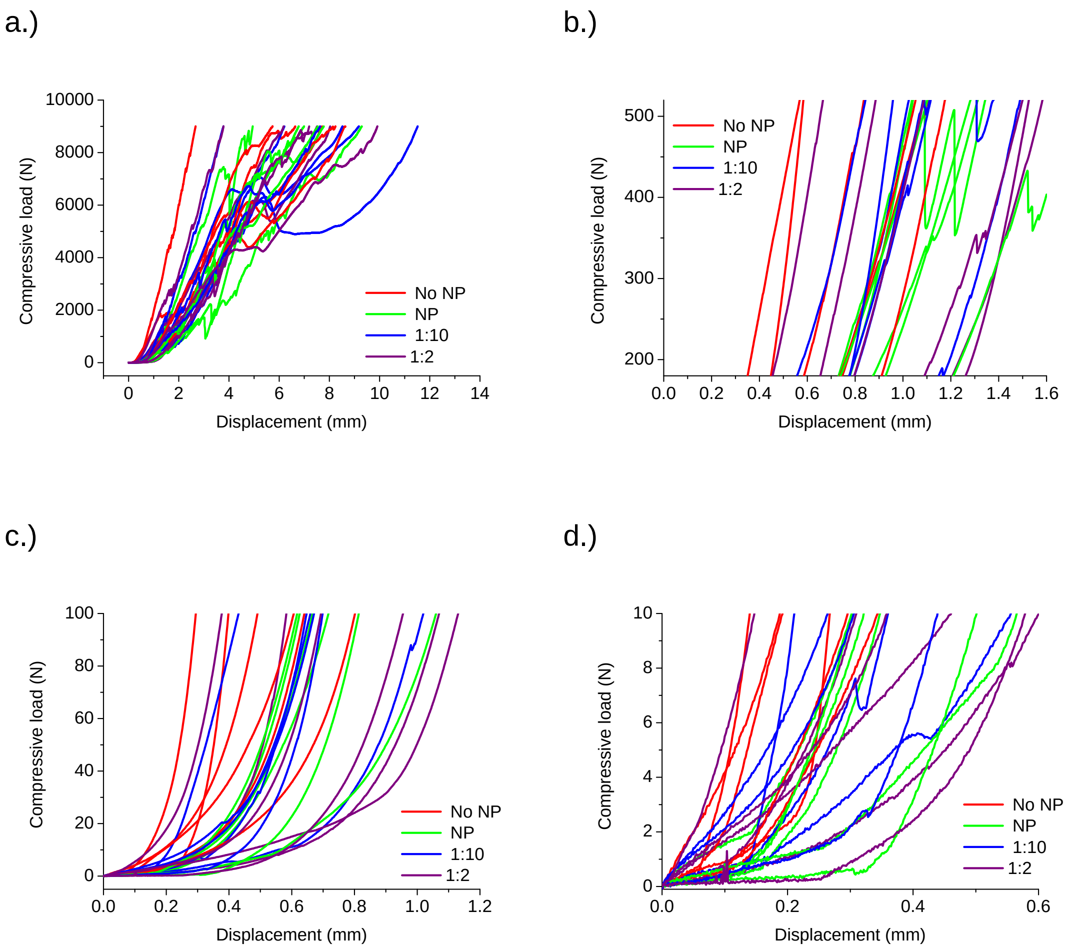

Figure 266 - Compressive extension vs. compressive load for all test samples a.) full scale, b.) showing the linear region 200-500 N used to calculate the normalised stiffness for each disc, c.) and d.) zoom in of the plot to show the lax zone.

The lax zone from the load-displacement plots (Figure 266 d.) is plotted as the compressive displacement at a force of 1 N (Figure 268). None of the groups were found to be significantly different.

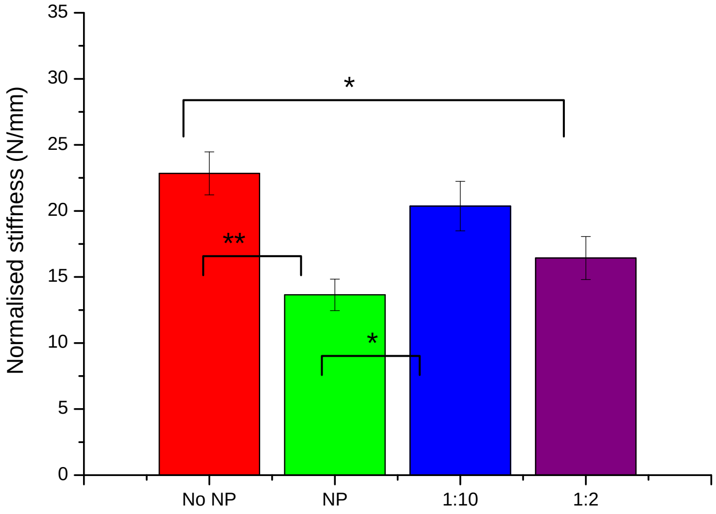

Figure 267 – Plot of normalised stiffness for each sample type as an average of the 6 discs tested. (Error bars = SEM, n=6, One way ANOVA carried out using GraphPad Prism v.5, [unless stated difference is non-significant, *≥95%, **≥98%, *≥99% confidence that the means are significantly different.]).**

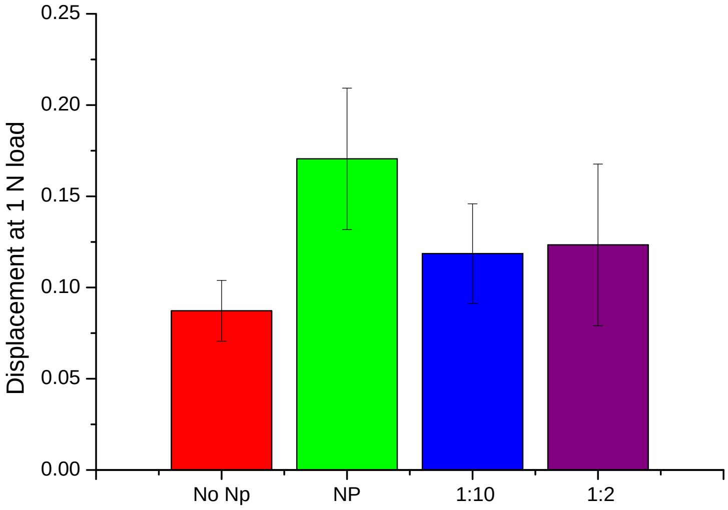

Figure 268 – Compressive extension at a load of 1N. (n=6, error bars = SEM, One way ANOVA carried out using GraphPad Prism v.5, [unless stated difference is non-significant, *≥95%, **≥98%, *≥99% confidence that the means are significantly different.]).**

5.4.3 Discussion

From the rheology investigation carried out in section 4.2.2, the P_{11}-12:GAG 1:2 gel was expected to restore the most similar biomechanics to the natural tissue as it had the most similar elastic modulus to that of the unconfined nucleus pulposus.[271] From Figure 267, it can be seen that the P_{11}-12:GAG 1:2 sample was significantly different from the denucleated disc; however, it was not significantly different from the disc with its nucleus still intact, indicating that the gel does indeed appear to have the desired effect. Although no significant difference is seen between the denucleated discs and the disc containing P_{11}-12:GAG 1:10, from observing the general trends it is clear that replacement of the nucleus with a P_{11}-12:GAG gel improves the stiffness to a value in the direction of the natural tissue.

Interestingly, the denucleated discs (no NP) were found to be stiffer than the discs with the nucleus still intact (NP). Compressive loading of an intact disc simultaneously produces narrowing of the disc height and outward bulging of the NP, placing axial and radial compressive stresses on the AF.[233] Meakin *et al.* carried out a study on the deformations of the disc with an intact and denucleated nucleus. They found that the outer margins of the annulus deform outwards both when an intact, and denucleated, disc is compressed. However, they found a difference in the inner margins of the annulus when the disc is compressed, with them deforming outwards with an intact disc but deforming inwards with a denucleated disc.[268] They also found the same behaviour in a partially denucleated disc (Figure 269).[272]

The observations seen here can be explained by how the compressive load is distributed by the tissue. When loading the intact nucleus, the fluid part of the tissue is pressurised, causing the AF to bulge outwards, whereas when loading the denucleated samples, only the solid phase of the tissue is loaded and the AF bulges into the denucleated cavity. Also when the discs are denucleated, it is likely that there is a relaxation of the AF and a reduction in height of the disc even before load is applied. Therefore the AF has already slightly compressed and so is stiffer than in the intact case. Effectively, the discs are starting from a different position.

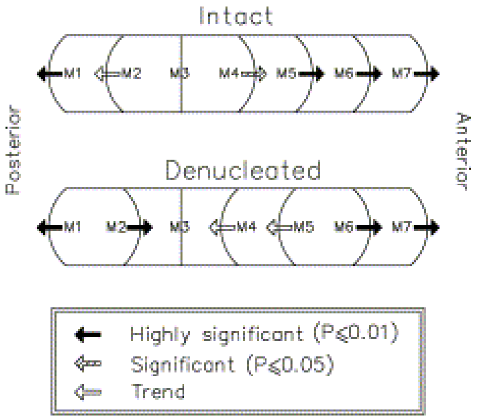

Figure 269 - Diagram showing the effects of partial denucleation on the response of human lumbar discs to a compressive load.[272]

The repaired samples fall somewhere between the intact and denucleated nuclei, which is thought to be due to two reasons. Firstly, because the AF has bulged slightly into the nucleated cavity prior to injection and loading, the load is carried partly by the solid phase of the AF and partly by the fluid phase of the hydrogel as demonstrated in Figure 270. Secondly, because the disc height will have been altered during the denucleation process prior to injection, this will again result in a different starting position.

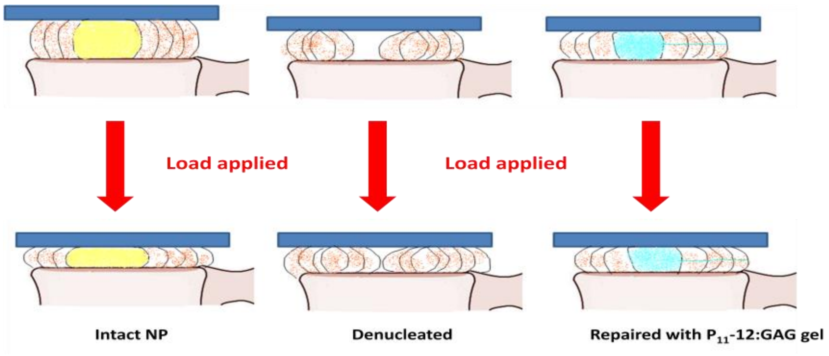

Figure 270 - Schematic diagram of loading

In another study by Meakin *et al.*, they found that when the nucleus was replaced with polymer materials, the inward bulging behaviour of the AF was prevented.[266]

The disc is known to exhibit biphasic behaviour, where the fluid phase dominates during compression and bending, and the solid phase dominates in shear directions of loading.[273] The biphasic response ensures that the fluid phase bears most of the applied stresses initially until the gradual movement of fluid out of the matrix transfers the stresses to the solid phase.[37] The observed lax zone may be due to the biphasic nature of the disc, with the lax zone being where the fluid phase is dominating and being expelled from the disc, whereas the linear elastic region that follows is dominated by the solid phase. Although no statistical difference was found in the lax zones, there was a clear trend of the intact discs having the longest lax zone and the denucleated discs having the shortest lax zone. Both the P_{11}-12:GAG containing discs fall somewhere in the middle of the two, suggesting that the natural biomechanics of the disc are heading towards being restored. The reduction of the fluid phase in the denucleated samples would explain why they have shortened lax zones.

While the NP is quite soft in unconfined compression, results in confined compression show it to withstand much larger loads, attributed directly to the considerable role of fluid pressurization in NP mechanics.[244] In the repaired samples, the pressurization of the disc may not yet be at the optimum level.

As the caudal discs increase in level distally, they become smaller in size and also decrease in GAG content. Although the experiment was designed such that for each group a disc of each level would be used to minimise these effects, the values were plotted as a function of disc level to check that the stiffness and lax zone values were not dependant on disc size or GAG content, (Figure 271 and Figure 272).

In both Figure 271 and Figure 272, no obvious trends were observed as the level changes, suggesting the results were not level dependant.

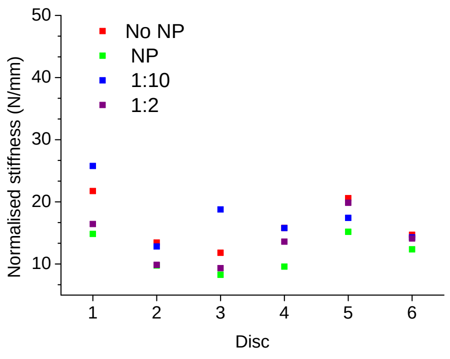

Figure 271 – Plot of normalised stiffness vs. disc level

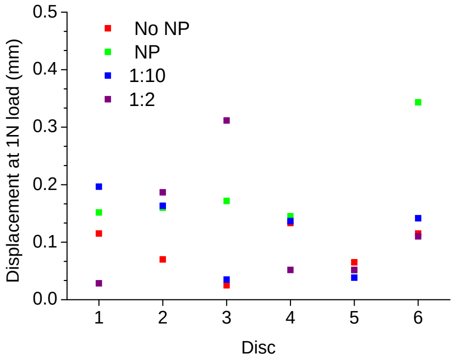

Figure 272 - Plot of lax zone vs. disc level

The correlation between the normalised stiffness and amount of nucleus removed (Figure 273) as well as the correlation between stiffness and ratio of injection weight:NP removed weight (Figure 274) were also examined.

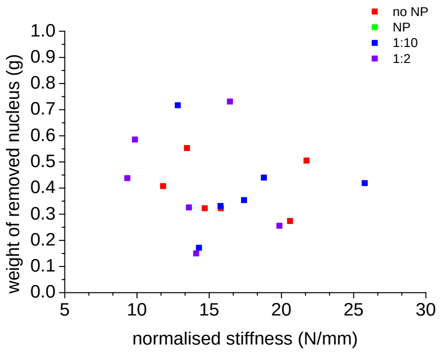

Figure 273 – Normalised stiffness vs. weight of nucleus removed from each disc

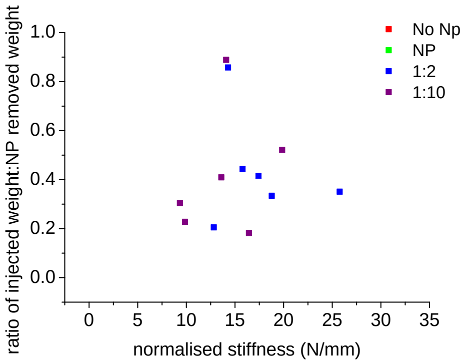

Figure 274 – Normalised stiffness vs. ratio of injection weight:nucleus removed weight for each disc.

Figure 273 shows that there was no bias between groups in terms of the baseline model, and that the variation in the amount of nucleus removed from specimen to specimen did not have an effect on the outcome. Figure 274 shows that the variation in the amount replaced as a fraction of the amount removed from specimen to specimen did not have a great effect either. From Figure 274, it can be observed that the ratio never got higher than 100%, i.e. there was never a case when more material was put in than was taken out, which could have potentially led to pressurisation issues. In fact, the ratio is mostly in the 30-50% region, which may explain why the stiffness was never fully restored in the repaired models.

5.5 Conclusions and future plans

The *de novo* bovine model developed here was used to compare the behaviour of the natural tissue, whether intact or denucleated with repaired tissue in order to act as a tool for choosing the best peptide:GAG combination to optimise and develop further.

Injections of GAG followed by P_{11}-12 successfully resulted in a gel forming *in situ* inside the denucleated cavity. The presence of P_{11}-12 minimised the amount of injected GAG that leaked through the AF and injection hole: in the case of P_{11}-12:GAG 1:10, the GAG loss over 48 hours was reduced from 42 ± 3 % to 5 ± 4 %. This provides further evidence for peptide - GAG interactions. However, it is vital that mixing and total gel formation occurs between the GAG and peptide within the disc to limit leakage. By using a narrow gauge needle, minimal leakage was seen, which is likely to be the result of minimal damage to the AF.

A denucleated disc repaired with P_{11}-12:GAG restored the mechanical behaviour of the disc under static loading to that not significantly different to a disc with a healthy nucleus intact. A peptide GAG combination of 1:2 gave the best results. As the 1:2 ratio had a similar G' to that of the natural nucleus, this suggests that rheology on the hydrogels alone could be used as an indicator of behaviour *in vivo.*

The next stage in the development of this therapy will be to test its behaviour in more advanced animal models that mimic the behaviour *in vivo*, and to use protocols developed by other researchers that mimic the natural physiological behaviour and loads experienced in the spine, such as loading the specimens in a PBS bath, employing cyclic loading rather than static loading and pre-loading the samples.[235,268,272,274] The tests should not only measure the compressive stiffness of the disc, but also capture the changes in disc height and AF bulging behaviour. A combination of the leakage study and loading study should also be carried out to assess the level of GAG and peptide leakage with loading.

Chapter 6

6 Summary, major findings and future work

6.1 Summary

Back pain affects 80% of adults at some stage during their lifetimes, costing the UK economy around £10 billion per year. One of the most common causes of lower back pain is disc degeneration. Currently, early stage interventions are limited and many patients continue to suffer further. A successful treatment requires a multidisciplinary approach, combining chemical, biological and mechanical expertise. The research carried out here is highly novel: it is the first time that designed self-assembling peptide hydrogels have been developed and assessed as a potential treatment for back pain. These solutions can be switched from fluid to gel inside the body, offering the opportunity to develop an injectable treatment as opposed to more costly and traumatic surgical interventions. Another exciting finding is strong evidence that the mechanical properties of the gels can be controlled by peptide design, a key issue for success in this application and also in other fields of regenerative medicine. The economic impact of this work could be significant due to its innovative nature and the increasing growth of the medical industry.

6.2 Major Findings

In summary, a gel material has been developed that:

- ✓ Has triggerable gelation and therefore is injectable, and potentially a minimally invasive treatment;
- ✓ Forms a stable hydrogel with mechanical properties similar to that of the natural tissue;
- ✓ Contains a high GAG content to aid in maintaining the swelling pressure of the disc.

The work of this thesis can be broken down into the three following sections:

6.2.1 Assessment of peptide self-assembly and design criteria for a suitable hydrogel

The behaviour of different peptide building blocks was examined and the design criteria for a suitable peptide hydrogel were established. The peptides were analysed using a series of complementary analytical techniques (NMR, FTIR, CDUV & TEM) to determine their behaviour at the molecular & nanoscale levels.

c* values were determined experimentally for three serine based peptides and, from these, their self-assembly curves were constructed and compared to that of their glutamine analogues. TEM, FTIR and CDUV were used to determine the secondary structure and morphology of the peptide aggregates. It was found that the serine along with glutamine based peptides follow a hierarchical self-assembly process similar to that in pure water and other solvents and so the same theoretical model can be used. Preliminary fitting with the theoretical model resulted in first estimates of the energetic parameters that govern self-assembly as well as magnitudes of overall Gibbs energies associated with the process.

In order to achieve a self-assembled peptide gel in physiological conditions, it was found that the peptide needs to have an overall ±2 charge.

Serine peptides have a higher c* than their glutamine analogues due to a lower ε_β. Complementary peptides will provide lower c* values than the single peptide systems and they also have the advantage of reaching an equilibrium state in much shorter timescales.

To form a gel with a low c* using a single peptide system, a negatively charged peptide would have to be used and one based on glutamine rather than serine will provide the lowest c*.

The efforts made to understand the kinetics and equilibrium behaviour of the peptides, as well as rigorous quality control, led to consistency and reproducibility of behaviour throughout the studies.

Rheological tests were carried out on the peptide gels. The results showed that the mechanical properties of the gels can be controlled, allowing up to a 10,000 fold variation in the stiffness. To achieve a stiff rather than weak hydrogel, a positively charged peptide should be used. The lower limit of the distance between nearest cross links was calculated using the plateau elastic moduli determined experimentally, which provided a picture of gel mesh size.

For the application of nucleus augmentation, a peptide with as low a c* as possible was deemed advantageous because this may lead to lower leakage from the disc, due to the monomer concentration being lower, i.e. P_{11}-4 or P_{11}-9. However, it is also vital that the peptide gel has a similar elastic modulus to that of the NP, i.e. P_{11}-12 or P_{11}-8. Another important criterion for the application was the possibility of triggering gelation *in situ*, which the mixing of the complementary peptides would provide. Therefore at this stage there was no clear optimum peptide and further optimisation was required.

6.2.2 Optimisation of the peptide hydrogels by combining them with glycosaminoglycans

The peptide materials were further optimised by mixing with glycosaminoglycans that are naturally found within the disc. A mixing study revealed that the addition of GAG to the peptide samples can affect their gelation kinetics and speed up gelation, possibly by lowering the c*, for example with P_{11}-12.

Rheology showed that the presence of GAGs in the peptide gels can enhance their material properties making them more like that of the natural nucleus. GAGs added to peptide were found to decrease the gel stiffness of positively charged peptides at high concentrations, but slightly increased stiffness at low GAG concentrations. By contrast, GAGs increased the gel stiffness values of negatively charged peptides at high concentrations, although the stiffness values were still lower overall than the positively charged peptides.

The effect of GAGs on the lower limit of the distance between nearest cross links was calculated, with stronger gels having smaller distances between cross links/entanglements/junction points.

From this work, the peptide:GAG hybrids P_{11}-12:CS 1:2 and 1:10 were discovered to have the most similar G' to natural nucleus and good gel lifetimes. The gelation of the peptide could be triggered by the addition of the GAG and after mixing the gel formed within seconds, making them an ideal candidate for an injectable therapy.

6.2.3 Assessment of the hydrogels' potential to remain in the disc and to restore disc mechanics

The bovine model that was developed here was used to compare the behaviour of the natural tissue, both intact and denucleated, with repaired tissue. This was used as a tool for choosing the best peptide:GAG combination to optimise and develop further, rather than to mimic the *in vivo* physiology or biomechanics.

Injections of GAG followed by P_{11}-12 successfully resulted in a gel forming *in situ* inside the denucleated cavity. The presence of P_{11}-12 minimised the amount of injected GAG that leaked through the AF and injection hole. This provided further evidence for peptide-GAG electrostatic interactions, cross linking the two biopolymer chains together. However, it is vital that thorough mixing and total gel formation occurred between the GAG and peptide within the disc to minimise leakage. By using a narrow gauge needle, minimal leakage was seen, which is likely to be the result of minimal damage to the AF.

A denucleated disc repaired with P_{11}-12:GAG restored the mechanical behaviour of the disc under static loading to that comparable to a disc with a healthy nucleus intact. A peptide:GAG combination of 1:2 gave the most positive results, which is thought to be due to the 1:2 ratio having the most similar G’ to that of the natural nucleus.

In summary, the P_{11}-12:GAG hydrogels have the potential to be a therapy in the treatment of disc degeneration and the results here demonstrate that the peptides could also have applications in other fields of regenerative medicine, e.g. as substrates for cell growth or cartilage tissue engineering.

6.3 Directions for future work

Although the aims of this thesis have been met, further work to gain a greater understanding of these novel systems could be carried out. Further optimisation is also required to discover the prime gel to use for the application of nucleus augmentation and better models for testing these gels would be beneficial.

To gain more knowledge on the self-assembly behaviour of the peptides themselves, further TEM studies could be carried out especially at concentrations around the estimated c* to enable more accurate fitting with the theoretical model. To aid with the fitting further, dilutions of a high concentration sample should be carried out and analysed again as a function of time by ^{1}HNMR in order to elucidate true equilibrium behaviour. In addition to this zeta potential measurements would be useful to determine the charges on the aggregates in solution.

To gain a better understanding of the GAG-peptide interactions, further TEM studies would again be useful, in particular to establish the effects of the GAGs on the peptide aggregate morphologies. It would also be beneficial to investigate the use of labelling the GAG chains with gold nanoparticles so that they could be detected in the TEM images. The use of immunochemistry and antibody labelling could also be employed to gain a better understanding of the interactions. Atomic force microscopy (AFM) could be used to look at the electrostatic bond strength between the GAG and peptide chains to establish if true cross linking has occurred. One of the reasons for including the GAGs in the gels was their osmotic effect and it would be useful to try to quantify/qualify this in comparison to the natural tissue, perhaps with the use of differential scanning calorimetry (DSC) and by measurement of the gels' swelling properties. It would be useful to gain a more in-depth knowledge of how the presence of GAG affects the self-assembly of the peptides by using ^{1}H NMR once more to study the monomer concentration as a function of total peptide concentration, in order to construct self-assembly curves in the presence of GAGs.

Continuing on from this, further rheological studies could be employed to study more GAG ratios and also to investigate the effect of changing the peptide concentration on the mechanical properties of the gels. It would be useful to carry out creep and recovery testing on the gels to characterise their rheological properties further, as well as using rheometry to measure the gelation times.

In order to develop the optimum gels chosen for the potential use in the application, a more sophisticated *in vitro* or *ex vivo* model is needed. In particular, a method to generate the necessary space in the nucleus is needed. It may be possible to use ultrasound to create a denucleated cavity without the need to remove an endplate.

Once a better model has been established, a similar leakage study should be carried out looking into the GAG leakage through the AF and injection hole. However, to make it more physiologically relevant, this should be done under loading. It would also be useful to develop a method to quantify the amount of peptide leakage at the same time, possibly using HPLC or even fluorescence spectroscopy and fluorescently labelled peptides. These leakage studies could be carried out initially with static loading, but cyclic loading would be more relevant to the application.

Once these basic tests have been performed, more complex directional loading should be investigated alongside fatigue testing to establish the life times of the gels in vivo. Parallel to this, an investigation into the gels' biological lifetime should be performed in order to examine the degradation profile of the gels and enzymatic activity.

Following on from these tests, further optimisation of the peptide may be required, such as the introduction of cysteine residues to the peptide to enable covalent cross-linking, which should provide stronger gels with less potential for leakage. It may also lead to cross linking of the gel to the AF tissue which would secure the gel in place even further.

Finally, due to the hostile conditions of the disc, tissue engineering techniques investigating regeneration of the nucleus using scaffolds and implanted cells are deemed to be extremely difficult to achieve. There has been some investigation into the migration of intervertebral disc cells into dense collagen scaffolds intended for functional replacement.[275] Although the peptide:GAG hybrids have not yet been tested for their propensity to act as cell culture scaffolds, certain peptides of the P_{11} series have been very successful in this application. Therefore it would be interesting to investigate the migration of disc cells through the chosen gels to establish if the materials could replace the nucleus, restoring the biomechanics of the disc, whilst at the same time become populated with the natural cells leading to possible regeneration of the tissue. Some of the P_{11} peptides have also had bioactive domains covalently linked to their ends such as the cell adhesion ligand RGD, and it may be possible to introduce these and other similar ligands into the gels to encourage the migration. Alongside this biological testing, the biocompatibility testing currently underway should be continued in addition to assessment of the inflammatory and angiogenesis activity of the gels.

6.4 Clinical Outlook

The diagnosis and treatment of degenerative disc disease remain major challenges in the management of back pain. In order for new treatments to be successful, it is essential that an approach able to identify those patients who will respond should be developed. Current techniques for identifying the source of pain, such as discography, are invasive and not always reliable at locating pain, and there is a poor relationship between the features observed in MRI imaging and patient pain. By improving diagnosis techniques alongside novel therapies, as well as increasing the understanding of the causes of pain, better patient management/treatment would be possible.

There is also a requirement for standardised testing procedures for new devices, with significant challenges in the development of appropriate preclinical models of degeneration, implantation, and more severe biomechanical tests including fatigue and extremes of bending. There are concerns that current technology is driven by what it is possible to measure and pre-clinically test, rather than by the end requirements.

There are numerous therapies currently under investigation and it may be that combining various treatment options will lead to a new gold standard in disc degeneration.

PUBLICATIONS

S.Maude, D. E. Miles, et al. (2011). "De novo designed positively charged tape-forming peptides: self-assembly and gelation in physiological solutions and their evaluation as 3D matrices for cell growth." Soft Matter **7**(18): 8085-8099.

D.E.Miles, R.K.Wilcox and A.Aggeli (2012), invited book chapter “Self -assembling peptides as a new class of medical device for regenerative medicine” in Self-Assembled peptide nanostructures: Advantages and challenges for their use in nanobiotechnology, Editor: Prof. Jaime Castillo, Technical University of Denmark, Publisher: Stanford Publishing Pte Ltd, Singapore**.**

REFEREED CONFERENCE PAPERS

D.E Miles, R.K.Wilcox and A.Aggeli, “Study of new self-assembling peptide gels for use biomaterials” *European Materials Research Society Spring Meeting 2010, Strasburg*.

D.E.Miles, S.Maude, S.H.Felton, R.K.Wilcox, E.Ingham and A.Aggeli, “Characterisation of optimised positively charged self-assembling peptide gels and evaluation of their cell biocompatibility” *23rd Annual Conference of the European Society for Biomaterials 2010, Tampere.*

D.E.Miles, S.Maude, S.H.Felton, R.K.Wilcox, E.Ingham and A.Aggeli “The self-assembly of optimised tape-forming *de novo* peptide gels and their evaluation as matrices for cell growth.” *The Tissue & Cell Engineering Society Annual Meeting 2011, Leeds. [http://www.ecmjournal.org/journal/supplements/vol022supp03/pdf/Vol22supp03a64.pdf]*

D.E. Miles, R.K. Wilcox and A. Aggeli, “*De novo* self-assembling peptide hydrogels for use in the treatmentof degenerative disc disease.” 24th *Annual Conference of the European Society for Biomaterials 2011, Dublin.*

D.E.Miles, E.Mitchell, N.Kapur, R.K.Wilcox, A.Aggeli “*Design of self-assembling peptide/glycosaminoglycan hydrogels for spinal therapies*.” *3rd Tissue Engineering and Regenerative Medicince in Science World congress 2012, Vienna. [http://0-onlinelibrary.wiley.com.wam.leeds.ac.uk/doi/10.1002/term.1609/pdf]*

PRESENTATIONS AND PUBLIC ENGAGEMENT

July 2009	Facilitator at disc disease and treatment workshop. *University of Leeds*.
Jan 2010	Poster: “Characterisation of optimised self-assembling peptide gels for biological applications.” *Centre for Molecular Nanoscience Launch, University of Leeds.*
June 2010	Poster: “A novel class of self-assembling β-sheet tape peptide gels in physiological solutions.” *School of Chemistry PG conference, University of Leeds.*
Dec 2010	Poster: **“**Can a new protein-like gel be used to cure back pain?**”** *The first Annual University of Leeds postgraduate researcher conference* ‘Celebrating Excellence in Postgraduate Research’.

Jan 2011	Invited Talk: “Can a new peptide hydrogel be used as a treatment for degenerative disc disease?” *iMBE Leeds Annual Day Conference 2011: Biomechanics of Spinal Interventions.*
Mar 2011	Great Bones Workshop with 30 year 7 pupils from Westborough High School, Dewsbury. *School of Mechanical Engineering, University of Leeds.*
May 2011	Invited talk: “Can a new protein like gel be used to cure back pain?’ – and how I got to asking this question.” *Women in Research Group, University of Leeds.*
June 2011	Talk: “*De novo* self-assembling peptide hydrogels for use in the treatment of degenerative disc disease” *School of Chemistry PG conference, University of Leeds.*
Oct 2011	Invited talk: “Exploring a new treatment for back pain using novel protein like gels.”*MAPS postgraduate conference, University of Leeds.*
Jan 2012	Invited Public Lecture: “Can a new protein like gel be used to treat back pain?” *Leeds Philosophical and literary societ.*
Mar 2012	Poster: “Can a new protein like gel be used to cure back pain?” *Set for Britain 2012 awards, Houses of Parliament.*
Mar 2012	Poster: “Can a new protein like gel be used to treat back pain?” *Make Some Noise competition, University of Leeds.*

SPECIAL AWARDS, HONOURS AND DISTINCTIONS

Leeds university postgraduate researcher of the year 2010 at the first Annual University of Leeds postgraduate researcher conference. ‘Celebrating Excellence in Postgraduate Research’ (£1000)

Best Poster at the Chemistry Postgraduate conference 2010 sponsored by Astra Zeneca. (£100)

Kate Furneaux prize for the most meritorious non-academic contribution to postgraduate life in the school of chemistry 2011 (£100)

Runner up oral presentation prize at the Chemistry postgraduate conference 2011 (£25)

Maths and Physical Sciences Faculty postgraduate researcher of the year 2011 (£200)

Shortlisted for the Set for Britain 2012 awards and invited to present a poster at the Houses of Parliament

2nd Place in the University of Leeds “Make Some Noise” poster competition 2012 (£100)

7 References

1 Bibby, S. R. S., Jones, D. A., Lee, R. B., Yu, J. & Urban, J. P. G. The pathophysiology of the intervertebral disc. *14th French Congress of Rheumatology*, Paris, France, 537-542 (2001).

2 Kandel, R., Roberts, S. & Urban, J. P. G. Tissue engineering and the intervertebral disc: the challenges. *First Japanese Meeting on Spine Research - The Intervertebral Disc*, Kyoto, JAPAN, S480-S491 (2008).

3 Bokhari, M. A., Akay, G., Zhang, S. G. & Birch, M. A. Enhancement of osteoblast growth and differentiation in vitro on a peptide hydrogel - polyHIPE polymer hybrid material. *Biomaterials*, **26**, 5198-5208, (2005).

4 Urban, J. P. G. & Roberts, S. Degeneration of the intervertebral disc. *Arthritis Research & Therapy*, **5**, 120-130, (2003).

5 Cassidy, J. J., Hiltner, A. & Baer, E. Hierarchical structure of the intervertebral-disk *Connective Tissue Research*, **23**, 75-88, (1989).

6 Filler, A., *Do You Really Need Back Surgery: A Surgeon's Guide to Neck and Back Pain and How to Choose Your Treatment*, http://www.backpain-guide.com/Chapter_Fig_folders/Ch05_Anatomy_Folder/6LumbarDisk.html, Accessed 10.10.08, 2008.

7 Yu, J., Peter, C., Roberts, S. & Urban, J. P. G. Elastic fibre organization in the intervertebral discs of the bovine tail. *Journal of Anatomy*, **201**, 465-475, (2002).

8 Johnstone, B. & Bayliss, M. T. The large proteoglycans of the human intervertebral disc - changes in their biosynthesis and structure with age, topography, and pathology. *21st Annual Meeting of the International-Society-for-the-Study-of-the-Lumbar-Spine*, Seattle, Wa, 674-684 (1994).

9 Urban, J. P. G., Roberts, S. & Ralphs, J. R. The nucleus of the intervertebral disc from development to degeneration. *Annual Meeting of the Society-for-Integrative-and-Comparative-Biology*, Denver, Colorado, 53-61 (1999).

10 Bertagnoli, R., Karg, A. & Voigt, S. Lumbar partial disc replacement. *Orthopedic Clinics of North America*, **36**, 341-347, (2005).

11 Roughley, P. J., Melching, L. I., Heathfield, T. F., Pearce, R. H. & Mort, J. S. The structure and degradation of aggrecan in human intervertebral disc. *European Spine Journal*, **15**, S326-S332, (2006).

12 Risbud, M. V., Shapiro, I. M., Vaccaro, A. R. & Albert, T. J. Stem cell regeneration of the nucleus pulposus *The Spine Journal*, **4**, S348-S353, (2004).

13 Di Martino, A., Vaccaro, A. R., Lee, J. Y., Denaro, V. & Lim, M. R. Nucleus pulposus replacement - Basic science and indications for clinical use. *Spine*, **30**, S16-S22, (2005).

14 Brinckmann, P. & Grootenboer, H. Change of disk height, radial disk bulge, and intradiscal pressure from discectomy - an invitro investigation on human lumbar disks. *Spine*, **16**, 641-646, (1991).

15 Wetzel, F. T., LaRocca, S. H., Lowery, G. L. & Aprill, C. N. The Treatment of Lumbar Spinal Pain Syndromes Diagnosed by Discography: Lumbar Arthrodesis. *Spine*, **19**, 792-800, (1994).

16 Gillet, P. The fate of the adjacent motion segments after lumbar fusion. *J. Spinal. Discord. Tech*, **16**, 338-345, (2003).

17 Guyer, R. D. *et al.* Prospective randomized, multicenter Food and Drug Administration investigational device exemption study of lumbar total disc replacement with the Charite artifical disc versus lumbar fusion: five year follow up. *Spine*, **9**, 374-386, (2009).

18 Zigler, J. *et al.* Results of the prospective, randomized, multicenter Food and Drug Administration investigational device exemption study of the ProDisc-L

total disc replacement versus circumferential fusion for the treatment of 1-level degenerative disc disease. *Spine*, **32**, 1155-1163, (2007).

19 Thomas, J., Lowman, A. & Marcolongo, M. Novel associated hydrogels for nucleus pulposus replacement. *Journal of Biomedical Materials Research Part A*, **67A**, 1329-1337, (2003).

20 Roberts, S., Menage, J., Sivan, S. & Urban, J. P. G. Bovine explant model of degeneration of the intervertebral disc. *BMc Musculoskeletal Disorders*, **9**, (2008).

21 Alini, M., Roughley, P. J., Antoniou, J., Stoll, T. & Aebi, M. A biological approach to treating disc degeneration: not for today, but maybe for tomorrow. *European Spine Journal*, **11**, S215-S220, (2002).

22 Hohaus, C., Ganey, T. M., Minkus, Y. & Meisel, H. J. Cell transplantation in lumbar spine disc degeneration disease. *First Japanese Meeting on Spine Research - The Intervertebral Disc*, Kyoto, JAPAN, S492-S503 (2008).

23 Meisel, H. J. *et al.* Clinical experience in cell-based therapeutics: Disc chondrocyte transplantation - A treatment for degenerated or damaged intervertebral disc. *Symposium on Nano-Structured and Intelligent Bioactive Materials held at the EMRS 2005 Spring Meeting*, Strasbourg, FRANCE, 5-21 (2005).

24 Ganey, T. *et al.* Disc chondrocyte transplantation in a canine model: A treatment for degenerated or damaged intervertebral disc. *Spine*, **28**, 2609-2620, (2003).

25 Luk, K. D. K., Ruan, D. K., Lu, D. S. & Fei, Z. Q. Fresh frozen intervertebral disc allografting in a bipedal animal model. *Spine*, **28**, 864-869, (2003).

26 Matsuzaki, H., Wakabayashi, K., Ishihara, K., Ishikawa, H. & Ohkawa, A. Allografting intervertebral discs in dogs - A possible clinical application. *Spine*, **21**, 178-183, (1996).

27 Ruan, D. K. *et al.* Intervertebral disc transplantation in the treatment of degenerative spine disease: a preliminary study. *Lancet*, **369**, 993-999, (2007).

28 Smith, L. J., Nerurkar, N. L., Choi, K.-S., Harfe, B. D. & Elliott, D. M. Degeneration and regeneration of the intervertebral disc: lessons from development. *Dis Model Mech*, **4**, 31-41, (2010).

29 Crevensten, G. *et al.* Intervertebral disc cell therapy for regeneration: Mesenchymal stem cell implantation in rat intervertebral discs. *Annals of Biomedical Engineering*, **32**, 430-434, (2004).

30 Risbud, M. V. *et al.* Differentiation of mesenchymal stem cells towards a nucleus pulposus-like phenotype in vitro: implications for cell-based transplantation therapy. *Spine*, **29**, 2627-2632, (2004).

31 Sakai, D. Future perspectives of cell-based therapy for intervertebral disc disease. *Eur Spine J.*, **17**, (2008).

32 Masuda, K., Oegema, T. R. & An, H. S. Growth factors and treatment of intervertebral disc degeneration. *Spine*, **29**, 2757-2769, (2004).

33 Li, J., Yoon, S. & Hutton, W. Effect of bone morphogenetic protein-2 (BMP-2) on matrix production, other BMPs, and BMP receptors in rat intervertebral disc cells. *J Spinal Disord Tech.*, **17**, 423-428, (2004).

34 Masuda, K. Biological repair of the degenerated intervertebral disc by the injection of growth factors. *Eur Spine J.* , **17**, 441-441, (2008).

35 Gruber, H. E., Hoelscher, G. L., Leslie, K., Ingram, J. A. & Hanley Jr, E. N. Three-dimensional culture of human disc cells within agarose or a collagen sponge: assessment of proteoglycan production. *Biomaterials*, **27**, 371-376, (2006).

36 Baer, A. E., Wang, J. Y., Kraus, V. B. & Setton, L. A. Collagen gene expression and mechanical properties of intervertebral disc cellâ€“alginate cultures. *Journal of Orthopaedic Research*, **19**, 2-10, (2001).

37 Costi, J. J., Freeman, B. J. C. & Elliott, D. M. Intervertebral disc properties: challenges for biodevices. *Expert Review of Medical Devices*, **8**, 357-376, (2011).

38 Nerurkar, N., Sen, S., Huang, A., Elliott, D. & Mauck, R. Engineered disc-like angle-ply structures for intervertebral disc replacement. *Spine*, **35**, 867-873, (2010).

39 Mizuno, H. *et al.* Biomechanical and biochemical characterization of composite tissue-engineered intervertebral discs. *Biomaterials*, **27**, 362-370, (2006).

40 Viscogliosi, A. G., Viscogliosi, J. J. & Viscogliosi, M. R. in *Spine Industry Analysis Series* (Viscogliosi LLC, 2004).

41 Eysel, P., Rompe, J. D., Schoenmayr, R. & Zoellner, J. Biomechanical behaviour of a prosthetic lumbar nucleus. *Acta Neurochirurgica*, **141**, 1083-1087, (1999).

42 Klara, P. M. & Ray, C. D. Artificial Nucleus Replacement: Clinical Experience. *Spine*, **27**, 1374-1377, (2002).

43 *DASCOR® Disc Arthroplasty System -- Disc Dynamics Folds, Unable to Secure FDA Clinical Trial Approval* http://www.spinepatientsociety.org/forum/emerging-spine-surgery-technologies/dascor-disc-arthroplasty-system-disc-dynamics-folds-unable-secure-fda-clinical-trial-approval-1184/, Accessed 24th March, 2011.

44 Husson, J. L. *et al.* A memory coiling spiral as nucleus pulposus prosthesis - Concept, specifications, bench testing, and first clinical results. *Journal of Spinal Disorders & Techniques*, **16**, 405-411, (2003).

45 Korge, A., Nydegger, T., Polard, J. L., Mayer, H. M. & Husson, J. L. A spiral implant as nucleus prosthesis in the lumbar spine. *European Spine Journal*, **11**, S149-S153, (2002).

46 Allen, M. J. *et al.* Preclinical evaluation of a poly (vinyl alcohol) hydrogel implant as a replacement for the nucleus pulposus. *Spine*, **29**, 515-523, (2004).

47 Bao, Q. B. & Yuan, H. A. New technologies in spine - Nucleus replacement. *Spine*, **27**, 1245-1247, (2002).

48 Vernengo, J., Fussell, G. W., Smith, N. G. & Lowman, A. M. Evaluation of novel injectable hydrogels for nucleus pulposus replacement. *Journal of Biomedical Materials Research Part B-Applied Biomaterials*, **84B**, 64-69, (2008).

49 *Gelstix - The 3 stick fix*, http://www.replicationmedical.com/joomla/products/gelstix, Accessed 2nd August, 2012.

50 *GelStix^{TM} - Scientific and Clinical Rationale*, http://d2grup.com/files/GelStix%20Datasheet%2009Mar2011-2.pdf, Accessed 2nd August, 2012.

51 CryoLife, *Biodisc Nucleus Pulposus Replacement*, http://www.cryolife.com/about/research/emerging/biodisc, Accessed 17th August, 2009.

52 SpineWave, *NuCore® Injectable Nucleus* http://www.spinewave.com/products/nucore.html, Accessed 24th March, 2011.

53 Voet, D. & Voet, J. G. *Biochemistry*. Second edn, (John Wiley & Sons, (1995)).

54 Ulijn, R. V. & Smith, A. M. Designing peptide based nanomaterials. *Chemical Society Reviews*, **37**, 664-675, (2008).

55 Stryer, L. *Biochemistry*. Fourth edn, (W.H. Freeman, (1995)).

56 Pasternak, C. A. *An Introduction to Human Biochemistry*. First edn, (Oxford University Press, (1979)).

57 Cojocari, D., *Amino acid*, http://en.wikipedia.org/wiki/Amino_acid, Accessed 18 January, 2011.

58 Danishefsky, I. *Biochemistry for Medical Sciences*. First edn, (Littel, Brown and Company, (1980)).

59 Woster, P. M., *Protein Structure and Function - An Overview Pharmaceutical Biochemistry I*, http://wiz2.pharm.wayne.edu/biochem/prot.html, Accessed 6th November, 2008.

60 Atkins, P. *Atkins The elements of physical chemistry*. Third edn, (Oxford University Press, (2004)).

61 Merrifield, R. B. Peptide Synthesis on a Solid Polymer. *Federation Proceedings*, **21**, 412, (1962).

62 Merrifield, R. B. Solid Phase Peptide Synthesis. I. The Synthesis of a Tetrapeptide. *Journal of the American Chemical Society*, **85**, 2149-2154, (1963).

63 Merrifield, R. B. Solid-phase peptide synthesis. *Endeavour*, **24**, 3-7, (1965).

64 Merrifield, R. B. Peptides methods of peptide synthesis. *Science*, **152**, 1735, (1966).

65 Merrifield, R. B. & Stewart, J. M. Automated Peptide Synthesis. *Nature*, **207**, 522-523, (1965).

66 Merrifield, R. B. Automated synthesis of peptides. *Science*, **150**, 178-185, (1965).

67 Semino, C. E. Self-assembling peptides: From bio-inspired materials to bone regeneration. *Journal of Dental Research*, **87**, 606-616, (2008).

68 Zhang, S. G. Emerging biological materials through molecular self-assembly. *Biotechnology Advances*, **20**, 321-339, (2002).

69 Gazit, E. Self-assembled peptide nanostructures: the design of molecular building blocks and their technological utilization. *Chemical Society Reviews*, **36**, 1263-1269, (2007).

70 Davies, R. P. W. *et al.* Self-assembling beta-sheet tape forming peptides. *Supramolecular Chemistry*, **18**, 435-443, (2006).

71 Israelachvili, J. N. *Intermolecular and Surface Forces*. Third edn, (Elsevier, (2011)).

72 *Aggregation of Vitamin C derivatives in water solution* http://www.netsci-journal.com/97v4/97014/vitc4.html, Accessed 23rd March, 2011.

73 López-Díaz, D. & Velázquez, M. M. Variation of the Critical Micelle Concentration with Surfactant Structure: A Simple Method To Analyze the Role of Attractive–Repulsive Forces on Micellar Association. *The Chemical Educator*, **12**, (2007).

74 NIH, *Regenerative Medicine* http://www.nih.gov/about/researchresultsforthepublic/Regen.pdf, Accessed 4th February, 2011.

75 FDA, *Medical Devices - Is The Product A Medical Device?*, http://www.fda.gov/MedicalDevices/DeviceRegulationandGuidance/Overview/ClassifyYourDevice/ucm051512.htm, Accessed 4th February 2011.

76 Vandermeulen, G. W. M. & Klok, H. A. Peptide/protein hybrid materials: Enhanced control of structure and improved performance through conjugation of biological and synthetic polymers. *Macromolecular Bioscience*, **4**, 383-398, (2004).

77 Kyle, S., Aggeli, A., Ingham, E. & McPherson, M. J. Production of self-assembling biomaterials for tissue engineering. *Trends Biotechnol.*, **27**, 423-433, (2009).

78 Zhang, S. G. *et al.* Self-complementary oligopeptide matrices support mammalian-cell attachment, *Biomaterials*, **16**, 1385-1393, (1995).

79 Ruoslahti, E. RGD and other recognition sequences for integrins. *Annual Review of Cell and Developmental Biology*, **12**, 697-715, (1996).

80 Vasita, R. & Katti, D. S. Nanofibers and their applications in tissue engineering. *International Journal of Nanomedicine*, **1**, 15-30, (2006).

81 Pauling, L. & Corey, R. B. The pleated sheet, a new layer configuration of polypeptide chains. *Proceedings of the National Academy of Sciences of the United States of America*, **37**, 251-256, (1951).

82 Ghadiri, M. R., Granja, J. R., Milligan, R. A., McRee, D. E. & Khazanovich, N. Self-assembling organic nanotubes based on a cyclic peptide architecture. *Nature*, **366**, 324-327, (1993).

83 Zhang, S. G., Holmes, T., Lockshin, C. & Rich, A. Spontaneous Assembly of a self-complementary oligopeptide to form a stable marcoscopic membrane. *Proceedings of the National Academy of Sciences of the United States of America*, **90**, 3334-3338, (1993).

84 Altman, M., Lee, P., Rich, A. & Zhang, S. G. Conformational behavior of ionic self-complementary peptides. *Protein Science*, **9**, 1095-1105, (2000).

85 Holmes, T. C. *et al.* Extensive neurite outgrowth and active synapse formation on self-assembling peptide scaffolds. *Proceedings of the National Academy of Sciences of the United States of America*, **97**, 6728-6733, (2000).

86 Jayawarna, V. *et al.* Nanostructured hydrogels for three-dimensional cell culture through self-assembly of fluorenylmethoxycarbonyl-dipeptides. *Advanced Materials*, **18**, 611-614, (2006).

87 Hartgerink, J. D., Beniash, E. & Stupp, S. I. Self-assembly and mineralization of peptide-amphiphile nanofibers. *Science*, **294**, 1684-1688, (2001).

88 Bell, C. J. *et al.* Self-assembling peptides as injectable lubricants for osteoarthritis. *Journal of Biomedical Materials Research Part A*, **78A**, 236-246, (2006).

89 Aggeli, A. *et al.* pH as a trigger of peptide beta-sheet self-assembly and reversible switching between nematic and isotropic phases. *Journal of the American Chemical Society*, **125**, 9619-9628, (2003).

90 Lowik, D., Leunissen, E. H. P., van den Heuvel, M., Hansen, M. B. & van Hest, J. C. M. Stimulus responsive peptide based materials. *Chemical Society Reviews*, **39**, 3394-3412, (2010).

91 Hong, Y. S., Legge, R. L., Zhang, S. & Chen, P. Effect of amino acid sequence and pH on nanofiber formation of self-assembling peptides EAK16-II and EAK16-IV. *Biomacromolecules*, **4**, 1433-1442, (2003).

92 Shu, J. Y., Tan, C., DeGrado, W. F. & Xu, T. New design of helix bundle peptide-polymer conjugates. *Biomacromolecules*, **9**, 2111-2117, (2008).

93 Gelain, F., Horii, A. & Zhang, S. G. Designer self-assembling peptide scaffolds for 3-D tissue cell cultures and regenerative medicine. *Macromolecular Bioscience*, **7**, 544-551, (2007).

94 Yokoi, H., Kinoshita, T. & Zhang, S. G. Dynamic reassembly of peptide RADA16 nanofiber scaffold. *Proceedings of the National Academy of Sciences of the United States of America*, **102**, 8414-8419, (2005).

95 Zhang, S. G., Gelain, F. & Zhao, X. J. Designer self-assembling peptide nanofiber scaffolds for 3D tissue cell cultures. *Seminars in Cancer Biology*, **15**, 413-420, (2005).

96 Kisiday, J. *et al.* Self-assembling peptide hydrogel fosters chondrocyte extracellular matrix production and cell division: Implications for cartilage tissue repair. *Proceedings of the National Academy of Sciences of the United States of America*, **99**, 9996-10001, (2002).

97 Semino, C. E., Kasahara, J., Hayashi, Y. & Zhang, S. G. Entrapment of migrating hippocampal neural cells in three-dimensional peptide nanofiber scaffold. *Tissue Engineering*, **10**, 643-655, (2004).

98 Semino, C. E., Merok, J. R., Crane, G. G., Panagiotakos, G. & Zhang, S. G. Functional differentiation of hepatocyte-like spheroid structures from putative liver progenitor cells in three-dimensional peptide scaffolds. *Differentiation*, **71**, 262-270, (2003).

99 Degano, I. R. *et al.* The effect of self-assembling peptide nanofiber scaffolds on mouse embryonic fibroblast implantation and proliferation. *Biomaterials*, **30**, 1156-1165, (2009).

100 Ellis-Behnke, R. G. *et al.* Nano neuro knitting: Peptide nanofiber scaffold for brain repair and axon regeneration with functional return of vision. *Proceedings of the National Academy of Sciences of the United States of America*, **103**, 5054-5059, (2006).

101 Thonhoff, J. R., Lou, D. I., Jordan, P. M., Zhao, X. & Wu, P. Compatibility of human fetal neural stem cells with hydrogel biomaterials in vitro. *Brain Research*, **1187**, 42-51, (2008).

102 McGrath, A. M., Novikova, L. N. & Wiberg, M. BD (TM) PuraMatrix (TM) peptide hydrogel seeded with Schwann cells for peripheral nerve regeneration. *Brain Research Bulletin*, **83**, 207-213, (2010).

103 Wang, X. M., Horii, A. & Zhang, S. G. Designer functionalized self-assembling peptide nanofiber scaffolds for growth, migration, and tubulogenesis of human umbilical vein endothelial cells. *Soft Matter*, **4**, 2388-2395, (2008).

104 Zou, Z. W. *et al.* Biocompatibility and bioactivity of designer self-assembling nanofiber scaffold containing FGL motif for rat dorsal root ganglion neurons. *Journal of Biomedical Materials Research Part A*, **95A**, 1125-1131, (2010).

105 Van Tomme, S. R., Storm, G. & Hennink, W. E. In situ gelling hydrogels for pharmaceutical and biomedical applications. *International Journal of Pharmaceutics*, **355**, 1-18, (2008).

106 Chow, D., Nunalee, M. L., Lim, D. W., Simnick, A. J. & Chilkoti, A. Peptide-based biopolymers in biomedicine and biotechnology. *Materials Science & Engineering R-Reports*, **62**, 125-155, (2008).

107 Sun, J. H. *et al.* Culture of nucleus pulposus cells from intervertebral disc on self-assembling KLD-12 peptide hydrogel scaffold. *Materials Science & Engineering C-Materials for Biological Applications*, **30**, 975-980, (2010).

108 Desii, A., Chiellini, F., Di Stefano, R., Tine, M. R. & Solaro, R. Hydrogel Scaffolds by Self-Assembly of a Complementary Ionic Tetrapeptide. *Journal of Polymer Science Part a-Polymer Chemistry*, **48**, 986-990, (2010).

109 Carrick, L. *et al.* The internal dynamic modes of charged self-assembled peptide fibrils. *Langmuir*, **21**, 3733-3737, (2005).

110 Aggeli, A. *et al.* Hierarchical self-assembly of chiral rod-like molecules as a model for peptide beta-sheet tapes, ribbons, fibrils, and fibers. *Proceedings of the National Academy of Sciences of the United States of America*, **98**, 11857-11862, (2001).

111 Aggeli, A. *et al.* Responsive gels formed by the spontaneous self-assembly of peptides into polymeric beta-sheet tapes. *Nature*, **386**, 259-262, (1997).

112 Fishwick, C. W. G. *et al.* Structures of helical beta-tapes and twisted ribbons: The role of side-chain interactions on twist and bend behavior. *Nano Letters*, **3**, 1475-1479, (2003).

113 Aggeli, A. *et al.* Engineering of peptide beta-sheet nanotapes. *Journal of Materials Chemistry*, **7**, 1135-1145, (1997).

114 Carrick, L. M. *et al.* Effect of ionic strength on the self-assembly, morphology and gelation of pH responsive beta-sheet tape-forming peptides. *Tetrahedron*, **63**, 7457-7467, (2007).

115 Protopapa, E., Maude, S., Aggeli, A. & Nelson, A. Interaction of Self-Assembling beta-Sheet Peptides with Phospholipid Monolayers: The Role of Aggregation State, Polarity, Charge and Applied Field. *Langmuir*, **25**, 3289-3296, (2009).

116 Protopapa, E., Ringstad, L., Aggeli, A. & Nelson, A. Interaction of self-assembling beta-sheet peptides with phospholipid monolayers: The effect of serine, threonine, glutamine and asparagine amino acid side chains. *Electrochim. Acta*, **55**, 3368-3375, (2010).

117 Maude, S. *et al.* De novo designed positively charged tape-forming peptides: self-assembly and gelation in physiological solutions and their evaluation as 3D matrices for cell growth. *Soft Matter*, **7**, 8085-8099, (2011).

118 Kirkham, J. *et al.* Self-assembling peptide scaffolds promote enamel remineralization. *Journal of Dental Research*, **86**, 426-430, (2007).

119 Ozbas, B., Kretsinger, J., Rajagopal, K., Schneider, J. P. & Pochan, D. J. Salt-triggered peptide folding and consequent self-assembly into hydrogels with tunable modulus. *Macromolecules*, **37**, 7331-7337, (2004).

120 Branco, M. C., Nettesheim, F., Pochan, D. J., Schneider, J. P. & Wagner, N. J. Fast Dynamics of Semiflexible Chain Networks of Self-Assembled Peptides. *Biomacromolecules*, **10**, 1374-1380, (2009).

121 Schneider, J. P. *et al.* Responsive hydrogels from the intramolecular folding and self-assembly of a designed peptide. *Journal of the American Chemical Society*, **124**, 15030-15037, (2002).

122 Ozbas, B., Rajagopal, K., Schneider, J. P. & Pochan, D. J. Semiflexible chain networks formed via self-assembly of beta-hairpin molecules. *Physical Review Letters*, **93**, (2004).

123 Rajagopal, K., Lamm, M. S., Haines-Butterick, L. A., Pochan, D. J. & Schneider, J. P. Tuning the pH Responsiveness of beta-Hairpin Peptide Folding, Self-Assembly, and Hydrogel Material Formation. *Biomacromolecules*, **10**, 2619-2625, (2009).

124 Rughani, R. V. *et al.* Folding, Self-Assembly, and Bulk Material Properties of a De Novo Designed Three-Stranded beta-Sheet Hydrogel. *Biomacromolecules*, **10**, 1295-1304, (2009).

125 Salick, D. A., Kretsinger, J. K., Pochan, D. J. & Schneider, J. P. Inherent antibacterial activity of a peptide-based beta-hairpin hydrogel. *Journal of the American Chemical Society*, **129**, 14793-14799, (2007).

126 Kretsinger, J. K., Haines, L. A., Ozbas, B., Pochan, D. J. & Schneider, J. P. Cytocompatibility of self-assembled ss-hairpin peptide hydrogel surfaces. *Biomaterials*, **26**, 5177-5186, (2005).

127 Geisler, I. M. & Schneider, J. P. Evolution-Based Design of an Injectable Hydrogel. *Advanced Functional Materials*, **22**, 529-537, (2012).

128 Valery, C. *et al.* Molecular origin of the self-assembly of lanreotide into nanotubes: A mutational approach. *Biophysical Journal*, **94**, 1782-1795, (2008).

129 Pouget, E. *et al.* Elucidation of the Self-Assembly Pathway of Lanreotide Octapeptide into beta-Sheet Nanotubes: Role of Two Stable Intermediates. *Journal of the American Chemical Society*, **132**, 4230-4241, (2010).

130 Ipsen, *Somatiline® Depot (Lanreotide) injection* http://www.somatulinedepot.com/, Accessed 18 January, 2011.

131 Castinetti, F., Saveanu, A., Morange, I. & Brue, T. Lanreotide for the treatment of acromegaly. *Advances in Therapy*, **26**, 600-612, (2009).

132 Ducreux, M. *et al.* The antitumoral effect of the long-acting somatostatin analog lanreotide in neuroendocrine tumors. *American Journal of Gastroenterology*, **95**, 3276-3281, (2000).

133 Reches, M. & Gazit, E. Casting metal nanowires within discrete self-assembled peptide nanotubes. *Science*, **300**, 625-627, (2003).

134 Smith, A. M. *et al.* Fmoc-Diphenylalanine self assembles to a hydrogel via a novel architecture based on pi-pi interlocked beta-sheets. *Advanced Materials*, **20**, 37-41, (2008).

135 Reches, M. & Gazit, E. Self-assembly of peptide nanotubes and amyloid-like structures by charged-termini-capped diphenylalanine peptide analogues. *Israel Journal of Chemistry*, **45**, 363-371, (2005).

136 Reches, M. & Gazit, E. Designed aromatic homo-dipeptides: formation of ordered nanostructures and potential nanotechnological applications. *Physical Biology*, **3**, S10-S19, (2006).

137 Vegners, R., Shestakova, I., Kalvinsh, I., Ezzell, R. M. & Janmey, P. A. Use of a gel-forming dipeptide derivative as a carrier for antigen presentation. *J Pept Sci*, **1**, 371-378, (1995).

138 Orbach, R. *et al.* Self-Assembled Fmoc-Peptides as a Platform for the Formation of Nanostructures and Hydrogels. *Biomacromolecules*, **10**, 2646-2651, (2009).

139 Mahler, A., Reches, M., Rechter, M., Cohen, S. & Gazit, E. Rigid, self-assembled hydrogel composed of a modified aromatic dipeptide. *Advanced Materials*, **18**, 1365-1370, (2006).

140 Liang, L. *et al.* Evaluation of the Biocompatibility of Novel Peptide Hydrogel in Rabbit Eye. *Journal of Biomedical Materials Research Part B-Applied Biomaterials*, **93B**, 324-332, (2010).

141 Niece, K. L., Hartgerink, J. D., Donners, J. & Stupp, S. I. Self-assembly combining two bioactive peptide-amphiphile molecules into nanofibers by electrostatic attraction. *Journal of the American Chemical Society*, **125**, 7146-7147, (2003).

142 Harrington, D. A. *et al.* Branched peptide-amphiphiles as self-assembling coatings for tissue engineering scaffolds. *Journal of Biomedical Materials Research Part A*, **78A**, 157-167, (2006).

143 Silva, G. A. *et al.* Selective differentiation of neural progenitor cells by high-epitope density nanofibers. *Science*, **303**, 1352-1355, (2004).

144 Taton, T. A. Nanotechnology - Boning up on biology. *Nature*, **412**, 491-492, (2001).

145 Cui, H., Muraoka, T., Cheetham, A. G. & Stupp, S. I. Self-Assembly of Giant Peptide Nanobelts. *Nano Letters*, **9**, 945-951, (2009).

146 Jin, Y. *et al.* Bioactive Amphiphilic Peptide Derivatives with pH Triggered Morphology and Structure. *Macromolecular Rapid Communications*, **29**, 1726-1731, (2008).

147 Beniash, E., Hartgerink, J. D., Storrie, H., Stendahl, J. C. & Stupp, S. I. Self-assembling peptide amphiphile nanofiber matrices for cell entrapment. *Acta Biomaterialia*, **1**, 387-397, (2005).

148 Huang, Z. *et al.* Bioactive Nanofibers Instruct Cells to Proliferate and Differentiate During Enamel Regeneration. *Journal of Bone and Mineral Research*, **23**, 1995-2006, (2008).

149 Tysseling-Mattiace, V. M. *et al.* Self-assembling nanofibers inhibit glial scar formation and promote axon elongation after spinal cord injury. *Journal of Neuroscience*, **28**, 3814-3823, (2008).

150 Ghanaati, S. *et al.* Dynamic in vivo biocompatibility of angiogenic peptide amphiphile nanofibers. *Biomaterials*, **30**, 6202-6212, (2009).

151 Galler, K. M., Aulisa, L., Regan, K. R., D'Souza, R. N. & Hartgerink, J. D. Self-Assembling Multidomain Peptide Hydrogels: Designed Susceptibility to Enzymatic Cleavage Allows Enhanced Cell Migration and Spreading. *Journal of the American Chemical Society*, **132**, 3217-3223, (2010).

152 Dong, H., Paramonov, S. E., Aulisa, L., Bakota, E. L. & Hartgerink, J. D. Self-assembly of multidomain peptides: Balancing molecular frustration controls conformation and nanostructure. *Journal of the American Chemical Society*, **129**, 12468-12472, (2007).

153 Aulisa, L., Dong, H. & Hartgerink, J. D. Self-Assembly of Multidomain Peptides: Sequence Variation Allows Control over Cross-Linking and Viscoelasticity. *Biomacromolecules*, **10**, 2694-2698, (2009).

154 Galler, K. M. *et al.* Self-Assembling Peptide Amphiphile Nanofibers as a Scaffold for Dental Stem Cells. *Tissue Engineering Part A*, **14**, 2051-2058, (2008).

155 Zou, Z. W., Zheng, Q. X., Wu, Y. C., Song, W. & Wu, B. Growth of rat dorsal root ganglion neurons on a novel self-assembling scaffold containing IKVAV

sequence. *Materials Science & Engineering C-Materials for Biological Applications*, **29**, 2099-2103, (2009).

156 Mitra, R. N., Shome, A., Paul, P. & Das, P. K. Antimicrobial activity, biocompatibility and hydrogelation ability of dipeptide-based amphiphiles. *Organic & Biomolecular Chemistry*, **7**, 94-102, (2009).

157 Apostolovic, B., Danial, M. & Klok, H. A. Coiled coils: attractive protein folding motifs for the fabrication of self-assembled, responsive and bioactive materials. *Chemical Society Reviews*, **39**, 3541-3575, (2010).

158 Bromley, E. H. C. *et al.* Assembly Pathway of a Designed alpha-Helical Protein Fiber. *Biophysical Journal*, **98**, 1668-1676, (2010).

159 Gribbon, C. *et al.* MagicWand: A single, designed peptide that assembles to stable, ordered alpha-helical fibers. *Biochemistry*, **47**, 10365-10371, (2008).

160 Burkhard, P., Meier, M. & Lustig, A. Design of a minimal protein oligomerization domain by a structural approach. *Protein Science*, **9**, 2294-2301, (2000).

161 Kammerer, R. A. *et al.* Exploring amyloid formation by a de novo design. *Proceedings of the National Academy of Sciences of the United States of America*, **101**, 4435-4440, (2004).

162 Kammerer, R. A. & Steinmetz, M. O. De novo design of a two-stranded coiled-coil switch peptide. *Journal of Structural Biology*, **155**, 146-153, (2006).

163 Banwell, E. F. *et al.* Rational design and application of responsive alpha-helical peptide hydrogels. *Nature Materials*, **8**, 596-600, (2009).

164 Porat, Y., Stepensky, A., Ding, F. X., Naider, F. & Gazit, E. Completely different amyloidogenic potential of nearly identical peptide fragments. *Biopolymers*, **69**, 161-164, (2003).

165 O'Nuallain, B., Williams, A. D., Westermark, P. & Wetzel, R. Seeding specificity in amyloid growth induced by heterologous fibrils. *Journal of Biological Chemistry*, **279**, 17490-17499, (2004).

166 Westermark, P., Lundmark, K. & Westermark, G. T. Fibrils from Designed Non-Amyloid-Related Synthetic Peptides Induce AA-Amyloidosis during Inflammation in an Animal Model. *Plos One*, **4**, (2009).

167 Glasoe, P. K. & Long, F. A. Use of glass electrodes to measure acidities in deuterium oxide, *Journal of Physical Chemistry*, **64**, 188-190, (1960).

168 Reid, D. G. *Protein NMR Techniques*. Vol. 60 (Humana Press, (1997)).

169 Lazar, K. L., Kurutz, J. W., Tycko, R. & Meredith, S. C. Encapsulation and NMR on an aggregating peptide before fibrillogenesis. *Journal of the American Chemical Society*, **128**, 16460-16461, (2006).

170 Williamson, M. P. & Waltho, J. P. PEPTIDE STRUCTURE FROM NMR. *Chemical Society Reviews*, **21**, 227-236, (1992).

171 Aggeli, A., Bell, M., Boden, N., Carrick, L. M. & Strong, A. E. Self-assembling peptide polyelectrolyte beta-sheet complexes form nematic hydrogels. *Angewandte Chemie-International Edition*, **42**, 5603-5606, (2003).

172 Wuthrich, K. *NMR of Proteins and Nucleic Acids*. (John Wiley & Sons, (1986)).

173 Davies, R. P. W. *Hierarchical self-assembly of de novo beta-sheet tape forming peptides in solution* Doctor of Philosophy thesis, PhD Thesis, University of Leeds, (2009).

174 Chary, K. V. R. & Govirl, G. *NMR in Biological Systems*. Vol. 6 (Springer, (2008)).

175 NobelPrize.Org, *The Transmission Electron Microscope*, http://nobelprize.org/educational_games/physics/microscopes/tem/index.html.

176 Brydson, P. R. Electron Microscopy Lectures. *SOMS 5100 Generic Methodologies for Nanotechnology*, (2008).

177 Greenfield, N. J. Using circular dichroism spectra to estimate protein secondary structure. *Nature Protocols*, **1**, 2876-2890, (2006).

178 Kelly, S. M., Jess, T. J. & Price, N. C. How to study proteins by circular dichroism. *BBA-Proteins Proteomics*, **1751**, 119-139, (2005).

179 Mitchell, S. A PHOTO-ELECTRIC METHOD FOR MEASURING CIRCULAR DICHROISM. *Nature*, **166**, 434-435, (1950).

180 Whitmore, L. & Wallace, B. A. Protein secondary structure analyses from circular dichroism spectroscopy: Methods and reference databases. *Biopolymers*, **89**, 392-400, (2008).

181 NMSU, *Circular Dichroism*, http://www.chemistry.nmsu.edu/Instrumentation/CD1.html, Accessed 11th March, 2009.

182 Dudley H Williams, I. F. *Spectroscopic methods in organic chemistry*. 5th edn, (McGraw-Hill Book Company, (1995)).

183 Susi, H. *Infrared spectroscopy—Conformation* Vol. 26 ((1972)).

184 Kong, J. & Yu, S. Fourier transform infrared spectroscopic analysis of protein secondary structures. *Acta Biochimica Et Biophysica Sinica*, **39**, 549-559, (2007).

185 Haris, P. I. & Chapman, D. The conformational-analysis of peptides using fourier-transform IR spectroscopy. *Biopolymers*, **37**, 251-263, (1995).

186 Susi, H. & Byler, D. M. Resolution-enhanced Fourier-transform infrared-spectroscopy of enzymes, *Methods in Enzymology*, **130**, 290-311, (1986).

187 Jackson, M. & Mantsch, H. H. The use and misuse of FTIR spectroscopy in the determination of protein-structure, *Critical Reviews in Biochemistry and Molecular Biology*, **30**, 95-120, (1995).

188 Chen, Y., Mehok, A. R., Mant, C. T. & Hodges, R. S. Optimum concentration of trifluoroacetic acid for reversed-phase liquid chromatography of peptides revisited. *Journal of Chromatography A*, **1043**, 9-18, (2004).

189 Maude, S. *Design and Characterisation of Functionalised Self-Assembled Peptide Nanostructures* PhD thesis, PhD Thesis, University of Leeds, (2010).

190 Stuart, B. *Modern Infrared Spectroscopy*. 1st edn, (John Wiley & Sons, (1996)).

191 Barnes, H. A. *A handbook of elementary rheology*. (The University of Wales Institute of Non-Newtonian Fluid Mechanics, Department of Mathematics, University of Wales Aberystwyth, (2000)).

192 Duffy, J. *Rheology - More than just viscosity!*, (Malvern 2010).

193 *High Inertia Rheometer Design* http://www.nobadscience.com/rheo1.htm, Accessed 28.8.10, 2010.

194 Yan, C. & Pochan, D. Rheological properties of peptide-based hydrogels for biomedical and other applications. *Chem Soc Rev.*, **39**, (2010).

195 Gosal, W. S. & Ross-Murphy, S. B. Globular protein gelation. *Current Opinion in Colloid & Interface Science*, **5**, 188-194, (2000).

196 Rammensee, S., Huemmerich, D., Hermanson, K. D., Scheibel, T. & Bausch, A. R. Rheological characterization of hydrogels formed by recombinantly produced spider silk. *Applied Physics a-Materials Science & Processing*, **82**, 261-264, (2006).

197 Scanlon, S. *Nanostructured Porous Materials Based on Designed Self-Assembling Biopolymers* PhD thesis, PhD Thesis, University of Leeds, (2006).

198 Nyrkova, I. A. *et al.* Self-assembly and structure transformations in living polymers forming fibrils. *European Physical Journal B*, **17**, 499-513, (2000).

199 David L. Nelson & Cox, M. M. *Lehninger Principles of Biochemistry*. 4th edn, 48 (W. H. Freemam, (2004)).

200 Perutz, M. *Protein Science*, **3**, 1629-1637, (1994).

201 Genove, E., Shen, C., Zhang, S. & Semino, C. E. The effect of functionalized self-assembling peptide scaffolds on human aortic endothelial cell function. *Biomaterials*, **26**, 3341-3351, (2005).

202 Sun, L. J. & Zhao, X. J. A self-assembling peptide RADA16-I integrated with spider fibroin uncrystalline motifs. *International Journal of Nanomedicine*, **7**, 571-580, (2012).

203 Hule, R. A. *et al.* Correlations between structure, material properties and bioproperties in self-assembled beta-hairpin peptide hydrogels. *Faraday Discussions*, **139**, 251-264, (2008).

204 Jayawarna, V. *et al.* Introducing chemical functionality in Fmoc-peptide gels for cell culture. *Acta Biomaterialia*, **5**, 934-943, (2009).

205 Gelain, F. *et al.* New bioactive motifs and their use in functionalized self-assembling peptides for NSC differentiation and neural tissue engineering. *Nanoscale*, **4**, 2946-2957, (2012).

206 Levine, A. J., Head, D. A. & MacKintosh, F. C. The deformation field in semiflexible networks. *Journal of Physics-Condensed Matter*, **16**, S2079-S2088, (2004).

207 Gardel, M. L. *et al.* Elastic Behavior of cross-linked and bundled actin networks. *Science*, **304**, 1301-1305, (2004).

208 King, M. W., *Glycosaminoglycans*, http://themedicalbiochemistrypage.org/glycans.php, Accessed 16th July, 2012.

209 Glycosan, *Glycosaminoglycans*, http://www.glycosan.com/glycosaminoglycans/, Accessed 16th July, 2012.

210 Iozzo, R. V. Matrix proteoglycans: From molecular design to cellular function. *Annual Review of Biochemistry*, **67**, 609-652, (1998).

211 Oussoren, E., Brands, M., Ruijter, G. J. G., van der Ploeg, A. T. & Reuser, A. J. J. Bone, joint and tooth development in mucopolysaccharidoses: Relevance to therapeutic options. *Biochimica Et Biophysica Acta-Molecular Basis of Disease*, **1812**, 1542-1556, (2011).

212 Cheng, F. *et al.* Variations in the chondroitin sulfate-protein linkage region of aggrecans from bovine nasal and human articular cartilages. *Journal of Biological Chemistry*, **271**, 28572-28580, (1996).

213 Garnjanagoonchorn, W., Wongekalak, L. & Engkagul, A. Determination of chondroitin sulfate from different sources of cartilage. *Chemical Engineering and Processing*, **46**, 465-471, (2007).

214 Lowther, D. A., Preston, B. N. & Meyer, F. A. Isolation and properties of chondroitin sulphates from bovine heart valves, *Biochemical Journal*, **118**, 595-601, (1970).

215 Takagi, M., Maeno, M., Yamada, T., Miyashita, K. & Otsuka, K. Nature and distribution of chondroitin sulphate and dermatan sulphate proteoglycans in rabbit alveolar bone. *Histochemical Journal*, **28**, 341-351, (1996).

216 Yamamoto, T. *et al.* Ultrastructural and immunohistochemical studies of medullary bone calcification, with special reference to sulphated glycosaminoglycans. *Journal of Electron Microscopy*, **54**, 29-34, (2005).

217 Altintas, A. *et al.* Hyaluronic Acid Levels and Physical Characteristics of Synovial Fluid in Healthy and Diarrheic Calves with Arthritis. *Turkish Journal of Biochemistry-Turk Biyokimya Dergisi*, **35**, 14-19.

218 Balazs, E. A., Watson, D., Duff, I. F. & Roseman, S. Hyaluronic acid in synovial fluid .I. Molecular parameters of hyaluronic acid in normal and arthritic human fluids. *Arthritis and Rheumatism*, **10**, 357-376, (1967).

219 Bignami, A., Hosley, M. & Dahl, D. Hyaluronic-acid and hyaluronic acid-binding proteins in brain extracellular-matrix, *Anatomy and Embryology*, **188**, 419-433, (1993).

220 Nusgens, B. V. Hyaluronic acid and extracellular matrix: a primitive molecule? *Annales De Dermatologie Et De Venereologie*, **137**, S3-S8, (2010).

221 Pirie, A. OX VITREOUS HUMOUR .2. HYALURONIC ACID RELATIONSHIPS. *British Journal of Ophthalmology*, **33**, 271-283, (1949).

222 Davis, Y. *et al.* Keratan sulphate in the trabecular meshwork and cornea. *Current Eye Research*, **16**, 677-686, (1997).

223 Fullwood, N. J. *et al.* Cell surface-associated keratan sulfate on normal and migrating corneal endothelium. *Investigative Ophthalmology & Visual Science*, **37**, 1256-1270, (1996).

224 Scott, J. E. KERATAN SULFATE - A RESERVE POLYSACCHARIDE. *European Journal of Clinical Chemistry and Clinical Biochemistry*, **32**, 217-223, (1994).

225 Postacchini, F. *Lumbar Disc Herniation*. 1st edn, (Springer, (1999)).

226 Buddecke, E. & Sziegoleit, M. Isolierung chemische zusammensetzung + altersabhangige verteilung von mucopolysacchariden menschlicher zwischenwirbelscheiben, *Hoppe-Seyler's Zeitschrift Für Physiologische Chemie*, **337**, 66-78, (1964).

227 McLaurin, J. & Fraser, P. E. Effect of amino-acid substitutions on Alzheimer's amyloid-beta peptide-glycosaminoglycan interactions. *European Journal of Biochemistry*, **267**, 6353-6361, (2000).

228 Fraser, P. E., Nguyen, J. T., Chin, D. T. & Kirschner, D. A. Effects of sulfate-ions on alzheimer-beta/A4 peptide assemblies - implications for amyloid fibril proteoglycan interactions. *Journal of Neurochemistry*, **59**, 1531-1540, (1992).

229 McLaurin, J., Franklin, T., Zhang, X. Q., Deng, J. P. & Fraser, P. E. Interactions of Alzheimer amyloid-beta peptides with glycosaminoglycans - Effects on fibril nucleation and growth. *European Journal of Biochemistry*, **266**, 1101-1110, (1999).

230 Gelman, R. A. & Blackwel.J. Heparin-polypeptide interactions in aqueous-solution, *Archives of Biochemistry and Biophysics*, **159**, 427-433, (1973).

231 Whatley, B. R. & Wen, X. J. Intervertebral disc (IVD): Structure, degeneration, repair and regeneration. *Materials Science & Engineering C-Materials for Biological Applications*, **32**, 61-77, (2012).

232 *FDA Briefing* http://www.fda.gov/ohrms/dockets/ac/05/briefing/2005-4181b2.htm, Accessed 4th June, 2012.

233 Nerurkar, N. L., Elliott, D. M. & Mauck, R. L. Mechanical design criteria for intervertebral disc tissue engineering. *Journal of Biomechanics*, **43**, 1017-1030, (2010).

234 Wilke, H. J., Heuer, F., Neidlinger-Wilke, C. & Claes, L. Is a collagen scaffold for a tissue engineered nucleus replacement capable of restoring disc height and stability in an animal model? *European Spine Journal*, **15**, S433-S438, (2006).

235 Joshi, A. *et al.* Functional compressive mechanics of a PVA/PVP nucleus pulposus replacement. *Biomaterials*, **27**, 176-184, (2006).

236 Gruber, H. E. *et al.* Deleterious effects of discography radiocontrast solution on human annulus cell in vitro: changes in cell viability, proliferation, and apoptosis in exposed cells. *Spine Journal*, **12**, 329-335, (2012).

237 Michalek, A. J., Buckley, M. R., Bonassar, L. J., Cohen, I. & Iatridis, J. C. The effects of needle puncture injury on microscale shear strain in the intervertebral disc annulus fibrosus. *Spine Journal*, **10**, 1098-1105, (2010).

238 Videman, T. *et al.* Progression and determinants of quantitative magnetic resonance imaging measures of lumbar disc degeneration - A five-year follow-up of adult male monozygotic twins. *Spine*, **33**, 1484-1490, (2008).

239 Sobajima, S. *et al.* A slowly progressive and reproducible animal model of intervertebral disc degeneration characterized by MRI, x-ray, and histology. *Spine*, **30**, 15-24, (2005).

240 Sobajima, S. *et al.* Quantitative analysis of gene expression in a rabbit model of intervertebral disc degeneration by real-time polymerase chain reaction. *Spine*, **5**, 14-23, (2005).

241 Elliott, D. M. *et al.* The effect of relative needle diameter in puncture and sham injection animal models of degeneration. *Spine*, **33**, 588-596, (2008).

242 Carragee, E. J. *et al.* 2009 ISSLS Prize Winner: Does Discography Cause Accelerated Progression of Degeneration Changes in the Lumbar Disc A Ten-Year Matched Cohort Study. *Spine*, **34**, 2338-2345, (2009).

243 J. C. Iatridis, M. Weidenbaum, L. A. Setton & V. C. Mow. *Spine*, **21**, 1174-1184, (1996).

244 Johannessen, W. & Elliott, D. M. Effects of degeneration on the biphasic material properties of human nucleus pulposus in confined compression. *Spine*, **30**, E724-E729, (2005).

245 Demers, C. N., Antoniou, J. & Mwale, F. Value and limitations of using the bovine tail as a model for the human lumbar spine. *Spine*, **29**, 2793-2799, (2004).

246 Beckstein, J. C., Sen, S., Schaer, T. P., Vresilovic, E. J. & Elliott, D. M. Comparison of animal discs used in disc research to human lumbar disc. *Spine*, **33**, E166-E173, (2008).

247 O'Connell, G. D., Vresilovic, E. J. & Elliott, D. M. Comparison of animals used in disc research to human lumbar disc geometry. *Spine*, **32**, 328-333, (2007).

248 Ishihara, H., Warensjo, K., Roberts, S. & Urban, J. P. G. Proteoglycan synthesis in the intervertebral disk nucleus: The role of extracellular osmolality. *American Journal of Physiology-Cell Physiology*, **272**, C1499-C1506, (1997).

249 Roberts, S., Eisenstein, S. M., Menage, J., Evans, E. H. & Ashton, I. K. Mechanoreceptors in intervertebral discs - Morphology, distribution, and neuropeptides. *Spine*, **20**, 2645-2651, (1995).

250 Oloyede, A., Broom, N. D. & Martinez, J. B. Experimental factors governing the internal stress state of the intervertebral disc. *Medical Engineering & Physics*, **20**, 631-637, (1998).

251 Race, A., Broom, N. D. & Robertson, P. Effect of loading rate and hydration on the mechanical properties of the disc. *Spine*, **25**, 662-669, (2000).

252 Akmal, M. *et al.* Effect of nicotine on spinal disc cells: A cellular mechanism for disc degeneration. *Spine*, **29**, 568-575, (2004).

253 Korecki, C. L., MacLean, J. J. & Iatridis, J. C. Dynamic compression effects on intervertebral disc mechanics and biology. *Spine*, **33**, 1403-1409, (2008).

254 Schechtman, H., Robertson, P. A. & Broom, N. D. Failure strength of the bovine caudal disc under internal hydrostatic pressure. *Journal of Biomechanics*, **39**, 1401-1409, (2006).

255 Simunic, D. I., Robertson, P. A. & Broom, N. D. Mechanically induced disruption of the healthy bovine intervertebral disc. *Spine*, **29**, 972-978, (2004).

256 Farndale, R. W., Buttle, D. J. & Barrett, A. J. Improved quantitation and discrimination of sulfated glycosaminoglycans by use of dimethylmethylene blue *Biochimica Et Biophysica Acta*, **883**, 173-177, (1986).

257 Sabiston, P., Adams, M. E. & Ho, Y. A. Automation of 1,9-dimethylmethylene blue dye-binding assay for sulfated glycosaminoglycans with application to cartilage microcultures. *Analytical Biochemistry*, **149**, 543-548, (1985).

258 Templeton, D. M. The basis and applicability of the dimethylmethylene blue binding assay for sulfated glycosaminoglycans, *Connective Tissue Research*, **17**, 23-32, (1988).

259 Gold, E. W. Simple spectrophotometric method for estimating glycosaminoglycan concentrations, *Analytical Biochemistry*, **99**, 183-188, (1979).

260 Enobakhare, B. O., Bader, D. L. & Lee, D. A. Quantification of sulfated glycosaminoglycans in chondrocyte/alginate cultures, by use of 1,9-dimethylmethylene blue. *Analytical Biochemistry*, **243**, 189-191, (1996).

261 Muller, G. & Hanschke, M. Quantitative and qualitative analyses of proteoglycans in cartilage extracts by precipitation with 1,9-dimethylmethylene blue. *Connective Tissue Research*, **33**, 243-248, (1996).

262 Oke, S. L., Hurtig, M. B., Keates, R. A., Wright, J. R. & Lumsden, J. H. Assessment of three variations of the 1,9-dimethylmethylene blue assay for measurement of sulfated glycosaminoglycan concentrations in equine synovial fluid. *American Journal of Veterinary Research*, **64**, 900-906, (2003).

263 Barbosa, I. *et al.* Improved and simple micro assay for sulfated glycosaminoglycans quantification in biological extracts and its use in skin and muscle tissue studies. *Glycobiology*, **13**, 647-653, (2003).

264 Wiseman, M. A., Birch, H. L., Akmal, M. & Goodship, A. E. Segmental variation in the in vitro cell metabolism of nucleus pulposus cells isolated from a series of bovine caudal intervertebral discs. *Spine*, **30**, 505-511, (2005).

265 Buser, Z. *et al.* Biological and Biomechanical Effects of Fibrin Injection Into Porcine Intervertebral Discs. *Spine*, **36**, E1201-E1209, (1976).

266 Meakin, J. R., Reid, J. E. & Hukins, D. W. L. Replacing the nucleus pulposus of the intervertebral disc. *Clinical Biomechanics*, **16**, 560-565, (2001).

267 Iatridis, J. C., Setton, L. A., Weidenbaum, M. & Mow, V. C. The viscoelastic behavior of the non-degenerate human lumbar nucleus pulposus in shear. *Journal of Biomechanics*, **30**, 1005-1013, (1997).

268 Meakin, J. R. & Hukins, D. W. L. Effect of removing the nucleus pulposus on the deformation of the annulus fibrosus during compression of the intervertebral disc. *Journal of Biomechanics*, **33**, 575-580, (2000).

269 Panjabi, M. M. The stabilizing system of the spine .2. Neutral zone and instability hypothesis. *Journal of Spinal Disorders*, **5**, 390-397, (1992).

270 Crawford, N. R., Peles, J. D. & Dickman, C. A. The spinal lax zone and neutral zone: Measurement techniques and parameter comparisons. *Journal of Spinal Disorders*, **11**, 416-429, (1998).

271 Bron, J. L., Koenderink, G. H., Everts, V. & Smit, T. H. Rheological Characterization of the Nucleus Pulposus and Dense Collagen Scaffolds Intended for Functional Replacement. *Journal of Orthopaedic Research*, **27**, 620-626, (2009).

272 Meakin, J. R., Redpath, T. W. & Hukins, D. W. L. The effect of partial removal of the nucleus pulposus from the intervertebral disc on the response of the human annulus fibrosus to compression. *Clinical Biomechanics*, **16**, 121-128, (2001).

273 Costi, J. J., Stokes, I. A., Gardner-Morse, M. G. & Iatridis, J. C. Frequency-dependent behavior of the intervertebral disc in response to each of six degree of freedom dynamic loading - Solid phase and fluid phase contributions. *Spine*, **33**, 1731-1738, (2008).

274 Perie, D., Korda, D. & Iatridis, J. C. Confined compression experiments on bovine nucleus pulposus and annulus fibrosus: sensitivity of the experiment in the determination of compressive modulus and hydraulic permeability. *Journal of Biomechanics*, **38**, 2164-2171, (2005).

275 Bron, J. L. *et al.* Migration of intervertebral disc cells into dense collagen scaffolds intended for functional replacement. *Journal of Materials Science-Materials in Medicine*, **23**, 813-821, (2012).